UNIVERSITY OF CALIFORNIA

Santa Barbara

Application of Mathematical Modeling in Cancer, Blood Clotting Abnormalities and Migraine Headaches Research

A dissertation submitted in partial satisfaction of the

requirements for the degree Doctor of Philosophy

in Mechanical Engineering

by

Hamed Ghaffari

Committee in charge:

Professor Linda Petzold, Chair

Professor Jeff Moehlis

Professor Carl Meinhart

Professor John Gilbert

March 2020

The dissertation of Hamed Ghaffari is approved.

_____

Jeff Moehlis

_____

Carl Meinhart

_____

John Gilbert

_____

Linda Petzold, Committee Chair

Application of Mathematical Modeling in Cancer, Blood Clotting Abnormalities and Migraine Headaches Research

by

Hamed Ghaffari

I would like to dedicate this dissertation to my loving parents and sister for their love and support throughout my life.

ACKNOWLEDGEMENTS

I would like to express my deepest gratitude to everyone who helped me during my PhD journey. First and foremost, I would like to thank my PhD adviser, Linda Petzold, not only for the years of advice, support and guidance, but also for giving me a chance. In addition, I would like to thank my committee members, Jeff Moehlis, Carl Meinhart and John Gilbert for generously offering their time and advice throughout the preparation and review of this dissertation. I would also like to thank my scientific collaborators, Michael Harrington and Jeff Varner for their advice and insight. I would also like to thank all the friends made in Santa Barbara. Last but not least, thanks to my parents and sister for their love, encouragement, and unwavering support over the years. Thank you very much for giving me strength to reach for the stars and chase my dreams.

Curriculum Vitæ OF HAMED GHAFFARI
March 2020

EDUCATION

Bachelor of Science in Mechanical Engineering, K.N. Toosi University of Technology, September 2011
Master of Science in Mechanical Engineering, Sharif University of Technology, January 2014
Doctor of Philosophy in Mechanical Engineering, University of California, Santa Barbara, March 2020

PROFESSIONAL EMPLOYMENT

2014-20: Research Assistant, Department of Mechanical Engineering, University of California, Santa Barbara
Summer 2017: Summer Internship, Celgene Corporation
Spring 2019: Teaching Assistant, College of Engineering, University of California, Santa Barbara
Summer 2019: Summer Internship, Gilead Sciences, Inc.
Fall 2019: Teaching Assistant, Department of Mechanical Engineering, University of California, Santa Barbara

PUBLICATIONS

"Identification of influential proteins in the classical retinoic acid signaling pathway," *Theoretical Biology and Medical Modelling*, (2018), 15(1):16.

"Analysis of the role of thrombomodulin in all-trans retinoic acid treatment of coagulation disorders in cancer patients," *Theoretical Biology and Medical Modelling*. (2019), 16(1):3.

"Regulation of cerebrospinal fluid and brain tissue sodium levels by choroid plexus and brain capillary endothelial cell sodium-potassium pumps during migraine," *bioRxiv*. (2019), 572727.

"Regulation of CSF and brain tissue sodium levels by the blood-CSF and blood-brain barriers during migraine." *Frontiers in Computational Neuroscience* 14 (2020): 4.

"Biomechanical analysis of actin cytoskeleton function based on a spring network cell model," *Proceedings of the Institution of Mechanical Engineers, Part C: Journal of Mechanical Engineering Science*, (2017), 231(7):1308-23.

"Analysis of free-surface effects on swimming by the application of the computational fluid dynamics method," *Proceedings of the Institution of Mechanical Engineers, Part P: Journal of Sports Engineering and Technology*, (2016), 230(3):135-48.

ABSTRACT

Application of Mathematical Modeling in Cancer, Blood Clotting Abnormalities and Migraine Headaches Research

by

Hamed Ghaffari

Mathematical modeling of biological processes has contributed significantly to improving our understanding of how different biological systems function, how and why different diseases start and develop, and how the diseases can be prevented or treated. In the first part of this dissertation, we use mechanistic modeling together with local and global sensitivity analyses to explore why different patients and/or different cancer types respond differently to retinoic acid (RA), an anticancer drug. Our findings indicate that the efficacy of RA treatment highly depends on intracellular levels of four main RA binding proteins namely, retinoic acid receptor (RAR), cellular retinoic acid binding proteins (CRABP1 and CRABP2) and cytochrome P450 (CYP). These proteins are expressed at different levels in different patients and/or cell types. Our results indicate that CRABP2 and RAR are the most and the least important receptors, respectively, in regulating the response to RA treatment at physiological concentrations (1–10 nM). However, at pharmacological concentrations of RA (0.1–1 μM), CYP and RAR are the most sensitive parameters of the model. These results can help in the development of pharmacological methods to increase the efficacy of

the drug. In the second part of this dissertation, we study the positive side effects of RA therapy on blood clotting abnormalities in cancer patients. Although there are several lines of evidence regarding the improvement of hemostatic complications such as thrombosis and disseminated intravascular coagulation (DIC) in cancer patients undergoing RA therapy, the mechanisms underlying this improvement have yet to be understood. We build mechanistic and pharmacokinetics models and use in vitro and pharmacokinetics data from the literature to test the hypothesis that this improvement is due to RA-induced upregulation of thrombomodulin (TM) on the endothelial cells. Our results indicate that treatment with a single daily oral dose of 110 $\frac{mg}{m^2}$ RA, increases the TM concentration by almost two folds. We then show that this RA-induced TM upregulation reduces the peak thrombin levels and endogenous thrombin potential (ETP) up to 50 and 49%, respectively. Our results demonstrate that progressive reductions in plasma levels of RA, observed in continuous RA therapy with a once-daily oral dose of 110 $\frac{mg}{m^2}$ RA do not influence TM-mediated decrease in thrombin generation. This observation raises the hypothesis that continuous RA treatment will have more consistent therapeutic effects on coagulation disorders than on cancer. Our results reveal that the upregulation of TM expression on the endothelial cells over the course of RA therapy could significantly contribute to the treatment of coagulation abnormalities in cancer patients. In the last part of this dissertation, we use mechanistic modeling to study sodium homeostasis disturbance in the brain during migraines. Previous animal and human studies have revealed that migraine sufferers have higher levels of cerebrospinal fluid (CSF) and brain tissue sodium than control groups, while the underlying mechanisms of this increase are not known. Under the hypothesis that disturbances in sodium transport mechanisms at the blood-CSF barrier (BCSFB) and/or the blood-brain barrier (BBB) are

the underlying cause of the elevated CSF and brain, we develop a mechanistic model of a rat's brain to compare the significance of the BCSFB and the BBB in controlling CSF and brain tissue sodium levels. Our model consists of the ventricular system, subarachnoid space, brain tissue and blood. We model sodium transport from blood to CSF across the BCSFB, and from blood to brain tissue across the BBB by influx permeability coefficients P_{BCSFB} and P_{BBB}, respectively, while sodium movement from CSF into blood across the BCSFB, and from brain tissue to blood across the BBB were modeled by efflux permeability coefficients P'_{BCSFB} and P'_{BBB}, respectively. We then perform a global sensitivity analysis to investigate the sensitivity of the ventricular CSF, subarachnoid CSF and brain tissue sodium levels to pathophysiological variations in P_{BCSFB}, P_{BBB}, P'_{BCSFB} and P'_{BBB}. Our findings indicate that the ventricular CSF sodium concentration is highly influenced by perturbations of P_{BCSFB}, and to a much lesser extent by perturbations of P'_{BCSFB}. Brain tissue and subarachnoid CSF sodium concentrations are more sensitive to pathophysiological variations of P_{BBB} and P'_{BBB} than variations of P_{BCSFB} and P'_{BCSFB} within 30 minutes of the onset of the perturbations. However, P_{BCSFB} is the most sensitive model parameter, followed by P_{BBB} and P'_{BBB}, in controlling brain tissue and subarachnoid CSF sodium levels within 3 hours of the perturbation onset. Our findings suggest that increased influx permeability of the BCSFB to sodium caused by altered homeostasis of the enzymes which transport sodium from blood to CSF is the potential cause of elevated brain sodium levels in migraines.

Chapter 1

Introduction

Mathematical modeling is a powerful tool for not only understanding how different diseases start and progress, but also for the development of new treatments for the diseases. In this dissertation, we use mathematical modeling to study the mechanism of action of retinoic acid (RA), an anticancer drug, in the treatment of cancer and blood clotting disorders, as well as explore the regulatory mechanisms of sodium levels in the brain during migraine headaches. In chapter 2, we use mathematical modeling to provide further insight into why different patients and/or different cancers respond differently to retinoic acid (RA), an anticancer drug. It is believed that RA exerts its therapeutic effects by regulating gene expression through the classical retinoic acid signaling pathway. In the classical pathway of retinoic acid (RA) mediated gene transcription, RA binds to a nuclear hormone receptor dimer composed of retinoic acid receptor (RAR) and retinoid X receptor (RXR), to induce the expression of its downstream target genes. In addition to nuclear receptors, there are other intracellular RA binding proteins such as cellular retinoic acid binding proteins (CRABP1 and CRABP2) and cytochrome P450 (CYP) enzymes, whose contributions to the RA signaling pathway have not been fully understood. In this work, we develop a mechanistic model of the classical retinoic acid signaling pathway that RAR, CRABP1, CRABP2, and CYP enzymes. We then use global sensitivity analysis to investigate the contribution of the RA binding proteins to RA-induced mRNA production, when the cells are treated with a wide range of RA levels, from physiological to pharmacological concentrations. Our results show that CRABP2 and RAR are the most and the least important proteins, respectively, in controlling the

model performance at physiological concentrations of RA (1–10 nM). However, at higher concentrations of RA, CYP and RAR are the most sensitive parameters of the system. Furthermore, we found that depending on the concentrations of all RA binding proteins, the rate of metabolism of RA can either change or remain constant following RA therapy. The cellular levels of CRABP1 are more important than that of CRABP2 in controlling RA metabolite formation at pharmacological conditions (RA = 0.1–1 μM). Our results indicate a significant negative correlation between total mRNA production and total RA metabolite formation at pharmacological levels of RA. Our simulations indicate that the significance of the RA binding proteins in the RA pathway of gene expression strongly depends on intracellular concentration of RA. Our findings not only can explain why various cell types and/or various patients respond to RA therapy differently, but also can potentially help develop pharmacological methods to increase the efficacy of the drug.

In chapter 3, we study the therapeutic effects of RA on coagulation disorders in cancer patients. Clinical studies have shown that RA, which is known as an anticancer drug, improves hemostatic parameters and bleeding complications such as thrombosis and disseminated intravascular coagulation (DIC) in cancer patients. However, the mechanisms underlying this improvement have yet to be elucidated. In vitro studies have reported that RA upregulates thrombomodulin (TM) expression on the endothelial cell surface. In this chapter, we investigate how and to what extent the TM concentration changes after RA treatment in cancer patients, and how this variation influences the blood coagulation cascade. In this regard, we introduce an ordinary differential equation (ODE) model of gene expression for the RA-induced upregulation of TM concentration. Coupling the gene expression model with a two-compartment pharmacokinetic model of RA, we obtain the

time-dependent changes in TM and thrombomodulin-mRNA (TMR) concentrations following oral administration of RA. Our results indicate that the TM concentration reaches its peak level almost 14 h after taking a single oral dose ($110\,\frac{mg}{m^2}$) of RA. Continuous treatment with RA results in oscillatory expression of TM on the endothelial cell surface. We then couple the gene expression model with a mechanistic model of the coagulation cascade, and show that the elevated levels of TM over the course of RA therapy with a single daily oral dose ($110\,\frac{mg}{m^2}$) of RA reduces the peak thrombin levels and endogenous thrombin potential (ETP) up to 50 and 49%, respectively. We show that progressive reductions in plasma levels of RA, observed in continuous RA therapy with a once-daily oral dose ($110\,\frac{mg}{m^2}$) of RA, do not affect TM-mediated reduction of thrombin generation significantly. This finding prompts the hypothesis that continuous RA treatment has more consistent therapeutic effects on coagulation disorders than on cancer. Our results indicate that the oscillatory upregulation of TM expression on the endothelial cells over the course of RA therapy could potentially contribute to the treatment of coagulation abnormalities in cancer patients. Further studies on the impacts of RA therapy on the procoagulant activity of cancer cells are needed to better elucidate the mechanisms by which RA therapy improves hemostatic abnormalities in cancer.

In chapter four, we investigate how sodium levels are regulated in the brain during the onset and propagation of migraine. There are several lines of evidence regarding that cerebrospinal fluid (CSF) and brain tissue sodium levels increase during migraine. However, little is known regarding the underlying mechanisms of sodium homeostasis disturbance in the brain during migraine. Exploring the cause of sodium dysregulation in

the brain is important, since correction of the altered sodium homeostasis could potentially treat migraine. Under the hypothesis that disturbances in sodium transport mechanisms at the blood-CSF barrier (BCSFB) and/or the blood-brain barrier (BBB) are the underlying cause of the elevated CSF and brain tissue sodium levels during migraines, we develop a mechanistic, differential equation model of a rat's brain to compare the significance of the BCSFB and the BBB in controlling CSF and brain tissue sodium levels. The model includes the ventricular system, subarachnoid space, brain tissue and blood. Sodium transport from blood to CSF across the BCSFB, and from blood to brain tissue across the BBB were modeled by influx permeability coefficients P_{BCSFB} and P_{BBB}, respectively, while sodium movement from CSF into blood across the BCSFB, and from brain tissue to blood across the BBB were modeled by efflux permeability coefficients P'_{BCSFB} and P'_{BBB}, respectively. We then perform a global sensitivity analysis to investigate the sensitivity of the ventricular CSF, subarachnoid CSF and brain tissue sodium concentrations to pathophysiological variations in P_{BCSFB}, P_{BBB}, P'_{BCSFB} and P'_{BBB}. Our results show that the ventricular CSF sodium concentration is highly influenced by perturbations of P_{BCSFB}, and to a much lesser extent by perturbations of P'_{BCSFB}. Brain tissue and subarachnoid CSF sodium concentrations are more sensitive to pathophysiological variations of P_{BBB} and P'_{BBB} than variations of P_{BCSFB} and P'_{BCSFB} within 30 minutes of the onset of the perturbations. However, P_{BCSFB} is the most sensitive model parameter, followed by P_{BBB} and P'_{BBB}, in controlling brain tissue and subarachnoid CSF sodium levels within 3 hours of the perturbation onset. Our findings prompt the hypothesis that increased influx permeability of the BCSFB to sodium caused by altered homeostasis of the enzymes which transport sodium from blood to CSF is the potential cause of elevated brain sodium levels in

migraines. This hypothesis needs to be tested experimentally. The current model can be used to simulate sodium transport across the BBB, the BCSFB and the ependymal surfaces for a particular migraine trigger, given that the effects of the migraine trigger on the BBB and the BCSFB permeabilities are known.

Chapter 2

Identification of influential proteins in the classical retinoic acid signaling pathway

2.1. Introduction

Retinoic acid (RA), a biologically active form of vitamin A, plays essential roles in the growth and development of various cell types. RA has also been widely used as an anticancer drug due to its ability to inhibit cancer cell growth and induce cell differentiation. It is believed that RA mainly exerts its effects by regulating gene expression. The classical pathway of RA-induced gene transcription involves binding of RA to retinoic acid receptor (RAR), a member of the nuclear hormone family. The liganded RAR binds as a heterodimer (RA:RAR:RXR) to DNA and regulates gene expression. RAR:RXR heterodimer is the main transcription factor in the classical RA signaling pathway. The formation rate of RA:RAR:RXR complex, is highly affected by other intracellular RA binding receptors such as cellular retinoic acid binding proteins (CRABPs) and cytochrome P450 (CYP) enzymes. CRABPs are high affinity cytosolic receptors for RA that can potentially limit the access of RA to the RARs; CRABP1 and CRABP2 are the main members of the CRABP family. It has been reported that CRABP1 is responsible for sequestering RA in the cytosol, and thus controlling the level of free intracellular RA available for binding to RARs [1]. CRABP1 can also facilitate RA degradation by directing RA molecules to RA-degrading enzymes, cytochrome P450 (CYP) [2]. However, other *in vitro* studies have indicated that CRABP1 is dispensable in the RA signaling pathway [3, 4]. CRABP2, whose expression

pattern is different from CRABP1 [5], delivers RA to both nuclear hormone receptors and CYP enzymes [6, 7]. CRABPs are bound to CYPs prior to adding RA to the cell [6, 8].

CYP enzymes are the main components of the pathway by which RA is cleared from the body. It is believed that liver cells which express high levels of CYP enzymes mainly mediate the synthesis and the clearance of RA [9, 10]. However, CYPs are found at various expression levels across different tissues and cell types [10]. Even though CRABP1, CRABP2, RAR and CYP are the main RA binding proteins, little is known about their expression levels across different human cell types. It is important to note that the cellular level of a protein can also vary considerably from cell to cell within a population of cells of the same type. Furthermore, to the best of our knowledge, the extent of contribution of the RA binding receptors to RA-induced gene transcription has yet to be elucidated. Understanding the roles and significance of RA binding receptors in the RA signaling pathway is important since it can help in the development of pharmacological approaches to limit or induce the activity of RA binding receptors, with the aim of increasing drug efficacy. Few previous *in vitro* studies have investigated the impacts of overexpression of CRABP1 and CRABP2 on RA-induced gene expression [3, 11]. However, their results were cell type-dependent, since different cell types have different expression levels of RA binding receptors. Furthermore, it is not clear whether the significance of the RA binding receptors in the RA pathway of gene expression depends on the RA concentration. In this study, we developed a new mathematical model to investigate the importance of various RA binding receptors in the RA signaling pathway in broad regions of RA concentrations. In this regard, we used a variance-based global sensitivity analysis (GSA) technique called Sobol's method [12], which assesses the impacts of the model's unknown parameters and

the interactions between them on the model output. Total mRNA production and total RA metabolite formation within 24 hours after RA treatment were selected as the model outputs, while the unknown parameters included kinetic rate constants and total concentrations of the RA binding receptors. Our results showed that all RA binding receptors could potentially influence mRNA production and RA metabolite formation by the RA pathway. However, the impact of a particular RA binding receptor on the model response largely depends on the concentrations of all RA binding receptors.

The main advantage of the current study over previous *in vitro* studies is that our results were obtained using wide ranges of RA receptor concentrations for any given RA concentration, thus our results are applicable to most cell types or to a population of cells of the same type. Furthermore, our study is able to reveal the synergistic effects of a combination of parameters across a broad range of parameter values. In contrast, the obtained results from previous experimental studies [3, 11] reveal the sensitivity of the system with respect to one parameter when the rest of the parameters remain unchanged.

2.2. Methods

2.2.1. Model development

We formulated a well-mixed ODE model of the RA signaling pathway. The model consisted of 17 species, which included proteins, mRNAs, protein-protein complexes and RA (Table 1).

Table 1. List of the model parameters

Parameter	Description
RA	Retinoic acid
CRABP1	Cellular retinoic acid binding protein 1
RA:CRABP1	Holo-cellular retinoic acid binding protein 1
CRABP2	Cellular retinoic acid binding protein 2
RA:CRABP2	Holo-cellular retinoic acid binding protein 2
CYP	CYP enzyme
RA:CYP	Liganded CYP
RAR	Retinoic acid receptor
RA:RAR	Activated retinoic acid receptor
RA:CRABP1:CYP	Activated CRABP1-CYP complex
RA:CRABP2:CYP	Activated CRABP2-CYP complex
RA:CRABP2:RAR	Activated CRABP2-RAR complex
CRABP1:CYP	CRABP1-CYP complex
CRABP2:CYP	CRABP2-CYP complex
$CRABP2_{mRNA}$	Cellular retinoic acid binding protein 2 mRNA
CYP_{mRNA}	CYP enzyme mRNA
RAR_{mRNA}	Retinoic acid receptor mRNA

The model included gene transcription, protein translation, and degradation of mRNA and protein. The model involved the mechanisms by which RA is degraded. The core set of reactions describing the RA metabolism process were taken directly from [6]. We simulated RA-induced gene transcription through the interactions between liganded transcription factor and DNA (Supplementary Information in Section 2.6). The model also describes how

RA binding receptors interact with each other in the absence or presence of RA (Fig. 1). In the absence of RA, CRABPs complex with CYP enzymes, while RARs are not bound to CRABPs or CYPs [6, 8]. Once RA diffuses into the cell, it binds to different RA binding receptors with various binding affinities. CRABP1, which has the highest binding affinity for RA compared to the other RA receptors, regulates the metabolic fate of RA by directing RA molecules to CYP enzymes. In theory, CRABP1 can also transport RA to RAR. This process involves dissociation of RA from CRABP1, followed by association of RA with RAR. CRABP2 is the second high-affinity receptor for RA [5] and can deliver RA to RAR and CYP. RA is transported from CRABP2 to RAR by a mechanism that involves direct interactions between CRABP2 and RAR [5].

RA is transferred to CYP enzymes either freely or bound to CRABPs. RA-induced gene transcription depends on the rate of transfer of RA to RAR. Free RA molecules can interact with RARs directly. CRABP1 and CRABP2 can also deliver RA to RAR by different mechanisms. Liganded transcription factors can enhance the transcriptional activation of *CYP*, *RAR* and *CRABP2* genes after binding to DNA at a retinoic acid response element (RARE). We also assumed that RA was degraded only by CYP, while RA binding receptors, i.e. RAR, CRABP1, CRABP2, CYP were degraded by first-order reactions.

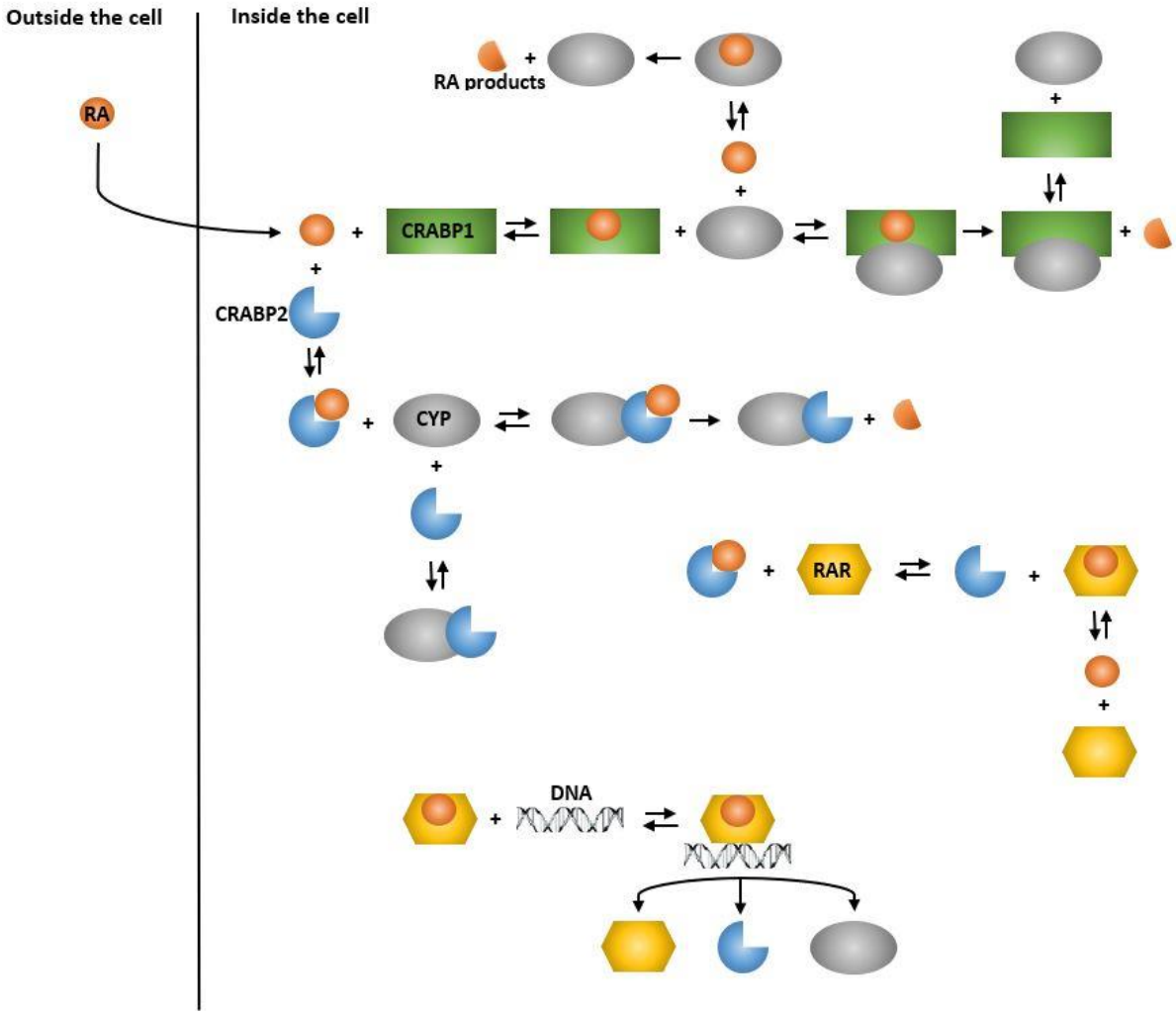

Figure 1. Simplified schematic of RA signaling pathway. CRABP1 is shown in green, while CRABP2 is shown in blue. Red circles, gray ellipsoids and yellow hexagons represent RA molecules, CYP enzymes and RAR molecules, respectively.

The full list of reactions in our model is presented in Table 2

Table 2. List of reactions in the RA signaling pathway

Number	Reaction
1	$\mathrm{RA} + \mathrm{CRABP1} \Leftrightarrow \mathrm{RA{:}\ CRABP1}$
2	$\mathrm{RA} + \mathrm{CRABP2} \Leftrightarrow \mathrm{RA{:}\ CRABP2}$
3	$\mathrm{RA} + \mathrm{CYP} \Leftrightarrow \mathrm{RA{:}\ CYP}$
4	$\mathrm{RA{:}\ CYP} \Rightarrow \mathrm{CYP} + (\mathrm{RA\ metabolites})$
5	$\mathrm{RA} + \mathrm{RAR} \Leftrightarrow \mathrm{RA{:}\ RAR}$
6	$RAR_{\mathrm{mRNA}} \Rightarrow \mathrm{RAR}$
7	$CRABP2_{\mathrm{mRNA}} \Rightarrow \mathrm{CRABP2}$
8	$CYP_{\mathrm{mRNA}} \Rightarrow \mathrm{CYP}$
9	$\mathrm{RA{:}\ CRABP1} + \mathrm{CYP} \Leftrightarrow \mathrm{RA{:}\ CRABP1{:}\ CYP}$
10	$\mathrm{RA{:}\ CRABP1{:}\ CYP} \Rightarrow \mathrm{CRABP1{:}\ CYP} + (\mathrm{RA\ metabolites})$
11	$\mathrm{RA{:}\ CRABP2} + \mathrm{CYP} \Leftrightarrow \mathrm{RA{:}\ CRABP2{:}\ CYP}$
12	$\mathrm{RA{:}\ CRABP2{:}\ CYP} \Rightarrow \mathrm{CRABP2{:}\ CYP} + (\mathrm{RA\ metabolites})$
13	$\mathrm{RA{:}\ CRABP2} + \mathrm{RAR} \Leftrightarrow \mathrm{RA{:}\ CRABP2{:}\ RAR}$
14	$\mathrm{RA{:}\ CRABP2{:}\ RAR} \Rightarrow \mathrm{RA{:}\ RAR} + \mathrm{CRABP2}$
15	$\mathrm{CRABP1} + \mathrm{CYP} \Leftrightarrow \mathrm{CRABP1{:}\ CYP}$
16	$\mathrm{CRABP2} + \mathrm{CYP} \Leftrightarrow \mathrm{CRABP2{:}\ CYP}$
17	$\mathrm{CRABP1} \Rightarrow \emptyset$
18	$\mathrm{CRABP2} \Rightarrow \emptyset$
19	$\mathrm{CYP} \Rightarrow \emptyset$
20	$\mathrm{RAR} \Rightarrow \emptyset$
21	$\mathrm{RA{:}\ CRABP1} \Rightarrow \mathrm{RA} + \emptyset$
22	$\mathrm{RA{:}\ CRABP2} \Rightarrow \mathrm{RA} + \emptyset$

23	$\mathrm{RA: RAR} \Rightarrow \mathrm{RA} + \emptyset$
24	$RAR_{\mathrm{mRNA}} \Rightarrow \emptyset$
25	$CRABP2_{\mathrm{mRNA}} \Rightarrow \emptyset$
26	$CYP_{\mathrm{mRNA}} \Rightarrow \emptyset$
27	$\mathrm{CRABP1: CYP} \Rightarrow \mathrm{CYP} + \emptyset$
28	$\mathrm{CRABP1: CYP} \Rightarrow \mathrm{CRABP1} + \emptyset$
29	$\mathrm{CRABP2: CYP} \Rightarrow \mathrm{CYP} + \emptyset$
30	$\mathrm{CRABP2: CYP} \Rightarrow \mathrm{CRABP2} + \emptyset$

RA-induced expression of *RAR, CRBAP2* and *CYP* genes are modeled using Eq. 4.

Analysis of the model behavior required the initial concentrations of the species and the kinetic parameters. Our model had 44 parameters, which included total concentrations of the RA binding receptors, the kinetic rate constants for binding/unbinding reactions, transcription and translation rate constants and mRNA and protein degradation rates. We assumed that total concentrations of CRABP1, CRABP2, CYP and RAR were unknown, which implies that these proteins are expressed in various levels across different tissues and across a population of cells of the same type. In the absence of RA, total concentrations of RA receptors were given by

$$[\mathrm{CRABP1}_t] = [\mathrm{CRABP1}_f] + [\mathrm{CRABP1: CYP}] \quad (1)$$

$$[\mathrm{CRABP2}_t] = [\mathrm{CRABP2}_f] + [\mathrm{CRABP2: CYP}] \quad (2)$$

$$[\mathrm{CYP}_t] = [\mathrm{CYP}_f] + [\mathrm{CRABP1: CYP}] + [\mathrm{CRABP2: CYP}] \quad (3)$$

where [] indicates molar concentration, while subscripts t and f stand for total and free receptors. RAR does not have any interaction with the remainder of the RA binding receptors, i.e. CRABP1, CRABP2 and CYP, before RA treatment. However, RAR can homodimerize, and heterodimerize with other proteins such as RXR in the absence of RA. In this study, we assumed that RA molecules can bind to free RARs, and to RARs bound to other proteins, with the same binding affinity. Thus, all RARs are receptive to RA binding.

We used *in vitro* values for 30 model parameters (see Supplementary Information in Section 2.6), while the remaining 14 parameters were unknown for which we considered some physiological bounds (Table 3). We also assumed that for a given gene the values of transcription rate constants, translation rate constants, forward and reverse rate constants of the binding reactions and the elimination rates of proteins and mRNAs can vary within the *in vitro* values by a factor of two. This is because not only can these parameters vary across cell type and across cells of the same type, but also all *in vitro* parameters are subject to error.

Table 3. List of the independent model parameters

Parameter	Description	Range	Reference
CRABP1	Total concentration of CRABP1	1 nM – 10 μM	Unknown. A large range is used.
CRABP2	Total concentration of CRABP2	1 nM – 10 μM	Unknown. A large range is used.
CYP	Total concentration of CYP	1 nM – 10 μM	Unknown. A large range is used.

RAR	Total concentration of RAR	1 nM – 1 µM	Unknown. A large range is used.
k_{d3}	Equilibrium dissociation constant of reaction #3	1nM -64 nM	[6]
k_{on13}	Forward rate of reaction #13	3.6×10^9 $- 3.6 \times 10^{10}$	[13]
k_{d13}	Equilibrium dissociation constant of reaction # 13	0.1 nM-10nM	[14]
k_{on14}	Forward rate of reaction #14	50-200 1/hr	[15]
k_{on15}	Forward rate of reaction #15	3.6×10^9 $- 3.6 \times 10^{10}$	[13]
k_{on16}	Forward rate of reaction #16	3.6×10^9 $- 3.6 \times 10^{10}$	[13]
f_{RAR}	Transcription factor fraction for RAR gene	0-1	By definition
f_{CRABP2}	Transcription factor fraction of CRABP2 gene	0-1	By definition
f_{CYP}	Transcription factor fraction for CYP gene	0-1	By definition
f_{GOI}	Transcription factor fraction for the GOI	0-1	By definition

Reactions are shown in Table 2.
Transcription factor fractions are defined in Section 3.1.

We used large ranges for unknown initial concentrations of CRABP1, CRABP2, CYP and RAR [16]. This is because the cellular levels of these proteins can vary significantly across cell types, or in a particular cell type as a consequence of cancer and cancer therapy. We then performed a global sensitivity analysis to identify the influential unknown parameters in the RA signaling pathway.

2.2.2. Global Sensitivity Analysis of the Model

Global sensitivity analysis (GSA) is a numerical technique designed to analyze the impacts of uncertain parameters on a model's output. In contrast to local sensitivity analysis

which analyzes the changes of model output by making small changes to each parameter while keeping the remaining parameters unchanged [17], GSA considers variations of all parameters over their entire range. Thus, GSA is useful for understanding the contribution of various model parameters to the variations in model output. In this study, we used a MATLAB toolbox for global sensitivity analysis, called SAFE [18]. We used a variance-based sensitivity analysis approach called Sobol's method, which can quantitatively rank the relative importance of the model's parameters [12, 19, 20]. Sobol's method evaluates the first- and total-order sensitivity indices for each parameter. The first-order index (S_i) represents the individual effects of each input on the variance of the output, while the total-effect index (S_{Ti}) accounts for the total contribution of the input that includes its first-order effect plus all higher-order effects. The higher-order effects for a given input are due to interactions of the input with other model inputs. The total-effect sensitivity indices are useful in identifying the noninfluential parameters which can be fixed anywhere over their range of variability without influencing the output significantly [12]. If $S_{Ti} \leq 0.01$ and the total-effect index of x_i is much smaller than that of the rest of parameters, then x_i can be fixed at any value within its range [21-23].

2.3. Results

2.3.1. Gene expression through RA pathway

We investigated the importance of various RA binding receptors in the RA signaling pathway after treating the model with various concentrations of RA. In this regard, we calculated the total mRNA production by a gene of interest (GOI) within 24 hours after RA therapy. The rate of production of a mRNA of interest by the classical RA signaling pathway is modeled by (see Supplementary Information in Section 2.6 for details)

$$\frac{\mathrm{d[mRNA]}}{\mathrm{dt}} = I_{\max\,(GOI)}\left(\frac{f_{GOI}[\mathrm{RA{:}\,RAR}]}{f_{GOI}[\mathrm{RA{:}\,RAR}] + k_{d(TF:DNA)}}\right), \tag{4}$$

where $I_{\max\,(GOI)}$ and $k_{d(TF:DNA)}$ are the maximal transcription rate by an activated transcription factor (TF_a) which initiates the transcription of the mRNA's gene, and the equilibrium dissociation constant of binding of the transcription factor to DNA, respectively. f_{GOI} is the transcription factor fraction of the GOI, defined as the ratio of the concentration of total transcription factor (TF_t) to the concentration of total RAR (RAR_t),

$$f_{GOI} = \frac{[\mathrm{TF}_t]}{[\mathrm{RAR}_t]}, \tag{5}$$

and is a number between 0 and 1. TF_t represents those heterodimerized RAR isotypes which can activate the transcription of the GOI after binding to RA. Some RA target genes can be expressed by various RAR:RXR heterodimers, while others are expressed by a particular heterodimer. Thus, the concentration of total transcription factor (TF_t) is less than or equal to total concentration of RAR (RAR_t). In general, the value of f_{GOI} depends on gene- and cell-type. For a given cell-type, f_{GOI} varies for different genes since the value of TF_t depends on gene-type.

Figure 2a shows the variations in the transcription rate of the GOI within 24 hours after adding various concentrations of RA to a model with a randomly sampled set of parameters.

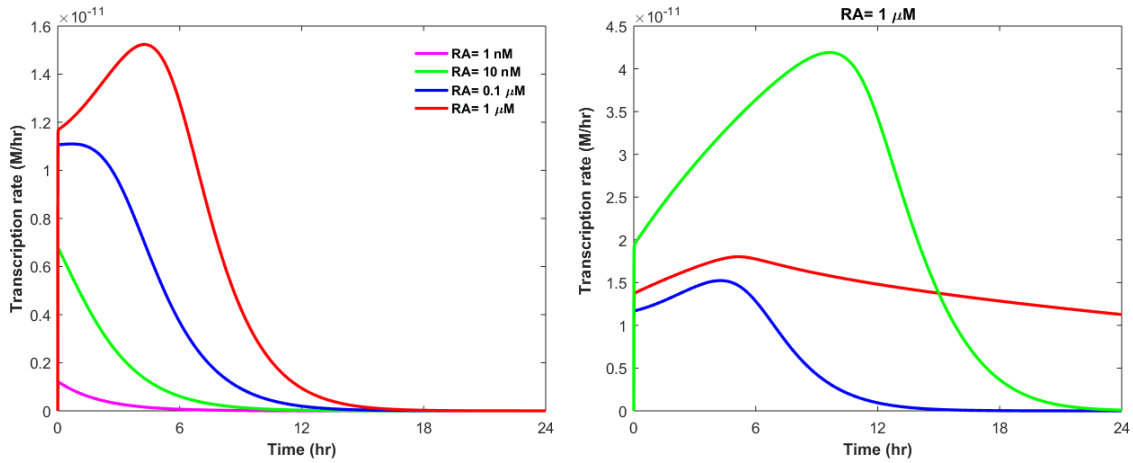

(a) (b)

Figure 2. Changes in the transcription rate of the GOI (a) after adding various concentrations of RA to a model with a set of random parameters: $[\mathrm{CRABP1}_t]$=10 nM, $[\mathrm{CRABP2}_t]$=1.9 μM, $[\mathrm{CYP}_t]$=15 nM, $[\mathrm{RAR}_t]$=0.17 μM. (b) after adding 1 μM of RA to various models with different sets of parameters; Green: $[\mathrm{CRABP1}_t]$=1 nM, $[\mathrm{CRABP2}_t]$=7.7 μM, $[\mathrm{CYP}_t]$=3.5 nM, $[\mathrm{RAR}_t]$=9 nM. Red: $[\mathrm{CRABP1}_t]$=10 nM, $[\mathrm{CRABP2}_t]$=1.9 μM, $[\mathrm{CYP}_t]$=15 nM, $[\mathrm{RAR}_t]$=0.17 μM. Blue: $[\mathrm{CRABP1}_t]$=2.6 nM, $[\mathrm{CRABP2}_t]$=3.2 μM, $[\mathrm{CYP}_t]$=0.1 μM, $[\mathrm{RAR}_t]$=3 nM.

The RA-induced transcription rate strongly depends on RA concentration and model parameters, i.e. initial concentrations of the RA receptors and kinetic rate constants (Fig. 2). The transcription rate peak time, duration of transcription, and transcription rate peak level can change or remain unchanged after modifying RA concentration or model parameters. In order to investigate the significance of the model's unknown parameters in the regulation of GOI expression, we calculated the time integral of the transcription rate within 24 hours after RA treatment.

$$\text{Model Output} = \int_0^{24} I_{\max\,(GOI)} \left(\frac{f_{GOI}[\text{RA: RAR}]}{f_{GOI}[\text{RA: RAR}] + k_{d(TF:DNA)}} \right) \mathrm{dt}\,. \qquad (6)$$

We then calculated the sensitivity of the model output to variations in the model parameters when the cells were treated with 1 nM of RA (Fig. 3). The model parameters, including total concentration of the RA binding proteins, kinetic rate constants, transcription factor fractions and maximal transcription rates were varied within their ranges of variability (full details in Supplementary Information in Section 2.6).

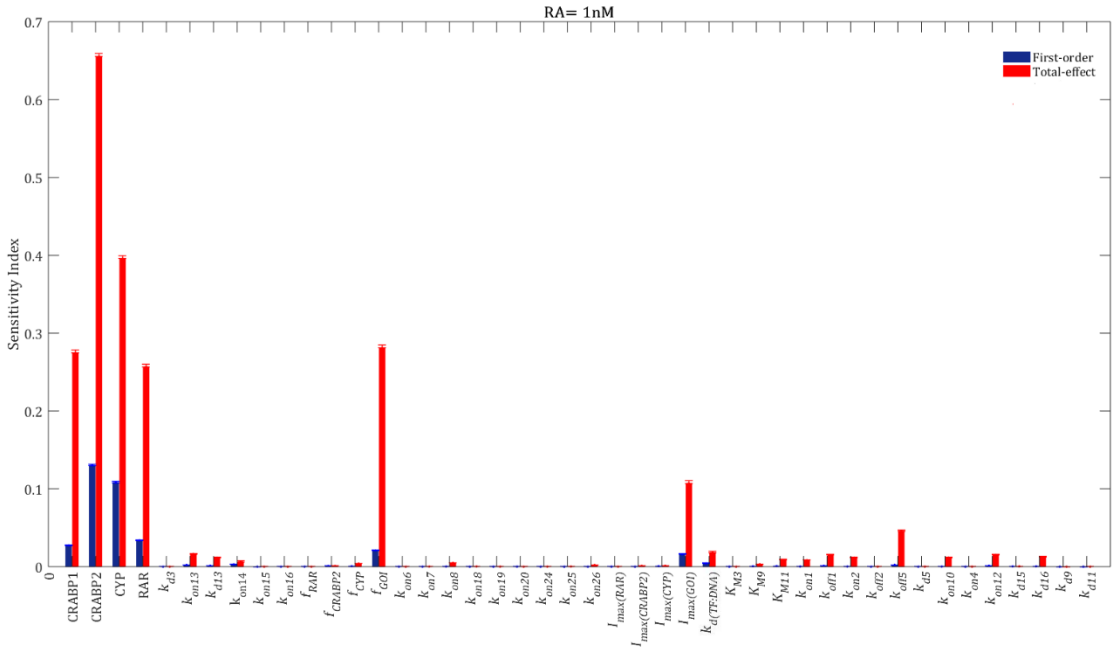

Figure 3. Sensitivity ranking of the model parameters. The model output was set to the time integral of the transcription rate of the GOI within 24 hours after adding 1 nM of RA to the model. Blue bars indicate first-order sensitivity indices, while red bars represent total-effect sensitivity indices. The error bars show the bootstrap confidence intervals (95% confidence intervals) of the mean values [24]. Detailed parameter description is provided in Supplementary Information in Section 2.6.

First-order and total-effect sensitivity indices of the model parameters indicated that the system performance was mainly controlled by the transcription factor fraction of the GOI (f_{GOI}) and the total concentrations of RA binding receptors (Fig. 3). The sensitivity of the

output to variations in f_{GOI} is trivial, since f_{GOI} represents what portion of RARs can activate the transcription of the GOI.

CRABP2 and RAR were the most and the least important RA receptors controlling RA-mediated mRNA production when RA= 1 nM, respectively. CYP was the second most sensitive parameter in the model, followed by CRABP1. The maximal transcription rate of the GOI ($I_{max(GOI)}$) and the equilibrium dissociation constant of the transcription factor binding to DNA ($k_{d(TF:DNA)}$) were other sensitive parameters in the model (Fig. 3). The maximal transcription rate of a given gene can change from cell to cell since the elongation rate of the gene by RNA polymerase can vary across cell lines and across a population of cells of the same type [25]. RA upregulates the expression of the *CRABP2*, *RAR* and *CYP* genes [26]. We modeled these pathways using Eq. 4 with different values of transcription factor fractions and maximal transcription rates, i.e. f_{CRABP2}, f_{RAR}, f_{CYP}, $I_{max(CRABP2)}$, $I_{max(RAR)}$, and $I_{max\,(CYP)}$ (see Supplementary Information in Section 2.6 for details). Our results, however, indicated that these pathways did not considerably affect the model output when RA= 1 nM, since the total-effect indices of f_{CRABP2}, f_{RAR}, f_{CYP}, $I_{max(CRABP2)}$, $I_{max(RAR)}$ and $I_{max\,(CYP)}$ were smaller than 0.01 (Fig. 3).

We then calculated the sensitivity indices of the model parameters when the model was treated with other concentrations of RA ranging from 10 nM to 1 μM. Our results showed that transcription factor fraction of the GOI, maximal transcription rate of the GOI and total concentration of RA binding receptors mainly controlled the system performance at all concentrations of RA (see Supplementary Information, Section 2.6, Fig. S1). Figure 4 compares the sensitivity indices of RA binding proteins at various concentrations of RA.

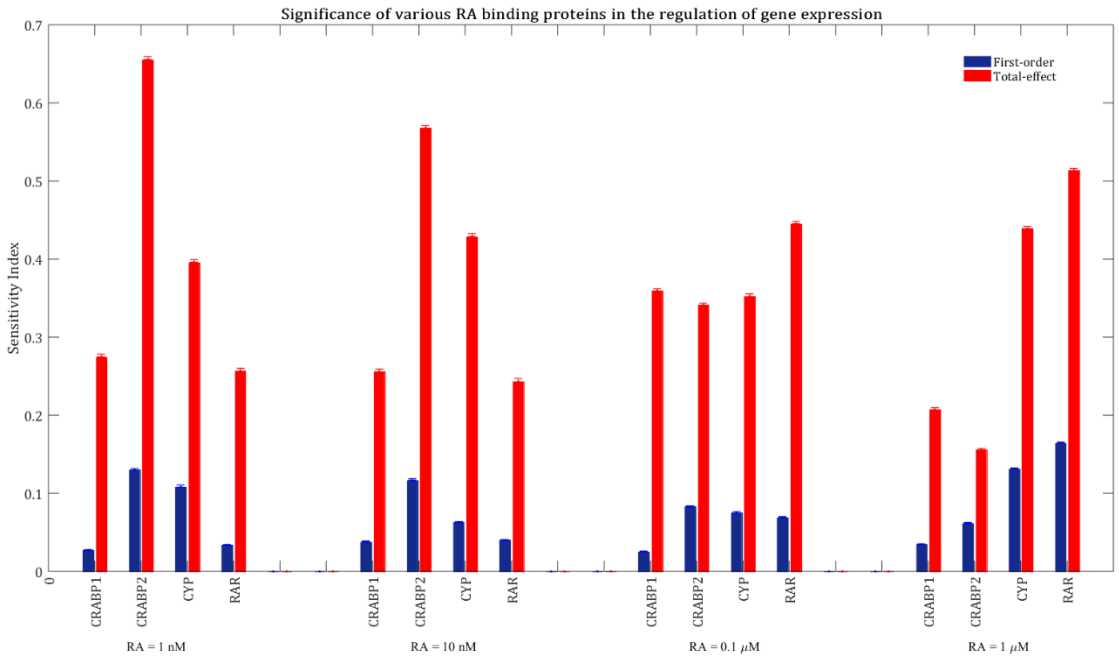

Figure 4. Significance of the RA binding proteins in influencing total mRNA production after treatment with various concentrations of RA. The blue bars show first-order sensitivity indices, while the red bars show total-effect sensitivity indices. The error bars indicate the bootstrap confidence intervals (95% confidence intervals) of the sensitivity indices.

RAR is the least important protein in influencing mRNA production when the cells are treated with physiological levels of RA (1-10 nM). That is because RA is mainly bound to CRABP1, CRABP2 and CYP at low concentrations of RA, as those proteins have higher binding affinities than RAR for RA. Thus, variation in total concentration of RAR is less important than variations of the rest of RA binding proteins concentrations in changing the formation rate of RA:RAR, since there are not many free RA molecules available to bind to RARs at physiological levels of RA. However, a change in CRABP2, CRABP1 and CYP concentrations can remarkably accelerate or slow down the transport of RA molecules to RARs, which are mainly unbound at physiological conditions. In other words, RA is the

limiting and RAR is the excess species at physiological levels of RA, while RAR is the limiting and RA is the excess species at higher concentrations of RA.

Total concentration of RAR is more important in influencing mRNA production when the RA concentration is RA=1 μM compared to physiological concentrations of RA. This is because RAR is close to saturation with RA at higher levels of RA, since there are more RA molecules accessible to RARs. Thus, enhancement of total RAR concentration can increase the activation rate of the transcription factor, which leads to an increase in the mRNA production rate according to Eq. 4. Figure 5 shows the variations of the RA binding receptors' saturation indices at different concentrations of RA. The saturation index of each receptor is defined as the maximum value of the bound fraction of the receptor within 24 hours after RA treatment. The bound fraction of a receptor changes over time, and is expressed as:

$$\text{Bound fraction of a receptor} = \frac{\text{Liganded receptor concentration}}{\text{Liganded receptor concentration} + \text{free receptor concentration}}$$

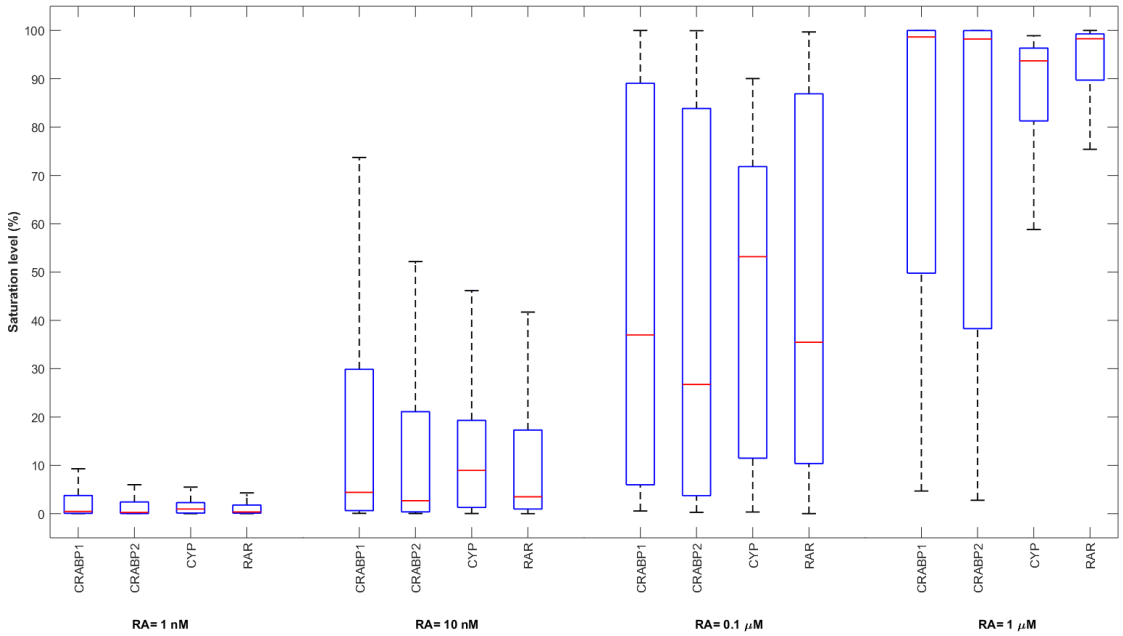

Figure 5. Variation in the saturation index of various RA binding proteins at different concentrations of RA. 10000 points were randomly sampled, following a uniform distribution over a 44-dimensional parameter space. The models were treated with various concentrations of RA and the saturation indices were calculated.

CRABP1 and CRABP2 are less important than RAR when the concentration of RA is 1 µM, even though they are also close to saturation (Fig. 5). This is because RAR is almost saturated with RA at high levels of RA, and providing RARs with more RA molecules through changing CRABP1 and CRABP2 concentrations does not change the formation rate of activated RAR significantly.

Another factor that makes RAR more important than other binding proteins in mRNA production at pharmacological conditions (RA= 0.1-1 µM) is the higher expression rate of CRABP2, RAR and CYP genes at pharmacological levels of RA compared to physiological levels. Total concentrations of RAR, CRABP2 and CYP increase after adding RA to the system. Figure 6 shows the variations in RA binding protein expression indices at different

RA concentrations. The expression index of each RA binding protein is defined as the average concentration of each RA binding protein within 24 hours after RA treatment, divided by the initial concentration of RA binding protein before the RA therapy. Our results show that the expression indices of all RA binding receptors increase with RA concentration. The expression indices of CRABP2 and CYP are larger than the expression index of RAR at all concentrations of RA. This is because CRABP2 and CYP have larger maximal transcription rates, translation constants, and smaller degradation rates than RAR (see Supplementary Information in Section 2.6).

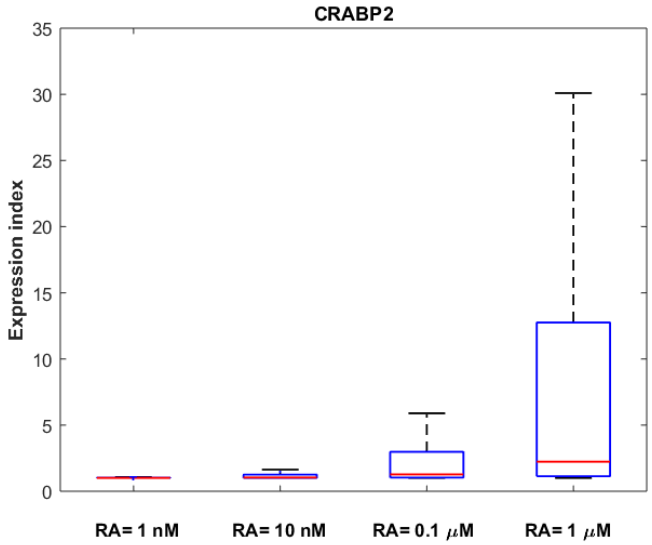

(a)

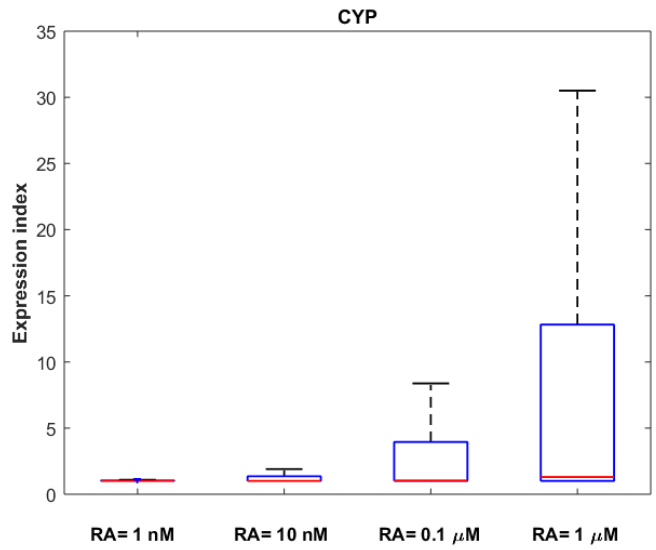

(b)

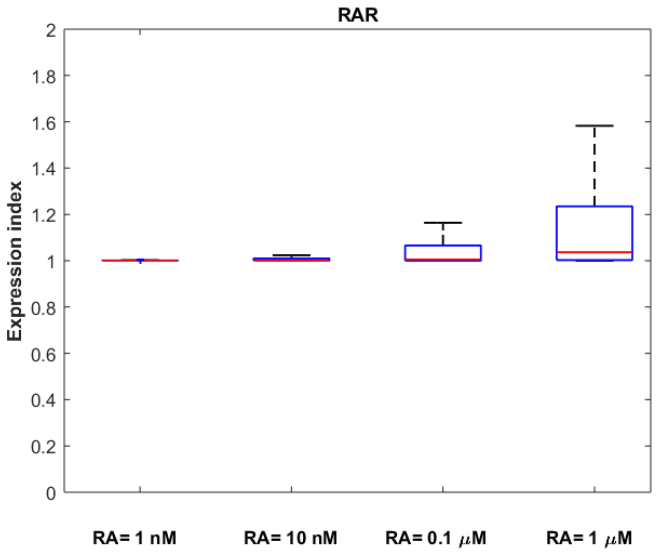

(c)

Figure 6. Variation in the expression index of (a) CRABP2, (b) CYP, (c) RAR at various concentrations of RA. 10000 points were randomly sampled following a uniform distribution over a 44-dimensional parameter space to generate this Figure.

The total concentration of CYP contributes almost equally to variations in mRNA production at all concentrations of RA (Fig. 4). This is because CYP level affects the concentrations of free CRABPs available for transferring RA to the nuclear receptors (according to Eq. 1 to Eq. 3).

From Figure 4, it can be understood that CRABP2 is a more important factor in the RA signaling pathway when the model was treated with physiological levels of RA (1-10 nM) compared to pharmacological levels of RA (0.1-1 μM). This is because RAR is barely saturated with RA at physiological conditions, so that variations in CRABP2 concentration can significantly change the rate of RA transport to RARs.

The fact that CRABP2 is more influential in mRNA production at physiological conditions compared to pharmacological conditions is in qualitative accordance with previous experimental studies [7]. A previous *in vitro* study [7] indicated that exogenous levels of CRABP2 increased the transcriptional activity of RAR only when the concentrations of RA or RAR were limiting (Fig. 7a-b). We performed a local sensitivity analysis to investigate the effect of a constant change in CRABP2 concentration on total mRNA production, over broad regions of RA and RAR concentrations. For this purpose, we sampled several sets of parameters within their ranges of variability, which characterized various cell types or various cells of the same type. We then calculated fold change values of the total mRNA production for each model after increasing CRABP2 concentration by 200% (Fig. 7c). Our results indicated that for a vast majority of cell types, a constant change in CRABP2 concentration is more important in the RA signaling pathway at lower concentrations of RA. We also obtained fold change values of total mRNA production after increasing CRABP2 concentration by 200% in the absence or presence of exogenous levels

of RAR. Our results showed that variation of CRABP2 concentration is more important at lower concentrations of RAR. This result is in qualitative agreement with experimental observations [7] in COS-7 cells culture (Fig.7).

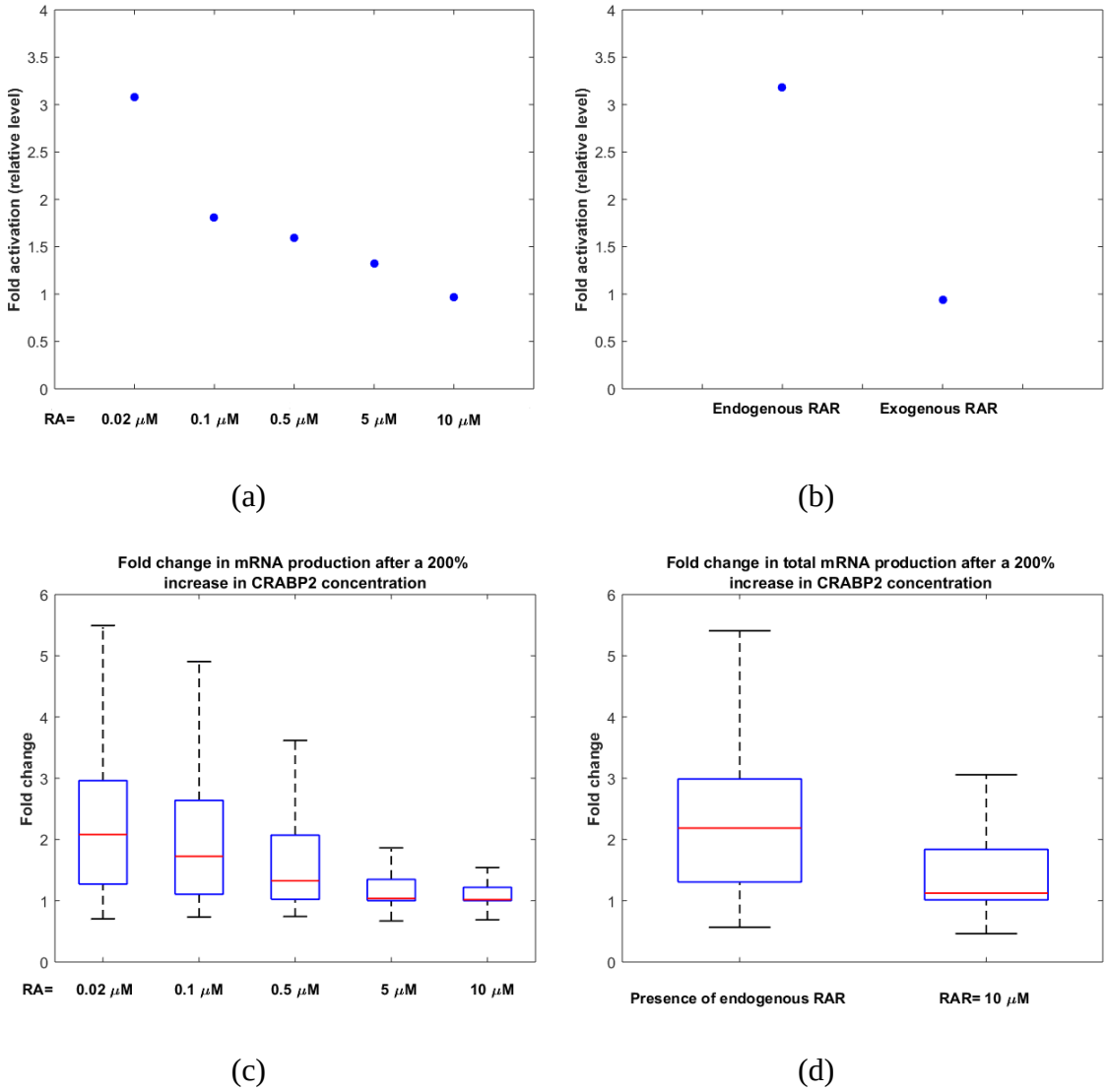

Figure 7. Effects of CRABP2 on transcriptional activity of RAR at various levels of RA and RAR. COS-7 cells were transfected with a luciferase reporter construct driven by a RAR responsive element and the activity level of the reporter was measured in different conditions. (a) Luciferase activity level after adding exogenous levels of CRABP2 to the cells at various

concentrations of RA. Data are presented as fold induction relative to luciferase reporter activity level before overexpression of CRABP2. Experimental data was obtained from [7]. (b) Luciferase activity level after adding exogenous levels of CRABP2 to the cells, in the presence of endogenous RAR or upon overexpression of RAR. Data are presented as fold induction relative to luciferase reporter activity level before overexpression of CRABP2. Experimental data was given from [7]. (c) Fold change in total mRNA production after increasing CRABP2 concentration by 200%. Data are normalized by total mRNA production before CRABP2 overexpression. 10000 points were randomly sampled following a uniform distribution over a 44-dimensional parameter space, to generate this Figure. (d) Fold change in total mRNA production after increasing CRABP2 concentration by 200% in the presence of endogenous RAR or exogenous RAR, i.e. RAR= 10 μM. Data are normalized by total mRNA production before CRABP2 overexpression. 10000 points were randomly sampled following a uniform distribution over a 44-dimensional parameter space, to generate this Figure.

The total-effect sensitivity index of CRABP2 is larger than that of CRABP1 when RA= 1-10 nM, while CRABP2 and CRABP1 contribute almost equally to variations in the model output when RA= 0.1-1 μM (Fig. 4). Total-effect sensitivity indices should be used to compare the total contributions of different inputs to variations in the model response. For example, CRABP2 has a larger first-order sensitivity index than CRABP1 when RA concentration is 0.1 or 1 μM, while the total-effect sensitivity index of CRABP1 is slightly larger than that of CRABP2 (Fig. 4). This suggests that CRABP1 interacts stronger than CRABP2 with other parameters.

The calculated sensitivity indices at each RA concentration indicate the relative importance of the parameters at the specified RA concentration. Thus, these indices cannot be used to compare the absolute values of the produced mRNA when the cells were treated with various levels of RA. CRABP2, for instance, has a larger sensitivity index in physiological concentration of RA compared to pharmacological concentrations. However,

this does not mean that a change in CRABP2 concentration results in a larger variation in molar production of the mRNA at physiological levels of RA compared to the pharmacological concentration of RA. In general, with a fixed set of values for RA binding receptor concentrations, total mRNA production increases by RA dose.

2.3.2. RA degradation pathway

RA metabolism is crucial in RA signaling not only because the CYP can limit the amount of RA available to interact with RARs, but also because some RA metabolites can induce the transcription of some target genes through specific pathways [27, 28]. Furthermore, RA resistance, observed in continuous RA treatment in cancer patients, is at least in part due to RA degradation. RA metabolism is mediated mainly by CYP enzymes, which are found in different cell types. Even though several studies have investigated the role of various families of CYP in biosynthesis of RA, little is known about the contribution of CRABPs and RARs in the RA degradation pathway. In this section we investigated the contributions of the RA binding receptors to production of RA metabolites. In our model, RA was only degraded via CYP enzymes, while interacting with CYP directly or indirectly. In the direct mechanism, free RA molecules can bind to CYP, while the indirect process involves CRABP1 and CRABP2 as carrier proteins that transfer RA to CYP. Thus, the total rate of RA degradation is obtained by

$$\frac{\mathrm{d[RA\ metabolites]}}{\mathrm{dt}} = k_{on4}[\mathrm{RA{:}\,CYP}] + k_{on10}[\mathrm{RA{:}\,CRABP1{:}\,CYP}] + k_{on12}[\mathrm{RA{:}\,CRABP2{:}\,CYP}], \quad (7)$$

where k_{on4}, k_{on10} and k_{on12} are degradation rates of $\mathrm{RA{:}\,CYP}$, $\mathrm{RA{:}\,CRABP1{:}\,CYP}$ and $\mathrm{RA{:}\,CRABP2{:}\,CYP}$, respectively.

We performed GSA to investigate the sensitivity of total RA metabolite production within 24 hours after RA therapy, to variations in the model's unknown parameters.

$$\text{Model Output} = \int_0^{24} k_{on4}[\text{RA: CYP}] + k_{on10}[\text{RA: CRABP1: CYP}] + k_{on12}[\text{RA: CRABP2: CYP}]\ \text{dt.} \qquad (8)$$

As in the previous section, we considered physiological bounds for the parameters and used the Sobol's method to calculate the sensitivity indices. Our results showed that the production of RA metabolites was mainly affected by cellular concentrations of the RA binding proteins (Fig. S2 in Supplementary Information, Section 2.6). CYP had the largest total-effect sensitivity index at all RA concentrations, which shows that total concentration of CYP was the most important parameter controlling the system performance (Fig. 8). CRABP1 and CRABP2 contribute almost equally to variation in the model response when RA= 1 nM, while CRABP1 is more important than CRABP2 in the RA degradation pathway when RA= 0.01-1 µM.

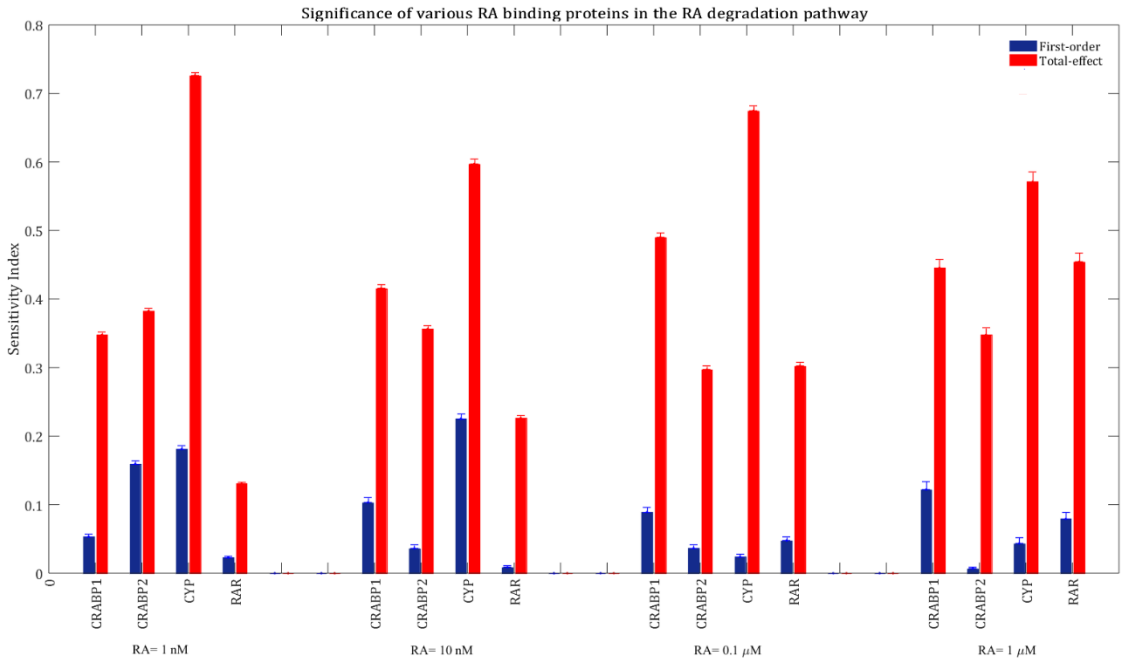

Figure 8. Relative importance of various RA binding proteins in total RA metabolite formation at various concentrations of RA. The model output was set to total RA metabolite formation within 24 hours of treatment with various concentrations of RA. The blue bars show first-order sensitivity indices, while the red bars show total-effect sensitivity indices. The error

bars indicate the bootstrap confidence intervals (95% confidence intervals) of the sensitivity indices.

RAR becomes more important in the RA degradation pathway as RA concentration increases. This can be explained by the fact that at high concentrations of RA, RAR is the most important parameter that controls RA-induced gene expression (Fig. 4). The cellular level of RAR can significantly influence RA-induced upregulation of CYP, CRABP2 and RAR. Our results indicated that RA-induced upregulation of CYP had significant effects on total RA metabolite formation when RA= 0.01-1 μM (see Section 2.6, Supplementary Information, Fig. S2). From Figure 8, it can be understood that for a given RA concentration, the rank order of first-order sensitivity indices of the parameters is not necessarily the same as the rank order of total-effect sensitivity indices. This is due to different levels of interaction of each parameter with the rest of the parameters. Furthermore, our results were obtained using GSA, which gives some insights into the functions of various receptors by covering the entire parameter space. However, it might be possible that for a specific set of initial concentrations the rank order of parameter sensitivities would be different.

Comparing Figure 4 with Figure 8, one can observe that for a given RA concentration, the rank order of sensitivity of the RA binding receptors is not the same for total mRNA production and total RA metabolite formation. To further investigate the relationship between mRNA production and RA metabolite formation by the RA signaling pathway, we calculated Spearman's rank correlation coefficient between total mRNA production and total RA product formation within 24 hours of treatment with 1 μM of RA. Our results revealed a significant negative correlation (ρ= - 0.7, p= 0, n= 10000) between total mRNA

production and total RA metabolite formation (Fig. 9). However, Spearman's rank correlation coefficient decreased with the reduction of RA concentration (Section 2.6, Supplementary Information, Fig. S3).

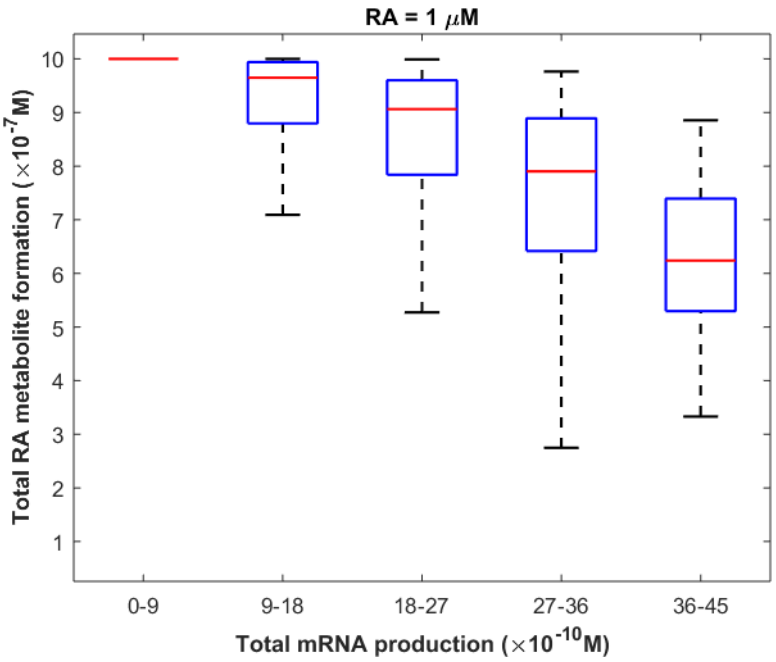

Figure 9. The relationship between total RA metabolite formation and total mRNA production within 24 hours of treatment with 1 μM of RA. 10000 points were randomly sampled following a uniform distribution over a 44-dimensional parameter space.

One serious drawback of the clinical use of RA is that RA has a rapid and variable degradation rate [29, 30]. Thus, a relatively high concentration of RA is required to induce the expression of target genes in various cell types. The pattern of RA degradation is important since it can directly influence cell differentiation and gene expression by RA. In this section, we simulated the variations in total concentration of RA within 24 hours after RA treatment. For this purpose, we sampled several sets of parameters within their ranges of variability, which characterized various cell types or various cells of the same type. We then added 0.1 μM of RA to each model and obtained the changes in total RA concentration

over time. Our results showed that RA exhibited different elimination patterns depending on intracellular concentrations of the RA binding proteins, i.e. CRABP1, CRABP2, CYP and RAR (Fig. 10). Furthermore, RA can both down- and up-regulate its own degradation.

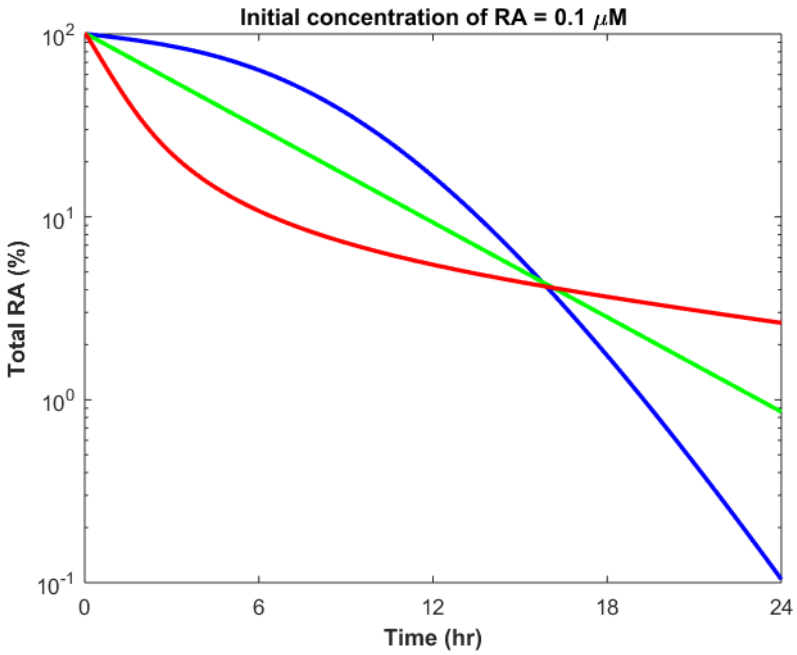

Figure 10. Various forms of elimination of RA after treating different models with 0.1 μM of RA. Three models with various parameter sets are shown in blue, green and red. Green: $[CRABP1_t]$=8.6 μM, $[CRABP2_t]$=16.1 nM, $[CYP_t]$=11.2 nM, $[RAR_t]$=0.24 μM. Red: $[CRABP1_t]$=2.7 nM, $[CRABP2_t]$=11.4 nM, $[CYP_t]$=30 nM, $[RAR_t]$=0.22 μM. Blue: $[CRABP1_t]$=3 μM, $[CRABP2_t]$=11 nM, $[CYP_t]$=2.26 nM, $[RAR_t]$=0.71 μM. Full list of the models' parameters is reported in Supplementary Information, Table S2.

2.3.3. Effects of the RA binding proteins on the efficacy and toxicity of RA

An understanding of the roles and significance of RA binding proteins in the RA signaling pathway is important for both therapeutic and toxicological reasons. The results presented in this study can be used to develop pharmacological methods to increase the maximal response produced by RA. These pharmacological approaches can vary depending

on cancer type, as different cell types have different expression levels of RA binding proteins. For example, in pharmacological conditions (RA= 1 µM), induction of expression of the *RAR* gene or inhibition of expression of the *CYP* gene have more significant effects than overexpression of the *CRABP2* gene on the expression levels of the GOI in a given cell type (Fig. 4). To further investigate how the total mRNA production at various RA concentrations is sensitive to variation in each RA binding protein concentration, we performed a local sensitivity analysis. In this regard, 10000 sets of parameters were randomly sampled, following a uniform distribution over a 44-dimensional parameter space. Variation in the total mRNA production was calculated for each model after increasing the concentration of each RA binding protein by 25% while the rest of the parameters remained unchanged (Fig. 11).

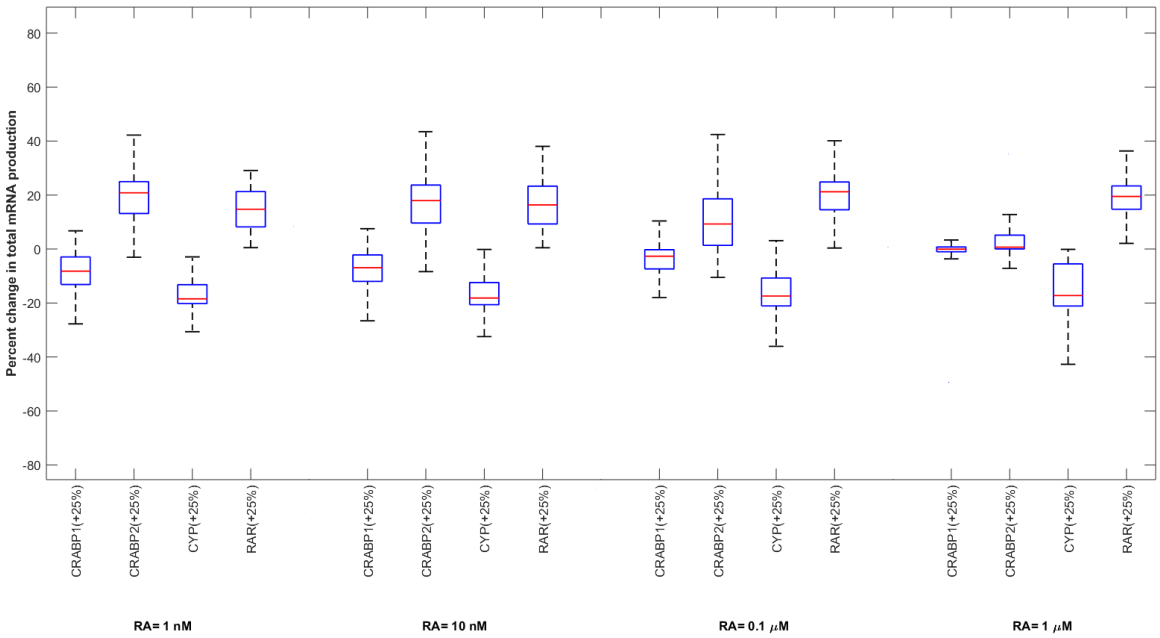

Figure 11. Variation in total mRNA production after a 25% increase in each RA binding protein concentration, while the rest of the parameters are constant. 10000 points were randomly

sampled following a uniform distribution over a 44-dimensional parameter space, to generate this Figure.

Our results indicate that a 25% increase in CRABP1 or CRABP2 concentrations is more important at physiological concentrations of RA compared to pharmacological concentrations, which is in accordance with our global sensitivity analysis results (Fig. 4). CRABP2 is the most influential protein at physiological concentration, while RAR and CYP are the most important proteins when RA= 1 μM. From Figure 11, it can be understood that a 25% increase in the total concentration of RAR enhances mRNA production for all models. A 25% increase in total concentration of CYP and CRABP1 decreases total mRNA production for most of the models, while a 25% increase in CRABP2 concentration enhances total mRNA production for the majority of models. In general, the way that the variation in total concentrations of CRABP1, CRABP2 or CYP affects mRNA production depends on the cellular concentrations of all RA binding receptors. Overexpression of CRABP1, for example, can increase or decrease the transcriptional activity of the target gene, depending on total concentrations of the other RA receptors. This is because these proteins complex with each other in the absence or presence of RA.

The results presented in this paper can provide insight into the efficacy and safety of RA therapy in treatment of different cancer types and cancer patients. CRABP1, CRABP2, CYP and RAR expressions can be upregulated or downregulated depending on the cancer type [31-34] and administrated anticancer drugs [35, 36]. Cancer patients usually take different medications at the same time. Concurrent use of other drugs with RA can influence the RA signaling pathway in at least two ways. First, interaction with other medicines can cause variations in the pharmacokinetics and pharmacodynamics of RA, significantly

changing its efficacy and toxicity. For instance, it is possible that two or more drugs compete for the same CYP enzyme in a cancer cell, since CYP-mediated metabolism is a major route of elimination for many drugs. This competitive inhibition can decrease the availability of CYP enzymes to RA, therefore decreasing its metabolism rate and increasing its toxicity. Second, some drugs can inhibit or induce the expression of RA binding proteins such as CYP [34, 35]. Variations in the concentrations of RA binding proteins may affect the efficacy of RA over the course of cancer therapy. For instance, CRABP1 and CRABP2 are the least important parameters in the model when RA= 1 μM (Fig. 4). Thus, up-regulation or down-regulation of these proteins due to other factors such as disease progress, drug interactions, etc should not change the rate of mRNA production by RA significantly. However, if for example use of a strong RAR inhibitor or CYP inducer is unavoidable for the patient, the therapeutic effects of RA may be decreased significantly.

2.4. Discussion

Retinoic acid, a metabolite of vitamin A, modulates a wide variety of biological processes such as cell growth, cell differentiation and cell proliferation. RA has also been known to be effective in treatment of various types of cancer. Even though a vast number of studies have focused on exploring the regulatory target genes for RA, the significance and roles of various intracellular RA receptors in transduction of the RA signal have not been fully understood. CRABP1, CRABP2, CYP enzymes and RARs are the main intracellular proteins which can bind to RA as receptors. Few previous studies have attempted to investigate the effects of overexpression of CRABPs on the RA signaling

pathway, and in some cases somewhat contradictory results have been reported for different cell lines [2-4]. In this study, we developed a mathematical model to analyze the importance of CRABP1, CRABP2, CYP and RAR in production of mRNA and RA metabolites. In this regard, after proposing a well-mixed model of the RA signaling pathway, we performed a global sensitivity analysis to investigate the relative importance of RA binding receptors in total mRNA production via the RA pathway. Our results indicate that CRABP2 is the most important RA receptor at physiological levels of RA, while RAR concentration has the least importance among all four RA receptors. At pharmacological levels of RA, the total mRNA production was more sensitive to variations in RAR and CYP levels than CRABP1 and CRABP2 levels. It is important to note that all RA binding receptors could influence RA-induced mRNA production within the entire region of parameter space where the concentrations of RA binding proteins change considerably. They are all important since their sensitivity indices were of the same order of magnitude. These results can explain the conflict between previous experimental results regarding the effects of CRABP1 on transcriptional activity of target genes [1, 3, 4]. Our results were obtained using GSA, which quantifies the effects of the model inputs on the model output by perturbing the inputs within large ranges. Therefore, our results indicate that in a broader region of parameter space, which represents various cells with various levels of RA receptors, all of the RA binding receptors are influential. However, there is a possibility that for a certain parameter set which specifies a specific tissue or cell, CRABP1 is unimportant in the RA pathway. Thus, for a given cell type, an accurate parameter set is necessary to determine whether a parameter has a substantial control on the system performance.

Our local sensitivity analysis indicated that CRABP2 is more important in the RA signaling pathway at lower concentrations of RA or RAR. This result is in qualitative agreement with *in vitro* observations in COS-7 cells[7]. Our model can be applied to various cell types and our results can be validated experimentally once more information is available about the expression levels of RA binding proteins in the cell types of interest.

Our GSA analysis indicated that RAR-mediated increases in CRABP2 and CYP concentrations after RA therapy were more important in the regulation of GOI expression than the RAR-mediated increase in RAR concentration (see Supplementary Information in Section 2.6, Fig. S1). This is because total-effect sensitivity indices of $I_{max(CRABP2)}$ and $I_{max\,(CYP)}$ were larger than total-effect sensitivity index of $I_{max(RAR)}$. Furthermore, total-effect sensitivity indices of f_{CRABP2} and f_{CYP} were larger than total-effect sensitivity index of f_{RAR} at all concentrations of RA (Supplementary Information in Section 2.6, Fig. S1). The time-dependent increases of CRABP2, CYP and RAR concentrations after RA therapy can alter the relative concentrations of RA binding proteins. Thus, RA receptors can become increasingly or decreasingly important in the RA signaling pathway as time goes on. In this study, we calculated the sensitivity of the model's outputs, i.e. total mRNA production and total RA metabolite formation, to variations in total concentrations of the RA binding receptors before RA treatment. Thus, the significance of RAR-mediated upregulation of *CRABP2*, *CYP* and *RAR* genes in the RA signaling pathway is mainly shown by the sensitivity index of total RAR concentration, since RAR is the only RA receptor mediating the transcription of target genes.

This study has some limitations. First, we assumed that RA influences gene expression through the classical pathway, which involves binding of RA to a nuclear hormone receptor

heterodimer (RAR:RXR). The liganded heterodimer can initiate the transcription of target genes after binding to a DNA response element. However, there may be other intermediate transcription factors or nonclassical pathways that can transduce RA signal, thus our results can only be applied to the genes which are direct targets of the classical RA signaling pathway. Second, we assumed that all RA binding proteins undergo first-order degradation processes. This may not be the case for all types of tissues with various expression levels of degradation enzymes. The mechanisms mediating the elimination of RA binding receptors have not been fully understood, thus the model can be improved once more information regarding these mechanisms is available. Third, we used the kinetic rate constants of CYP26B1 in the model. CYP26B1 is a member of the 26 family (CYP26s) of the CYP enzymes which is mainly responsible for metabolism of RA during adult life [6, 37-39]. However, RA can also be degraded by other families of CYP which are different from CYP26B1 in terms of rate constants and binding affinities. In the current model, we assumed that the kinetic rate constants of degrading enzymes can vary by a factor of two around the *in vitro* values for CYP26B1. This assumption increases the applicability of our results to other cell types with different types of CYP. Thus, our results are applicable to those cell lines that express higher levels of CYP26B1 compared to other CYP families and to those cell types which have CYP enzymes with kinetic rate constants within the specified ranges in this study. The current simulation can be run using the kinetic rate constants of any arbitrary CYP enzyme. In that case, this model can be expanded to include the effects of RA metabolites on RA-induced gene expression if the CYP of interest forms high levels of active RA metabolites. The current model is applicable to those cell types whose main degrading enzyme is CYP26B1. The primary metabolite formed by CYP26B1 from RA is

4-OH-RA [40, 41]. CYP26B1 forms non-bioactive dehydroxylated products from 4-OH-RA[41]. Thus, we believe that the endogenous levels of RA metabolites formed by CYP26B1 do not play significant roles in the RA signaling pathway. However, there are other active RA metabolites such as 4-oxo-RA which can potentially compete with RA for binding to RAR and activate the transcription of target genes [28]. Fourth, we neglected the possible effects of RA treatment on the model parameters such as translation rate constants, transcription rate constants, and degradation rate constants of proteins and mRNAs. Fifth, for simplicity, we proposed a well-mixed model, thus our model is not able to capture the dynamics of protein diffusion through the nuclear membrane. RARs are located inside the cell nucleus. RA must diffuse across the nucleus membrane to be able to bind to RARs. In reality, RA binds to CRABPs after diffusing across the cellular membrane. RA can diffuse across the nuclear membrane alone or bound to CRABPs. We believe that our well-mixed model can approximate this process due to the rank order of binding affinity of RA for various RA receptors. RA binds to CRABP1 and CRABP2 with higher affinity than to RAR, which implies that RA is primarily available for CRABPs. The remaining RA molecules can bind to RARs and CYP enzymes. Finally, we assumed that the ratio of total transcription factor concentration to total RAR concentration (f) remains constant after adding RA to the cell. However, this depends on the gene- and cell-type. It is believed that RARs and RXRs each have three isotypes, namely RAR_{α}, RAR_{β}, RAR_{γ}, RXR_{α}, RXR_{β}, RXR_{γ}, which can form nine different heterodimers. Depending on the gene-type, one or some of these heterodimers can initiate the transcription of the target gene after binding to RA. Little is known about the expression levels of the nuclear hormone receptors in various cell types, and their

interactions with each other. The model presented in this paper can be expanded once there is more information about the nuclear hormone receptor expression levels and functions.

2.5. Conclusions

Cellular levels of retinoic acid receptor (RAR), cytochrome P450 (CYP) enzymes and cellular retinoic acid binding proteins (CRABP1 and CRABP2) significantly affect the rate of gene expression through the classical retinoic acid (RA) signaling pathway. In this study, we used computational modeling to investigate the significance of various RA binding proteins in the regulation of expression of a gene of interest (GOI) under physiological or pharmacological conditions. A better understanding of the roles and significance of RA binding proteins in the RA signaling pathway could lead to the development of pharmacological methods to induce or block the activity of specific RA binding receptor (s), thereby improving the efficacy of the RA. Our results indicate that CRABP2 and CYP concentrations are more influential than CRABP1 and RAR concentrations in controlling mRNA production by the RA signaling pathway in physiological concentrations of RA (1-10 nM). However, RAR is the most sensitive parameter of the model in pharmacological conditions (RA=0.1-1 μM). We also identified the critical proteins in the RA metabolism pathway, and showed that there is a significant negative correlation between RA-induced mRNA production and RA metabolite formation after 24 hours of treatment with 1 μM of RA. Our results demonstrate that the pattern of RA degradation following RA therapy depends on the cell type.

2.6. Supplementary Information

2.6.1. Formulation of the model

The model described how RA is eliminated from the cell by CYP enzymes. CYP enzymes can metabolize not only free RA but also RA molecules bound to CRABP1 and CRABP2 [6]. RA degradation was modeled by Michaelis-Menten kinetics with *in vitro* enzyme kinetics parameters

$$\mathrm{E} + \mathrm{S} \underset{k_d}{\Leftrightarrow} \mathrm{ES} \overset{k_{cat}}{\Longrightarrow} \mathrm{E} + \mathrm{Product},$$

$$K_M = \frac{k_{off} + k_{cat}}{k_{on}},$$

$$k_d = \frac{k_{off}}{k_{off}},$$

where K_M and k_d are the Michaelis constant and the equilibrium dissociation constant of the enzyme substrate complex. Formation of products from RA:CRABP1 had a k_d of 0.024 nM and a K_M of 21.7 nM, while formation of products from RA:CRABP2 had a k_d of 0.059 nM and a K_M of 24.3 nM [6]. The K_M value was set at 64.6 nM for the interaction between CYP and free RA, while the equilibrium dissociation constant of RA:CYP complex was unknown. Formation of RA metabolites had catalytic rate constants of 10.2, 16.8 and 27 $1/hr$ from RA:CRABP1, RA:CRABP2 and free RA, respectively [6].

Most of the cellular impacts of RA rely on variation in gene expression. The expression of a gene of interest (GOI) is initiated once the activated transcription factor (TF_a) binds to DNA at a retinoic acid response element (RARE). RAR/RXR heterodimer is the main transcription factor in the classical RA signaling pathway, and becomes activated once it binds to RA. The transcription rate of a target gene depends on the promoter occupancy. The binding of an activated transcription factor to a promoter can be described by

$$\mathrm{TF}_a + \mathrm{Promoter} \underset{k_{d(TF:DNA)}}{\Longleftrightarrow} \mathrm{TF}_a\mathrm{:Promoter}$$

where $k_{d(TF:DNA)}$ is the equilibrium dissociation constant of the transcription factor binding to the promoter, and ranges from 15 to 33 nM [42]. The fraction of time that any given promoter spends in the transcription factor-bound state is given by [43-45]

$$\text{Fraction of binding time} = \frac{[\text{TF}_a]}{[\text{TF}_a] + k_{d(TF:DNA)}}. \tag{S1}$$

The rate of the gene transcription is proportional to the fraction of the binding time,

$$\frac{I}{I_{\max\,(GOI)}} = \frac{[\text{TF}_a]}{[\text{TF}_a] + k_{d(TF:DNA)}}, \tag{S2}$$

where $I_{\max\,(GOI)}$ is the maximal transcription rate of the GOI by the activated transcription factor (TF_a). The value of $I_{\max\,(GOI)}$ depends on gene-type, cell-type and the transcription factor [16]. RA can regulate the expression of *RAR*, *CRABP2* and *CYP* genes [26]. The values of $I_{\max\,(RAR)}$, $I_{\max\,(CRABP2)}$ and $I_{\max\,(CYP)}$ were set at 4.1×10^{-11}, 1.5×10^{-10}, and 1.06×10^{-10} $\frac{\text{M}}{\text{hr}}$, respectively. These values were obtained by dividing the average elongation rate of RNA polymerase by the gene lengths. The average elongation rate for RNA polymerase is 2 $\frac{\text{kbp}}{\text{min}}$ [46], while the lengths of *RAR*, *CRABP2* and *CYP* genes are 48.4 kbp (chr 17, GRCh38.p7), 13.4 kbp (chr 1, GRCh38.p7) and 18.6 kbp (chr 2, GRCh38.p7), respectively [47-49].

Assuming that RA binds to various RAR isoforms with the same binding affinity, the ratio of the activated transcription factor (TF_a) concentration to the total transcription factor (TF_t) concentration is the same as the ratio of the liganded RAR concentration to total RAR concentration, thus

$$\frac{[\text{TF}_a]}{[\text{TF}_t]} = \frac{[\text{RA: RAR}]}{[\text{RAR}_t]} \tag{S3}$$

The concentration of total transcription factor which can activate the transcription of the GOI is a portion of the concentration of total RAR,

$$f_{GOI} = \frac{[\mathrm{TF}_t]}{[\mathrm{RAR}_t]} \tag{S4}$$

where f_{GOI} represents the transcription factor fraction of the GOI with a value between 0 and 1. Transcription factor fraction is cell-dependent for a given gene. The rate of mRNA production via the RA pathway is obtained by combining Eqs. S2 to S4.

$$\frac{I}{I_{\max\,(GOI)}} = \frac{f_{GOI}[\mathrm{RA{:}\,RAR}]}{f_{GOI}[\mathrm{RA{:}\,RAR}] + k_{d(TF:DNA)}}\,. \tag{S5}$$

It is important to note that we assumed that the association/dissociation between DNA and transcription factor is in equilibrium because it occurs much faster than the other binding/unbinding reactions in the model [43, 50-52].

In our model, proteins and mRNAs are degraded by first-order reactions. Species are degraded in both bound and unbound forms. For example, CRABP1:CYP may undergo either CRABP1 degradation or CYP degradation.

CRABP2, *CYP* and *RAR* genes had both basal transcription rate (I_0) and RA-induced transcription rate (Eq. S5), while CRABP1 had a constant rate of protein expression, since *CRABP1* gene is not a target for RA [26, 53].

The full set of reactions and rate constants in the current model are shown in Table 2 and Table S1, respectively.

We then modeled the chemical reactions by ODEs.

$$\frac{\mathrm{d[RA]}}{\mathrm{dt}}$$
$$= -k_{on1}[\mathrm{RA}][\mathrm{CRABP1}] + k_{off1}[\mathrm{RA{:}\ CRABP1}] - k_{on2}[\mathrm{RA}][\mathrm{CRABP2}] + k_{off2}[\mathrm{RA{:}\ CRABP2}]$$
$$- k_{on3}[\mathrm{RA}][\mathrm{CYP}] + k_{off3}[\mathrm{RA{:}\ CYP}] - k_{on5}[\mathrm{RA}][\mathrm{RAR}] + k_{off5}[\mathrm{RA{:}\ RAR}] + k_{on21}[RA{:}\ CRABP1]$$
$$+ k_{on22}[\mathrm{RA{:}\ CRABP2}]$$
$$+ k_{on23}[\mathrm{RA{:}\ RAR}] \qquad \text{(S6)}$$

$$\frac{\mathrm{d[CRABP1]}}{\mathrm{dt}}$$
$$= -k_{on1}[\mathrm{RA}][\mathrm{CRABP1}] + k_{off1}[\mathrm{RA{:}\ CRABP1}] - k_{on17}[\mathrm{CRABP1}] + K - k_{on15}[\mathrm{CYP}][\mathrm{CRABP1}]$$
$$+ k_{off15}[\mathrm{CYP{:}\ CRABP1}]$$
$$+ k_{off28}[\mathrm{CYP{:}\ CRABP1}] \qquad \text{(S7)}$$

$$\frac{\mathrm{d[RA{:}\ CRABP1]}}{\mathrm{dt}}$$
$$= k_{on1}[\mathrm{RA}][\mathrm{CRABP1}] - k_{off1}[\mathrm{RA{:}\ CRABP1}] - k_{on21}[\mathrm{RA{:}\ CRABP1}] - k_{on9}[\mathrm{CYP}][\mathrm{RA{:}\ CRABP1}]$$
$$+ k_{off9}[\mathrm{RA{:}\ CRABP1{:}\ CYP}] \qquad \text{(S8)}$$

$$\frac{\mathrm{d[CRABP2]}}{\mathrm{dt}}$$
$$= -k_{on2}[\mathrm{RA}][\mathrm{CRABP2}] + k_{off2}[\mathrm{RA{:}\ CRABP2}] + k_{on25}[CRABP2_{\mathrm{mRNA}}] - k_{on16}[\mathrm{CYP}][\mathrm{CRABP2}]$$
$$+ k_{off16}[\mathrm{CYP{:}\ CRABP2}] + k_{on30}[\mathrm{CYP{:}\ CRABP2}] + \mathrm{k_{on14}}[\mathrm{RA{:}\ CRABP2{:}\ RAR}]$$
$$- k_{on18}[\mathrm{CRABP2}] \qquad \text{(S9)}$$

$$\frac{\mathrm{d[RA{:}\ CRABP2]}}{\mathrm{dt}}$$
$$= k_{on2}[\mathrm{RA}][\mathrm{CRABP2}] - k_{off2}[\mathrm{RA{:}\ CRABP2}] - k_{on22}[\mathrm{RA{:}\ CRABP2}] - k_{on13}[\mathrm{RA{:}\ CRABP2}][\mathrm{RAR}]$$
$$+ k_{off13}[\mathrm{RA{:}\ CRABP2{:}\ RAR}] - k_{on11}[\mathrm{RA{:}\ CRABP2}][\mathrm{CYP}]$$
$$+ k_{off11}[\mathrm{RA{:}\ CRABP2{:}\ CYP}] \qquad \text{(S10)}$$

$$\frac{\mathrm{d[CYP]}}{\mathrm{dt}} = -k_{on15}[\mathrm{CYP}][\mathrm{CRABP1}] + k_{off15}[\mathrm{CYP{:}\ CRABP1}] - k_{on16}[\mathrm{CYP}][\mathrm{CRABP2}]$$
$$+ k_{off16}[\mathrm{CYP{:}\ CRABP2}] + k_{on8}[CYP_{\mathrm{mRNA}}] - k_{on9}[\mathrm{CYP}][\mathrm{RA{:}\ CRABP1}]$$
$$+ k_{off9}[\mathrm{RA{:}\ CYP{:}\ CRABP1}] - k_{on11}[\mathrm{RA{:}\ CRABP2}][\mathrm{CYP}] + k_{off11}[\mathrm{RA{:}\ CRABP2{:}\ CYP}]$$
$$+ k_{on27}[\mathrm{CRABP1{:}\ CYP}] + k_{on29}[\mathrm{CRABP2{:}\ CYP}] - k_{on19}[\mathrm{CYP}]$$
$$+ k_{on4}[\mathrm{RA{:}\ CYP}] \qquad \text{(S11)}$$

$$\frac{\mathrm{d}[\mathrm{RA{:}\ CYP}]}{\mathrm{dt}} = k_{on3}[\mathrm{RA}][\mathrm{CYP}] - k_{off3}[\mathrm{RA{:}\ CYP}] - k_{on4}[\mathrm{RA{:}\ CYP}] \quad \text{(S12)}$$

$$\frac{\mathrm{d}[\mathrm{RAR}]}{\mathrm{dt}} = -k_{on5}[\mathrm{RA}][\mathrm{RAR}] + k_{off5}[\mathrm{RA{:}\ RAR}] - k_{on20}[\mathrm{RAR}] - k_{on13}[\mathrm{RA{:}\ CRABP2}][\mathrm{RAR}] + k_{off13}[\mathrm{RA{:}\ CRABP2{:}\ RAR}] + k_{on6}[RAR_{\mathrm{mRNA}}] \quad \text{(S13)}$$

$$\frac{\mathrm{d}[\mathrm{RA{:}\ RAR}]}{\mathrm{dt}} = k_{on5}[\mathrm{RA}][\mathrm{RAR}] - k_{off5}[\mathrm{RA{:}\ RAR}] + k_{on30}[\mathrm{RA{:}\ CRABP2{:}\ RAR}] - k_{on23}[\mathrm{RA{:}\ RAR}] \quad \text{(S14)}$$

$$\frac{\mathrm{d}[RAR_{\mathrm{mRNA}}]}{\mathrm{dt}} = I_{0(RAR)} + I_{max\,(RAR)}\left(\frac{f_{RAR}[\mathrm{RA{:}\ RAR}]}{f_{RAR}[\mathrm{RA{:}\ RAR}] + k_{d(TF:DNA)}}\right) - k_{on24}[RAR_{\mathrm{mRNA}}] \quad \text{(S15)}$$

$$\frac{\mathrm{d}[CRABP2_{\mathrm{mRNA}}]}{\mathrm{dt}} = I_{0(CRABP2)} + I_{max\,(CRABP2)}\left(\frac{f_{CRABP2}[\mathrm{RA{:}\ RAR}]}{f_{CRABP2}[\mathrm{RA{:}\ RAR}] + k_{d(TF:DNA)}}\right) - k_{on25}[CRABP2_{\mathrm{mRNA}}] \quad \text{(S16)}$$

$$\frac{\mathrm{d}[CYP_{\mathrm{mRNA}}]}{\mathrm{dt}} = I_{0(CYP)} + I_{max\,(CYP)}\left(\frac{f_{CYP}[\mathrm{RA{:}\ RAR}]}{f_{CYP}[\mathrm{RA{:}\ RAR}] + k_{d(TF:DNA)}}\right) - k_{on26}[CYP_{\mathrm{mRNA}}] \quad \text{(S17)}$$

$$\frac{\mathrm{d}[\mathrm{RA{:}\ CRABP1{:}\ CYP}]}{\mathrm{dt}} = k_{on9}[\mathrm{CYP}][\mathrm{RA{:}\ CRABP1}] - k_{off9}[\mathrm{RA{:}\ CRABP1{:}\ CYP}] - k_{on10}[\mathrm{RA{:}\ CRABP1{:}\ CYP}] \quad \text{(S18)}$$

$$\frac{\mathrm{d}[\mathrm{RA{:}\ CRABP2{:}\ RAR}]}{\mathrm{dt}} = k_{on13}[\mathrm{RA{:}\ CRABP2}][\mathrm{RAR}] - k_{off13}[\mathrm{RA{:}\ CRABP2{:}\ RAR}] - k_{on14}[\mathrm{RA{:}\ CRABP2{:}\ RAR}] \quad \text{(S19)}$$

$$\frac{\mathrm{d}[\mathrm{RA{:}\ CRABP2{:}\ CYP}]}{\mathrm{dt}} = k_{on11}[\mathrm{CYP}][\mathrm{RA{:}\ CRABP2}] - k_{off11}[\mathrm{RA{:}\ CRABP2{:}\ CYP}] - k_{on12}[\mathrm{RA{:}\ CRABP2{:}\ CYP}] \quad \text{(S20)}$$

$$\frac{d[\text{CRABP1:CYP}]}{dt} = k_{on15}[\text{CYP}][\text{CRABP1}] - k_{off15}[\text{CRABP1:CYP}] - k_{on27}[\text{CRABP1:CYP}] - k_{on28}[\text{CRABP1:CYP}] + k_{on10}[\text{RA:CRABP1:CYP}] \quad (S21)$$

$$\frac{d[\text{CRABP2:CYP}]}{dt} = k_{on16}[\text{CYP}][\text{CRABP2}] - k_{off16}[\text{CRABP2:CYP}] - k_{on29}[\text{CRABP2:CYP}] - k_{on30}[\text{CRABP2:CYP}] + k_{on12}[\text{RA:CRABP2:CYP}] \quad (S22)$$

where the numbers in the subscripts of the rate constants refer to the index of the reactions (Table 2).

The model had 14 independent unknown parameters including unknown rate constants, unknown initial concentrations and unknown transcription factor fractions (Main Text, Table 3). We considered some physiological bounds for the unknown parameters. We also assumed that the values of maximal transcription rate constants, translation rate constants, forward and reverse rate constants, equilibrium dissociation rate constants, Michaelis constants, catalytic rate constants and elimination rates of proteins and mRNAs varied within a factor of two around the *in vitro* values. Overall, our model had 44 independent parameters varying within their ranges.

2.6.2. Uncertainty Analysis of the Model

The independent parameters were sampled uniformly over their range of possible values (number of samples=10000). The rest of the unknown parameters (Table S1), and the unknown initial concentrations (Main Text, Table 1) were obtained using the independent parameters. To do so, we assumed that the system was at steady state prior to RA treatment. After obtaining all the parameters, the model was used to obtain total mRNA production

within 24 hours of RA treatment. We then used a GSA technique to assess the sensitivity of the model output to variations in model inputs.

2.6.3. Global Sensitivity Analysis

In this study, we used a MATLAB toolbox for global sensitivity analysis, called SAFE [18]. We ranked the model's parameters in terms of their importance using Sobol's method, which has been shown to be one of the most effective GSA methods for determining individual and cooperative sensitivities [54-56]. Sobol's method is a variance-based sensitivity analysis approach that uses the principle of variance decomposition to obtain the sensitivity of each parameter. Given an integrable function f over a k-dimensional parameter space Ω^k,

$$y = f(x_1, x_2, \dots, x_k) \tag{S23}$$

Sobol's method decomposes the response into a set of functions of increasing dimensionality,

$$f(x) = f_0 + \sum_{i=1}^{k} f_i + \sum_{i=1}^{k} \sum_{j>i}^{k} f_{ij} + \cdots + f_{123\dots k} \ , \tag{S24}$$

where each individual term is a function of the parameters in its index. The unconditional variance of the output $V(Y)$ is defined as

$$V(Y) = \int_{\Omega^k} f^2(x)\, dx - \left(\int_{\Omega^k} f(x)\, dx \right)^2 . \tag{S25}$$

The total variance is decomposed into partial variances using the expansion of f into terms of increasing dimensions (Eq. S24).

$$V(Y) = \sum_{i=1}^{k} V_i(Y) + \sum_{i=1}^{k}\sum_{j>i}^{k} V_{ij}(Y) + \cdots + V_{123\ldots k}(Y)\,. \tag{S26}$$

Based on Sobol's method, the first-order sensitivity index for each parameter is calculated by

$$S_i = \frac{V_i(Y)}{V(Y)}\,, \tag{S27}$$

where $V_i(Y)$ is the fraction of the total variance, which is related to changes in the parameter x_i over its range of variability. The Sobol total-effect index for the parameter x_i is obtained by the sum of all sensitivity indices which have i in their index

$$S_{Ti} = S_i + \sum_{i \neq j} S_{ij} + \sum_{i \neq j, i \neq l, j<l} S_{ijl} + \cdots \tag{S28}$$

The total-effect indices account for total contribution of the input to response variation. Total-effect indices can be used to determine the noninfluential parameters in the model. x_i can be fixed anywhere within its range of uncertainty if $S_{Ti} = 0$. However, previous studies have shown that parameters with total-effect indices smaller than 0.01 can be considered noninfluential [21-23].

Table S1. Reaction rate constants

	k_{on}			k_{off}		
Number	**Range**	**Unit**	**Reference**	**Range**	**Unit**	**Reference**
1	2.13e11	$M^{-1}hr^{-1}$	[5]	13.2	hr^{-1}	[5]
2	1.85e11	$M^{-1}hr^{-1}$	[5]	25.2	hr^{-1}	[5]
3	Unknown	$M^{-1}hr^{-1}$		Unknown	hr^{-1}	
4	27	hr^{-1}	[6]	-		
5	Unknown*	$M^{-1}hr^{-1}$		36-140	hr^{-1}	[57]
6	135.6	hr^{-1}	[16]	-		
7	870.7	hr^{-1}	[16]	-		
8	190.4	hr^{-1}	[16]	-		
9	Unknown	$M^{-1}hr^{-1}$		Unknown	hr^{-1}	
10	10.2	hr^{-1}	[6]	-		
11	Unknown	$M^{-1}hr^{-1}$		Unknown	hr^{-1}	
12	16.8	hr^{-1}	[6]	-		
13	Unknown	$M^{-1}hr^{-1}$		Unknown	hr^{-1}	
14	Unknown	hr^{-1}		-		
15	Unknown	$M^{-1}hr^{-1}$		Unknown	hr^{-1}	
16	Unknown	$M^{-1}hr^{-1}$		Unknown	hr^{-1}	
17	0.0385	hr^{-1}	[58]	-		
18	0.0385	hr^{-1}	[58]	-		
19	0.00835	hr^{-1}	[16]	-		
20	0.173	hr^{-1}	[14]	-		

21	0.0385	hr^{-1}	[58]	-		
22	0.0385	hr^{-1}	[58]	-		
23	0.173	hr^{-1}	[14]	-		
24	0.138	hr^{-1}	[59]	-		
25	0.0347	hr^{-1}	[60]	-		
26	0.11	hr^{-1}	[16]	-		
27	0.0385	hr^{-1}	[58]	-		
28	0.00835	hr^{-1}	[16]	-		
29	0.0385	hr^{-1}	[58]	-		
30	0.00835	hr^{-1}	[16]	-		

* Forward rate constant of reaction 5 is obtained using an equilibrium dissociation constant between 6 and 20 nM [51, 57].

Table S2. Randomly sampled parameters of the models shown in Figure 10.

Parameters	**Blue curve**	**Green curve**	**Red curve**
CRABP1	2.99E-06	8.60E-06	2.73E-09
CRABP2	1.09E-08	1.61E-08	1.14E-08
CYP	2.26E-09	1.12E-08	2.91E-08
RAR	7.08E-07	2.36E-07	2.22E-07
k_{d3}	1.72E-08	2.68E-08	2.45E-08
k_{on13}	4.25E+09	1.2E+10	2E+10
k_{d13}	7.88E-10	1.60E-10	1.84E-10

k_{on14}	152.592	74.9655	72.16303
k_{on15}	2.58E+10	1.85E+10	1.96E+10
k_{on16}	7.51E+09	2.96E+10	3.46E+10
f_{RAR}	0.790299	0.083393	0.332411
f_{CRABP2}	0.116596	0.543783	0.287017
f_{CYP}	0.826228	0.558422	0.03116
f_{GOI}	0.592287	0.978981	0.404229
k_{on6}	103.5768	75.87115	71.91922
k_{on7}	439.5742	962.9376	978.0601
k_{on8}	145.5691	276.7654	234.8322
k_{on18}	0.067334	0.051427	0.049882
k_{on19}	0.005092	0.005032	0.014976
k_{on20}	0.227853	0.125652	0.149364
k_{on24}	0.245181	0.074328	0.119889
k_{on25}	0.049549	0.027726	0.049374
k_{on26}	0.146517	0.154336	0.12501
$I_{\max\,(RAR)}$	7.17E-11	6.33E-11	3.20E-11
$I_{\max\,(CRABP2)}$	2.61E-10	8.20E-11	7.56E-11
$I_{\max\,(CYP)}$	1.37E-10	1.99E-10	9.54E-11
$I_{\max\,(GOI)}$	0.780444	1.926296	1.293431
$k_{\mathrm{d}\,(TF:DNA)}$	2.10E-08	2.70E-08	1.64E-08
K_{M3}	1.20E-07	9.41E-08	5.53E-08
K_{M9}	1.55E-08	1.15E-08	4.23E-08

K_{M11}	3.86E-08	2.79E-08	4.81E-08
k_{on1}	1.99E+11	2.51E+11	2.46E+11
k_{off1}	18.31229	22.79166	20.27421
k_{on2}	3.22E+11	2.62E+11	1.03E+11
k_{off2}	22.66635	29.69411	14.14157
k_{off5}	98.29141	76.1627	117.3805
k_{d5}	1.01E-08	1.66E-08	8.89E-09
k_{on10}	20.04989	17.52512	19.15578
k_{on4}	35.2612	49.85688	15.49563
k_{on12}	19.36441	18.11537	8.855135
k_{d15}	8.16E-08	8.86E-08	8.18E-08
k_{d16}	4.64E-08	7.50E-08	9.29E-08
k_{d9}	1.57E-11	4.00E-11	3.07E-11
k_{d11}	1.08E-10	7.91E-11	7.74E-11

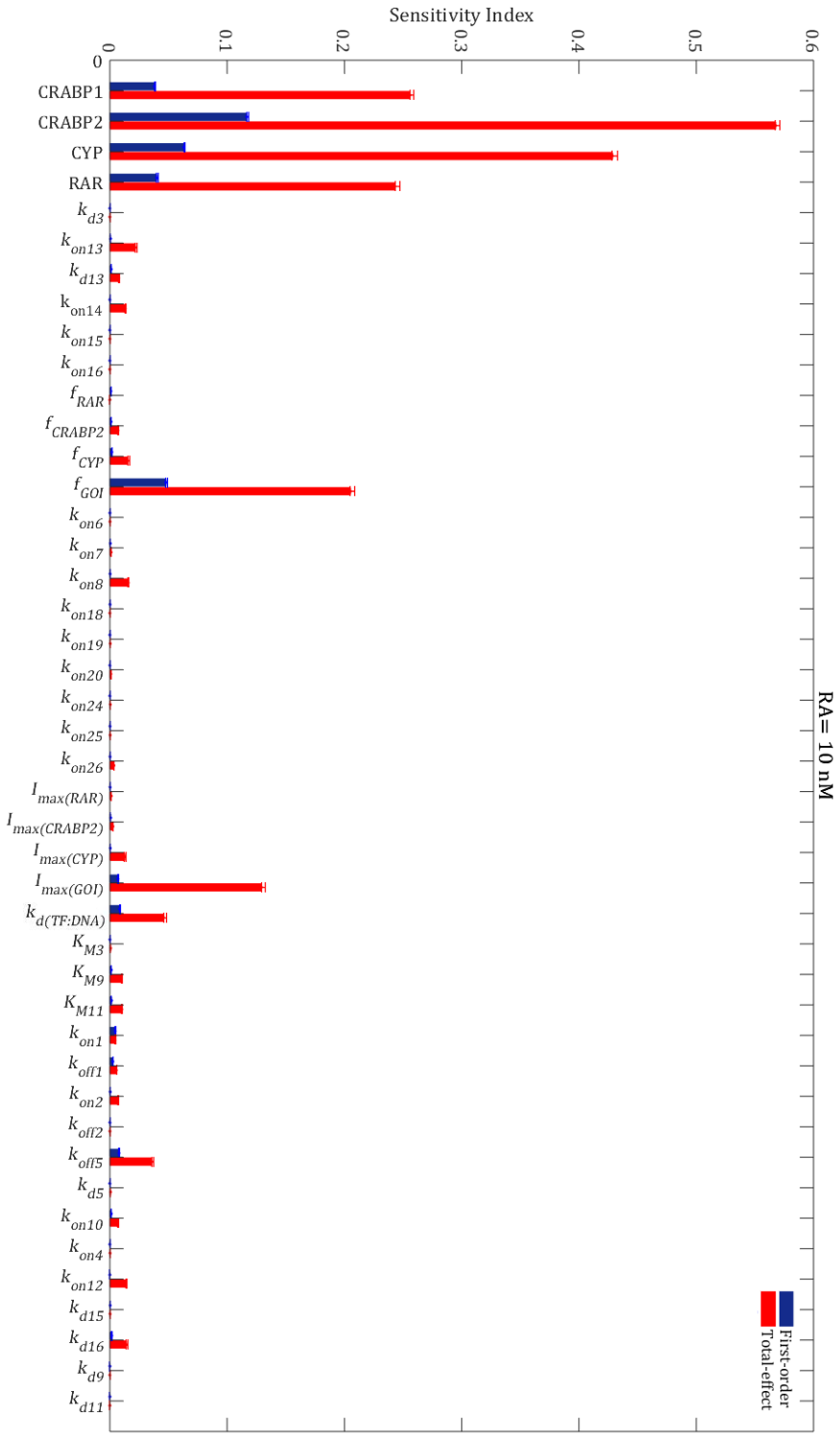
Sensitivity Index
0
0.1
0.2
0.3
0.4
0.5
0.6
CRABP1
CRABP2
CYP
RAR
k_{d3}
k_{on13}
k_{d13}
k_{on14}
k_{on15}
k_{on16}
f_{RAR}
f_{CRABP2}
f_{CYP}
f_{GOI}
k_{on6}
k_{on7}
k_{on8}
k_{on18}
k_{on19}
k_{on20}
k_{on24}
k_{on25}
k_{on26}
$I_{max(RAR)}$
$I_{max(CRABP2)}$
$I_{max(CYP)}$
$I_{max(GOI)}$
$k_{d(TF:DNA)}$
K_{M3}
K_{M9}
K_{M11}
k_{on1}
k_{off1}
k_{on2}
k_{off2}
k_{off5}
k_{d5}
k_{on10}
k_{on4}
k_{on12}
k_{d15}
k_{d16}
k_{d9}
k_{d11}
RA= 10 nM
First-order
Total-effect

Figure S1. (a)

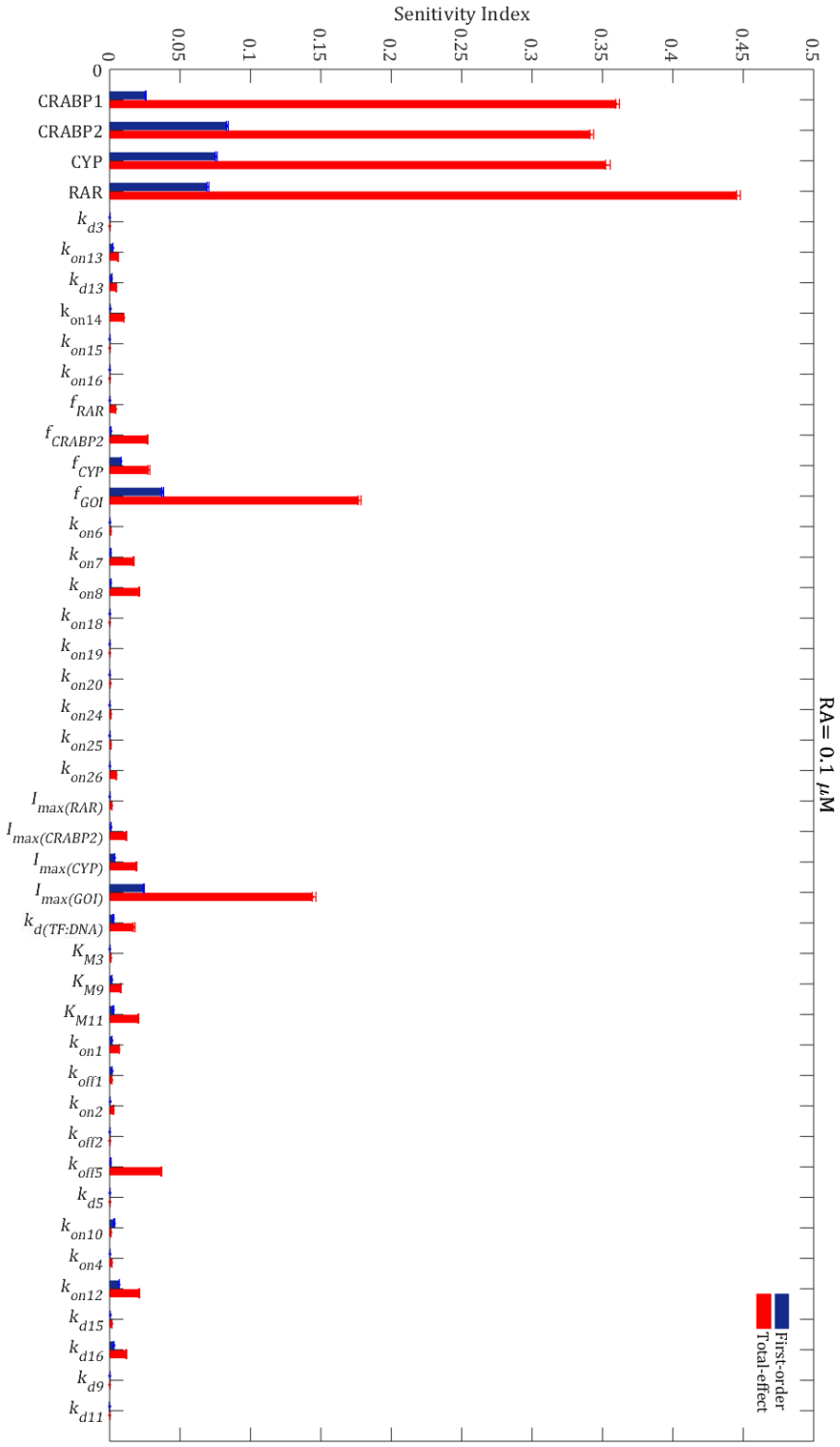
Senitivity Index
0
0.05
0.1
0.15
0.2
0.25
0.3
0.35
0.4
0.45
0.5
CRABP1
CRABP2
CYP
RAR
k_{d3}
k_{on13}
k_{d13}
k_{on14}
k_{on15}
k_{on16}
f_{RAR}
f_{CRABP2}
f_{CYP}
f_{GOI}
k_{on6}
k_{on7}
k_{on8}
k_{on18}
k_{on19}
k_{on20}
k_{on24}
k_{on25}
k_{on26}
$I_{max(RAR)}$
$I_{max(CRABP2)}$
$I_{max(CYP)}$
$I_{max(GOI)}$
$k_{d(TF:DNA)}$
K_{M3}
K_{M9}
K_{M11}
k_{on1}
k_{off1}
k_{on2}
k_{off2}
k_{off5}
k_{d5}
k_{on10}
k_{on4}
k_{on12}
k_{d15}
k_{d16}
k_{d9}
k_{d11}
RA= 0.1 μM
First-order
Total-effect

Figure S1. (b)

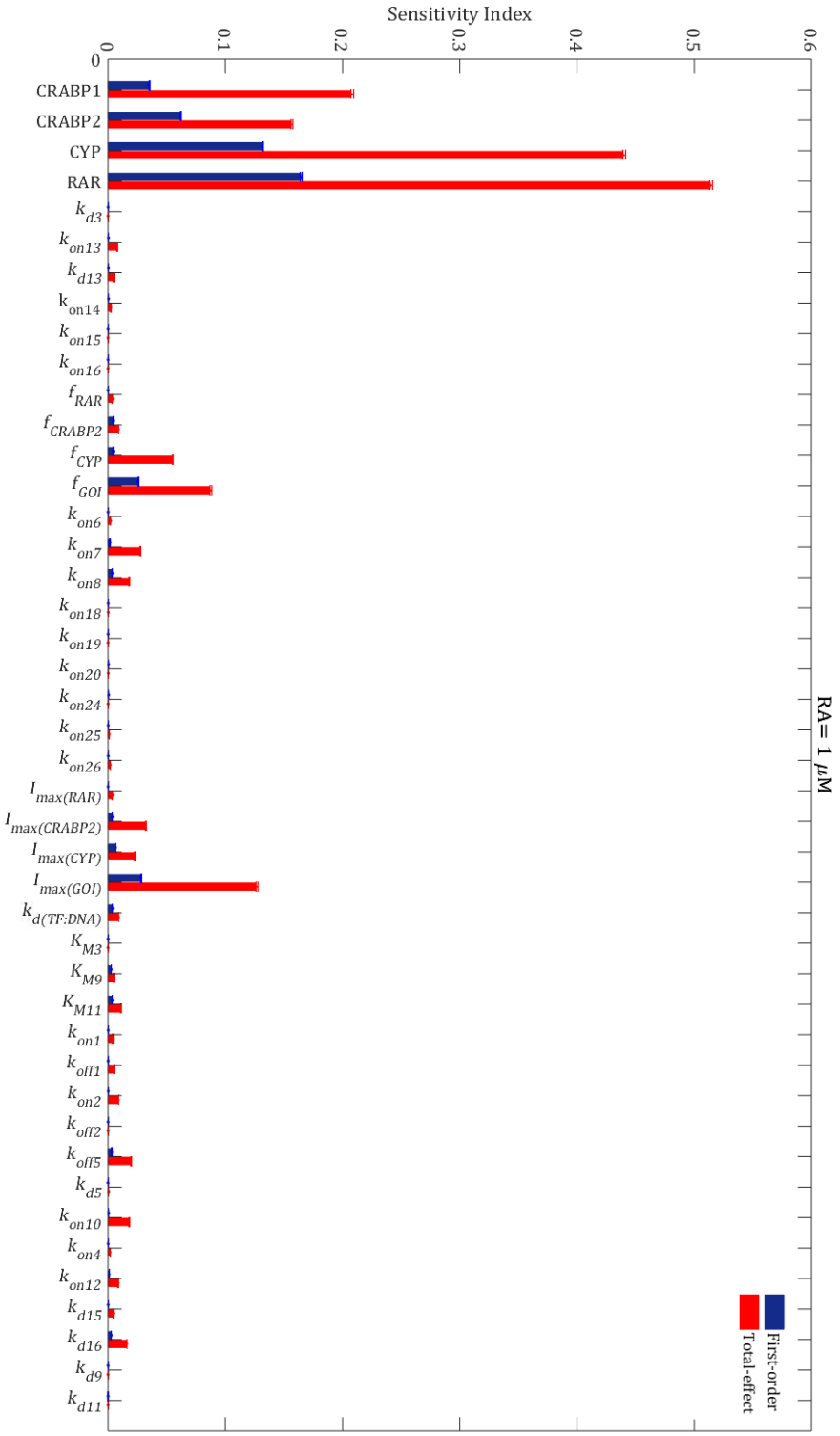
Sensitivity Index
0
0.1
0.2
0.3
0.4
0.5
0.6
CRABP1
CRABP2
CYP
RAR
k_{d3}
k_{on13}
k_{d13}
k_{on14}
k_{on15}
k_{on16}
f_{RAR}
f_{CRABP2}
f_{CYP}
f_{GOI}
k_{on6}
k_{on7}
k_{on8}
k_{on18}
k_{on19}
k_{on20}
k_{on24}
k_{on25}
k_{on26}
$I_{max(RAR)}$
$I_{max(CRABP2)}$
$I_{max(CYP)}$
$I_{max(GOI)}$
$k_{d(TF:DNA)}$
K_{M3}
K_{M9}
K_{M11}
k_{on1}
k_{off1}
k_{on2}
k_{off2}
k_{off5}
k_{d5}
k_{on10}
k_{on4}
k_{on12}
k_{d15}
k_{d16}
k_{d9}
k_{d11}
RA= 1 μM
First-order
Total-effect

Figure S1. (c)

Figure S1. Sensitivity ranking of the model parameters. The model output was set to the time integral of the transcription rate of the GOI within 24 hours after adding (a) 10 nM, (b) 0.1 μM and (c) 1 μM of RA to the model. Blue bars indicate the first-order sensitivity indices, while the red bars represent total-effect sensitivity indices. The error bars show the bootstrap confidence intervals (95% confidence intervals) of the mean values.

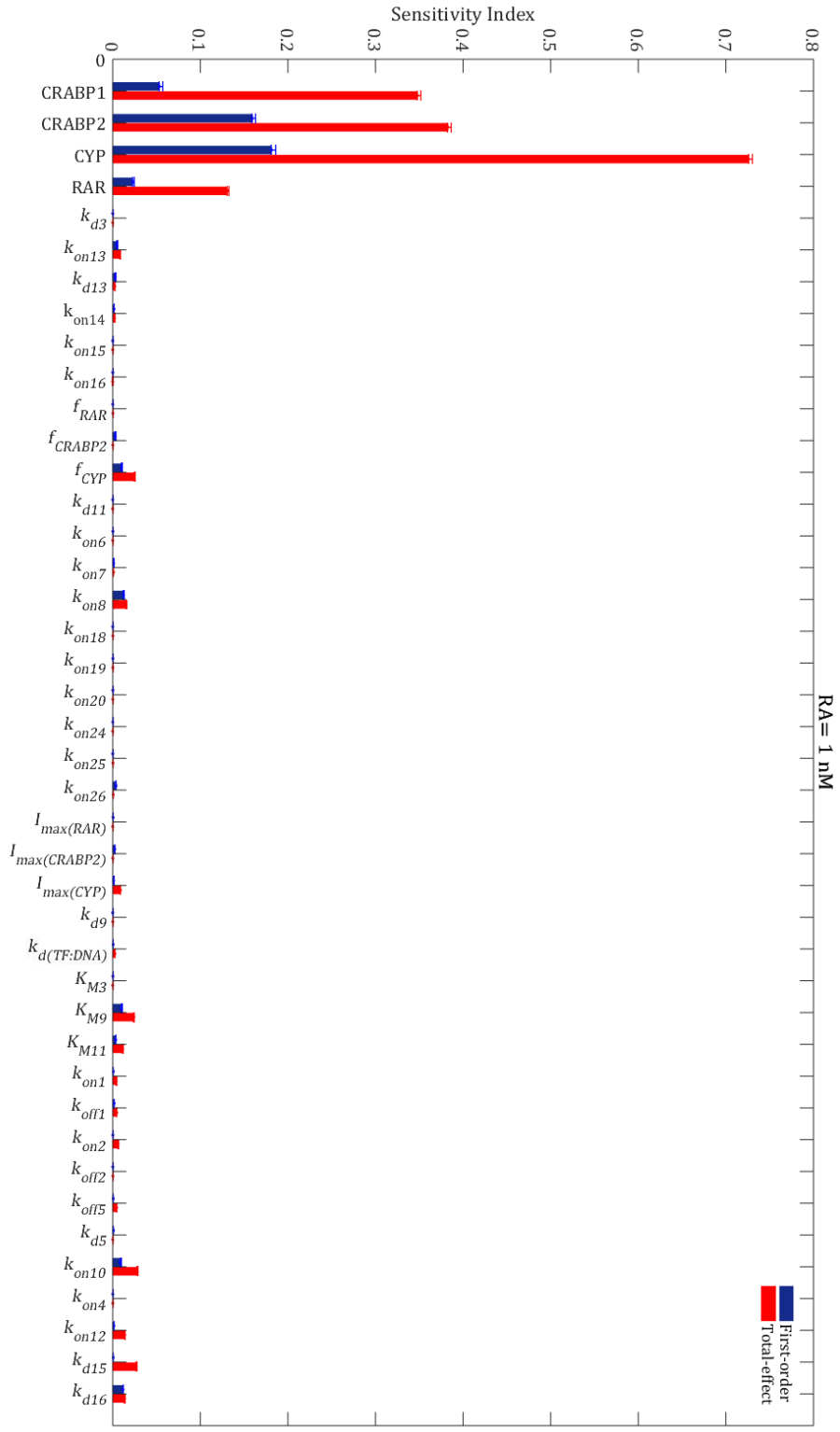
Sensitivity Index
0
0.1
0.2
0.3
0.4
0.5
0.6
0.7
0.8
CRABP1
CRABP2
CYP
RAR
k_{d3}
k_{on13}
k_{d13}
k_{on14}
k_{on15}
k_{on16}
f_{RAR}
f_{CRABP2}
f_{CYP}
k_{d11}
k_{on6}
k_{on7}
k_{on8}
k_{on18}
k_{on19}
k_{on20}
k_{on24}
k_{on25}
k_{on26}
$I_{max(RAR)}$
$I_{max(CRABP2)}$
$I_{max(CYP)}$
k_{d9}
$k_{d(TF:DNA)}$
K_{M3}
K_{M9}
K_{M11}
k_{on1}
k_{off1}
k_{on2}
k_{off2}
k_{off5}
k_{d5}
k_{on10}
k_{on4}
k_{on12}
k_{d15}
k_{d16}
RA= 1 nM
First-order
Total-effect

Figure S2. (a)

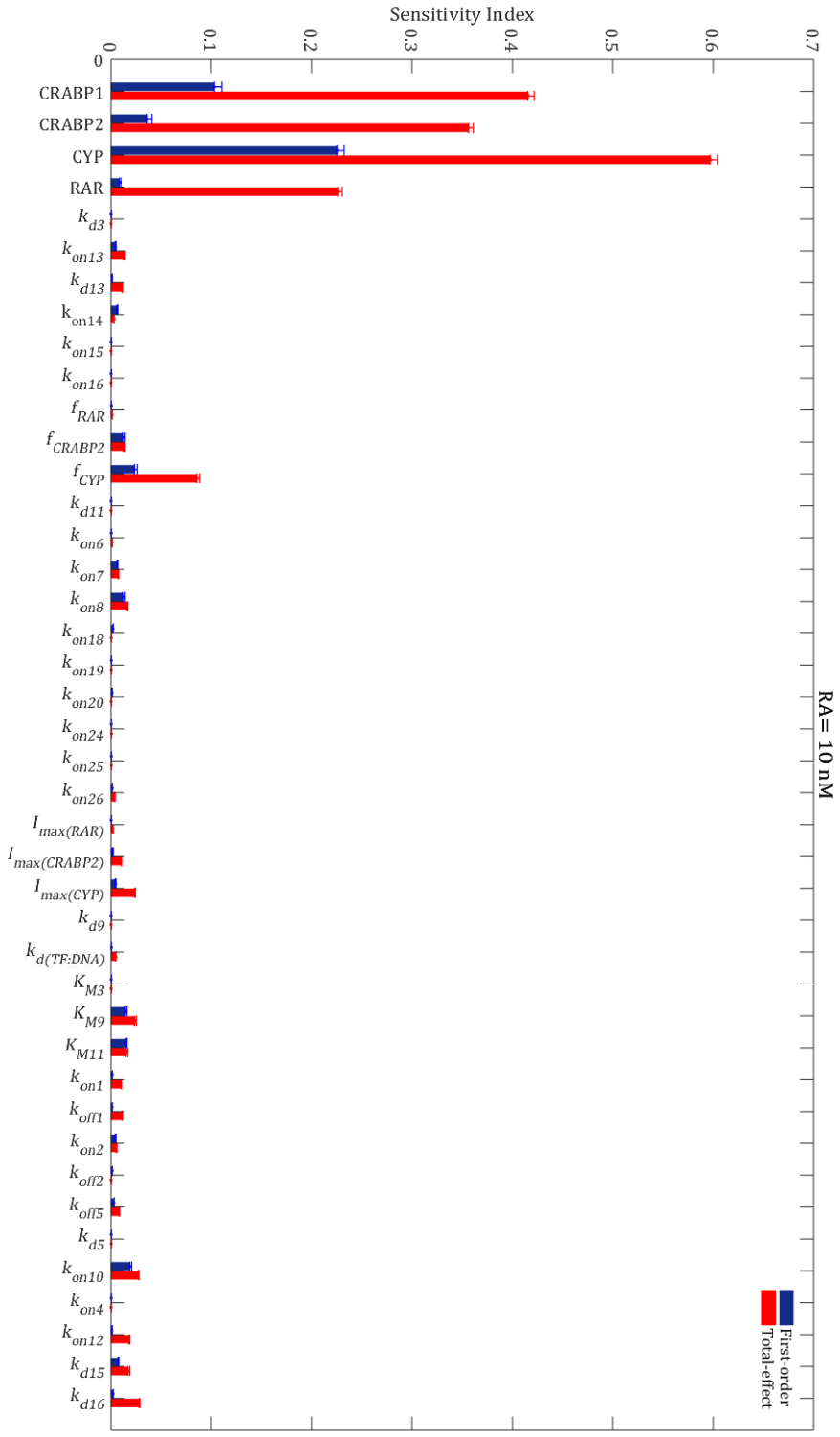
Sensitivity Index
0
0.1
0.2
0.3
0.4
0.5
0.6
0.7
CRABP1
CRABP2
CYP
RAR
k_{d3}
k_{on13}
k_{d13}
k_{on14}
k_{on15}
k_{on16}
f_{RAR}
f_{CRABP2}
f_{CYP}
k_{d11}
k_{on6}
k_{on7}
k_{on8}
k_{on18}
k_{on19}
k_{on20}
k_{on24}
k_{on25}
k_{on26}
$I_{max(RAR)}$
$I_{max(CRABP2)}$
$I_{max(CYP)}$
k_{d9}
$k_{d(TF:DNA)}$
K_{M3}
K_{M9}
K_{M11}
k_{on1}
k_{off1}
k_{on2}
k_{off2}
k_{off5}
k_{d5}
k_{on10}
k_{on4}
k_{on12}
k_{d15}
k_{d16}
RA= 10 nM
First-order
Total-effect

Figure S2. (b)

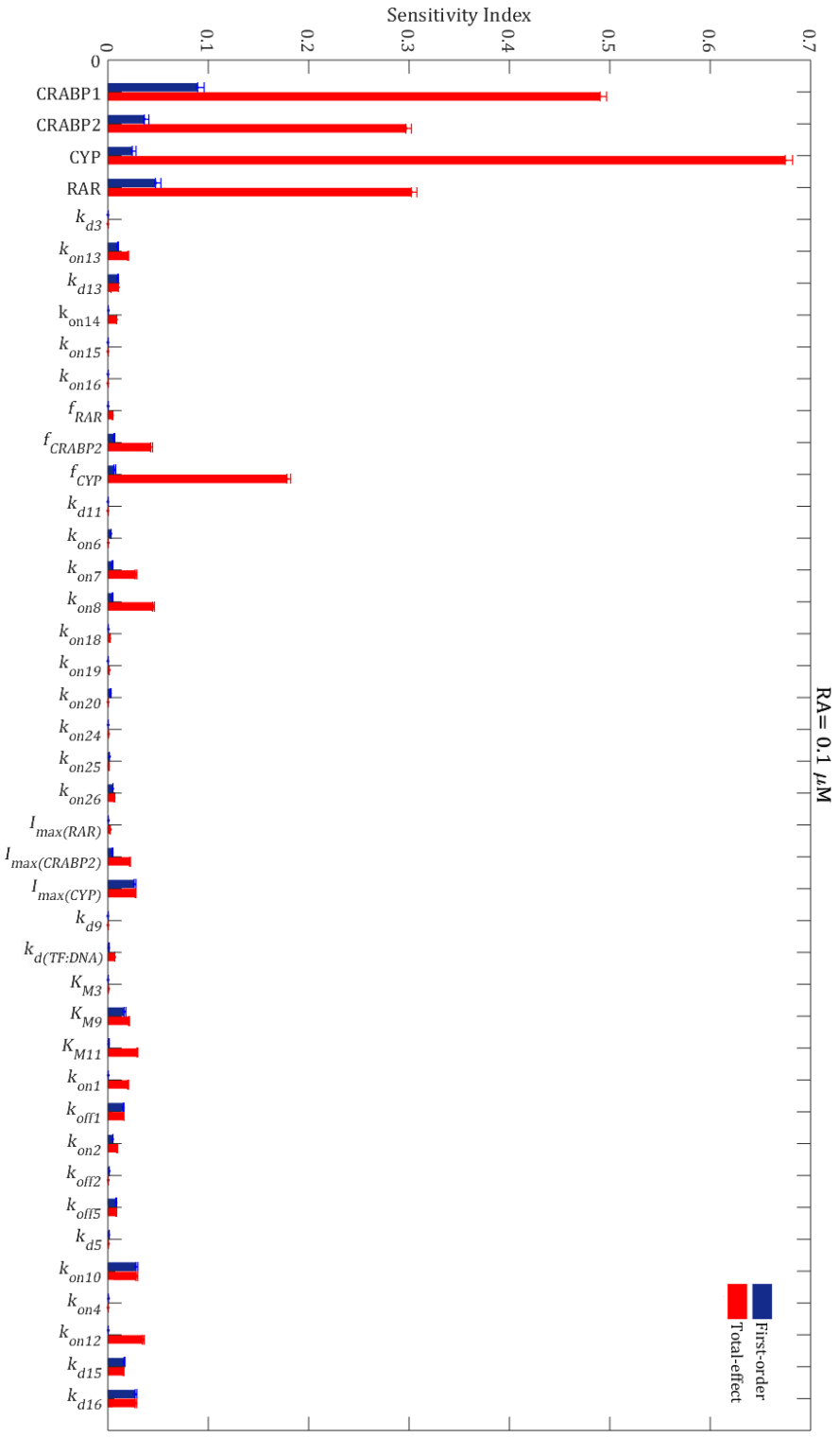
Sensitivity Index
0
0.1
0.2
0.3
0.4
0.5
0.6
0.7
CRABP1
CRABP2
CYP
RAR
k_{d3}
k_{on13}
k_{d13}
k_{on14}
k_{on15}
k_{on16}
f_{RAR}
f_{CRABP2}
f_{CYP}
k_{d11}
k_{on6}
k_{on7}
k_{on8}
k_{on18}
k_{on19}
k_{on20}
k_{on24}
k_{on25}
k_{on26}
$I_{max(RAR)}$
$I_{max(CRABP2)}$
$I_{max(CYP)}$
k_{d9}
$k_{d(TF:DNA)}$
K_{M3}
K_{M9}
K_{M11}
k_{on1}
k_{off1}
k_{on2}
k_{off2}
k_{off5}
k_{d5}
k_{on10}
k_{on4}
k_{on12}
k_{d15}
k_{d16}
RA= 0.1 μM
First-order
Total-effect

Figure S2. (c)

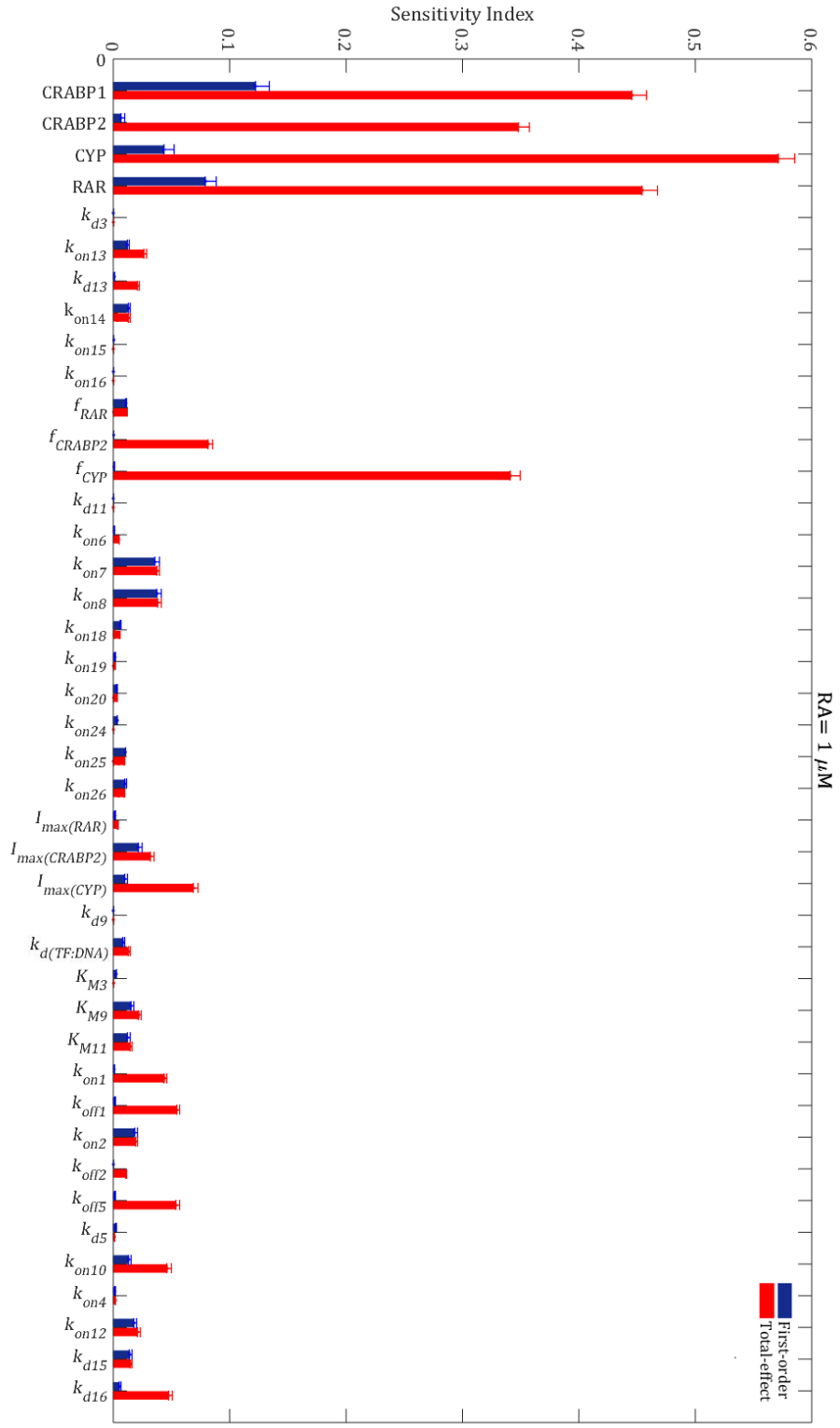
Sensitivity Index
0
0.1
0.2
0.3
0.4
0.5
0.6
CRABP1
CRABP2
CYP
RAR
k_{d3}
k_{on13}
k_{d13}
k_{on14}
k_{on15}
k_{on16}
f_{RAR}
f_{CRABP2}
f_{CYP}
k_{d11}
k_{on6}
k_{on7}
k_{on8}
k_{on18}
k_{on19}
k_{on20}
k_{on24}
k_{on25}
k_{on26}
$I_{max(RAR)}$
$I_{max(CRABP2)}$
$I_{max(CYP)}$
k_{d9}
$k_{d(TF:DNA)}$
K_{M3}
K_{M9}
K_{M11}
k_{on1}
k_{off1}
k_{on2}
k_{off2}
k_{off5}
k_{d5}
k_{on10}
k_{on4}
k_{on12}
k_{d15}
k_{d16}
RA= 1 μM
First-order
Total-effect

Figure S2. (d)

Figure S2. Sensitivity ranking of the model parameters. The model output was set to the time integral of the total RA metabolite formation within 24 hours after adding (a) 1 nM, (b) 10 nM, (c) 0.1 μM and (d) 1 μM of RA to the model. Blue bars indicate the first-order sensitivity indices, while the red bars represent total-effect sensitivity indices. The error bars show the bootstrap confidence intervals (95% confidence intervals) of the mean values.

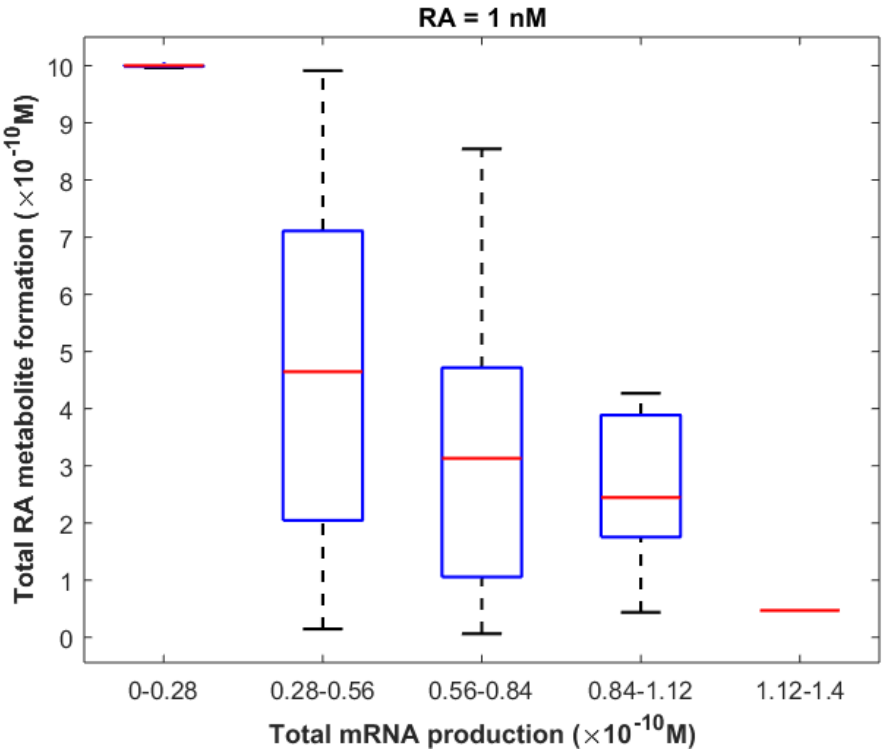

Figure S3. (a)

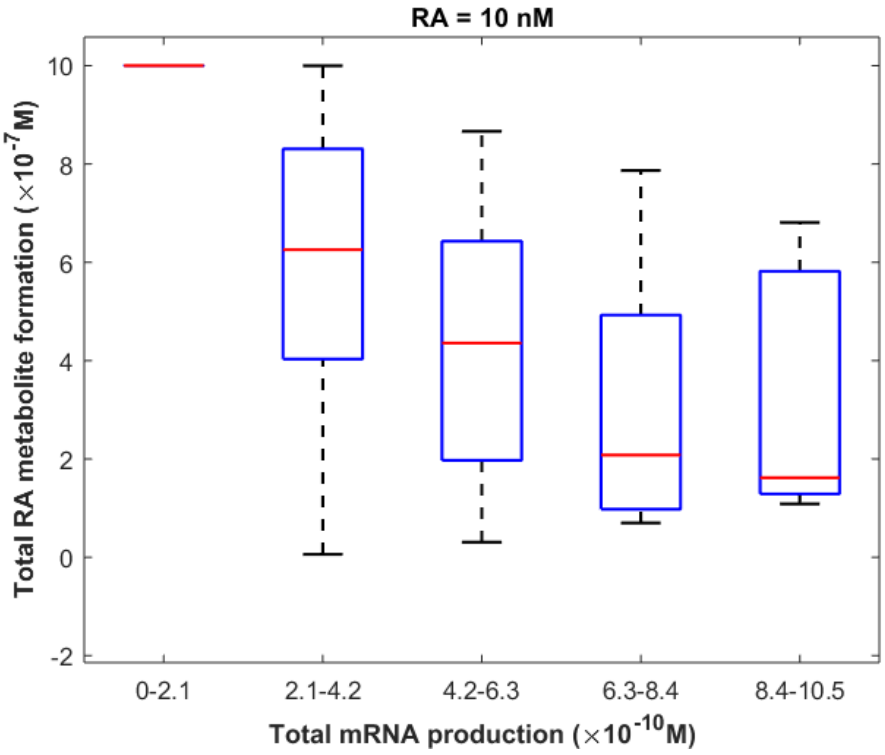

Figure S3. (b)

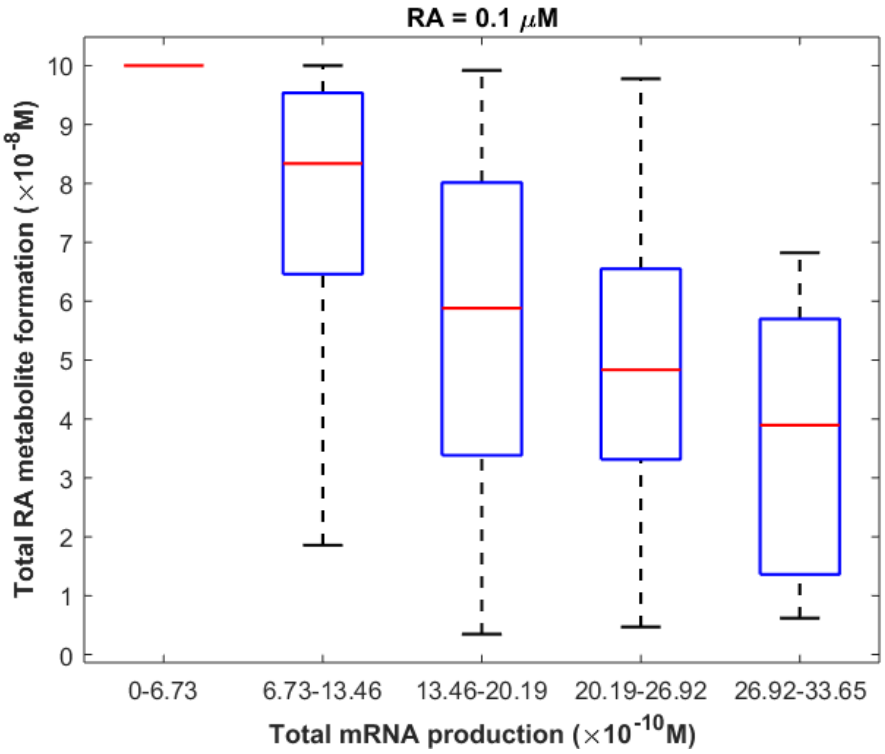

Figure S3. (c)

Figure S3. The relationship between total RA metabolite formation and total mRNA production within 24 hours of treatment with (a) 1 nM, (b) 10 nM, (c) 0.1 μM of RA. The results were obtained by random sampling of 10000 points following a uniform distribution over a 44-dimensional parameter space. The Spearman's correlation coefficients and P values were (a) ρ=-0.44, p=0, (b) ρ=-0.5, p=0, (c) ρ=-0.63, p=0.

2.7. References

1. Boylan JF, Gudas LJ: Overexpression of the cellular retinoic acid binding protein-I (CRABP-I) results in a reduction in differentiation-specific gene expression in F9 teratocarcinoma cells. The Journal of Cell Biology 1991, 112(5):965-979.
2. Boylan J, Gudas L: The level of CRABP-I expression influences the amounts and types of all-trans-retinoic acid metabolites in F9 teratocarcinoma stem cells. Journal of Biological Chemistry 1992, 267(30):21486-21491.
3. Venepally P, Reddy LG, Sani BP: Analysis of the effects of CRABP I expression on the RA-induced transcription mediated by retinoid receptors. Biochemistry 1996, 35(31):9974-9982.
4. GoRRY P, Lufkin T, Dierich A, Rochette-Egly C, Decimo D, Dolle P, Mark M, Durand B, Chambon P: The cellular retinoic acid binding protein I is dispensable. Proceedings of the National Academy of Sciences 1994, 91(19):9032-9036.
5. Dong D, Ruuska SE, Levinthal DJ, Noy N: Distinct roles for cellular retinoic acid-binding proteins I and II in regulating signaling by retinoic acid. Journal of Biological Chemistry 1999, 274(34):23695-23698.
6. Nelson CH, Peng CC, Lutz JD, Yeung CK, Zelter A, Isoherranen N: Direct protein–protein interactions and substrate channeling between cellular retinoic acid binding proteins and CYP26B1. FEBS letters 2016, 590(16):2527-2535.
7. Budhu AS, Noy N: Direct channeling of retinoic acid between cellular retinoic acid-binding protein II and retinoic acid receptor sensitizes mammary carcinoma cells to retinoic acid-induced growth arrest. Molecular and cellular biology 2002, 22(8):2632-2641.
8. Majumdar A, Petrescu AD, Xiong Y, Noy N: Nuclear translocation of cellular retinoic acid-binding protein II is regulated by retinoic acid-controlled SUMOylation. Journal of Biological Chemistry 2011, 286(49):42749-42757.
9. Pelkonen O, Turpeinen M, Hakkola J, Honkakoski P, Hukkanen J, Raunio H: Inhibition and induction of human cytochrome P450 enzymes: current status. Archives of toxicology 2008, 82(10):667-715.
10. Hrycay EG, Bandiera SM: Cytochrome P450 enzymes. Pharmaceutical Sciences Encyclopedia 2007.
11. Delva L, Bastie J-N, Rochette-Egly C, Kraïba R, Balitrand N, Despouy G, Chambon P, Chomienne C: Physical and functional interactions between cellular retinoic acid binding protein II and the retinoic acid-dependent nuclear complex. Molecular and cellular biology 1999, 19(10):7158-7167.
12. Saltelli A, Ratto M, Andres T, Campolongo F, Cariboni J, Gatelli D, Saisana M, Tarantola S: Global sensitivity analysis: the primer: John Wiley & Sons; 2008.
13. Pollard TD: A guide to simple and informative binding assays. Molecular biology of the cell 2010, 21(23):4061-4067.
14. Boskovic G, Desai D, Niles RM: Regulation of retinoic acid receptor α by protein kinase C in B16 mouse melanoma cells. Journal of Biological Chemistry 2002, 277(29):26113-26119.
15. Stormo GD, Zhao Y: Determining the specificity of protein–DNA interactions. Nature Reviews Genetics 2010, 11(11):751.

16. Schwanhäusser B, Busse D, Li N, Dittmar G, Schuchhardt J, Wolf J, Chen W, Selbach M: Global quantification of mammalian gene expression control. Nature 2011, 473(7347):337.
17. Barthel ER: On the utility of a compartmental population kinetics model of intestinal epithelial stem cell proliferation and differentiation. Theoretical Biology and Medical Modelling 2017, 14(1):25.
18. Pianosi F, Sarrazin F, Wagener T: A Matlab toolbox for global sensitivity analysis. Environmental Modelling & Software 2015, 70:80-85.
19. Ghaffari H, Grant SC, Petzold LR, Harrington MG: Regulation of cerebrospinal fluid and brain tissue sodium levels by choroid plexus and brain capillary endothelial cell sodium-potassium pumps during migraine. bioRxiv 2019:572727.
20. Ghaffari H, Petzold LR: Identification of influential proteins in the classical retinoic acid signaling pathway. Theoretical Biology and Medical Modelling 2018, 15(1):16.
21. Tang T, Reed P, Wagener T, Van Werkhoven K: Comparing sensitivity analysis methods to advance lumped watershed model identification and evaluation. Hydrology and Earth System Sciences Discussions 2006, 3(6):3333-3395.
22. Sin G, Gernaey KV, Neumann MB, van Loosdrecht MC, Gujer W: Global sensitivity analysis in wastewater treatment plant model applications: prioritizing sources of uncertainty. Water research 2011, 45(2):639-651.
23. Cosenza A, Mannina G, Vanrolleghem PA, Neumann MB: Global sensitivity analysis in wastewater applications: A comprehensive comparison of different methods. Environmental modelling & software 2013, 49:40-52.
24. Iwanami S, Kakizoe Y, Morita S, Miura T, Nakaoka S, Iwami S: A highly pathogenic simian/human immunodeficiency virus effectively produces infectious virions compared with a less pathogenic virus in cell culture. Theoretical Biology and Medical Modelling 2017, 14(1):9.
25. Veloso A, Kirkconnell KS, Magnuson B, Biewen B, Paulsen MT, Wilson TE, Ljungman M: Rate of elongation by RNA polymerase II is associated with specific gene features and epigenetic modifications. Genome research 2014, 24(6):896-905.
26. Balmer JE, Blomhoff R: Gene expression regulation by retinoic acid. Journal of lipid research 2002, 43(11):1773-1808.
27. Pijnappel W, Hendriks H, Folkers G, Van den Brink C: Dekker, EJ Edelenbosch, C. van der Saag, PT Durston, AJ 1993. The retinoid ligand 4-oxo-retinoic acid is a highly active modulator of positional specification. Nature, 366:340-344.
28. Idres N, Marill J, Flexor MA, Chabot GG: Activation of retinoic acid receptor-dependent transcription by all-trans-retinoic acid metabolites and isomers. Journal of Biological Chemistry 2002, 277(35):31491-31498.
29. Lansink M, Bennekum AMV, Blaner WS, Kooistra T: Differences in Metabolism and Isomerization of All-trans-Retinoic Acid and 9-cis-Retinoic Acid between Human Endothelial Cells and Hepatocytes. The FEBS Journal 1997, 247(2):596-604.
30. Williams JB, Napoli JL: Metabolism of retinoic acid and retinol during differentiation of F9 embryonal carcinoma cells. Proceedings of the National Academy of Sciences 1985, 82(14):4658-4662.
31. Liu R-Z, Garcia E, Glubrecht DD, Poon HY, Mackey JR, Godbout R: CRABP1 is associated with a poor prognosis in breast cancer: adding to the complexity of breast cancer cell response to retinoic acid. Molecular cancer 2015, 14(1):129.
32. Favorskaya I, Kainov Y, Chemeris G, Komelkov A, Zborovskaya I, Tchevkina E: Expression and clinical significance of CRABP1 and CRABP2 in non-small cell lung cancer. Tumor Biology 2014, 35(10):10295-10300.

33. Roman SD, Clarke CL, Hall RE, Alexander IE, Sutherland RL: Expression and regulation of retinoic acid receptors in human breast cancer cells. Cancer research 1992, 52(8):2236-2242.
34. Murray GI, Patimalla S, Stewart KN, Miller ID, Heys SD: Profiling the expression of cytochrome P450 in breast cancer. Histopathology 2010, 57(2):202-211.
35. Mast N, Lin JB, Pikuleva IA: Marketed Drugs Can Inhibit Cytochrome P450 27A1 (CYP27A1), a Potential New Target for Breast Cancer Adjuvant Therapy. Molecular pharmacology 2015:mol. 115.099598.
36. Desai PB, Nallani SC, Sane RS, Moore LB, Goodwin BJ, Buckley DJ, Buckley AR: Induction of cytochrome P450 3A4 in primary human hepatocytes and activation of the human pregnane X receptor by tamoxifen and 4-hydroxytamoxifen. Drug metabolism and disposition 2002, 30(5):608-612.
37. White JA, Ramshaw H, Taimi M, Stangle W, Zhang A, Everingham S, Creighton S, Tam S-P, Jones G, Petkovich M: Identification of the human cytochrome P450, P450RAI-2, which is predominantly expressed in the adult cerebellum and is responsible for all-trans-retinoic acid metabolism. Proceedings of the National Academy of Sciences 2000, 97(12):6403-6408.
38. Catharine Ross A, Zolfaghari R: Cytochrome P450s in the regulation of cellular retinoic acid metabolism. Annual review of nutrition 2011, 31:65-87.
39. Thatcher JE, Isoherranen N: The role of CYP26 enzymes in retinoic acid clearance. Expert opinion on drug metabolism & toxicology 2009, 5(8):875-886.
40. Buttrick BR: Characterization of selective and potent inhibitors of the human retinoic acid hydroxylases CYP26A1 and CYP26B1. 2013.
41. Topletz AR: The Relative Importance of CYP26A1 and CYP26B1 in Mediating Retinoid Homeostasis: Studies on the Formation, Elimination and Biological Activity of All-Trans-Retinoic Acid Metabolites. 2013.
42. Angulo A, Chandraratna RA, LeBlanc JF, Ghazal P: Ligand induction of retinoic acid receptors alters an acute infection by murine cytomegalovirus. Journal of virology 1998, 72(6):4589-4600.
43. Ingalls BP: Mathematical modeling in systems biology: an introduction: MIT press; 2013.
44. Sauro HM: Enzyme kinetics for systems biology: Future Skill Software; 2011.
45. Stormo GD, Zhao Y: Determining the specificity of protein–DNA interactions. Nature Reviews Genetics 2010, 11(11):751-760.
46. Fuchs G, Voichek Y, Benjamin S, Gilad S, Amit I, Oren M: 4sUDRB-seq: measuring genomewide transcriptional elongation rates and initiation frequencies within cells. Genome biology 2014, 15(5):R69.
47. Zody MC, Garber M, Adams DJ, Sharpe T, Harrow J, Lupski JR, Nicholson C, Searle SM, Wilming L, Young SK: DNA sequence of human chromosome 17 and analysis of rearrangement in the human lineage. Nature 2006, 440(7087):1045-1049.
48. Gregory S, Barlow K, McLay K, Kaul R, Swarbreck D, Dunham A, Scott C, Howe K, Woodfine K, Spencer C: The DNA sequence and biological annotation of human chromosome 1. Nature 2006, 441(7091):315-321.
49. Hillier LW, Graves TA, Fulton RS, Fulton LA, Pepin KH, Minx P, Wagner-McPherson C, Layman D, Wylie K, Sekhon M: Generation and annotation of the DNA sequences of human chromosomes 2 and 4. Nature 2005, 434(7034):724-731.
50. Halford SE, Marko JF: How do site-specific DNA-binding proteins find their targets? Nucleic acids research 2004, 32(10):3040-3052.
51. Crettaz M, Baron A, Siegenthaler G, Hunziker W: Ligand specificities of recombinant retinoic acid receptors RAR α and RAR β. Biochemical journal 1990, 272(2):391-397.

52. Mirny L, Slutsky M, Wunderlich Z, Tafvizi A, Leith J, Kosmrlj A: How a protein searches for its site on DNA: the mechanism of facilitated diffusion. Journal of Physics A: Mathematical and Theoretical 2009, 42(43):434013.
53. Giguere V, Lyn S, Yip P, Siu C-H, Amin S: Molecular cloning of cDNA encoding a second cellular retinoic acid-binding protein. Proceedings of the National Academy of Sciences 1990, 87(16):6233-6237.
54. Zi Z: Sensitivity analysis approaches applied to systems biology models. IET systems biology 2011, 5(6):336-346.
55. Zhang XY, Trame M, Lesko L, Schmidt S: Sobol sensitivity analysis: a tool to guide the development and evaluation of systems pharmacology models. CPT: pharmacometrics & systems pharmacology 2015, 4(2):69-79.
56. Mokhtari A, Frey HC, Zheng J: Evaluation and recommendation of sensitivity analysis methods for application to stochastic human exposure and dose simulation models. Journal of Exposure Science and Environmental Epidemiology 2006, 16(6):491-506.
57. Kersten S, Dawson MI, Lewis BA, Noy N: Individual subunits of heterodimers comprised of retinoic acid and retinoid X receptors interact with their ligands independently. Biochemistry 1996, 35(12):3816-3824.
58. Cambridge SB, Gnad F, Nguyen C, Bermejo JL, Krüger M, Mann M: Systems-wide proteomic analysis in mammalian cells reveals conserved, functional protein turnover. Journal of proteome research 2011, 10(12):5275-5284.
59. Tsou HC, Lee X, Si SP, Peacocke M: Regulation of retinoic acid receptor expression in dermal fibroblasts. Experimental cell research 1994, 211(1):74-81.
60. Redfern C, Lovat P, Malcolm A, Pearson A: Differential effects of 9-cis and all-trans retinoic acid on the induction of retinoic acid receptor-β and cellular retinoic acid-binding protein II in human neuroblastoma cells. Biochemical Journal 1994, 304(1):147-154.

Chapter 3

Analysis of the role of thrombomodulin in all-trans retinoic acid treatment of coagulation disorders in cancer patients

3.1. Introduction

All-trans retinoic acid (RA) plays key roles in cancer treatment and prevention. Breast, lung, bladder, prostate, and acute promyelocytic leukemia (APL) cancers were shown to be suppressed by RA [1-5]. RA therapy can also improve blood clotting disorders such as thrombosis and disseminated intravascular coagulation (DIC) in cancer patients [6-12]. DIC, a life-threatening coagulation disorder associated with uncontrolled clot formation and/or excessive bleeding, was reported in patients with different types of cancer[13-16]. Some of the mechanisms involved in the occurrence of DIC in cancer patients are known, and others are still under investigation. Tissue factor (TF) upregulation by tumor cells is one of the main causes of the observed hypercoagulable state in cancer patients [17-20]. TF binds to factor VIIa and forms a complex which activates factors X and IX. Activation of factor X leads to formation of the prothrombinase complex, which converts prothrombin to thrombin. Expression of the cancer procoagulant (CP), a specific enzyme that directly activates factor X, by tumor cells is another important mechanism for the initiation of the coagulation cascade in cancer [21, 22]. Tumor cells can also affect the coagulation cascade through interactions with other cell types such as monocytes and endothelial cells. Previous studies showed that circulating tumor cells increased the expression of TF by monocytes and endothelial cells [17, 23-25]. Platelet aggregation and induction of inflammatory cytokine release are the other phenomena which can be responsible for blood clotting system abnormalities in cancer patients [26, 27].

Clinical studies have indicated that RA treatment improved the plasma levels of hemostatic markers such as D-dimer, thrombin-antithrombin complex, and fibrinogen in APL patients in hypercoagulable states [11, 12]. Theories have been proposed to explain how RA therapy improves coagulation disorders. *In vitro* studies showed that RA significantly decreased the expression of TF in cancer cells [28, 29]. An *in vivo* study on the procoagulant activity of bone marrow blasts from APL patients under RA treatment revealed that TF and CP in the patients' marrow blasts decreased after RA therapy [12]. RA can also affect the fibrinolytic system by increasing the synthesis of urokinase plasminogen activator (u-PA) in cancer cells and tissue plasminogen activator (t-PA) in endothelial cells [30, 31]. Thereafter, however, RA induces the expression of plasminogen activator inhibitors (PAIs), such as PAI-1 and PAI-2 [32]. The way these two contradictory pathways influence fibrinolysis in cancer patients has not been fully understood. RA also affects the procoagulant and anticoagulant properties of endothelial cells and monocytes [33, 34]. Previous studies have reported that RA increased the antithrombotic potential of microvascular endothelial cells by downregulating TF and upregulating thrombomodulin (TM) expression [34-36]. TM, a surface high-affinity receptor for thrombin, plays a key role in activation of the protein C (PC) anticoagulant pathway. Activated PC, produced by the TM-thrombin complex, inactivates cofactors fVa and FVIIIa, thus inhibiting thrombin generation. Although TM has significant effects on the blood coagulation system, its role in RA treatment of coagulation disorders in cancer patients has not yet been studied. Furthermore, to the best of our knowledge, there is no experimental or computational study that has investigated the extent and forms of variation in TM levels over the course of RA therapy in cancer. Thus, the main objective of this study was to investigate if, how and to

what extent the RA-induced TM upregulation over the course of RA therapy with a single daily oral dose of RA affects thrombin generation profiles in cancer patients. Analysis of the variations of the thrombin generation profile is a classic/standard way of studying the significance of blood factors in the coagulation cascade. In this regard, we developed an ordinary differential equation (ODE) model of gene expression for the RA-induced upregulation of TM concentration on the endothelium. The expression rate of TM on the endothelium depends on the rate of RA diffusion from plasma into the endothelial cells. In plasma, a large fraction of RA (~99%) circulates bound to albumin. However, only free RA molecules in plasma can diffuse passively across the endothelial cell membrane and subsequently bind to RA receptors and activate transcription of the TM gene. The large amount of bound RA in plasma acts as a reservoir from which the RA is slowly released to the unbound form to maintain the equilibrium. Thus, we derived a new formula which expresses the TM transcription rate as a function of free RA concentration. Coupling the gene expression model with three other models, namely a two-compartment pharmacokinetic model of RA, an sTM release model and a mechanistic model of the human coagulation cascade, we investigated the effects of RA-induced TM upregulation on thrombin generation. Our results indicated that overexpression of TM over the course of RA therapy with a daily oral dose of 45 $\frac{mg}{m^2}$ or 110 $\frac{mg}{m^2}$ reduced thrombin level significantly. We also investigated how the progressive reduction in the plasma concentrations of RA over the course of continuous RA therapy with a single daily dose of (110 $\frac{mg}{m^2}$) RA can affect the corrective effects of RA therapy on thrombin generation. Increasing reductions in plasma concentration of RA over the course of RA treatment with a constant daily dose of RA is a potential sign of RA resistance at least in some cancer patients. The exact

mechanism of development of resistance to RA has yet to be determined. Genetic mutations of retinoic acid receptors, increased metabolism of RA, and upregulation of cellular retinoic acid binding proteins which play important roles in the RA signaling pathway [37], have been proposed as possible reasons for RA resistance [38]. Our model predictions of RA resistance effects on the efficacy of RA therapy in treatment of coagulation abnormalities are applicable only to those cancer patients whose plasma levels of RA decrease over continuous treatment days.

3.2. Method

In this section, we first develop a gene expression model that describes TM upregulation on the endothelial cell surface following RA treatment. We train the gene expression model using *in vitro* data from the literature. We then build a two-compartment pharmacokinetic model of RA, which describes the plasma concentration of RA in cancer patients. We couple the gene expression model with the pharmacokinetic model, to obtain the variations of TM level on the endothelial cell surface during the course of RA therapy. We then simulate the time-dependent variations of soluble thrombomodulin (sTM) concentration using an ODE model, called the sTM release ODE model. Finally, we use the output of the sTM release ODE model in an ODE model of the coagulation cascade to investigate the effects of RA-induced TM upregulation on thrombin generation. The gene expression model, pharmacokinetic model and sTM release model are explained in the following sub-sections, while the ODE model of the coagulation cascade is fully explained in [39]. Figure 1 shows the interactions between the different models in this study.

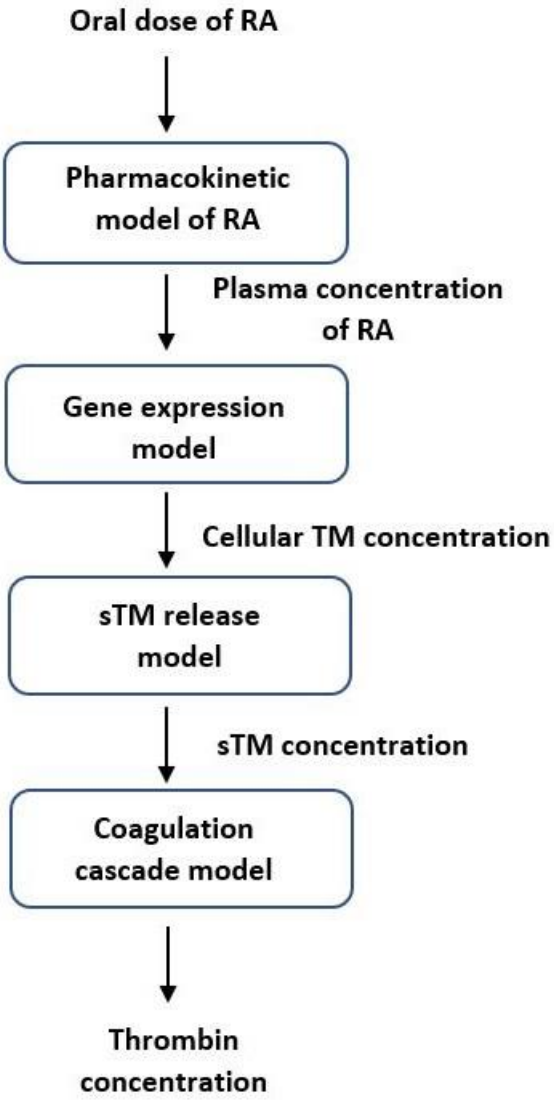

Figure 1. Coupling four models to study how taking an oral dose of RA affects thrombin generation. Each block represents a model, while the arrows before and after each block indicate the input and output of the model, respectively.

3.2.1. Gene expression model

3.2.1.1. Experimental Data

There are several lines of evidence regarding the upregulation of TM gene expression by RA [35, 40, 41]. This upregulation is due to transcriptional changes in the TMR expression level [41]. In this study, we used the experimental data presented by Horie et al. [40], which includes time-dependent variations in TMR levels, and dose-dependent changes in TM levels after treating human pancreas BxPC-3 cells with RA (Fig. 2). Human pancreas BxPC-3 cells were used in that study, as their characteristics of RA-dependent TM expression are the same as those of endothelial cells [40]. The cultured BxPC-3 cells became confluent with fetal calf serum, whose major component is albumin, prior to adding RA to the medium. The TM levels in Fig. 2a were measured after treating the cells with various concentrations of RA for 24 hours. The relative values for TMR level in Fig. 2b were obtained after treating the cells with 10μM of RA.

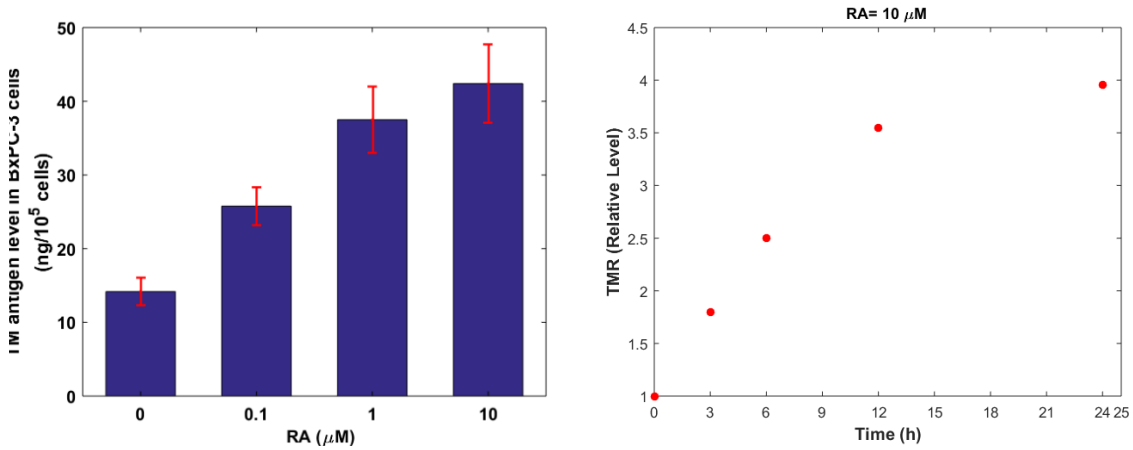

(a) (b)

Figure 2. (a) Effects of RA treatment on TM levels in BxPC-3 cells. The reported values for TM level were obtained after treating the cells with RA for 24 h. Figure adopted from [40]. (b)

Changes in relative levels of TMR in BxPC-3 cells treated with 10μM RA. The mRNA level without incubation is defined as 1. Figure adopted from [40].

3.2.1.2. Formulation of the model

We formulated an ODE model to study the RA-induced upregulation of TM gene expression. The model included gene transcription, protein translation, and mRNA and protein degradation. The model consisted of two species, namely TM and TMR, with ten parameters (Table 1).

$$\frac{\mathrm{d[TMR]}}{\mathrm{dt}} = I + I_0 - k_{\mathrm{dm}}[\mathrm{TMR}] \quad (1)$$

$$\frac{\mathrm{d[TM]}}{\mathrm{dt}} = k_{\mathrm{trans}}[\mathrm{TMR}] - k_{\mathrm{dp}}[\mathrm{TM}], \quad (2)$$

where [TMR] and [TM] indicate molar concentration of TMR and TM, respectively. [TM] and [TMR] are functions of time. The molar concentration of TM, which is a membrane-bound protein, was calculated by dividing the number of moles of TM by the cell volume. The cell volume was set to [42-44]

$V_{\mathrm{cell}} = 10^{-13}\mathrm{L}$.

The transcription rate (I) of the TM gene was the only parameter in the model that depended on RA concentration. An increase in RA concentration leads to activation of a transcription factor, which is responsible for the activation of the TM gene. Considering the mechanism of action of RA, we derived an expression for the TM transcription rate (I), (Proof in Supplementary Information in Section 3.6)

$$I = I_{max} \frac{[\mathrm{RA}][\mathrm{REC_{1t}}]}{[\mathrm{RA}][\mathrm{REC_{1t}}] + k_{\mathrm{d2}}([\mathrm{RA}] + k_{\mathrm{d1}})}, \quad (3)$$

where [RA] and $[\mathrm{REC_{1t}}]$ in Eq. 3 indicate free RA concentration and total concentration of the specific transcription factor which can activate the transcription of the TM gene, respectively. I is time-dependent, since [RA] can change over time, while $I_{\max}$ and $[\mathrm{REC_{1t}}]$ are constant for the TM gene in a given cell type. The rest of the parameters in Eq. 3 are defined in Table 1. RA is highly bound to albumin in the culture medium [40] and in plasma [45]. We assumed that the unbound fraction of RA is about 1% of the total RA concentration[45, 46]. It is important to note that only the free drug in the culture medium or plasma is able to have a therapeutic effect.

Table 1. List of the model parameters

Parameters	Description	Range	Reference
I_0	Basal transcription rate by transcription factors, which are not affected by RA (M/hr)	$1.6 \times 10^{-12} - 1.6 \times 10^{-9}$	[47]
k_{dm}	TMR degradation rate (1/hr)	0.256	[48]
k_{trans}	Translation rate(1/hr)	1-10000	[47]
k_{dp}	TM degradation rate (1/hr)	0.0845	[49]
IC_{TMR}	TMR initial concentration (M)	$1.6 \times 10^{-11} - 1.6 \times 10^{-8}$	[47, 50]
IC_{TM}	TM initial concentration (M)	$1.65 \times 10^{-5} - 2.14 \times 10^{-5}$	[40]
$I_{\max}$	Maximal transcription rate of the TM gene (M/hr)	$1.6 \times 10^{-12} - 1.6 \times 10^{-9}$	[47]

k_{d1}	Equilibrium dissociation constant of RA binding to retinoic acid receptor (M)	8×10^{-9}	[51]
k_{d2}	Equilibrium dissociation constant of DNA-transcription factor complex (M)	15×10^{-9}	[52]
$[\mathrm{REC}_{1\mathrm{t}}]$	Total concentration (M) of the specific transcription factor which can activate the TM gene transcription	$1 \times 10^{-11} - 1 \times 10^{-6}$	Unknown. A large range is used.

The translation rate (k_{trans}) and basal transcription rate (I_0) were the only parameters that depended on the other parameters. Assuming that the TM and TMR concentrations were in steady state before RA treatment, we calculated k_{trans} and I_0 by

$$k_{\mathrm{trans}} = \frac{k_{\mathrm{dp}} IC_{\mathrm{TM}}}{IC_{\mathrm{TMR}}}, \tag{4}$$

$$I_0 = k_{\mathrm{dm}} IC_{\mathrm{TMR}} . \tag{5}$$

The model had six unknown parameters, for which we considered some bounds (Table 1). The bounds for IC_{TM} were due to the experimental errors, while the other unknown parameters, namely I_{max}, IC_{TMR}, k_{trans}, I_0 and $[\mathrm{REC}_{1\mathrm{t}}]$ had physiological bounds. We estimated the model's unknown parameters by minimizing the residual between simulation results and empirical measurements, following a parameter estimation algorithm. In this regard, we used a particle swarm optimization (PSO) technique [53] (See Supplementary Information in Section 3.6 for full details regarding the parameter estimation algorithm and PSO). Our simulation results for the time-dependent variations in TM and TMR concentrations compared reasonably well with the experimental data (Fig. 3).

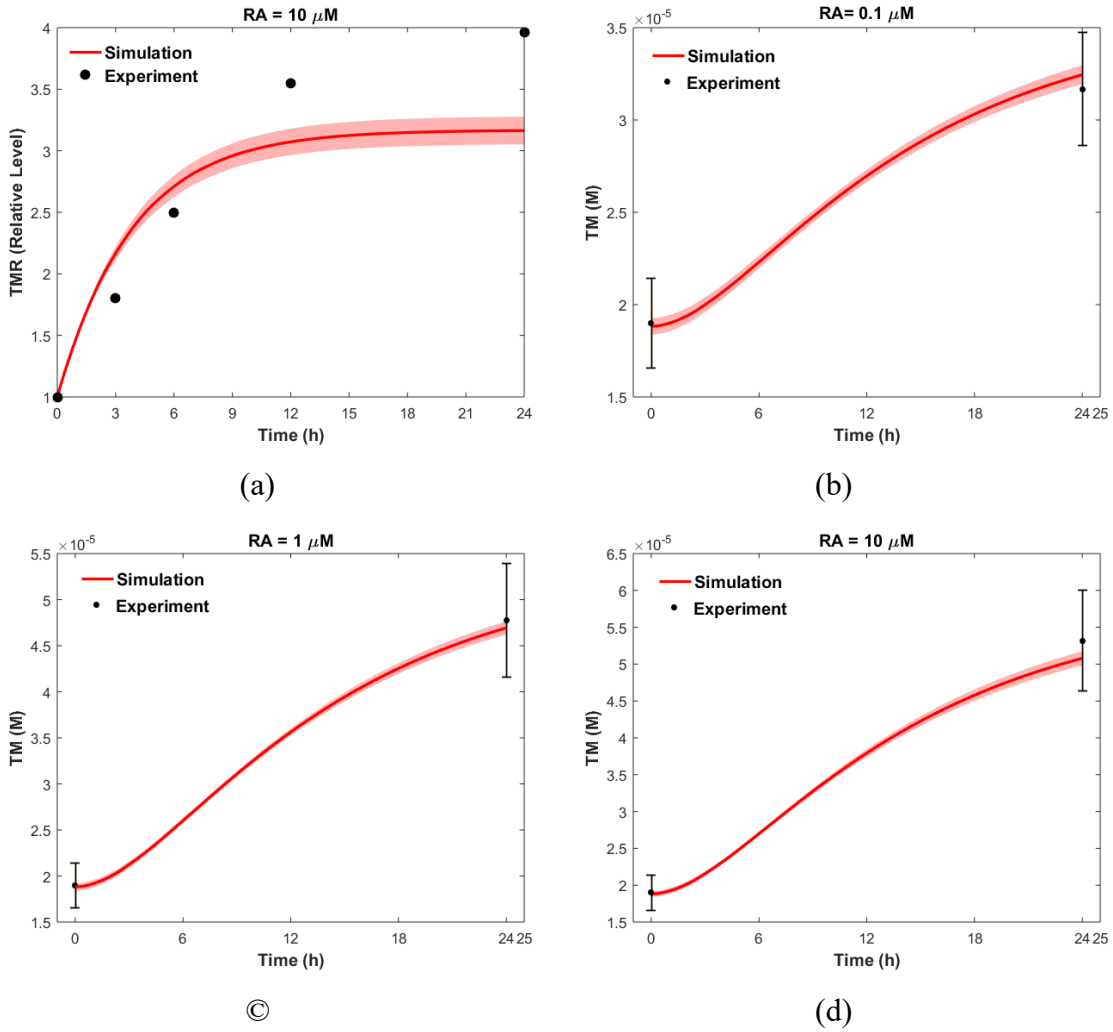

Figure 3. The gene expression model training simulations. The model's unknown parameters were estimated using PSO. The red lines show the mean simulated results for (a) TMR, (b) TM at RA= 0.1 µM, (c) TM at RA= 1 µM and (d) TM at RA= 10 µM. The shaded regions denote 99% confidence interval of the mean results [53, 54]. The black dots indicate the experimental data, while the standard deviation of each experimental data point is half the length of the total error bar.

The solid lines in Figure 3 show the mean simulated results, while the shaded regions in Figure 2 show the 99% confidence interval of the mean simulated results. From Figure 3a, it can be seen that TMR reached steady state almost 18 hours after administration of RA, while TM did not reach steady state even after 24 hours (Fig. 3b-d).

Using the estimated parameters from the training data set [40], we compared the model's predictions with another data set [41] for the RA-induced upregulation of TM on endothelial cells. In this regard, fold change values of TM concentration after 24 hours of treatment with various concentrations of RA were obtained (Fig. 4). Figure 4 indicates that simulation results compared reasonably well with experimental data.

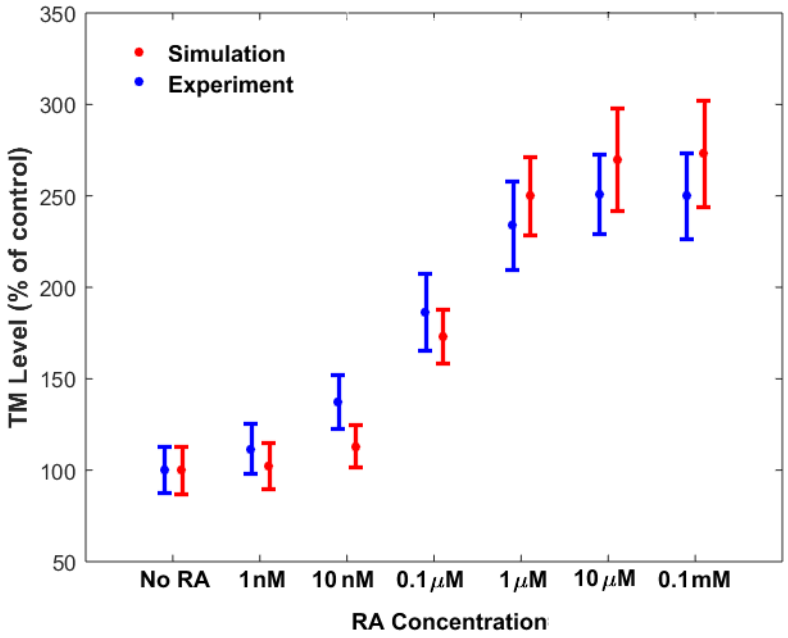

Figure 4. Comparison between the simulated results for fold change values of TM concentration after 24 hours of treatment with various concentrations of RA with experimental data not used during model training. The simulation results were obtained using the gene expression model trained by the experimental data shown in Fig. 2, while the experimental data in Figure was reproduced from [41].

3.2.2. Pharmacokinetic model

Some cancer patients take RA as a part of their cancer treatment within three to four months of diagnosis [55]. The plasma concentration of RA changes significantly after oral administration of various doses of the drug (Fig. 5).

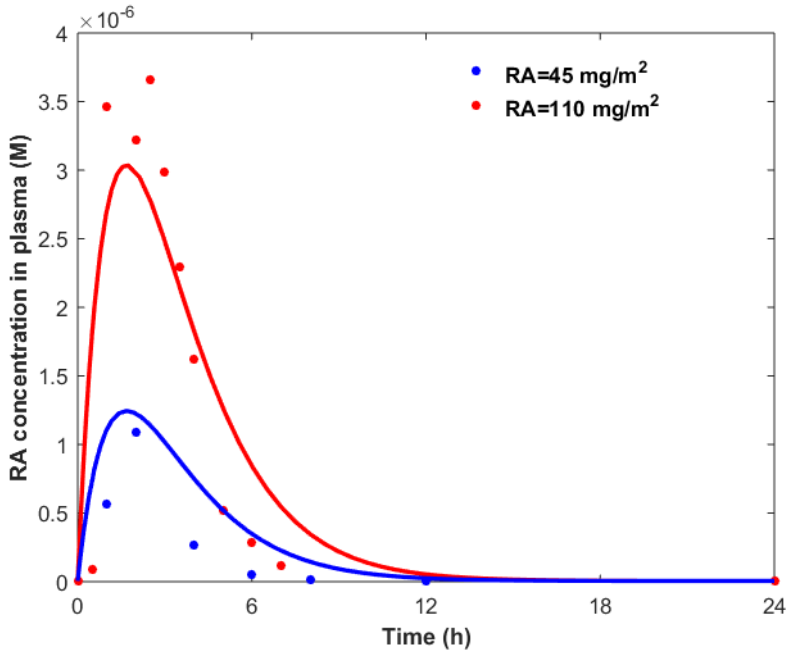

Figure 5. Plasma concentration of RA after ingestion of various doses of RA on day 1 of treatment [48, 49]. Dots show the pharmacokinetic data, while lines indicate the simulation results by a two-compartment pharmacokinetic model.

Oral administration of RA can be modeled via a two-compartment pharmacokinetic model (Fig. 6), since the plasma concentration-time curve of RA exhibits a biexponential decline [56, 57]. After oral administration of the drug, RA is absorbed into the bloodstream, which is a part of the central compartment. The central compartment includes the plasma and organs, where the distribution of RA is assumed to be instantaneous. The RA is eliminated by a first order process from the central compartment or distributed to the rest

of the body that represents the peripheral compartment. RA elimination mainly occurs in the liver and kidney, which are included in the central compartment. The peripheral compartment includes tissues where RA distribution occurs with a slower rate than in the central compartment.

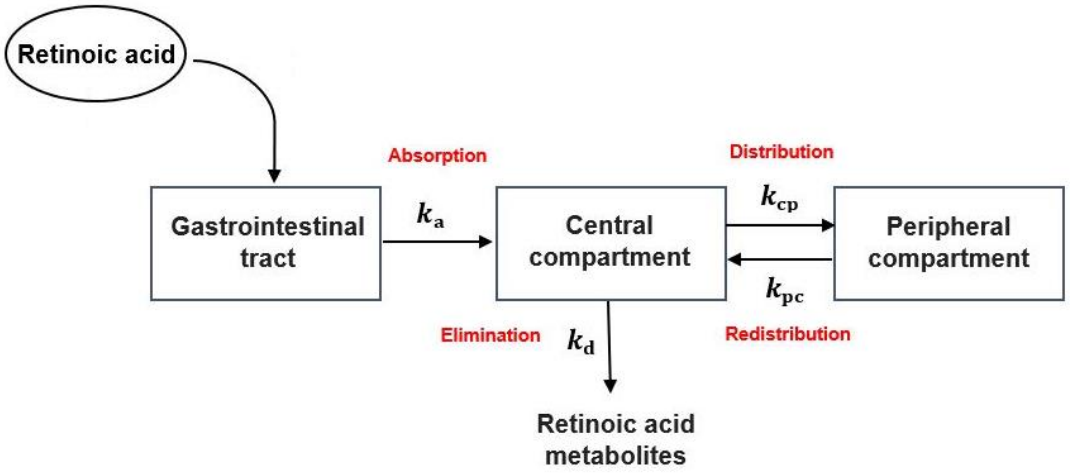

Figure 6. Schematic of a two compartments model for describing RA pharmacokinetics. The model included two main compartments namely, central compartment and peripheral compartment. k_a, k_d, k_{cp}, k_{pc} are first order absorption rate constant, degradation rate constant, distribution rate constant and redistribution rate constant.

RA exchange between different compartments can be described by a system of ODEs

$$\frac{dD}{dt} = -k_a D \tag{6}$$

$$\frac{d[RA_c]}{dt} = \frac{k_a D}{V_c M} - (k_d + k_{cp})[RA_c] + \frac{k_{pc} V_p}{V_c}[RA_p] \tag{7}$$

$$\frac{d[RA_p]}{dt} = \frac{k_{pc} V_c}{V_p}[RA_c] - k_{pc}[RA_p] \tag{8}$$

where D, $[RA_c]$ and $[RA_p]$ represent RA dose, total RA concentration in the central compartment, and total RA concentration in the peripheral compartment, respectively. D, $[RA_c]$ and $[RA_p]$ vary over time, and are represented in g, molar and molar, respectively.

k_a, k_d , k_{cp}, k_{pc}, V_c and V_p are the first-order absorption rate constant, first-order degradation rate constant, distribution rate constant, redistribution rate constant, central compartment volume and peripheral compartment volume, respectively. M is the molar mass of RA, and is set to 300.4 $gmol^{-1}$. We also assumed that the average body surface area is 1.75 m^2. We built the model, shown in Figure 6, in MATLAB SimBiology and fit the model parameters to the pharmacokinetic data (dots in Figure 5). Solid lines in Figure 5 show the model prediction for plasma concentration of RA ($[RA_c]$) after taking an oral dose of 45 or 110 mg/m^2 of RA. Further details regarding the pharmacokinetic model were provided in the Supplementary Information file (section 3.6). We coupled the gene expression model with the pharmacokinetic model to study the effects of oral administration of RA on the expression levels of TM and TMR during the course of RA therapy (Section 3.1). Free RA concentration in the gene expression model ([RA] in Eq. 3) is obtained by

$$[RA] = 0.01[RA_c]. \quad (9)$$

3.2.3. sTM release model

TM plays a key role in controlling fibrin formation. A modified form of TM is also found in human plasma and urine [58]. Both cellular TM and soluble TM (sTM) act as an anticoagulant by activating protein C [59, 60]. It is believed that soluble TM (sTM) is a marker for endothelial cell injury [61, 62]. Endothelial cell injury can occur due to several reasons, such as elevated levels of cytokines, hyperlipidemia, activation of leukocytes and neutrophils, hypercholesterolemia, obesity, diabetes and smoking. Blood vessel damage is also a common occurrence in cancer patients, as many of them undergo surgery or chemotherapy. It has been reported that TM is cleaved from the endothelium and released

into the plasma by some degrading enzymes such as protease and glycosidase upon endothelial cell injury [61]. Assuming the RA therapy does not affect the mechanisms mediating the release of cellular TM into the plasma, we modeled the rate of sTM production by

$$\frac{\mathrm{d[sTM]}}{\mathrm{dt}} = c_1[\mathrm{TM}] - c_2[\mathrm{sTM}]\,, \tag{10}$$

where c_1 and c_2 are the release rate constant of cellular TM into the plasma by the degrading enzymes and the elimination rate constant of sTM from plasma, respectively. [TM] represents the cellular concentration of TM, while [sTM] indicates the plasma concentration of sTM. c_2 was set at $0.11\ \frac{1}{hr}$ [63]

Assuming the sTM concentration to be at steady state prior to RA treatment, we calculated the value of c_1 using the physiological concentrations of TM and sTM

$$c_1 = \frac{c_2[\mathrm{sTM}]_0}{[\mathrm{TM}]_0}, \tag{11}$$

where $[\mathrm{sTM}]_0$ and $[\mathrm{TM}]_0$ are physiological concentrations of sTM and TM, and are expressed in molar. We assumed that $[\mathrm{sTM}]_0 = 1\mathrm{nM}$, while $[\mathrm{TM}]_0$ is the steady state level of TM in Eq. 2 after treating the model with a physiological concentration of RA ($\mathrm{RA_{plasma}} = 5$ nM) [46].

The sTM release model was used to link the gene expression model to the ODE model of the coagulation cascade (Section 3.3)

3.3. Results

3.3.1. Pharmacokinetics-pharmacodynamics

RA is mainly transported in plasma bound to serum albumin [45, 57]. The unbound fraction of RA in plasma is about 1% of the total RA concentration [45, 46]. Since the bound drugs are pharmacologically inactive, we calculated the unbound fraction of RA in plasma by multiplying the total concentration of RA by 0.01 (Eq. 9). We then used the plasma concentration of free RA as input to the gene expression model, with the parameters estimated in the section 2.1, to study the dynamics of the TM concentration on the first day of treatment. To do so, the free RA concentration in Eq. 3 varied according to the time-dependent levels of free drug in plasma ([RA]) following RA therapy.

RA treatment resulted in variations in TM and TMR concentrations (Fig. 7). The TMR and TM concentrations reached their peak levels almost 7 and 13 hours after taking a 45 mg/m^2 oral dose of RA, respectively (Fig. 7a). However, the peak times of TMR and TM levels were shifted by almost 1 hour when the RA dose was increased to 110 mg/m^2 (Fig. 7b).

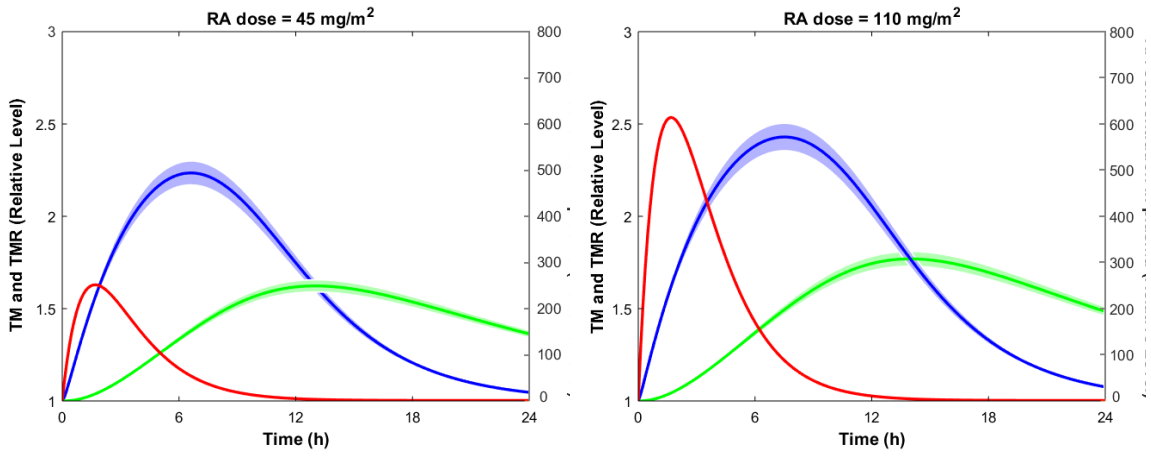

(a) (b)

Figure 7. Variations in RA, TMR, and TM concentrations following a single dose of RA (a) $45\,\frac{mg}{m^2}$ and (b) $110\,\frac{mg}{m^2}$. The lines show the mean simulated results, while the shaded regions denote the 99% confidence interval of the mean simulated results.

The solid lines in Fig. 7 denote mean simulated results, while the shaded regions denote 99% confidence interval of the mean simulated values. The maximum concentration of TM after taking a $110\,\frac{mg}{m^2}$ oral dose of RA (Fig. 7b) was similar to that of taking a $45\,\frac{mg}{m^2}$ oral dose of RA (Fig. 7a). This is because the transcription rate levels were comparable for both RA doses (Fig. 8).

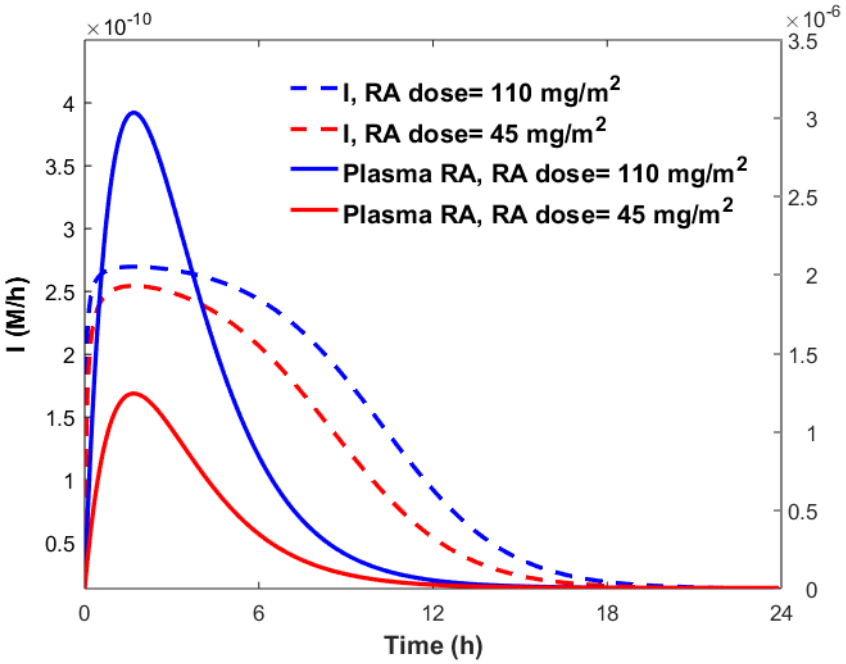

Figure 8. Variation of the TM transcription rate (I) following various doses of RA.

3.3.2. Continuous treatment with RA

Patients on RA therapy usually take the drug on a daily basis. We simulated the effects of daily administration of RA for three days, on TM expression (Fig. 9).

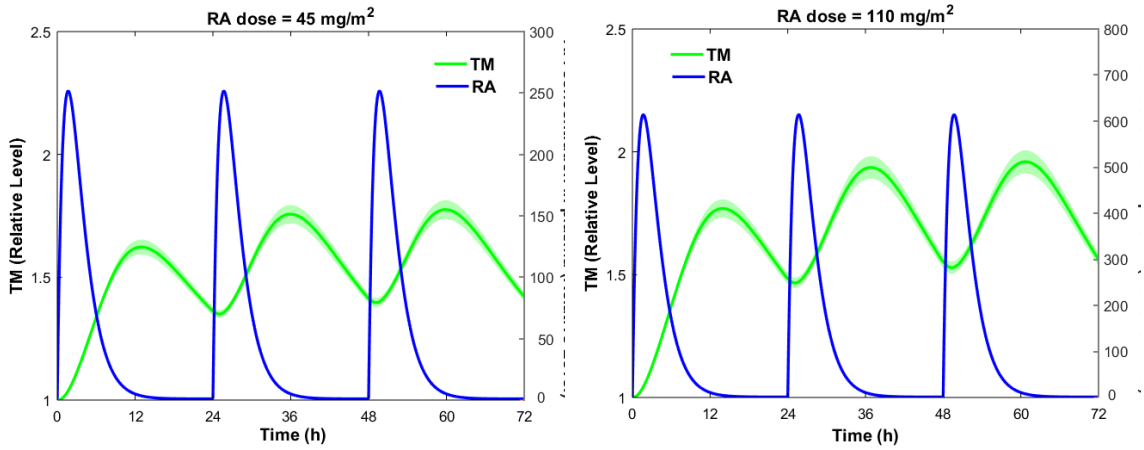

(a) (b)

Figure 9. TM expression on the endothelial cell surface within three days of RA treatment. Daily doses of RA are taken at t=0 hr, t= 24 hr, and t=48 hr. (a) 45 $\frac{mg}{m^2}$ and (b) 110 $\frac{mg}{m^2}$. The lines show the mean simulated results, while the shaded regions denote the 99% confidence interval of the mean simulated results.

Continuous treatment with RA resulted in oscillatory alterations in the TM concentration. These oscillatory changes are important, as they can affect the blood coagulation cascade (Section 3.3). Taking 110 $\frac{mg}{m^2}$ RA per day increased the TM concentration to approximately twice its normal level (i.e. no RA treatment) almost 14 hours after drug ingestion. Daily administration of RA did not allow the TM level to return to its initial concentration, since it took almost 72 hours for TM to return to its initial concentration (data not shown).

3.3.3. RA resistance

In some cancers, RA resistance is associated with increasing reductions in the plasma concentration of RA [57]. A clinical trial of RA [64] showed that continuous treatment with RA caused a progressive reduction in the plasma level of RA in half of the patients that were on RA treatment (Fig. 10). The mechanisms involved in the progressive reduction in RA plasma concentration over the course of continuous RA therapy are not known. The mechanisms might be cancer- and patient- specific. Other pharmacokinetic patterns were observed in the remainder of the patients under study [64]. In some patients, the peak plasma level of RA remained unchanged during the RA treatment, while other patients had peaks that varied weekly.

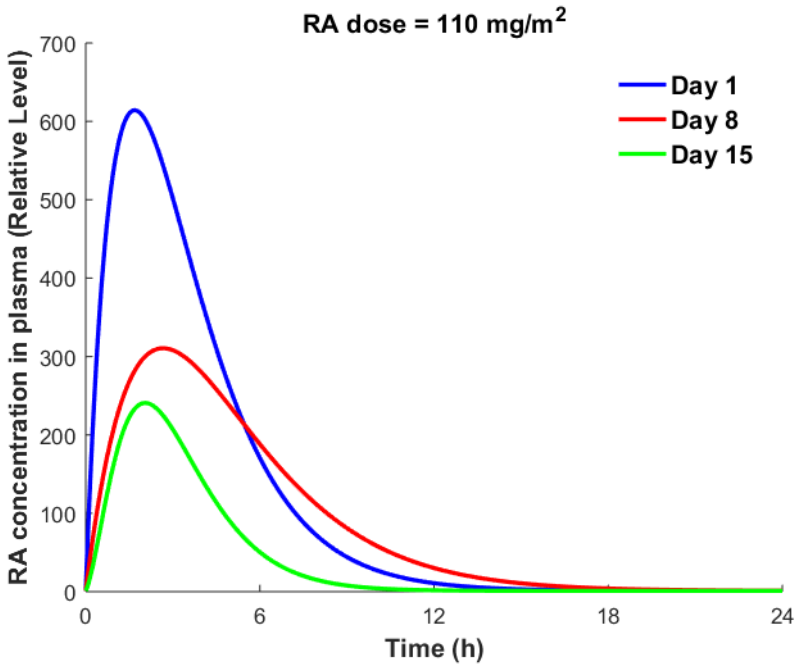

Figure 10. Changes in the total plasma level of RA concentration on treatment days 1, 8 and 15 of a continuous treatment period with daily dose of 110 $\frac{mg}{m^2}$ RA [49].

Using the clinical data shown in Fig. 10, we simulated the effects on TM expression of the consistent decrease in peak plasma level of RA (Fig. 11).

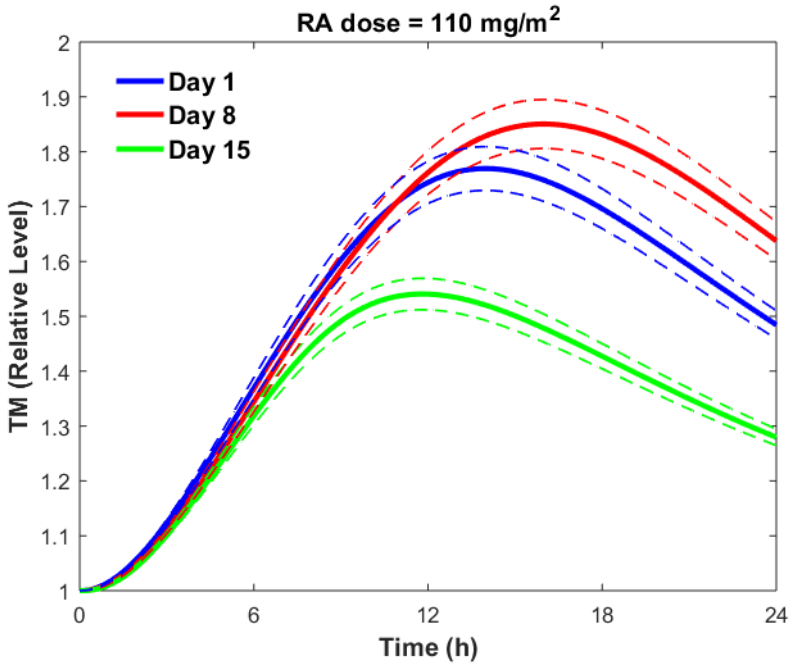

Figure 11. TM expression on day 1, day 8, and day 15 of the treatment period. Solid lines are the mean simulated values. Dotted lines show the 99% confidence estimate of the mean results.

The solid lines in Fig. 11 show the mean simulated values of the TM concentration, while the dotted lines denote the 99% confidence interval of the mean results. Figure 11 shows that the peak level of TM on various days decreased in the order of day 8 > day 1 > day 15, while the peak RA plasma concentration decreased in the order of day 1 > day 8 > day 15. Higher TM levels on day 8 compared to day 1 was because of higher plasma levels of RA after 6 hours of drug administration on day 8 compared to day 1 (Fig. 10). The results presented in Figure 11 were obtained using the pharmacokinetic data from [64]. Thus, these results are not applicable to all patients with different cancer types. However, the current

model can be used to study the variation of TM expression over the course of RA therapy for different patients with different cancer types, once more pharmacokinetic data on different treatment days is available. In the next section we will investigate the effects of RA-induced TM upregulation on the coagulation cascade. We also investigate how the progressive reduction in the RA concentration over the course of RA therapy can decrease the corrective effects of RA therapy on the coagulation disorders.

3.3.4. Effects of RA-induced TM upregulation on the blood coagulation system

3.3.4.1. Effects of continuous RA therapy on thrombin generation

In this section, we investigate whether the elevated levels of TM over the course of RA therapy can affect thrombin generation. In this regard, we used an ODE model of the blood coagulation cascade that incorporates a mechanistic description of the protein C pathway [39]. The coagulation model was developed based on *in vitro* phospholipid-based assays to study the contribution of various coagulation factors to thrombin generation in protein C deficient patients. TM was modeled at 1 nM in that study, which is an estimate of the physiological concentration of soluble TM (sTM) in plasma. However, our gene expression model predicts the variation in the concentration of TM in endothelial cells. It is believed that sTM is entirely derived from the TM expressed on the endothelial cell surface. To couple the RA model with the coagulation model, we need to obtain the time-dependent variations in the sTM level following the RA therapy. In this regard, we coupled the gene expression model with the sTM release model to obtain the variations of sTM over the

course of RA therapy. Figure 12 compares the variation of the cellular level of TM with that of the plasma level of sTM when the patient takes the drug on a daily basis for three consecutive days.

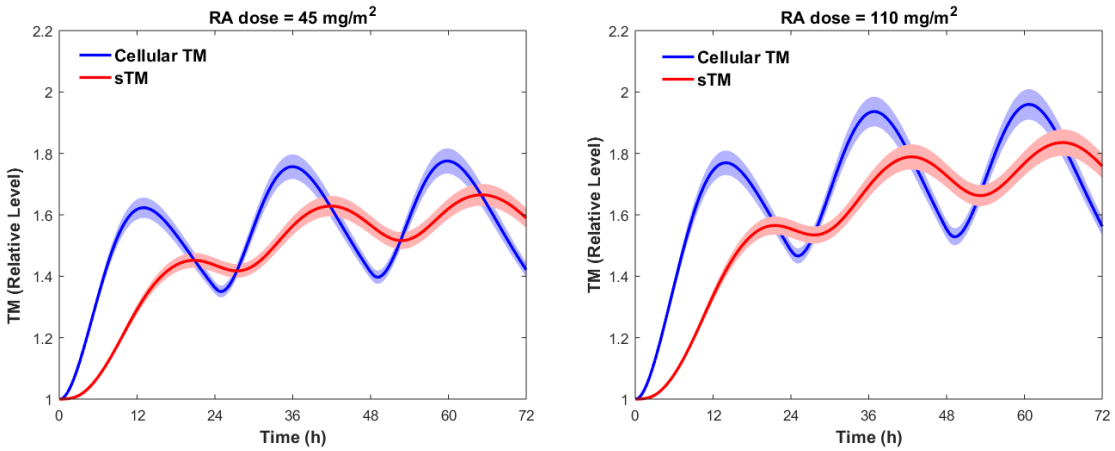

(a) (b)

Figure 12. Variations in the cellular level of TM and the plasma concentration of sTM within three days of RA treatment. Daily doses of RA are taken at t=0 hr, t= 24 hr, and t=48 hr. (a) 45 $\frac{mg}{m^2}$ and (b) 110 $\frac{mg}{m^2}$. Solid lines are the mean simulated values. Shaded regions show the 99% confidence interval of the mean results.

To run the coagulation model, we assumed that all coagulation factor concentrations were physiological concentrations, except the TF and sTM concentrations. The TF concentration was set to 5 pM to initiate the clot formation process, while the sTM concentration varied according to the RA treatment (Fig. 12). Since the time scale of the coagulation cascade (20 min) is much shorter than that of TM expression (days), the sTM concentration was assumed to be constant during the coagulation process. Taking once-daily oral dose 45 $\frac{mg}{m^2}$ or 110 $\frac{mg}{m^2}$ of RA for three consecutive days reduced the peak level of thrombin up to 45% and 50%, respectively (Fig. 13). The endogenous thrombin profile

(ETP), which is defined as the time integral of thrombin generation, was decreased up to 45% and 49% within three days of treatment with 45 $\frac{mg}{m^2}$ or 110 $\frac{mg}{m^2}$ oral dose of RA, respectively (Fig. 13).

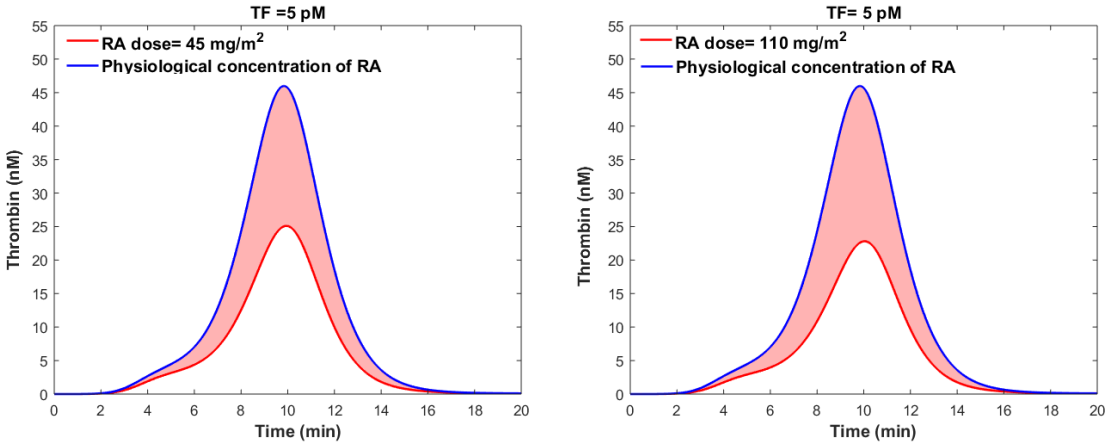

(a) (b)

Figure 13. Impacts of RA-induced TM upregulation following drug ingestion (a) 45 $\frac{mg}{m^2}$ and (b) 110 $\frac{mg}{m^2}$, on thrombin generation. The blue lines indicate the thrombin generation profile in the control group with physiological levels of RA. The red lines show the maximum impact of RA therapy on thrombin generation. The shaded red regions indicate the range of the thrombin generation profile within three days of continuous RA therapy.

The shaded regions in Fig. 13 indicate the range of thrombin generation after RA therapy, with different doses of RA. The shaded regions in Fig. 13 are not only due to the uncertainty of the results caused by the error bars in the experimental data (Fig. 2), but also due to the changes in sTM level after RA treatment (Fig. 12). In fact, we obtained the range of thrombin generation profiles using different values of sTM, that could be expected over the course of RA therapy (Fig. 12). Our results indicate that the endothelium could potentially play a key role in RA treatment of coagulation disorders, by upregulating TM

and sTM. Since the sTM concentration fluctuates over time, the efficacy of RA treatment in preventing or treating hemostatic abnormalities is dependent upon the timing of the treatment.

3.3.4.2. Effects of RA resistance on thrombin generation

Our results indicated that the progressive reductions in plasma concentration of RA over the course of RA therapy with a daily oral dose (110 $\frac{mg}{m^2}$) of RA (Fig. 10) resulted in variations of cellular TM concentration (Fig. 11). Using the sTM release model, we obtained the variations of sTM concentration on different treatment days. We then ran the coagulation model using the predicted values of sTM concentration on different treatment days (Fig. 14), according to the procedure explained in the previous section. The blue line in Figure 14 indicates the thrombin generation profile for the control condition with a physiological level of RA, while the dashed lines show thrombin generation profiles at sTM peak time after taking different oral doses of RA. Thus, the area between the blue line and a given day's dashed line shows the range of variation of thrombin generation on the given day.

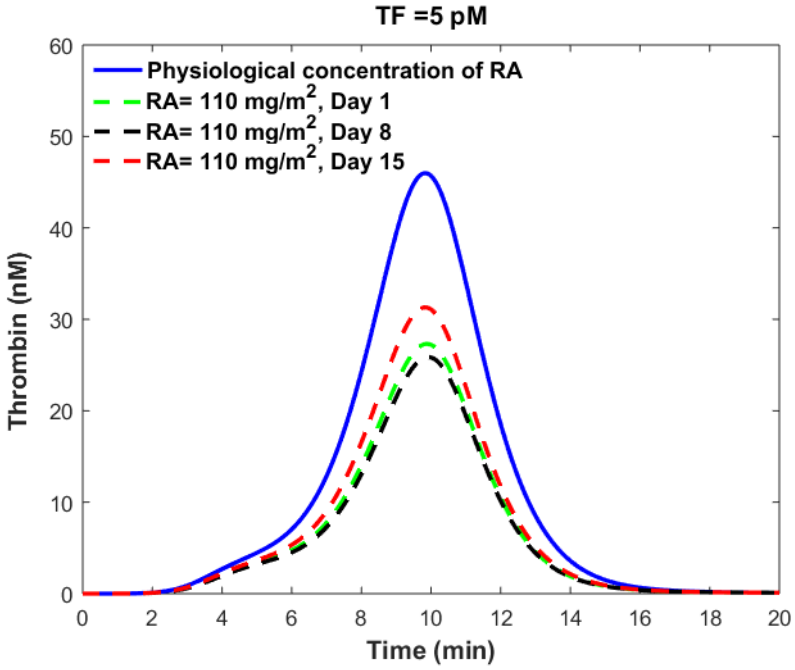

Figure 14. Thrombin generation profile on days 1, 8 and 15 of treatment period with a daily dose of 110 $\frac{mg}{m^2}$ RA. Dashed lines show the maximum impact of RA therapy on thrombin generation on different treatment days. The area between each dashed line and the solid blue line indicates the range of the thrombin generation profile on different treatment days. RA concentration in plasma on different treatment days is shown in Fig. 10.

Our simulation results indicated that the peak thrombin level was reduced up to 41%, 44% and 32% on day 1, day 8 and day 15 of treatment period, respectively. However, the ETP was reduced up to 40%, 43% and 32% on days 1, 8 and 15 of continuous treatment with a once-daily dose of 110 $\frac{mg}{m^2}$ RA, respectively. It is important to note that the maximum reduction happens at the sTM peak time after oral administration of RA.

Our results indicated that the reduced levels of RA on days 8 and 15 of continuous treatment with a single daily dose of 110 $\frac{mg}{m^2}$ RA could decrease thrombin peak levels and ETP significantly. However, the way this progressive reduction affects the efficacy of RA in treating cancer depends on cancer type, stage and the patient's health conditions. In

general, drug dose and route of administration are determined in such a way that the plasma concentration of drug lies within the therapeutic window of the drug. Any significant reduction in plasma concentration of RA over the course of treatment can potentially decrease the efficacy of RA in treatment of cancer in at least some patients. Figure 10 indicates that the peak plasma concentration of RA decreases by almost 60% within two weeks of RA treatment, while our results show that the peak thrombin level is reduced up to 44% and 32% on days 8 and 15 of treatment, respectively. The obtained values for percent decrease in peak thrombin level on days 8 and 15 of RA therapy are comparable with a 41% decrease in peak thrombin level on day 1 of treatment. Our results raise the hypothesis that RA therapy has more consistent, corrective effects on clotting abnormalities than on cancer. Further studies on different patients with different cancer types and stages are needed to reveal how the observed reductions in plasma levels of RA over the course of RA therapy affect the efficacy of RA in treatment of cancers versus hemostatic abnormalities.

3.3.4.3. Effects of physiological levels of RA on thrombin generation

We used our RA model to obtain the elevated levels of cellular TM and sTM, when the cells were treated with a physiological concentration of RA, $\mathrm{RA_{plasma}} = 5\ \mathrm{nM}$ [46]. Treating the combination of the gene expression model and the sTM model with 5 nM of RA resulted in a 9% increase in the mean cellular TM level and subsequently the mean plasma level of sTM. We then investigated the effects of physiological concentrations of RA on the thrombin generation profile (Fig. 15). The absence of vitamin A in the diet increased the peak level of thrombin up to 10%, while this increase was up to 11% for the ETP.

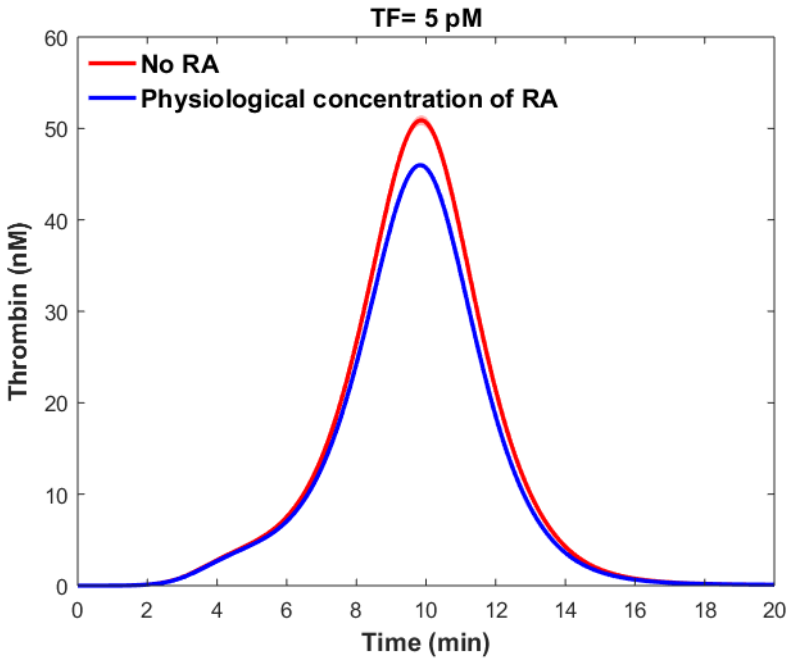

Figure 15. Impacts of physiological levels of RA on thrombin generation profile. The blue line indicates thrombin generation profile for the control condition with physiological level of RA. The red line shows the mean thrombin generation profile when there is no RA in the plasma. The shaded red region indicates the 99% confidence interval of the mean result.

3.4. Discussion

Clinical observations have shown that RA has therapeutic effects on blood coagulation disorders such as DIC and thrombosis in cancer patients. Previous studies have mainly looked at RA as a treatment for cancer. Corrective effects of RA on coagulation disorders, which is a positive side effect of RA therapy, have rarely been studied. Elucidating the mechanism of action of RA in the treatment of coagulation disorders is important, since this can help to understand why some patients respond to the drug better than others. This is also useful in developing new drugs with better therapeutic effects. Down regulation of TF and CP on cancer cells and monocytes, upregulation of u-PA, PAI-1 and PAI-2 in cancer

cells, and upregulation of TM and t-PA in endothelial cells have been introduced as the possible mechanisms for RA to ameliorate blood coagulation disorders. In this study, we investigated how RA therapy regulates TM expression and how this variation affects the thrombin generation profile. We developed a gene expression model for the RA-induced upregulation of TM. Coupling the gene expression model with a two-compartment pharmacokinetic model of RA, we simulated the time-dependent variations of TM and TMR concentrations after taking different oral doses of RA. Our results indicate that the TM concentration increases almost twofold after taking a 110 $\frac{mg}{m^2}$ oral dose of RA. Since most of the patients who are under RA treatment take RA on a daily basis, TM expression on the endothelial cell surface changes over time. Our results indicate that RA treatment increases the mean value of TM concentration, while the nature of this regulation is oscillatory. To examine the effects of the upregulated TM on the blood coagulation system, we used a mathematical model for the human coagulation cascade [39]. Our simulations show that taking a 45 $\frac{mg}{m^2}$ or 110 $\frac{mg}{m^2}$ oral dose of RA reduces ETP by 45% and 49%, respectively. Furthermore, our results are useful in predicting the times when a patient is at a higher risk of clot formation. Almost fourteen hours after drug ingestion, the TM concentration begins to decrease, and reaches its minimum level almost before taking the next dose of the drug. However, the minimum level of TM during the RA treatment period is higher than the normal level of TM when there is no RA treatment. We also investigated the effects of progressive reductions in the plasma concentration of RA over a course of continuous treatment on thrombin generation. Our results indicated that the progressive reductions in plasma concentration of RA over the course of RA therapy with daily oral dosing (110 $\frac{mg}{m^2}$

), which has been observed in some cancer patients, do not affect the corrective effects of RA therapy on thrombin generation significantly. These results prompt the hypothesis that coagulation abnormalities may become resistance later than cancer to RA. The validity of this hypothesis depends on various patient- and cancer-specific factors such as the RA route of administration, the adequate plasma concentration of RA for cancer treatment, the acceptable range of reduction in plasma RA over the course of RA therapy, and the allowable range of toxicity. Thus, the validity of this hypothesis should be tested for different groups of patients with various cancer types, stages and health conditions such as liver and kidney health, independently. Taken together, our simulations indicate that oscillatory expression of TM over the course of RA therapy can play a critical role in the regulation of thrombin production. This finding may explain why RA therapy improves DIC and thrombosis in some cancer patients better than in others. Our simulation results suggest that one possible reason might be the impairment of PC pathway because of cancer, cancer treatment, etc. It is important to note that the current study cannot compare the significance of TM with other potentially important proteins such as t-PA, u-PA, PAI-1, PAI-2, TF and CP, in RA-induced improvement of clotting disorders in cancer patients. Further experimental and numerical studies are needed to investigate the contributions of the above pathways to RA therapy of DIC in cancer. This study can be considered as a starting point for research studies exploring the possible effects of oscillatory protein expression after drug administration, on the blood coagulation cascade.

There are some limitations to this study. First, we simulated the thrombin generation process using the physiological levels of all blood factors except TF and TM. This is because some cancer patients have coagulation factor levels within the normal ranges [65,

66]. However, this is not true for all cancer patients. Plasma concentrations of coagulation factors in cancer patients depend on several factors such as type and stage of the cancer, and type of the antitumor therapy. Thus, the quantitative aspect of our results on corrective effects of RA therapy on thrombin generation, cannot be applied to all patients with different disease conditions. Second, we did not consider the effects of RA treatment on the cancer cells' ability to produce inflammatory cytokines. Previous *in vitro* studies have indicated that RA treatment increased the production of some inflammatory cytokines such as IL-1β by cancer cells [67, 68]. In theory, induction of cytokine release can favor the prothrombotic potential of the endothelium by upregulating TF and downregulating TM expression [69, 70]. However, we believe that the elevated levels of plasma cytokines after treatment with the specified doses of RA in this study should not influence the TF and TM expression significantly [67, 69, 71]. Third, the model we used for simulating thrombin generation was developed based on *in vitro* assays. Even though all coagulation factor concentrations were physiological concentrations, the model cannot capture some essential features of the coagulation *in vivo*, such as the cellular involvement and the effects of flow. In fact, our model cannot describe exactly how RA therapy improves clotting disorders *in vivo*. Instead, our simulation results indicate that the oscillatory variation in TM expression over the course of RA therapy significantly influenced *in vitro* thrombin generation. *In vivo* studies are needed to confirm the key role of TM in RA treatment of coagulopathy. Fourth, in constructing the sTM release model, for simplicity we assumed that the cellular TM is degraded by a first-order reaction. The kinetic order of the reaction depends upon the types and concentrations of degradation enzymes and the severity of cell injury. However, little is known about the types and concentrations of the enzymes which are primarily responsible

for producing sTM from cellular TM. Furthermore, the severity of cell injury depends on the type and stage of the cancer. Thus, the model presented in this section cannot describe TM cleavage for all cancer patients with different conditions. The model can be improved once more information about the degradation pathway is available. We have also assumed that the amount of cellular TM is not significantly reduced due to release of the TM into the plasma. This is because the number of sTM molecules in plasma is much smaller than the number of TM molecules on the endothelium under physiological conditions. Next, we assumed that the unbound fraction of RA in plasma was constant over the course of RA treatment. However, the unbound fraction of RA depends on different variables, such as the serum albumin concentration in plasma, the total concentration of RA in plasma, and the levels of other drugs in blood. Cancer patients usually take different medications at the same time. Furthermore, the serum albumin level can be affected by cancer and cancer treatment. Thus, the exact quantitative effects of RA therapy on TM expression can vary from patient to patient.

3.5. Conclusions

All-trans retinoic acid (RA) has been widely used to treat various types of cancer. RA treatment also improves coagulation abnormalities in cancer patients. However, it is not clear how RA therapy ameliorates coagulation disorders. In this study, for the first time, we developed a mechanistic model to investigate the role of thrombomodulin (TM) in RA therapy of cancer-induced coagulation disorders. Our results indicate that RA-induced TM upregulation reduces thrombin generation significantly. Daily administration of the drug results in oscillatory expression of TM on endothelial cells. We also demonstrate that within two weeks of continuous RA treatment, TM expression patterns remain almost unchanged,

while some cancers become resistant to RA therapy. This result raises the hypothesis that RA therapy has longer lasting corrective effects on coagulation disorders than on cancer. Clinical studies and *in vivo* experiments are required to test the validity of this hypothesis. Overall, our findings indicate the key role of TM in RA treatment of blood coagulation abnormalities in cancer patients. These results are in line with recent clinical observations regarding the therapeutic effects of recombinant human thrombomodulin, an anticoagulant drug with the same external structure of TM, in the treatment of DIC [72-76].

Moving forward, we plan to couple this model with other mechanistic models that simulate the effects of RA therapy on the expression levels of TF, CP, PAI-1, PAI-2, t-PA and u-PA, and compare the significance of different pathways in RA therapy of clotting disorders in cancer patients. Such models should be able to simulate how the RA treatment downregulates the expression of TF and CP and upregulates the synthesis of PAI-1, PAI-2, t-PA and u-PA in various cell types such as endothelial cells, monocytes, and tumor cells. Mechanistic modeling of these pathways requires concurrent experimental studies to explore the relevant biological pathways.

3.6. Supplementary information

3.6.1. All-trans retinoic acid pathway

RA is highly bound to albumin in plasma [45] and in the cell culture medium [40]. Free RA molecules start to passively diffuse across the cellular membrane once the cultured cells are treated by RA. Passive diffusion continues to occur until the concentration of free RA on both sides of the cellular membrane are equal. Equilibrium is achieved relatively quickly due to the high permeability coefficient of RA across the endothelial cell membrane [77] and high surface area per volume of endothelial cells. After diffusing across the membrane,

RA molecules bind to different receptors (Fig. S1). Some of the RA binding receptors can initiate the transcription of target genes after binding to RA. When the transcription factors bind to RA molecules, they become activated and trigger the transcription of the TM gene by binding to DNA at a retinoic acid response element (RARE) located in enhancer regions of the gene [78, 79].

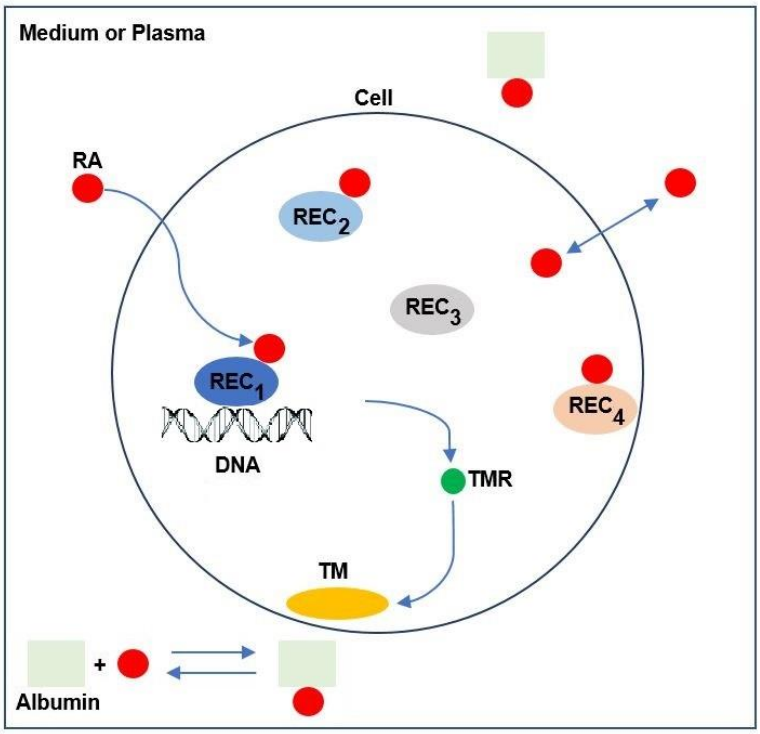

Figure S1. Simplified schematic of the RA signaling pathway. RA is mainly bound to albumin outside of the cells. RA molecules (red circles) can diffuse across the cellular membrane and bind to different receptors (REC_1, REC_2, REC_3, etc). Some of the RA binding receptors (REC_1, in this cartoon diagram) can initiate the transcription of the TM gene after binding to RA molecules.

The binding of RA to a single site on a RA binding receptor (REC) is expressed by

$$\mathrm{RA} + \mathrm{REC} \underset{k_{\mathrm{d1}}}{\Longleftrightarrow} \mathrm{RA{:}\,REC}\,,$$

where k_{d1} is the equilibrium dissociation constant,

$$k_{\mathrm{d1}} = \frac{[\mathrm{RA}][\mathrm{REC}]}{[\mathrm{RA{:}\,REC}]}, \tag{S1}$$

and [] indicates molar concentration. Thus, $[\mathrm{RA}]$, $[\mathrm{REC}]$ and $[\mathrm{RA{:}\,REC}]$ represent molar concentrations of free RA, free RA binding receptor and bound receptor ($\mathrm{RA{:}\,REC}$), respectively. Assuming that RA is either free in the cell or bound to the RA binding receptors (REC), Eq. S1 can be written as

$$k_{\mathrm{d1}} = \frac{[\mathrm{RA}]([\mathrm{REC_t}] - [\mathrm{RA{:}\,REC}])}{[\mathrm{RA{:}\,REC}]}, \tag{S2}$$

where $[\mathrm{REC_t}]$ stands for molar concentration of all RA binding receptors,

$$[\mathrm{REC_t}] = [\mathrm{REC_1}] + [\mathrm{REC_2}] + \cdots \tag{S3}$$

Solving Eq. S2 for the bound fraction of RA binding receptors yields

$$\frac{[\mathrm{RA{:}\,REC}]}{[\mathrm{REC_t}]} = \frac{[\mathrm{RA}]}{[\mathrm{RA}] + k_{\mathrm{d1}}}. \tag{S4}$$

The concentration of the specific transcription factor ($\mathrm{REC_1}$) which can activate the transcription of the TM gene is a portion of the total concentration of RA binding receptors ($\mathrm{REC_t}$). Assuming that RA has the same affinity to bind to different RA binding receptors, the ratio of the activated transcription factor concentration ($[\mathrm{RA{:}\,REC_1}]$) to the total transcription factor concentration ($[\mathrm{REC_{1t}}]$) is the same as the ratio of the activated RA receptors concentration ($[\mathrm{RA{:}\,REC}]$) to the total RA receptors concentration ($[\mathrm{REC_t}]$), thus

$$\frac{[\mathrm{RA{:}\,REC}]}{[\mathrm{REC_t}]} = \frac{[\mathrm{RA{:}\,REC_1}]}{[\mathrm{REC_{1t}}]}. \tag{S5}$$

The assumption that RA binds to various types of RA binding receptors with the same affinity is reasonable, since the majority of RA binding receptors found in endothelial cells are from the nuclear hormone receptor family. The retinoic acid receptors

(RAR_α, RAR_β, RAR_γ) and retinoid X receptors (RXR_α, RXR_β, RXR_γ) are the main members of the nuclear hormone receptor family.

The transcription rate of the TM gene depends on the promoter occupancy. The binding of an activated transcription factor to a promoter can be described by

$$\mathrm{RA{:}\,REC_1} + \mathrm{Promoter} \underset{k_{d2}}{\Longleftrightarrow} \mathrm{RA{:}\,REC_1{:}\,Promoter}\,,$$

where k_{d2} is the equilibrium dissociation constant of the transcription factor binding to the promoter. The fraction of time that any given promoter spends in the transcription factor-bound state is given by [80-82]

$$\text{Fraction of binding time} = \frac{[\mathrm{RA{:}\,REC_1}]}{[\mathrm{RA{:}\,REC_1}] + k_{d2}}\,. \tag{S6}$$

The rate of the gene transcription is proportional to the fraction of the binding time,

$$\frac{I}{I_{\max}} = \frac{[\mathrm{RA{:}\,REC_1}]}{[\mathrm{RA{:}\,REC_1}] + k_{d2}}\,, \tag{S7}$$

where $I_{\max}$ is the maximum transcription rate by a specific transcription factor (REC_1).

The transcription rate (I) can be obtained as a function of RA, REC_{1t}, and $I_{\max}$ by combining Eqs. S4, S5 and S7,

$$I = I_{\max}\frac{[\mathrm{RA}][\mathrm{REC_{1t}}]}{[\mathrm{RA}][\mathrm{REC_{1t}}] + k_{d2}([\mathrm{RA}] + k_{d1})}\,. \tag{S8}$$

It is important to note that we assumed the association/dissociation event between RA and REC, and the binding/unbinding of $\mathrm{RA{:}\,REC_1}$ to promoter are in equilibrium. This is because these reactions occur on much faster time scales than gene transcription [51, 83, 84]. Furthermore, DNA-transcription factor reactions are much faster than protein-ligand reactions [84, 85].

3.6.2. Estimation of gene expression model parameters

3.6.2.1. Parameter estimation algorithm

The gene expression model had four species, i.e. TMR, TM, RA and $\mathrm{REC_{1t}}$, and seven parameters, namely I_0, k_{trans}, I_{max}, k_{dp}, k_{dm}, k_{d1} and k_{d2}. The model parameters and species were defined in Table 1. The values of k_{dp}, k_{dm}, k_{d1} and k_{d2} were taken from the literature (Table 1), while the values of the remaining parameters, and the initial concentrations of the model species, i.e. IC_{TM}, IC_{TMR} and $[\mathrm{REC_{1t}}]$ were unknown. k_{trans} and basal transcription rate (I_0) were the only parameters that depended on the other parameters. Assuming that the TM and TMR concentrations were in steady state before RA treatment (t=0), we calculated k_{trans} and I_0 by

$$k_{\mathrm{trans}} = \frac{k_{\mathrm{dp}} IC_{\mathrm{TM}}}{\mathrm{IC_{TMR}}}, \tag{S9}$$

$$I_0 = k_{\mathrm{dm}} IC_{\mathrm{TMR}}\,. \tag{S10}$$

Overall, the gene expression model had three independent unknown parameters namely, I_{max}, IC_{TMR}, $[\mathrm{REC_{1t}}]$, and two dependent parameters, namely k_{trans} and I_0. We instituted some bounds for all model unknown parameters (Table 1). The bounds for IC_{TM} were due to the experimental errors (Fig. 2), while the other unknown parameters had physiological bounds. The gene expression model unknown parameters were estimated by minimizing the squared difference between simulation results and the experimental data following a parameter estimation algorithm. The parameter estimation process was designed in such a way that the simulation results for the TMR concentration at different time points, i.e. 0, 3, 6, 12, 24 h, when RA =10 μM and the simulation results for TM concentration at different RA concentrations, i.e. 0.1, 1, 10 μM, when t= 24 h fit the experimental data shown in Fig 2. The objective function was defined by

$$E = \sum_{i=1}^{5} (M_i^s - [TMR]_i^s)^2 + \sum_{j=1}^{3} (1 - [TM]_j^s)^2. \quad (S11)$$

The first term in the objective function quantified the difference between the scaled experimental TMR concentration (M_i^s) and scaled numerical results for TMR level ($[TMR]_i^s$) at time point i. Time points i=1, 2, 3, 4 and 5 stand for t=0, 3, 6, 12 and 24, respectively, while the superscript s shows that the values are scaled. Scaled experimental TMR concentration and scaled numerical TMR levels were given by

$$M_i^s = \frac{M_i - M_1}{M_5 - M_1} \quad (S12)$$

$$[TMR]_i^s = \frac{[TMR]_i - [TMR]_1}{[TMR]_5 - [TMR]_1} \quad (S13)$$

where the indices i=1 and 5 correspond to t=0 and 24 h, respectively. The values of M_i were shown in Fig. 2b, while [TMR] was the output of gene expression model. It is important to note that the experimental results presented in Fig. 2b were normalized by TMR concentration before RA treatment. However, under the new scaling (Eq. S12), the lowest TMR concentration in the data set was 0, while the largest TMR concentration was 1 ($0 \leq M_i^s \leq 1$).

The second term in Eq. S11 represented the sum of squared differences between the scaled numerical results and the experimental observations for TM concentration at t= 24h for different RA concentrations, i.e. 0.1 μM, 1μM and 10 μM. Different values of index j in Eq. S11 represent different RA concentrations; j=1, 2 and 3 represent RA=0.1, 1 and 10 μM, respectively. The scaled numerical TM level ($[TM]_j^s$) was defined as the TM concentration from the model divided by experimental observation

$$[TM]_j^s = \frac{[TM]_j^{t=24}}{N_j^{t=24}} \quad (S14)$$

where [TM] and N denote simulation results and experimental data for TM concentration, respectively. Subscript j denotes RA concentration, while superscript (t=24) indicates that the values are for 24 hours after RA treatment. The ranges of variation of N_i were shown in Fig. 2a, while [TM] was the output of gene expression model.

The parameter estimation process was initiated by determining TM initial concentration (IC_{TM}) at various concentrations of RA. The experimental measurements for the TM concentration contained error bars (Fig. 2a). However, we needed to have constant values for the TM concentration at the different concentrations of RA. Thus, we randomly selected values for the TM concentration at the various concentrations of RA following a normal distribution. The bars in Fig. 2a denote the mean values of the TM level at various concentrations of RA, while the standard deviation is half the length of the total error bar. Using Particle swarm optimization (PSO), a population-based stochastic optimization technique, we estimated the independent unknown parameters, i.e. $I_{\max}$, IC_{TMR} and $[\mathrm{REC}_{1t}]$ in a way such that the simulation results for TMR and TM levels fit the experimental data for various concentrations of RA (Fig. 3). After estimating the unknown parameters, we calculated the dependent parameters, i.e. translation rate constant and basal transcription rate via Eq. 4 and Eq. 5, respectively. If the calculated values were within the physiological ranges shown in Table 1, the obtained set of the parameters was accepted. Otherwise, we took a step back and chose a new set of values for the TM concentration at the various concentrations of RA, and the same procedure for fitting the parameters was repeated. Figure S2 outlines the implemented procedure for model parameter estimation.

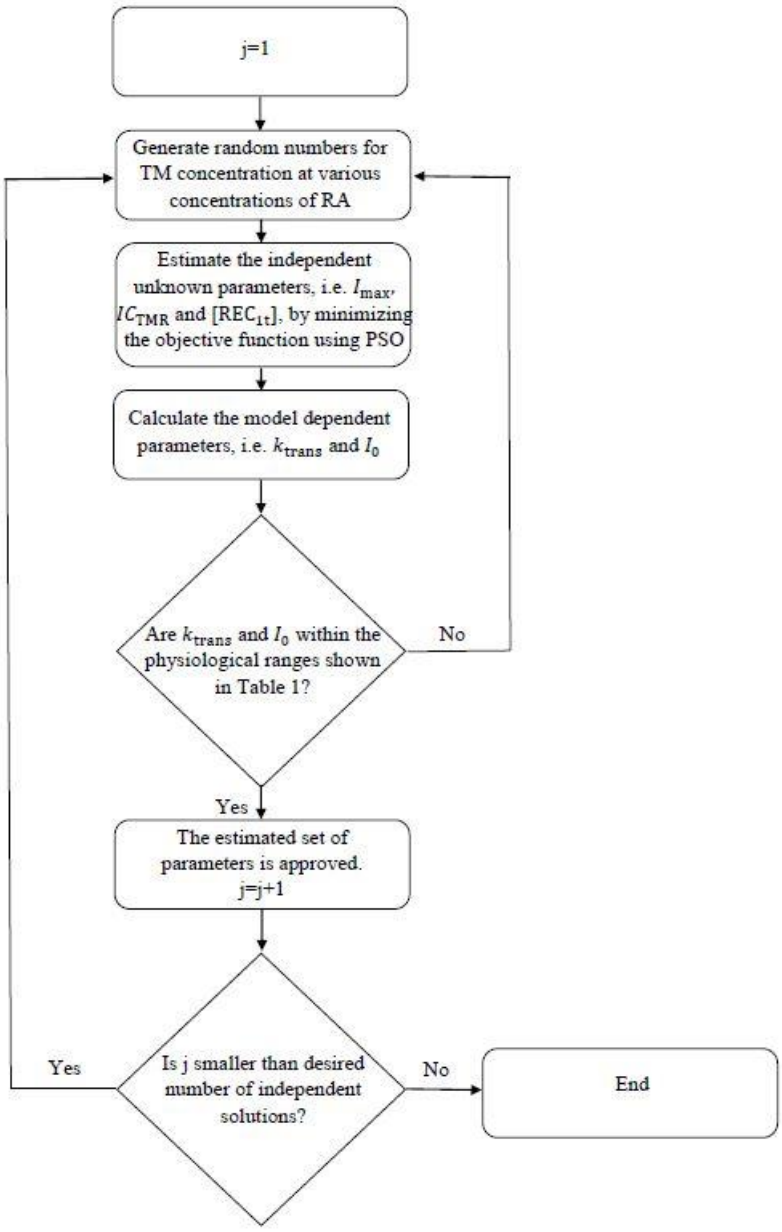

Figure S2. Flow chart of the parameter estimation algorithm.

It is important to note that our problem does not have a unique solution, since the experimental data used for fitting the model parameters is subject to error (Fig. 2a). The estimated values for the unknown parameters depend on the randomly selected values for the TM concentration at RA=10 μM, RA= 1 μM, and RA=0.1 μM. Thus, we repeated the

parameter estimation algorithm 150 times independently and obtained several sets of valid solutions.

The obtained values for IC_{TMR}, I_{max} and $[\mathrm{REC}_{1\mathrm{t}}]$ were within the ranges shown in Fig. S3. The y-axis range in Fig. S3 shows the physiological range for each parameter.

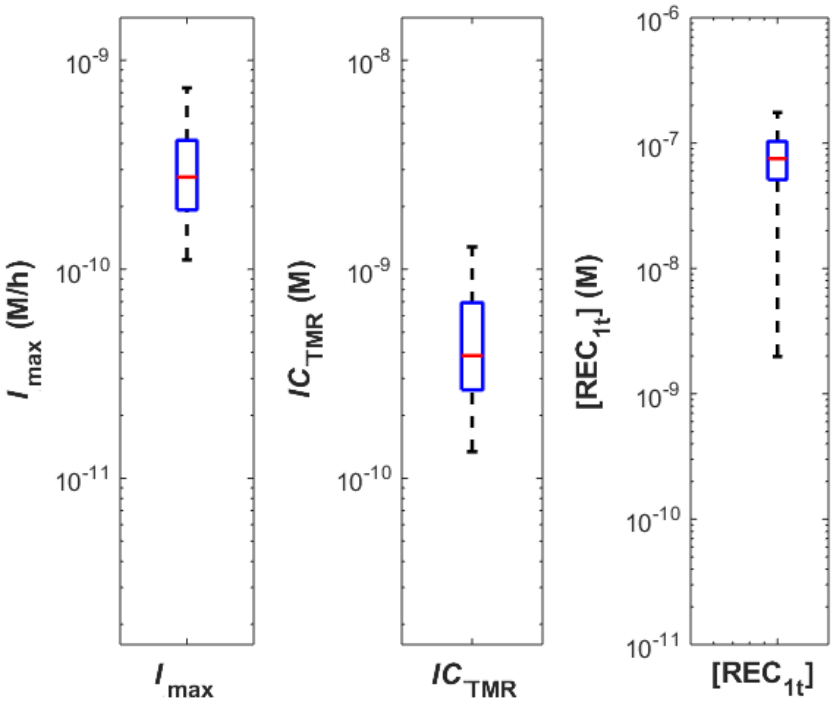

Figure S3. Ranges of the obtained values for the TM transcription rate, the TMR initial concentration, and the total concentration of the transcription factor that activates TM gene. These results were based on 150 valid solutions.

The mean estimated value for total transcription factor concentration were $7 \times 10^{-8}\mathrm{M}$ (Fig. S3), which is comparable with the reported value of $5 \times 10^{-8}\mathrm{M}$ for RAR concentration in promyelocytic leukemia cells [86]. The obtained values for dependent unknown parameters, i.e. k_{trans} and I_0 were within the ranges shown in Fig. S4. The y-axis range in Fig. S4 shows the physiological range for each parameter.

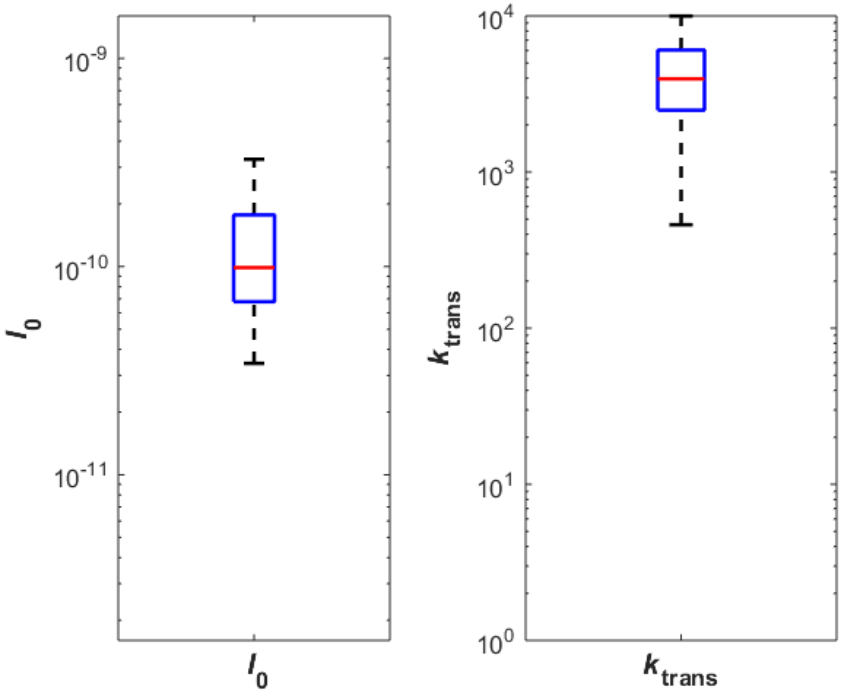

Figure S4. Ranges of the obtained values for the translation rate constant and the basal transcription rate.

3.6.2.2. Particle swarm optimization

The particle swarm optimization (PSO) method has been shown to be efficient in estimating ODE model parameters [53, 87, 88]. PSO involves a swarm of particles, where each particle represents a point in a D-dimensional space, where D is the number of parameters to be estimated. PSO finds the global optimum of the objective function by iteratively changing the positions of the particles. In PSO, the position of each particle in the parameter space is changed based on the experience, or knowledge, of the particle and its neighbors. Suppose that particles are randomly distributed in the parameter space at t=0, and the position of the ith particle in a D dimensional parameter space can be described by the vector

$$\boldsymbol{x}_{\mathrm{i}} = [x_{\mathrm{i}1}, x_{\mathrm{i}2}, \dots, x_{\mathrm{i}\mathrm{D}}]. \quad \text{(S15)}$$

PSO calculates the objective function value (aka fitness value) for each particle and iteratively updates the position of each particle by

$$\boldsymbol{x}_{\mathrm{i}}(t+1) = \boldsymbol{x}_{\mathrm{i}}(t) + \boldsymbol{v}_{\mathrm{i}}(t+1) \quad \text{(S16)}$$

where t and $t+1$ are two consecutive iterations of the algorithm, and $\boldsymbol{v}_{\mathrm{i}}$ indicates the vector of velocity components of the ith particle in the D-dimensional parameter space. The velocity of the ith particle is defined by

$$\boldsymbol{v}_{\mathrm{i}}(t+1) = \boldsymbol{v}_{\mathrm{i}}(t) + \theta_1\big(\mathrm{p}_{\mathrm{i}} - \boldsymbol{x}_{\mathrm{i}}(t)\big)\mathrm{R}_1 + \theta_2\big(\mathrm{g} - \boldsymbol{x}_{\mathrm{i}}(t)\big)\mathrm{R}_2, \quad \text{(S17)}$$

where p_{i} and g denote the local best solution found by the ith particle and the best solution found over the entire population of the particles. θ_1 and θ_2, which are cognitive and social coefficients, respectively, modulate the magnitude of the steps taken by the particle. In this study, we used (θ_1, θ_2)=(0.05564, 0.02886), [53]. R_1 and R_2 are random vectors generated from a uniform distribution in [0,1]. The first term in Eq. S17 is called the inertia component and prevents the particle from significantly changing direction, while the second term in Eq. S17 is called the cognitive component, which indicates that the particles prefer to return to their own previously found best positions. The third term in Eq. S17 is named the social component, which accounts for the tendency of the particles to move towards the position of the particle which has the lowest objective function value. After updating the particle positions at each time step, PSO calculates the objective function value for all particles. PSO then updates the personal best position for each particle and the global best position over the whole population of the particles. This iterative optimization continues until a stopping criterion is met. The global best particle is represented as the best solution at the end of optimization process. Figure S5 shows the flow diagram of the PSO. In this study,

the population size (number of particles) was 1000, while the number of generations (Gen) was 100.

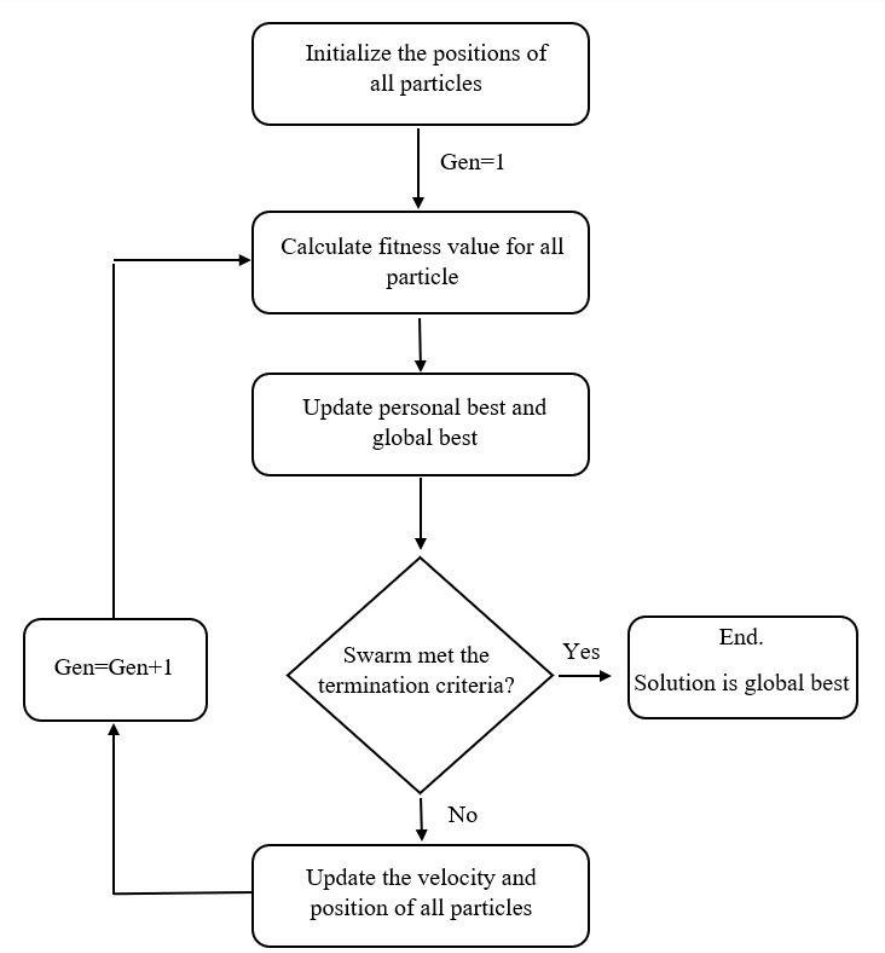

Figure S5. Flow chart of the particle swarm optimization algorithm.

3.6.3. Population pharmacokinetic modelling of RA

We constructed a two-compartment pharmacokinetic model (Fig. 6) in MATLAB SimBiology and fit the model parameters, i.e. $k_{\mathrm{a}}, k_{\mathrm{d}}$, k_{cp}, k_{pc}, V_{c} and V_{p} to the data shown in Fig. 5. k_{cp} and k_{pc} were the distribution rate constant from the central compartment to the peripheral compartment, and the distribution rate constant from the peripheral compartment to the central compartment, respectively. k_{cp} and k_{pc} were defined by

$$k_{\mathrm{cp}} = \frac{Q_{\mathrm{cp}}}{V_{\mathrm{c}}} \tag{S18}$$

$$k_{\mathrm{pc}} = \frac{Q_{\mathrm{cp}}}{V_{\mathrm{p}}}, \tag{S19}$$

where Q_{cp} is the intercompartmental clearance [89]. We used a MATLAB function called nlmefista, which is designed to find the maximum likelihood estimates of the parameters by fitting a nonlinear mixed-effects regression model. Nonlinear mixed-effects regression models have been widely used for the analysis of pharmacokinetic data, as they can consider inter-subject variability in parameters by incorporating random effects into the model [90]. The estimated values for $k_{\mathrm{a}}, k_{\mathrm{d}}$, Q_{cp}, V_{c} and V_{p} were 0.62 1/h, 0.56 1/h, 0.011 L/h , 81.92 L and 3.01 L, respectively. The simulation results corresponding to these estimated values were shown by solid lines in Fig. 5. We used other fitting methods in MATLAB SimBiology such as fminsearch and lsqcurvefit which are used to fit a model to data using a derivative free method [91] and a nonlinear least-square curve fitting technique [92]. The curves fit by different methods looked very similar. The estimated values for $k_{\mathrm{a}}, k_{\mathrm{d}}$ and V_{c} by different methods were very close, while the estimated values for Q_{cp} and V_{p} depended strongly on

the fitting method. Thus, Q_{cp} and V_{p} were not identifiable considering the size of the data set. Additional data points were needed to obtain more accurate estimates for the parameter. However, the main goal of this study was not estimating the pharmacokinetic parameters following oral administration of RA. We aimed to investigate the effects of RA therapy on thrombin generation by coupling four different models, i.e. the pharmacokinetic model, the gene expression model, the sTM release model and the ODE model of the coagulation cascade. Since the curves fit to the pharmacokinetic data through different methods were almost the same, we used the output of the pharmacokinetic model, i.e. fitted curves, as input in the gene expression model to investigate the variations of TM and TMR following RA therapy. Pharmacokinetic parameters of RA following oral dosing can be better estimated using the presented model in this paper once there is more clinical data available.

3.7. References

1. Tang X-H, Gudas LJ: Retinoids, retinoic acid receptors, and cancer. *Annual Review of Pathology: Mechanisms of Disease* 2011, 6:345-364.
2. Chen M-C, Hsu S-L, Lin H, Yang T-Y: Retinoic acid and cancer treatment. *BioMedicine* 2014, 4(4).
3. Di Masi A, Leboffe L, De Marinis E, Pagano F, Cicconi L, Rochette-Egly C, Lo-Coco F, Ascenzi P, Nervi C: Retinoic acid receptors: from molecular mechanisms to cancer therapy. *Molecular aspects of medicine* 2015, 41:1-115.
4. Suganuma M, Oya Y, Umsumarng S, Iida K, Rawangkhan A, Sakai R, Kagechika H, Shudo K, Fujiki H: Innovative cancer treatment of human lung cancer cells PC-9 with a synthetic retinoid Am80 and EGCG via inhibition of HDAC4 and HDAC5. In.: AACR; 2016.
5. Aouad P, Saikali M, Abdel-Samad R, El–Houjeiri L, Pisano C, Talhouk R, Darwiche N: Combination treatments with retinoic acid and the synthetic retinoid ST1926 in 2D and 3D breast cancer models overcome retinoic acid resistance and eradicate breast cancer stem/progenitor cells. In.: AACR; 2016.
6. Barbui T, Finazzi G, Falanga A: The impact of all-trans-retinoic acid on the coagulopathy of acute promyelocytic leukemia. *Blood* 1998, 91(9):3093-3102.

7. Dombret H, Scrobohaci M, Ghorra P, Zini J, Daniel M, Castaigne S, Degos L: Coagulation disorders associated with acute promyelocytic leukemia: corrective effect of all-trans retinoic acid treatment. *Leukemia* 1993, 7(1):2-9.
8. Tallman M, Lefebvre P, Baine R, Shoji M, Cohen I, Green D, Kwaan H, Paietta E, Rickles F: Effects of all-trans retinoic acid or chemotherapy on the molecular regulation of systemic blood coagulation and fibrinolysis in patients with acute promyelocytic leukemia. *Journal of Thrombosis and Haemostasis* 2004, 2(8):1341-1350.
9. Barbui T, Falanga A: Disseminated intravascular coagulation in acute leukemia. In: *Seminars in thrombosis and hemostasis: 2001*. Copyright© 2001 by Thieme Medical Publishers, Inc., 333 Seventh Avenue, New York, NY 10001, USA. Tel.:+ 1 (212) 584-4662: 593-604.
10. Falanga A, Toma S, Marchetti M, Palumbo R, Raffo P, Consonni R, Marziali S, Dastoli G, Barbui T: Effect of all-trans-Retinoic acid on the hypercoagulable state of patients with breast cancer. *American journal of hematology* 2002, 70(1):9-15.
11. Kawai Y, Watanabe K, Kizaki M, Murata M, Kamata T, Uchida H, Moriki T, Yokoyama K, Tokuhira M, Nakajima H: Rapid improvement of coagulopathy by all-trans retinoic acid in acute promyelocytic leukemia. *American journal of hematology* 1994, 46(3):184-188.
12. Falanga A, Iacoviello L, Evangelista V, Belotti D, Consonni R, D'orazio A, Robba L, Donati M, Barbui T: Loss of blast cell procoagulant activity and improvement of hemostatic variables in patients with acute promyelocytic leukemia administered all-trans-retinoic acid. *Blood* 1995, 86(3):1072-1081.
13. Murray J: Coagulation and cancer. *British journal of cancer* 1991, 64(3):422.
14. Duran I, Tannock IF: Disseminated intravascular coagulation as the presenting sign of metastatic prostate cancer. *Journal of general internal medicine* 2006, 21(11).
15. Mast C, Ramanathan RK, Feinstein DI, Rosen P: Disseminated intravascular coagulation secondary to advanced pancreatic cancer treated successfully with combination chemotherapy. *Oncology* 2014, 87(5):266-269.
16. Levi M: Disseminated intravascular coagulation in cancer patients. *Best Practice & Research Clinical Haematology* 2009, 22(1):129-136.
17. Kasthuri RS, Taubman MB, Mackman N: Role of tissue factor in cancer. *Journal of Clinical Oncology* 2009, 27(29):4834-4838.
18. Andoh K, Kubota T, Takada M, Tanaka H, Kobavashi N, Maekawa T: Tissue factor activity in leukemia cells. Special reference to disseminated intravascular coagulation. *Cancer* 1987, 59(4):748-754.
19. Contrino J, Hair G, Kreutzer DL, Rickles FR: In situ detection of tissue factor in vascular endothelial cells: correlation with the malignant phenotype of human breast disease. *Nature medicine* 1996, 2(2):209-215.
20. Joanne LY, May L, Lhotak V, Shahrzad S, Shirasawa S, Weitz JI, Coomber BL, Mackman N, Rak JW: Oncogenic events regulate tissue factor expression in colorectal cancer cells: implications for tumor progression and angiogenesis. *Blood* 2005, 105(4):1734-1741.
21. Falanga A, Gordon SG: Isolation and characterization of cancer procoagulant: a cysteine proteinase from malignant tissue. *Biochemistry* 1985, 24(20):5558-5567.
22. Donati MB, Gambacorti-Passerini C, Casali B, Falanga A, Vannotti P, Fossati G, Semeraro N, Gordon SG: Cancer procoagulant in human tumor cells: evidence from melanoma patients. *Cancer research* 1986, 46(12 Part 1):6471-6474.
23. Maiolo A, Tua A, Grignani G: Hemostasis and cancer: tumor cells induce the expression of tissue factor-like procoagulant activity on endothelial cells. *haematologica* 2002, 87(6):624-628.
24. Lorenzet R, Peri G, Locati D, Allavena P, Colucci M, Semeraro N, Mantovani A, Donati MB: Generation of procoagulant activity by mononuclear phagocytes: a possible

mechanism contributing to blood clotting activation within malignant tissues. *Blood* 1983, 62(2):271-273.
25. Lwaleed BA, Francis JL, Chisholm M: Monocyte tissue factor levels in cancer patients. *Saudi medical journal* 2000, 21(8):722-729.
26. Tsuruo T, Fujita N: Platelet aggregation in the formation of tumor metastasis. *Proceedings of the Japan Academy, Series B* 2008, 84(6):189-198.
27. Levi M, van der Poll T: Inflammation and coagulation. *Critical care medicine* 2010, 38:S26-S34.
28. Marchetti M, Russo L, Balducci D, Falanga A: All trans-retinoic acid modulates the procoagulant activity of human breast cancer cells. *Thrombosis research* 2011, 128(4):368-374.
29. Falanga A, Consonni R, Marchetti M, Locatelli G, Garattini E, Passerini CG, Gordon S, Barbui T: Cancer procoagulant and tissue factor are differently modulated by all-trans-retinoic acid in acute promyelocytic leukemia cells. *Blood* 1998, 92(1):143-151.
30. Kooistra T, Opdenberg JP, Toet K, Hendriks HF, van den Hoogen RM, Emeis JJ: Stimulation of tissue-type plasminogen activator synthesis by retinoids in cultured human endothelial cells and rat tissues in vivo. *Thrombosis and haemostasis* 1991, 66(05):565-572.
31. Tapiovaara H, Matikainen S, Hurme M, Vaheri A: Induction of differentiation of promyelocytic NB4 cells by retinoic acid is associated with rapid increase in urokinase activity subsequently downregulated by production of inhibitors. *Blood* 1994, 83(7):1883-1891.
32. Marchetti M, Falanga A, Giovanelli S, Oldani E, Barbui T: All-trans-retinoic acid increases adhesion to endothelium of the human promyelocytic leukaemia cell line NB4. *British journal of haematology* 1996, 93(2):360-366.
33. Conese M, Montemurro P, Fumarulo R, Giordano D, Riccardi S, Colucci M, Semeraro N: Inhibitory effect of retinoids on the generation of procoagulant activity by blood mononuclear phagocytes. *Thrombosis and haemostasis* 1991, 66(6):662-665.
34. Ishii H, Horie S, Kizaki K, Kazama M: Retinoic acid counteracts both the downregulation of thrombomodulin and the induction of tissue factor in cultured human endothelial cells exposed to tumor necrosis factor. *Blood* 1992, 80(10):2556-2562.
35. Koyama T, Hirosawa S, Kawamata N, Tohda S, Aoki N: All-trans retinoic acid upregulates thrombomodulin and downregulates tissue-factor expression in acute promyelocytic leukemia cells: distinct expression of thrombomodulin and tissue factor in human leukemic cells. *Blood* 1994, 84(9):3001-3009.
36. Aoshima K, Asakura H, Yamazaki M, Saito M, Kumabashiri I, Morishita E, Ontachi Y, Mizutani T, Ichino T, Matsuda T: Treatment of disseminated intravascular coagulation (DIC) with all-trans retinoic acid in an endotoxin-induced rat model. In: *Seminars in thrombosis and hemostasis: 1998*. Copyright© 1998 by Thieme Medical Publishers, Inc.: 227-231.
37. Ghaffari H, Petzold LR: Identification of influential proteins in the classical retinoic acid signaling pathway. *Theoretical Biology and Medical Modelling* 2018, 15(1):16.
38. Tomita A, Kiyoi H, Naoe T: Mechanisms of action and resistance to all-trans retinoic acid (ATRA) and arsenic trioxide (As 2 O 3) in acute promyelocytic leukemia. *International journal of hematology* 2013, 97(6):717-725.
39. Brummel-Ziedins KE, Orfeo T, Callas PW, Gissel M, Mann KG, Bovill EG: The prothrombotic phenotypes in familial protein C deficiency are differentiated by computational modeling of thrombin generation. *PloS one* 2012, 7(9):e44378.
40. Horie S, Ishii H, Matsumoto F, Kusano M, Kizaki K, Matsuda J, Kazama M: Acceleration of Thrombomodulin Gene Transcription by Retinoic Acid RETINOIC ACID RECEPTORS AND Sp1 REGULATE THE PROMOTER ACTIVITY THROUGH INTERACTIONS WITH TWO DIFFERENT SEQUENCES IN THE 5′-FLANKING REGION OF HUMAN GENE. *Journal of Biological Chemistry* 2001, 276(4):2440-2450.

41. Horie S, Kizaki K, Ishii H, Kazama M: Retinoic acid stimulates expression of thrombomodulin, a cell surface anticoagulant glycoprotein, on human endothelial cells. Differences between up-regulation of thrombomodulin by retinoic acid and cyclic AMP. *Biochemical Journal* 1992, 281(1):149-154.
42. Christenson LK, Stouffer RL: Isolation and culture of microvascular endothelial cells from the primate corpus luteum. *Biology of reproduction* 1996, 55(6):1397-1404.
43. Ngwa W, Makrigiorgos GM, Berbeco RI: Gold nanoparticle-aided brachytherapy with vascular dose painting: Estimation of dose enhancement to the tumor endothelial cell nucleus. *Medical physics* 2012, 39(1):392-398.
44. Ghaffari H, Saidi MS, Firoozabadi B: Biomechanical analysis of actin cytoskeleton function based on a spring network cell model. *Proceedings of the Institution of Mechanical Engineers, Part C: Journal of Mechanical Engineering Science* 2017, 231(7):1308-1323.
45. Thatcher JE, Zelter A, Isoherranen N: The relative importance of CYP26A1 in hepatic clearance of all-trans retinoic acid. *Biochemical pharmacology* 2010, 80(6):903-912.
46. Eckhoff C, Nau H: Identification and quantitation of all-trans-and 13-cis-retinoic acid and 13-cis-4-oxoretinoic acid in human plasma. *Journal of lipid research* 1990, 31(8):1445-1454.
47. Schwanhäusser B, Busse D, Li N, Dittmar G, Schuchhardt J, Wolf J, Chen W, Selbach M: Global quantification of mammalian gene expression control. *Nature* 2011, 473(7347):337-342.
48. Ishii H, Tezuka T, Ishikawa H, Takada K, Oida K, Horie S: Oxidized phospholipids in oxidized low-density lipoprotein down-regulate thrombomodulin transcription in vascular endothelial cells through a decrease in the binding of RARβ-RXRα heterodimers and Sp1 and Sp3 to their binding sequences in the TM promoter. *Blood* 2003, 101(12):4765-4774.
49. Lentz SR, Tsiang M, Sadler JE: Regulation of thrombomodulin by tumor necrosis factor-alpha: comparison of transcriptional and posttranscriptional mechanisms. *Blood* 1991, 77(3):542-550.
50. Islam S, Zeisel A, Joost S, La Manno G, Zajac P, Kasper M, Lönnerberg P, Linnarsson S: Quantitative single-cell RNA-seq with unique molecular identifiers. *Nature methods* 2014, 11(2):163-166.
51. Crettaz M, Baron A, Siegenthaler G, Hunziker W: Ligand specificities of recombinant retinoic acid receptors RAR α and RAR β. *Biochemical journal* 1990, 272(2):391-397.
52. Angulo A, Chandraratna RA, LeBlanc JF, Ghazal P: Ligand induction of retinoic acid receptors alters an acute infection by murine cytomegalovirus. *Journal of virology* 1998, 72(6):4589-4600.
53. Sagar A, Varner JD: Dynamic modeling of the human coagulation cascade using reduced order effective kinetic models. *Processes* 2015, 3(1):178-203.
54. Klement RJ, Bandyopadhyay PS, Champ CE, Walach H: Application of Bayesian evidence synthesis to modelling the effect of ketogenic therapy on survival of high grade glioma patients. *Theoretical Biology and Medical Modelling* 2018, 15(1):12.
55. Adamson PC: All-trans-retinoic acid pharmacology and its impact on the treatment of acute promyelocytic leukemia. *The oncologist* 1996, 1(5):305-314.
56. Saadeddin A, Torres-Molina F, Cárcel-Trullols J, Araico A, Peris J-E: Pharmacokinetics of the time-dependent elimination of all-trans-retinoic acid in rats. *The AAPS journal* 2004, 6(1):1-9.
57. Muindi JR, Frankel SR, Huselton C, DeGrazia F, Garland WA, Young CW, Warrell RP: Clinical pharmacology of oral all-trans retinoic acid in patients with acute promyelocytic leukemia. *Cancer Research* 1992, 52(8):2138-2142.
58. Ishii H, Majerus PW: Thrombomodulin is present in human plasma and urine. *The Journal of clinical investigation* 1985, 76(6):2178-2181.

59. Takahashi Y, Hosaka Y, Niina H, Nagasawa K, Naotsuka M, Sakai K, Uemura A: Soluble thrombomodulin purified from human urine exhibits a potent anticoagulant effect in vitro and in vivo. *Thrombosis and haemostasis* 1995, 74(05):805-811.
60. Wada H, Sakakura M, Kushiya F, Nisikawa M, Onishi K, Nakatani K, Shiku H, Nobori T: Thrombomodulin accelerates activated protein C production and inhibits thrombin generation in the plasma of disseminated intravascular coagulation patients. *Blood coagulation & fibrinolysis* 2005, 16(1):17-24.
61. Ishii H, Uchiyama H, Kazama M: Soluble thrombomodulin antigen in conditioned medium is increased by damage of endothelial cells. *Thrombosis and haemostasis* 1991, 66(05):618-623.
62. Boffa M-C: Considering cellular thrombomodulin distribution and its modulating factors can facilitate the use of plasma thrombomodulin as a reliable endothelial marker? *Pathophysiology of Haemostasis and Thrombosis* 1996, 26(Suppl. 4):233-243.
63. Ehrlich H, Esmon N, Bang N: In vivo behavior of detergent-solubilized purified rabbit thrombomodulin on intravenous injection into rabbits. *The Journal of laboratory and clinical medicine* 1990, 115(2):182-189.
64. Conley BA, Egorin MJ, Sridhara R, Finley R, Hemady R, Wu S, Tait NS, Van Echo DA: Phase I clinical trial of all-trans-retinoic acid with correlation of its pharmacokinetics and pharmacodynamics. *Cancer chemotherapy and pharmacology* 1997, 39(4):291-299.
65. Ferrigno D, Buccheri G, Ricca I: Prognostic significance of blood coagulation tests in lung cancer. *European Respiratory Journal* 2001, 17(4):667-673.
66. Green D, Maliekel K, Sushko E, Akhtar R, Soff GA: Activated-protein-C resistance in cancer patients. *Pathophysiology of Haemostasis and Thrombosis* 1997, 27(3):112-118.
67. Jiang G-s, Tang T-h, Bi K-h, Zhang Y-k, Ren H-q, Jiang F-q, Ren Q-h, Zhen G, Liu C-f, Peng J: Cytokine secretion in patients with acute promyelocytic leukemia after treatment with all-trans retinoic acid. *Chinese Journal of Cancer Research* 2003, 15(1):33-37.
68. Dubois C, Schlageter M, Balitrand N, Toubert M, Krawice I, Fenaux P, Castaigne S, Najean Y, Degos L: Modulation of IL-8, IL-1 beta, and G-CSF secretion by all-trans retinoic acid in acute promyelocytic leukemia. *Leukemia* 1994, 8(10):1750-1757.
69. Archipoff G, Beretz A, Freyssinet J, Klein-Soyer C, Brisson C, Cazenave J: Heterogeneous regulation of constitutive thrombomodulin or inducible tissue-factor activities on the surface of human saphenous-vein endothelial cells in culture following stimulation by interleukin-1, tumour necrosis factor, thrombin or phorbol ester. *Biochemical journal* 1991, 273(3):679-684.
70. Nawroth PP, Stern DM: Modulation of endothelial cell hemostatic properties by tumor necrosis factor. *Journal of Experimental Medicine* 1986, 163(3):740-745.
71. Visani G, Tosi P, Ottaviani E, Zaccaria A, Baccini C, Manfroi S, Pastano R, Remiddi C, Morelli A, Molinari A: All-trans retinoic acid and in vitro cytokine production by acute promyelocytic eukemia cells. *European journal of haematology* 1996, 57(4):301-306.
72. Kato T, Sakai T, Kato M, Hagihara M, Hasegawa T, Matsuura K, Nakagawa T: Recombinant human soluble thrombomodulin administration improves sepsis-induced disseminated intravascular coagulation and mortality: a retrospective cohort study. *Thrombosis journal* 2013, 11(1):3.
73. Aota T, Wada H, Yamashita Y, Matsumoto T, Ohishi K, Suzuki K, Imai H, Usui M, Isaji S, Katayama N: The efficacy of the administration of recombinant human soluble thrombomodulin in patients with DIC. *International journal of hematology* 2016, 103(2):173-179.
74. Sano T, Terai Y, Daimon A, Nunode M, Nagayasu Y, Okamoto A, Fujita D, Hayashi M, Ohmichi M: Recombinant human soluble thrombomodulin as an anticoagulation therapy improves recurrent miscarriage and fetal growth restriction due to placental insufficiency–The leading cause of preeclampsia. *Placenta* 2018, 65:1-6.

75. Ookura M, Hosono N, Tasaki T, Oiwa K, Fujita K, Ito K, Lee S, Matsuda Y, Morita M, Tai K: Successful treatment of disseminated intravascular coagulation by recombinant human soluble thrombomodulin in patients with acute myeloid leukemia. *Medicine* 2018, 97(44):e12981.
76. Yoshihara M, Uno K, Tano S, Mayama M, Ukai M, Kondo S, Kokabu T, Kishigami Y, Oguchi H: The efficacy of recombinant human soluble thrombomodulin for obstetric disseminated intravascular coagulation: a retrospective study. *Critical Care* 2015, 19(1):369.
77. Franke H, Galla H-J, Beuckmann CT: Primary cultures of brain microvessel endothelial cells: a valid and flexible model to study drug transport through the blood–brain barrier in vitro. *Brain Research Protocols* 2000, 5(3):248-256.
78. Duester G: Retinoic acid synthesis and signaling during early organogenesis. *Cell* 2008, 134(6):921-931.
79. Marchetti M, Vignoli A, Bani MR, Balducci D, Barbui T, Falanga A: All-trans retinoic acid modulates microvascular endothelial cell hemostatic properties. *Haematologica* 2003, 88(8):895-905.
80. Ingalls B: Mathematical modelling in systems biology: An introduction. *Internet[cited at p 117]* 2013.
81. Sauro HM: Enzyme kinetics for systems biology: Future Skill Software; 2011.
82. Stormo GD, Zhao Y: Determining the specificity of protein–DNA interactions. *Nature Reviews Genetics* 2010, 11(11):751-760.
83. Ingalls BP: Mathematical modeling in systems biology: an introduction: MIT press; 2013.
84. Halford SE, Marko JF: How do site-specific DNA-binding proteins find their targets? *Nucleic acids research* 2004, 32(10):3040-3052.
85. Mirny L, Slutsky M, Wunderlich Z, Tafvizi A, Leith J, Kosmrlj A: How a protein searches for its site on DNA: the mechanism of facilitated diffusion. *Journal of Physics A: Mathematical and Theoretical* 2009, 42(43):434013.
86. Nervi C, Grippo JF, Sherman MI, George MD, Jetten AM: Identification and characterization of nuclear retinoic acid-binding activity in human myeloblastic leukemia HL-60 cells. *Proceedings of the National Academy of Sciences* 1989, 86(15):5854-5858.
87. Sagar A, Dai W, Minot M, LeCover R, Varner JD: Reduced order modeling and analysis of the human complement system. *PloS one* 2017, 12(11):e0187373.
88. Ghaffari H, Grant SC, Petzold LR, Harrington MG: Regulation of cerebrospinal fluid and brain tissue sodium levels by choroid plexus and brain capillary endothelial cell sodium-potassium pumps during migraine. *bioRxiv* 2019:572727.
89. Hill S: Pharmacokinetics of drug infusions. *Continuing education in anaesthesia, critical care & Pain* 2004, 4(3):76-80.
90. Drikvandi R: Nonlinear mixed-effects models for pharmacokinetic data analysis: assessment of the random-effects distribution. *Journal of pharmacokinetics and pharmacodynamics* 2017, 44(3):223-232.
91. Rios LM, Sahinidis NV: Derivative-free optimization: a review of algorithms and comparison of software implementations. *Journal of Global Optimization* 2013, 56(3):1247-1293.
92. Griva I, Nash SG, Sofer A: Linear and nonlinear optimization, vol. 108: Siam; 2009.

Chapter 4

Regulation of CSF and brain tissue sodium levels by the blood-CSF and blood-brain barriers during migraine

4.1. Introduction

Migraine is ranked among the top five causes of disability in the world [1]. Although the exact underlying causes of migraine are not known, common triggers of migraine include dehydration, stress, sleep disorders, hunger, etc. Understanding the pathophysiology of migraine is challenging because migraine triggering is different for everyone. Many of the triggers of migraine change the sodium balance in the brain. Animal and human studies [2-5] have revealed that migraine sufferers have higher levels of cerebrospinal fluid (CSF) and brain interstitial fluid (ISF) sodium than control groups, while there is no significant difference between blood concentration of sodium in migraineurs and healthy controls. Studies have indicated that elevated levels of ISF sodium increase neuronal excitability [6, 7], which subsequently results in migraine Brain sodium levels ultimately derive from peripheral circulation. Sodium is exchanged between the blood and brain across two major blood-brain interfaces, namely the blood-brain barrier (BBB) and the blood-CSF barrier (BCSFB). The BBB is formed by specialized endothelial cells lining the cerebral microvasculature and controls sodium exchange between the ISF and blood, while the BCSFB is formed by choroid plexus epithelial cells and regulates sodium transport between ventricular CSF and blood. Transfer of sodium across the BBB and the BCSFB predominantly take places via active, hence transcellular mechanisms. However, sodium may be able to cross the BCSFB and the BBB via a paracellular route through tight

junctions between epithelial cells at the BCSFB and between endothelial cells at the BBB [8].

It is believed that the BCSFB and BBB are highly responsible for maintaining ion homeostasis in the brain. Thus, a disturbance in sodium transport mechanisms at the BCSFB and/or BBB can alter CSF and brain tissue sodium concentrations. However, the relative contributions of the two interfaces in the regulation of brain sodium homeostasis have yet to be determined. In this work, we use mechanistic modeling to study the significance of the BCSFB and BBB in controlling brain tissue and CSF sodium levels. We develop a mathematical model consisting of four compartments: the ventricular system, subarachnoid space, brain tissue and blood. Net movement of sodium across the BCSFB and BBB through different active and passive transport mechanisms is modeled by influx and efflux permeability coefficients of the interfaces to sodium. Influx permeability coefficients of the BCSFB and BBB to sodium refer to sodium movement from blood to CSF and brain tissue, respectively, whereas efflux permeability coefficients of the BCSFB and BBB to sodium represent sodium movement from CSF and brain tissue to blood, respectively. We study the dynamics of sodium distribution in the brain following a perturbation in the influx and efflux permeabilities of the BCSFB and BBB to sodium. We then perform a global sensitivity analysis (GSA) to assess the significance of the BCSFB and BBB in controlling sodium concentrations in the brain tissue, ventricular CSF and subarachnoid CSF. Our results reveal that the influx permeability coefficient of the BCSFB to sodium is the most sensitive model parameter in controlling ventricular CSF sodium concentration. Depending on the time elapsed from perturbations of the permeability coefficients, brain tissue and

subarachnoid space CSF sodium levels can be significantly controlled by the BCSFB and/or BBB.

The computational model presented in this study can not only shed light on the dynamics of sodium exchange between CSF, brain tissue and blood, but can also provide insight for future experimental studies. In addition, this work can potentially offer a new strategy to normalize the elevated levels of brain sodium in migraine sufferers and potentially treat migraines.

4.2. Methods

4.2.1. Model Development

We modeled a rat's brain by three concentric spheres representing the ventricular system, brain tissue and subarachnoid space (Fig. 1). Brain tissue was modeled as a single compartment. We assumed that blood vessels are distributed randomly, following a uniform distribution, throughout the brain tissue.

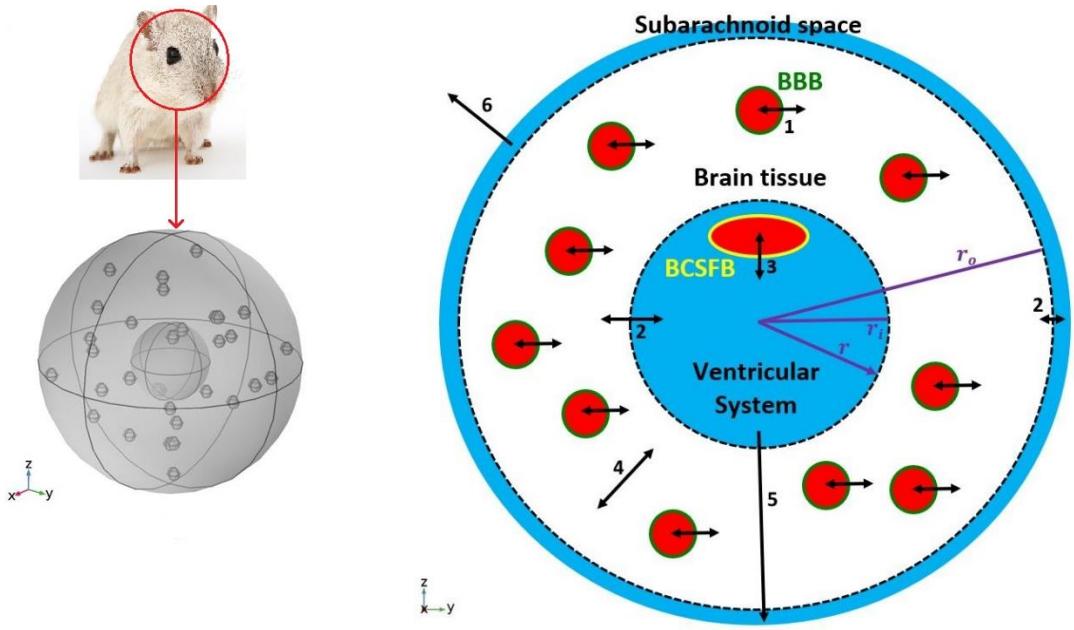

(a) (b)

Figure 1. Schematic of the model. (a) A 3D model of a rat's brain. (b) A 2D view of the cross section of the 3D model. The inner circle, shown in blue, represents the ventricular system, while the outer ring, shown in blue, is subarachnoid space. The white region between two dashed circles is brain tissue. Blood vessels, shown in red filled circles, are distributed uniformly in the brain tissue. The green circular border which separates blood from the brain tissue is the BBB. The BCSFB which is depicted by a yellow ellipsoid separates blood from the ventricular CSF. Numbers in the figure specify the types and locations of sodium transport: 1. capillary-brain transport across the BBB; 2. exchange between CSF and ISF; 3. blood-CSF exchange across the BCSFB; 4. diffusive transport in the radial direction in the brain tissue; 5. transport by the CSF flow from the ventricular system to the subarachnoid space; 6 transport by the CSF flow from the subarachnoid space to the blood. Arrows 5 and 6 indicate CSF flow direction from the ventricular system to the subarachnoid space, and from the subarachnoid space to the blood. Although CSF flow has been modeled (Eqs 1-2), the model does not include actual channels for transferring CSF flow between the ventricular system, subarachnoid space and blood. It should be noted that the size and number of the graphic symbols of blood vessels, as well as the size of the graphic symbol of choroid plexus (a.k.a BCSFB) do not represent their realistic values given in Table 1.

The inner sphere, which represents the ventricular system, includes the BCSFB. CSF is secreted by the BCSFB cells, a.k.a the choroid plexus epithelial cells, flows into the ventricular system, and then passes through small openings (foramina) into the subarachnoid space where it is absorbed through blood vessels into the bloodstream. It has also been suggested that a part of subarachnoid CSF moves into the brain along paravascular routes surrounding cerebral arteries, where it mixes with brain ISF and leaves the brain along veins [9, 10]. In the current model, we have ignored CSF flow from subarachnoid space to brain ISF (See Section 4 for further discussion of this subject). Thus, we have assumed that the CSF secretion rate is equal to the CSF absorption rate from the subarachnoid space to the blood. We have also assumed that sodium can be easily exchanged between the brain tissue and the CSF at the interface of brain tissue and the ventricular system, and at the contact surface of the subarachnoid space and brain tissue (dashed circles in Fig. 1b). This is due to the negligible permeability of the contact surfaces. This transport can be considered as a diffusive transport with a very large diffusion coefficient, and is different from the convective CSF flow from the subarachnoid space to the ISF, which has been ignored in this work. Sodium is also exchanged between blood and brain tissue across the BBB, and can also diffuse in the brain tissue down its concentration gradient.

4.2.2. Formulation of the model

Ventricular and subarachnoid CSF sodium concentrations were modeled by ordinary differential equations (ODEs) represented by Eqs. 1-2, while the variation of sodium level

across brain tissue was modeled by a partial differential equation (PDE), represented by Eq. 3.

$$\frac{\partial C_v(t)}{\partial t} = \frac{P_{BCSFB}A_{BCSFB}}{V_v}C_{blood} - \frac{P'_{BCSFB}A_{BCSFB}}{V_v}C_v + \frac{P_{vb}A_v\lambda}{V_v}\left(\frac{C_{br}(t,r_i)}{f_d} - C_v\right) - \frac{Q_{csf}}{V_v}C_v \quad (1)$$

$$\frac{\partial C_s(t)}{\partial t} = \frac{P_{sb}A_s\lambda}{V_s}\left(\frac{C_{br}(t,r_o)}{f_d} - C_s\right) + \frac{Q_{csf}}{V_s}C_v - \frac{Q_{csf}}{V_s}C_s \quad (2)$$

$$\frac{\partial C_{br}(t,r)}{\partial t} = P_{BBB}A_{BBB}C_{blood} - \frac{P'_{BBB}A_{BBB}}{f_d}C_{br} + \frac{\lambda}{\rho f_d r^2}\frac{\partial}{\partial r}\left(Dr^2\frac{\partial C_{br}}{\partial t}\right), \qquad r_i < r < r_o \quad (3)$$

where $C_v, C_s,\ C_{blood},\ C_{br}$ and t represent ventricular CSF sodium concentration, subarachnoid CSF sodium concentration, blood sodium concentration, sodium level in brain tissue and time, respectively. C_v, C_s and C_{blood} are expressed in mole ml^{-1}, while C_{br} is defined as moles of sodium per gram of brain (mole g^{-1}). C_{br} includes sodium content in brain ISF and in brain cells. The ISF sodium concentration (mole ml^{-1}) was estimated from the brain tissue sodium level (mole g^{-1}) by [11]

$$C_{ISF}(t,r) = \frac{C_{br}(t,r)}{f_d} \quad (4)$$

where C_{ISF} and f_d are the ISF sodium concentration and sodium distribution factor, respectively. The model's parameters are defined in Table 1.

Table 1. Physiological values of the model's parameters for an adult rat

Parameters	Description	Value	Reference
P_{BCSFB}	BCSFB influx permeability coefficient to sodium (from blood to CSF)	3.8×10^{-5} (cm s^{-1})	[11]
A_{BCSFB}	Surface area of BCSFB	1 (cm^2)	[11]

P'_{BCSFB}	BCSFB efflux permeability coefficient to sodium (from CSF to blood)	6.9×10^{-7} (cm s^{-1})	Calculated
V_s	Subarachnoid space volume	0.2 (cm^3)	[11, 12]
V_v	Ventricular system volume	0.1 (cm^3)	[11, 12]
V_b	Brain tissue volume	1.1 (cm^3)	[13]
P_{BBB}	BBB influx permeability coefficient to sodium (from blood to brain tissue)	1.4×10^{-7} (cm s^{-1})	[11]
A_{BBB}	Surface area of the BBB	140 (cm^2 g^{-1})	[11]
P'_{BBB}	BBB efflux permeability coefficient to sodium (from brain tissue to blood)	1.35×10^{-7} cm s^{-1}	Calculated
f_d	Sodium distribution factor	0.34 (cm^3 g^{-1})	[11]
D	Diffusion coefficient of sodium in the brain ISF	1.15×10^{-5} (cm^2 s^{-1})	[14]
Q_{csf}	CSF flow rate	3.6×10^{-5} (cm^3 s^{-1})	[11]
P_{vb}	Permeability coefficient of the contact surface of brain tissue and ventricular system to sodium	10^6 (cm s^{-1})	A large value was used
P_{sb}	Permeability coefficient of the contact surface of brain tissue and subarachnoid space to sodium	10^6 (cm s^{-1})	A large value was used
λ	ISF/brain volume fraction	0.2 (dimensionless)	[11, 15]
ρ	Rat brain density	1 (g cm^{-3})	[11]

The parameters r_i and r_o, which specify the boundaries of brain tissue in Eq. 3 and Figure 1b, were obtained via the relationships

$$V_v = \frac{4}{3}\pi {r_i}^3 \tag{5}$$

and

$$V_v + V_b = \frac{4}{3}\pi {r_o}^3, \tag{6}$$

where V_v and V_b represent the ventricular system volume and brain tissue volume, respectively. r_i is the radius of the inner sphere representing the ventricular system, while r_o is the radius of the middle sphere that represents the outer boundary of the brain tissue (Fig 1b). The terms on the left-hand side of Eqs. 1 and 2 represent the rate of change of sodium concentration (mole ml^{-1}) in the ventricular and subarachnoid CSF, respectively, while the term on the left-hand side of Eq. 3 represents the rate of change of sodium level (mole g^{-1}) in the brain tissue. The four terms on the right-hand side of Eq. 1 represent sodium transport from the blood to the ventricular CSF, sodium movement from the ventricular CSF to the blood, exchange of sodium between the ventricular CSF and the brain tissue, and sodium loss from the ventricular system due to bulk flow of CSF from the ventricular system to the subarachnoid space, from left to right, respectively. The three terms on the right-hand side of Eq. 2 denote exchange of sodium between the subarachnoid CSF and the brain tissue, sodium input to the subarachnoid CSF due to the bulk flow of CSF, and sodium loss from the subarachnoid space due to CSF absorption into the blood, from left to right, respectively. The three terms on the right-hand side of Eq. 3 represent sodium transport from the blood to the brain tissue, sodium movement from the brain tissue to the blood, and diffusive transport of sodium across the brain tissue, from left to right, respectively.

The initial conditions for the ODEs (Eqs. 1-2) are given by [16, 17]

$$C_v = C_s = 145 \text{ mM}. \tag{7}$$

We have also assumed that C_{blood} is 140 mM at steady state [16].

Rates of exchange of sodium at the boundaries of Eq. 3 are defined by

$$Q_v = P_{vb} A_v \lambda \left(C_v - \frac{C_{br}(t,r)}{f_d} \right) \qquad r = r_i \tag{8}$$

$$Q_s = P_{sb} A_s \lambda \left(C_s - \frac{C_{br}(t,r)}{f_d} \right). \qquad r = r_o \tag{9}$$

We used large values for P_{sb} and P_{vb} due to high permeability of the contact surfaces to sodium. Thus, the ISF sodium concentration is approximately in equilibrium with ventricular and subarachnoid sodium concentrations at the interface of brain tissue and CSF. It is important to note that passive transport of sodium across the boundaries of brain tissue and CSF is regulated by the concentration gradient between the CSF and brain ISF (Eqs. 7-8). Brain ISF sodium concentration is estimated from brain tissue sodium level by Eq. 4. A_v and A_s in Eqs. 8 and 9 represent the contact surface area of the brain tissue and the ventricular system, and the contact surface area of the brain tissue and the subarachnoid space, respectively. The contact surfaces were modeled as concentric spheres with the radiuses of r_i and r_o (Fig. 1). A_v and A_s were obtained by

$$A_v = 4\pi {r_i}^2 \tag{10}$$

and

$$A_s = 4\pi {r_o}^2 \tag{11}$$

where r_i and r_o were calculated from Eqs. 5 and 6 using the physiological values of V_v and V_b (Table 1). In this model, A_v and A_s were obtained to be 1 and 5.5 cm^2, respectively, consistent with experimental estimates of the contact surfaces areas [18, 19].

P'_{BCSFB} and P'_{BBB} were calculated assuming that the CSF sodium level is in equilibrium with the brain tissue sodium concentration at t=0 (steady state):

$$C_{br}(t,r) = C_v \times f_d = C_s \times f_d. \qquad \text{for} \qquad r_i \le r \le r_o \qquad (12)$$

This assumption implies that there is no sodium exchange between the CSF and the brain tissue at the two contact surfaces of brain tissue and CSF at t=0 [20, 21]. The obtained values for P'_{BCSFB} and P'_{BBB} were 6.9×10^{-7} cm s^{-1} and 1.35×10^{-7} cm s^{-1}, respectively. In order to assess the validity of the obtained value for P'_{BBB}, we calculated the rate constant for total sodium efflux from the brain tissue to the blood, defined by $\frac{P'_{BBB}A_{BBB}}{f_d}$ [22]. The average value of $\frac{P'_{BBB}A_{BBB}}{f_d}$ was 5.5×10^{-5} s^{-1} in this work, which is consistent with the value of 1×10^{-4} s^{-1} reported by Cserr et al [22].

In Section 3, we perform a local sensitivity analysis to investigate how perturbations in P_{BCSFB}, P_{BBB}, P'_{BCSFB} or P'_{BBB} affect brain and CSF sodium concentrations. We also perform a global sensitivity analysis (GSA) to further analyze the significance of variations in the permeability coefficients in controlling the levels of sodium in the CSF and brain tissue. To solve the system of differential equations described by Eqs 1-3, we discretize Eq. 3 with respect to the variable r using the central difference approximation, and we approximate the time derivatives via backward differences. The main advantage of this fully implicit scheme, a.k.a. backward time central space, is that it is unconditionally stable.

4.2.3. Global sensitivity analysis

Global sensitivity analysis (GSA) is a numerical method designed to analyze the impacts of uncertain parameters on a model's output. Compared to local sensitivity analysis, which assesses the changes of model response by making small perturbations to each parameter while keeping the remaining parameters unchanged, GSA analyzes the variations in the model output when all model parameters can vary simultaneously over specified ranges. In

other words, GSA investigates how the uncertainty of the model's output is apportioned to variations in multiple model inputs. This feature makes GSA useful for understanding the contributions of uncertain model parameters to the variations of the model output. In this work, we use GSA to compare the importance of P_{BCSFB}, P_{BBB}, P'_{BCSFB} and P'_{BBB} in controlling brain tissue and CSF sodium concentrations, while taking into account the inter-subject variability in all of the model's parameters. We use a MATLAB toolbox for GSA, called SAFE [23]. We perform Sobol's sensitivity analysis, which quantitively ranks the relative importance of the parameters by decomposing the model's output variance into the contributions associated with each model's input. Sobol's method, which has been widely applied to complex systems biology and pharmacology models [24-32], calculates the first-order and total-effect sensitivity indices for each model parameter. The first-order indices (S_i) measure the individual contributions of each input to the variance of the model output, while the total-effect indices (S_{Ti}) represent the total contribution of the input, including its first-order effect and all higher-order interactions. The total-effect sensitivity indices can be used to identify unimportant model parameters. Non-influential parameters can be fixed at any value within their range of variability without significantly affecting the model response. In Sobol's sensitivity analysis technique, the model parameters that have total-effect sensitivity indices below 0.01 are often considered non-influential [33, 34] (see Supplementary Information in Section 4.6 for further details).

4.3. Results

It is believed that brain sodium homeostasis is highly regulated by the BCSFB and the BBB. Elevated levels of sodium in the CSF and brain tissue of migraine sufferers can be due to variations in the influx and/or efflux permeability coefficients of the BCSFB and/or

the BBB to sodium. Heuristically, one may expect that the elevated CSF sodium concentration is due to increased transport of sodium from blood into CSF and/or decreased uptake of sodium from CSF into blood. Figure 2 shows the variations in brain tissue, ventricular and subarachnoid CSF sodium concentrations within 2 hours after either a 20% increase in the influx permeability coefficient of the BCSFB to sodium (P_{BCSFB}), or a 20% decrease in the efflux permeability coefficient of the BCSFB to sodium (P'_{BCSFB}).

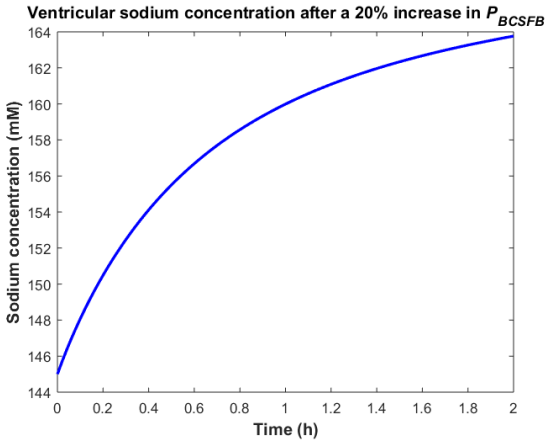

(a)

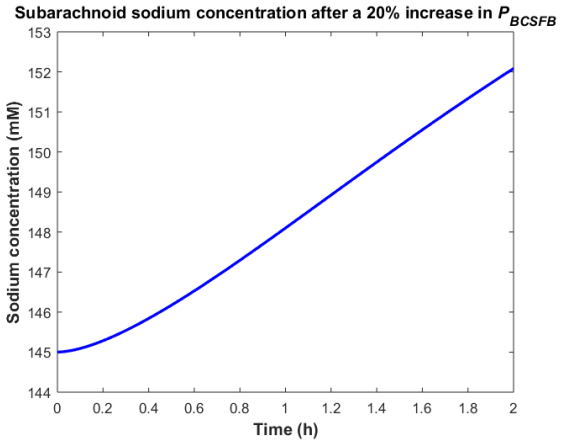

(b)

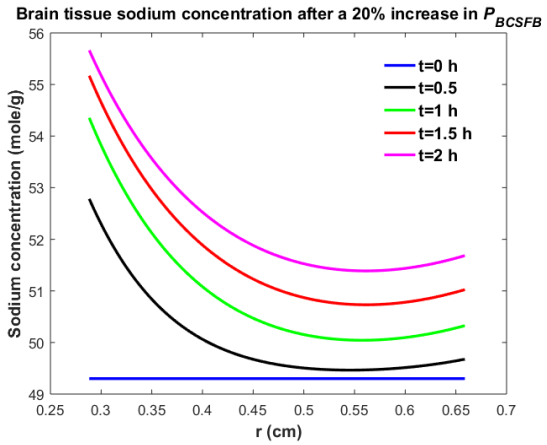

(c)

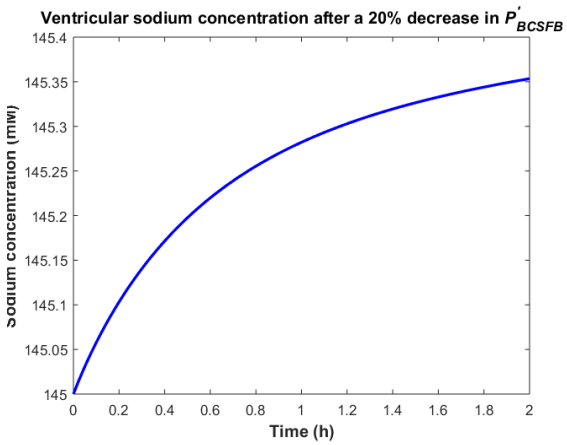

(d)

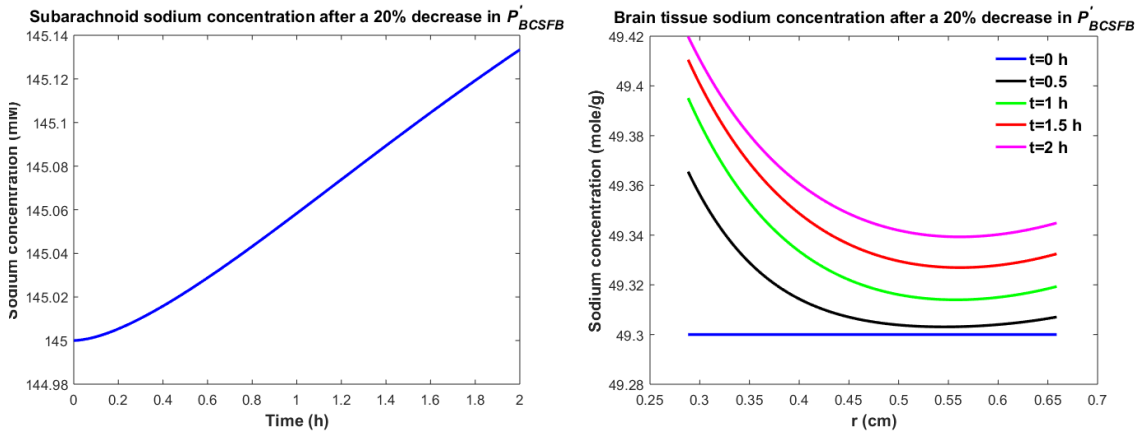

(e) (f)

Figure 2. Variations of (a) C_v after increasing P_{BCSFB} by 20%, (b) C_s after increasing P_{BCSFB} by 20%, (c) C_{br} after increasing P_{BCSFB} by 20%, (d) C_v after decreasing P'_{BCSFB} by 20%, (e) C_s after decreasing P'_{BCSFB} by 20% (f) C_{br} after decreasing P'_{BCSFB} by 20%.

Ventricular CSF sodium concentration increases after a 20% rise in P_{BCSFB} or a 20% decrease in P'_{BCSFB} (Figs. 2a and 2d). We assumed that sodium exchange between blood and CSF does not change blood concentration of sodium significantly, due to the large volume of blood compared to CSF. Thus, C_{blood} remains unchanged after changing the influx or efflux permeability coefficients of BCSFB to sodium. Figures 2c and 2f show that the elevated levels of sodium in the ventricular CSF lead to diffusion of sodium from CSF to brain tissue and distribution of sodium into the brain tissue over time [11, 35]. Sodium moves by bulk flow of CSF from the ventricular system to the subarachnoid space, where it can be exchanged between CSF and brain tissue. Subarachnoid CSF sodium concentration increases after increasing P_{BCSFB} or decreasing P'_{BCSFB} by 20% (Figs. 2b and 2e). Our results indicate that ventricular CSF and subarachnoid CSF sodium concentration values at any given time point are more sensitive to variations of P_{BCSFB} than of P'_{BCSFB}.. Similarly, brain

tissue sodium concentration values at any given time point and spatial location are more sensitive to changes of P_{cp} than of P'_{cp}. These behaviors can be explained by the observation that steady state loss of ventricular CSF sodium is largely due to bulk flow of CSF from the ventricular system into the subarachnoid space rather than to sodium uptake by blood across the BCSFB (Eq. 1 and physiological data in Table 1). However, the only source for sodium in the ventricular system is the choroid plexus epithelial cells, a.k.a BCSFB cells, at steady state. Thus, a 20% decrease in P'_{BCSFB} has a less significant impact than a 20% increase in P_{BCSFB} on CSF sodium content. It should be noted that we assume that there is no sodium exchange between the ventricular CSF and brain tissue at steady state (t=0).

Similarly, one may expect that the elevated brain tissue sodium levels during migraine are due to increased sodium transport from blood to brain tissue and/or reduced sodium uptake from brain tissue into blood. Figure 3 depicts the changes in ventricular CSF, subarachnoid CSF and brain tissue sodium levels within 2 hours of either increasing the influx permeability coefficient of the BBB to sodium (P_{BBB}) by 20%, or decreasing the efflux permeability coefficient of the BBB to sodium (P'_{BBB}) by 20%.

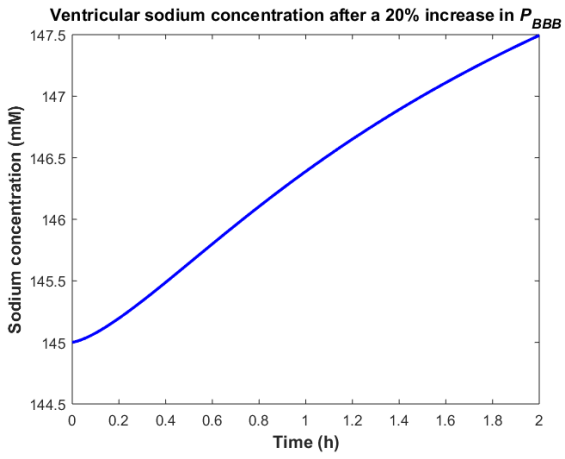

(a)

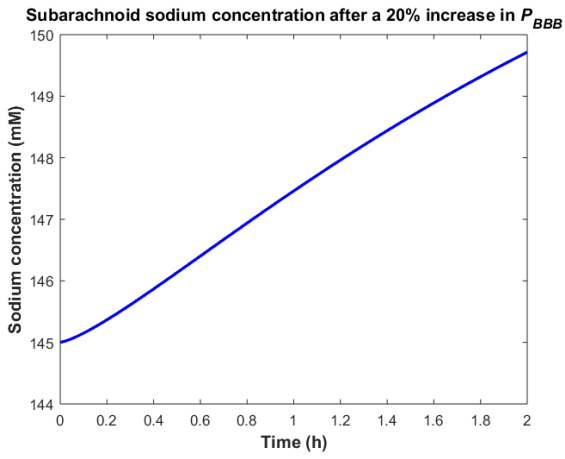

(b)

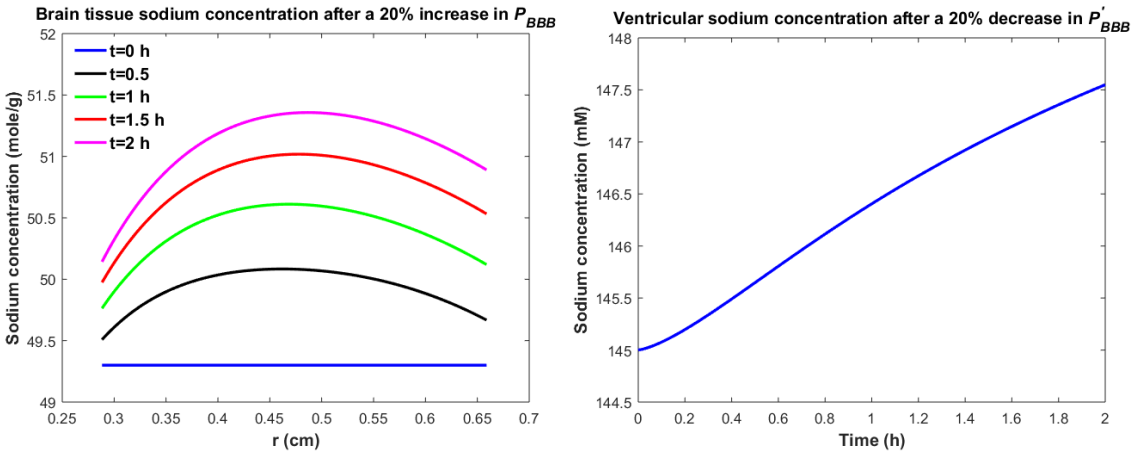

(c)

(d)

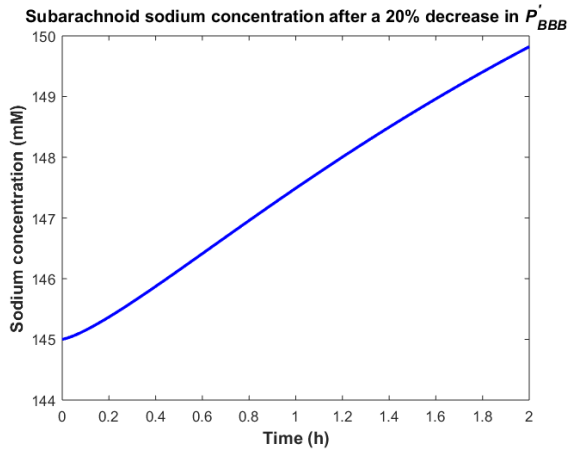

(e)

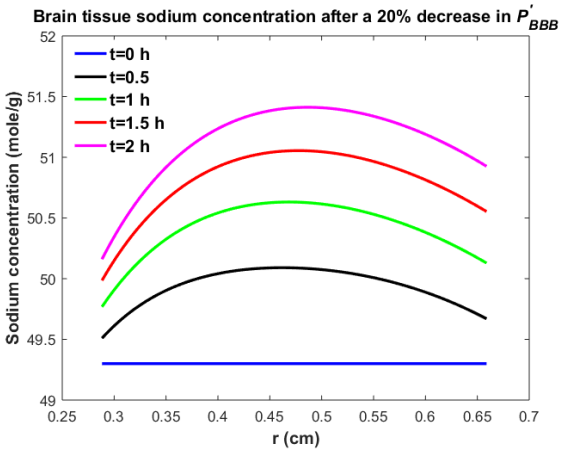

(f)

Figure 3. Variations of (a) C_v after increasing P_{BBB} by 20%, (b) C_s after increasing P_{BBB} by 20%, (c) C_{br} after increasing P_{BBB} by 20%, (d) C_v after decreasing P'_{BBB} by 20%, (e) C_s after decreasing P'_{BBB} by 20% (f) C_{br} after decreasing P'_{BBB} by 20%

A 20% increase in P_{BBB} or a 20% decrease in P'_{BBB} results in an accumulation of sodium in the brain tissue (Figs. 3c and 3f). The elevated levels of sodium in the brain tissue increase sodium transport from brain tissue to the ventricular system and subarachnoid space (Figs. 3a, 3b, 3d and 3e). Our results indicate that brain tissue, ventricular CSF and subarachnoid CSF sodium levels are almost equally sensitive to variations in P_{BBB} and P'_{BBB}.

Figure 4 shows the sodium flux between the brain tissue and CSF at the interface of brain tissue and the ventricular system, and at the contact surface of brain tissue and the subarachnoid space, after perturbation of P_{BCSFB}, P_{BBB}, P'_{BCSFB} or P'_{BBB} by 20%. Our results indicate that sodium flux from the ventricular system to the brain tissue is larger than sodium flux from the subarachnoid space to the brain tissue.

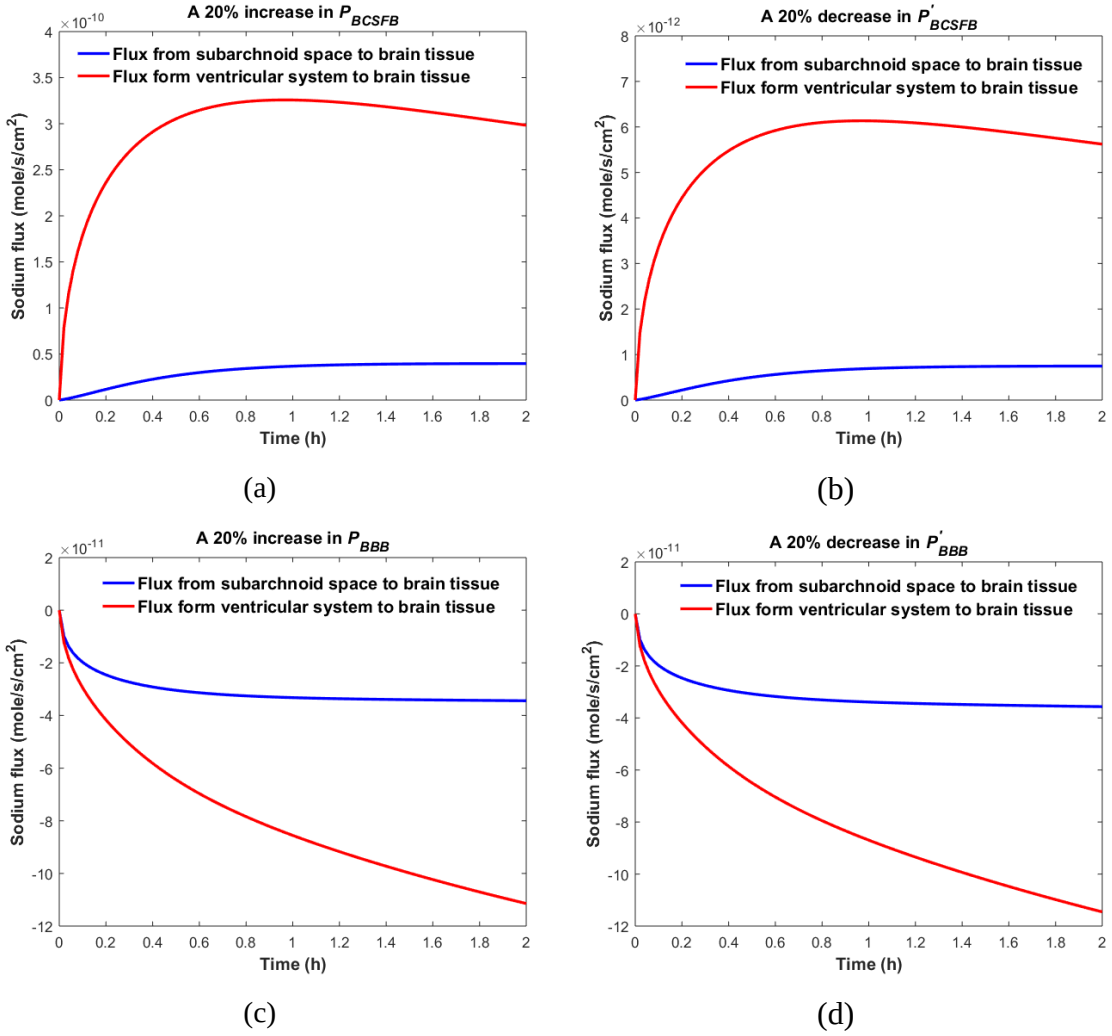

Figure 4. Comparison of sodium flux at the interface of the brain tissue and the ventricular system with sodium flux at the interface of the brain tissue and the subarachnoid space after (a) increasing P_{BCSFB}, (b) decreasing P'_{BCSFB}, (c) increasing P_{BBB} (d) decreasing P'_{BBB} by 20%. The positive sign of the flux indicates that sodium is diffusing from the CSF to the brain tissue, while the negative sign indicates that sodium is diffusing from the brain tissue to the CSF.

Figure 2 and Figure 3 compare the variations in C_v, C_s, and C_{br} when a single parameter (i.e. P_{BCSFB}, P_{BBB}, P'_{BCSFB} or P'_{BBB}) is perturbed and the rest of the parameters remain unchanged. However, in the case of migraines, all influx and efflux permeability coefficients can potentially vary. Additionally, Table 1 shows the average values of the physiological model's parameters. These values can change across a population of rats of the same type. Thus, we used GSA [23] to consider the effects of variations in all model parameters. In this regard, we assumed that physiological concentration of sodium in CSF and blood can vary within 5% of the *in vitro* values (i.e. $C_v = C_s = 145$ mM, $C_{blood} = 140$ mM), while the remaining independent model parameters (P_{BCSFB}, A_{BCSFB}, V_s, V_v, V_b, P_{BBB}, A_{BBB}, f_d, D, Q_{csf}, λ, ρ) can vary within 25% of the *in vitro* values (Table 1). This is due to considering the impacts of intrinsic variations between a population of rats of the same type, and the effects of measurement errors in the estimations of physiological model parameters on our simulations. Following a uniform distribution, we sampled 10^5 sets of parameters within their ranges of variability. We then calculated the dependent parameters, i.e. P'_{BCSFB} and P'_{BBB} for each set of parameters, assuming that the model is at steady state at t=0. Each of these 10^5 sets of parameters characterizes one healthy rat with different physiological parameters. We then assumed that P_{BCSFB}, P_{BBB}, P'_{BCSFB}, and P'_{BBB} can undergo pathophysiological changes within 50% of their control values due to migraine triggers. We performed a GSA to investigate the significance of pathophysiological variations of P_{BCSFB}, P_{BBB}, P'_{BCSFB}, and P'_{BBB} in influencing ventricular sodium concentration during episodic migraines. The model output was defined as the percent

change of total ventricular sodium concentration within 2 hours after perturbations of physiological P_{BCSFB}, P_{BBB}, P'_{BCSFB}, and P'_{BBB}:

Model Output= $\frac{(\frac{\int_0^{tmax} C_v\, dt}{t_{max}}) - C_v(t=0)}{C_v(t=0)}$.

Our results indicate that pathophysiological variation of P_{BCSFB} is much more important than that of P_{BBB}, P'_{BCSFB}, and P'_{BBB} in influencing ventricular CSF sodium concentration (Fig. 5). It is important to note that each permeability coefficient is defined at two states: physiological and pathophysiological. A given permeability coefficient (e.g. P_{BCSFB}) in the physiological and pathophysiological state is shown by $P_{BCSFB}(\,physiological)$ and $P_{BCSFB}(\,pathophysiological)$, respectively. Variations in $P_{BCSFB}(physiological\,)$ account for intrinsic variations between a population of rats of the same type and/or measurement errors in the estimations of the permeability coefficients. However, migraine triggers can cause a disturbance in sodium transport mechanisms at the BCSFB and/or BBB [36, 37]. This implies that migraine triggers can change physiological permeability coefficients. $P_{BCSFB}(pathophysiological)$ represents the extent of variations in $P_{BCSFB}(physiological)$ due to migraine triggers. For a given rat with a given $P_{BCSFB}(physiological)$, different migraine triggers can change $P_{BCSFB}(physiological)$ differently; these changes are represented by $P_{BCSFB}(pathophysiological)$. Our results indicate that variations of $P_{BCSFB}(physiological)$ and $P_{BBB}(physiological)$ are much less important than those of $P_{BCSFB}(pathophysiological)$ and $P_{BBB}(pathophysiological)$ in influencing the percent change of total ventricular sodium concentration during migraines. This is mainly because the model output was defined as the percent change of total ventricular CSF sodium concentration between the pathophysiological and physiological

states. These results suggest that the ventricular CSF sodium concentration is more sensitive to an alteration in homeostasis of the transporters which mediate sodium influx into CSF across the BCSFB than to a variation in homeostasis of the transporters which regulate sodium uptake from the CSF across the BCSFB. In addition, these results indicate that the BBB plays a much less important role than the BCSFB in regulation of the ventricular CSF sodium concentration. It is important to note that total-effect sensitivity indices, which account for total contribution of the inputs to variations in the model response, should be used to compare the significance of the model inputs in controlling the model output. P_{BCSFB} has a larger S_{Ti} than P_{BBB}, P'_{BCSFB}, and P'_{BBB}, which indicates that P_{BCSFB} is a more influential parameter in the model.

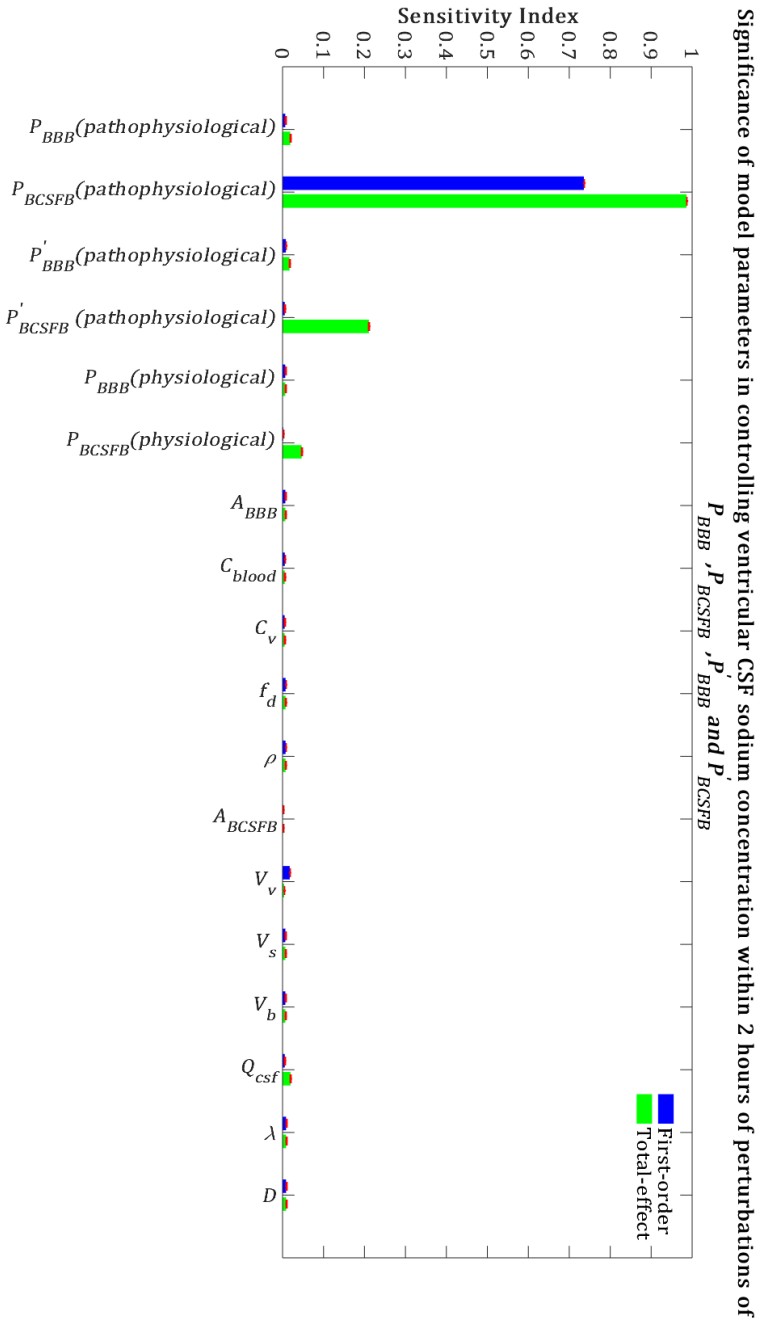

Figure 5. Sensitivity ranking of the model parameters. The model output was set to the time integral of C_v within 2 hours after perturbation of the model's parameters. The blue bars represent first-order sensitivity indices, while the green bars show the total-effect sensitivity indices. The error bars, shown in red, indicate the bootstrap confidence intervals (95% confidence intervals) of the mean values.

Total-effect sensitivity indices of some of the parameters are smaller than 0.01 (Fig. 5). This means that the variations of these parameters do not influence the variance of the model output significantly; thus these parameters can be fixed at arbitrary values within their ranges [33, 34]. Figure 6 demonstrates the rank order of the model parameters when the model output was defined as the percent change of total subarachnoid sodium concentration within 2 hours after perturbations of physiological P_{BCSFB}, P_{BBB}, P'_{BCSFB}, and P'_{BBB} due to migraine triggers:

Model Output= $\frac{(\frac{\int_0^{tmax} C_S\, dt}{t_{max}}) - C_S(t=0)}{C_S(t=0)}$.

Our results indicate that subarachnoid CSF sodium concentration is highly sensitive to pathophysiological changes in P_{BCSFB}, P_{BBB} and P'_{BBB} (Fig.6). The fact that pathophysiological variations of P_{BBB} and P'_{BBB} are more important in influencing subarachnoid sodium concentration than ventricular sodium concentration (Figs. 5-6) is because variations in P_{BBB} and P'_{BBB} not only can affect sodium exchange at the contact surface of subarachnoid CSF and brain tissue, but also can influence sodium exchange between the ventricular system and brain tissue, thus affecting the amount of sodium entering the subarachnoid space from the ventricular system.

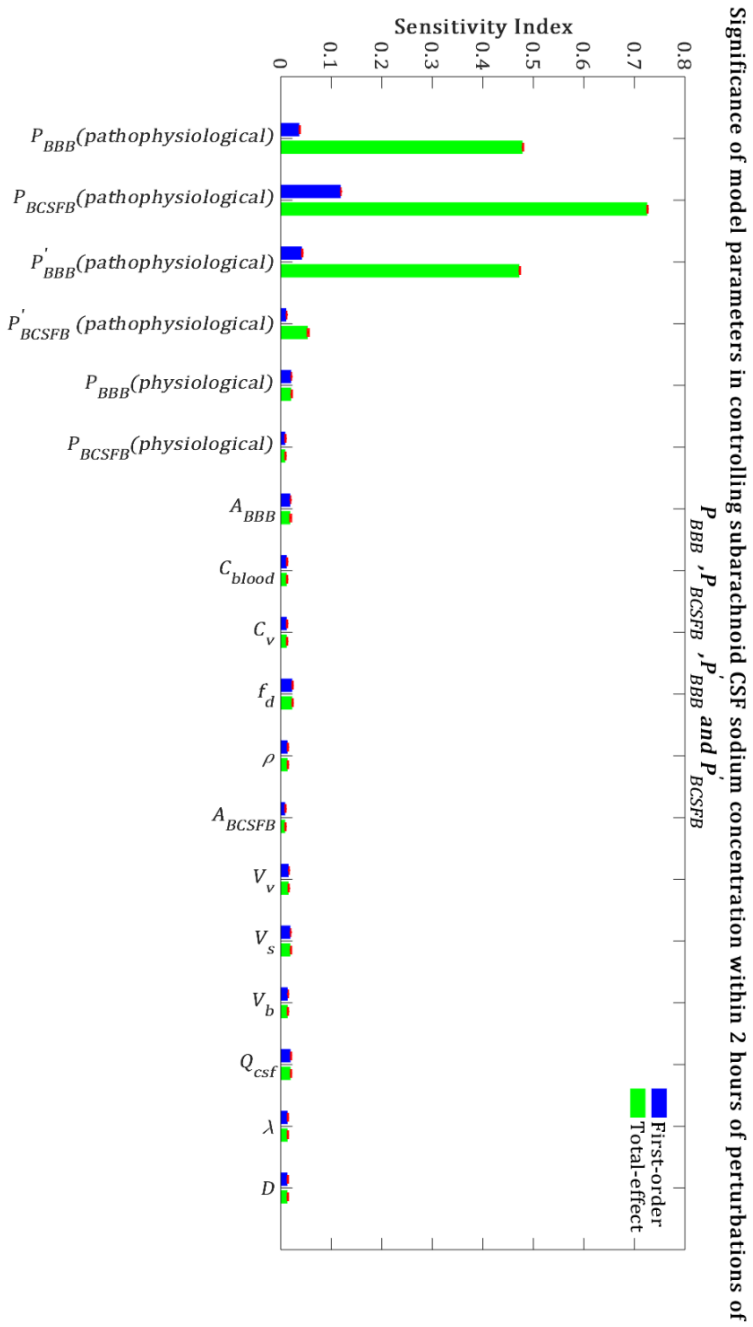

Figure 6. Relative significance of the model parameters in controlling subarachnoid CSF sodium concentration (C_s) within 2 hours of the perturbation onset ($t_{max} = 2$ h). The blue bars represent first-order sensitivity indices, while the green bars show the total-effect sensitivity indices. The error bars, shown in red, indicate the bootstrap confidence intervals (95% confidence intervals) of the mean values.

We also performed a GSA to identify the influential parameters when the model output was the percent change in total level of brain sodium after 2 hours of perturbations of the physiological P_{BCSFB}, P_{BBB}, P'_{BCSFB}, and P'_{BBB} due to migraine triggers:

$$\text{Model Output} = \frac{\left(\int_{r_i}^{r_o} C_{br}\, 4\pi r^2 dr\right) - C_{br}(t=0) \times (total\ volume\ of\ brain\ tissue)}{C_{br}(t=0) \times (total\ volume\ of\ brain\ tissue)}, \qquad t = 2\ \text{hr}.$$

Our results demonstrate that brain tissue sodium level is highly sensitive to pathophysiological variations in P_{BCSFB}, P_{BBB}, P'_{BBB} and P'_{BCSFB} in order of decreasing sensitivity (Fig. 7). This result implies that sodium exchange between CSF and brain tissue at the contact surface of the ventricular system and brain tissue, as well as at the contact surface of the subarachnoid space and brain tissue can significantly influence brain sodium levels during migraine.

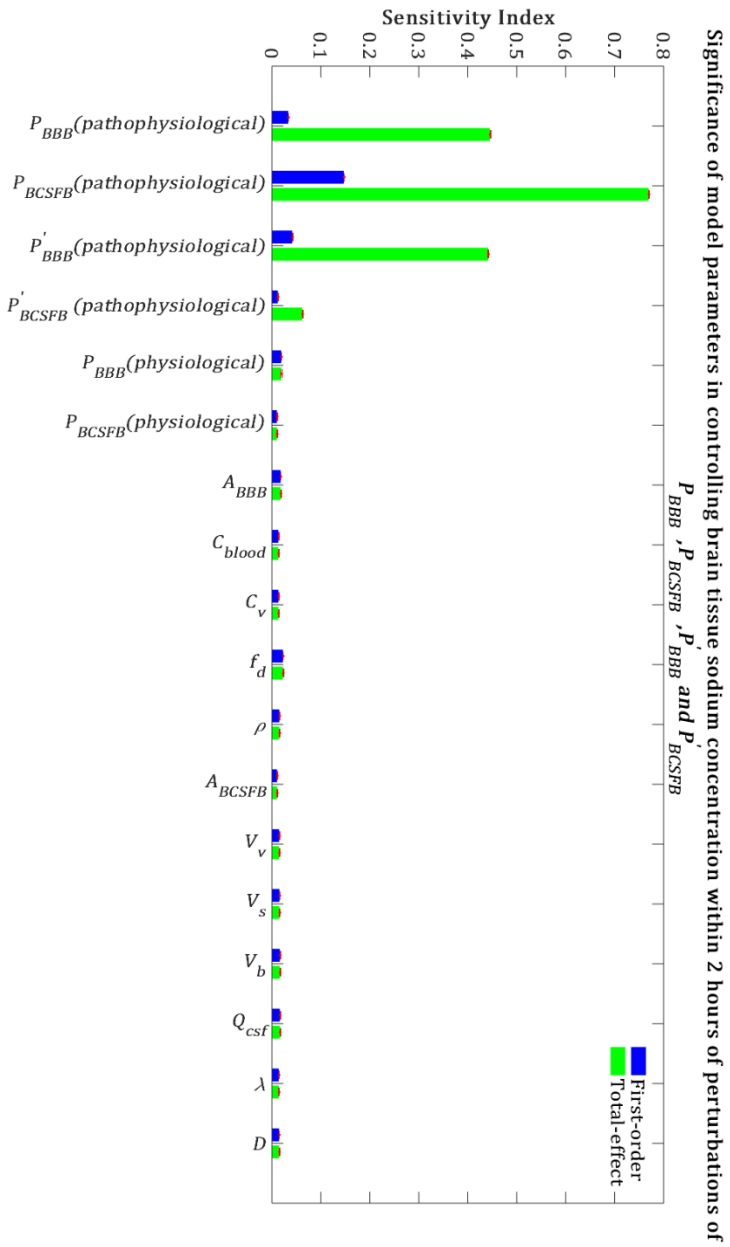

Figure 7. Relative importance of the model parameters in controlling brain tissue sodium levels within 2 hours of the perturbation onset ($t_{max} = 2$ h). The blue bars represent first-order sensitivity indices, while the green bars show the total-effect sensitivity indices. The error bars, shown in red, indicate the bootstrap confidence intervals (95% confidence intervals) of the mean values.

The above results were obtained after perturbing P_{BCSFB}, P_{BBB}, P'_{BCSFB}, and P'_{BBB} at t=0 and keeping them unchanged during the experiment time, i.e. t= 2 h. In order to investigate the impact of total experiment time on our results, we repeated our numerical experiments using different total experiment times including t= 1min, t= 5 min, t= 10 min, t= 30 min, t= 1 h and t=3 h. Our results show that brain tissue, ventricular CSF and subarachnoid CSF sodium levels are mainly sensitive to pathophysiological variations in P_{BCSFB}, P_{BBB}, P'_{BBB} and P'_{BCSFB} (See Supplementary Information in Section 4.6: Figures S1-S18). The significance of pathophysiological changes of P_{BCSFB}, P_{BBB}, P'_{BBB} and P'_{BCSFB} in influencing the ventricular CSF, subarachnoid CSF and brain tissue sodium levels at different total experiment times is shown in Table 2.

Table 2. Total-effect sensitivity indices of the permeability coefficients at different total experiment times

t_{max} / Parameter	Model output: ventricular CSF sodium						Model output: brain tissue sodium						Model output: subarachnoid CSF sodium					
	1 min	5 min	10 min	30 min	1 h	2 h	3 h	1 min	5 min	10 min	30 min	1 h	2 h	3 h	1 min	5 min	10 min	30 min	1 h	2h	3 h
P_{BBB}	0.01	0.01	0	0	0.04	0.02	0.03	0.78	0.77	0.73	0.58	0.51	0.45	0.45	0.75	0.73	0.69	0.58	0.54	0.48	0.47
P_{BCSFB}	0.93	0.95	0.95	0.97	0.97	0.98	0.99	0	0.13	0.23	0.48	0.67	0.77	0.82	0.01	0.18	0.29	0.48	0.62	0.73	0.79
P'_{BBB}	0	0.01	0	0	0.05	0.01	0.03	0.78	0.77	0.73	0.58	0.49	0.44	0.46	0.75	0.73	0.69	0.58	0.53	0.47	0.48
P'_{BCSFB}	0.2	0.21	0.2	0.2	0.2	0.21	0.2	0	0.01	0	0.02	0.03	0.06	0.1	0.01	0.01	0.01	0.01	0.03	0.05	0.09

Our results demonstrate that the ventricular CSF sodium concentration is highly sensitive to pathophysiological variations in P_{BCSFB}, independent of experiment duration time. However, brain tissue and subarachnoid CSF sodium levels are more sensitive to pathophysiological variations of P_{BBB} and P'_{BBB} than pathophysiological variations of P_{BCSFB} at short total experiment times (such as 1, 5, 10 and 30 minutes). Pathophysiological variations of P_{BCSFB} become more important than variations of P_{BBB} and P'_{BBB} in controlling brain tissue and subarachnoid CSF sodium concentrations at longer experiment times (such as 1, 2 and 3 hours). This implies that the BCSFB becomes more important in controlling brain tissue sodium homeostasis as time passes. This change in the significance of BCSFB and BBB in the regulation of brain tissue and subarachnoid CSF sodium levels over time is mainly due to the model structure, physiological model parameters and the model output expression. For instance, increasing brain tissue volume by two-fold (which is not realistic) makes the BBB permeability coefficients (P_{BBB} and P'_{BBB}) the most sensitive parameters in controlling brain tissue and subarachnoid CSF sodium levels, independent of the duration of the experiment (data not shown). This trend is due also in part to the fact that the ventricular CSF, whose sodium content is largely regulated by the BCSFB, would have enough time to influence sodium levels of its downstream compartments, including the brain tissue and the subarachnoid space.

To investigate the dynamics of sodium exchange between the CSF and brain tissue at the interface of brain tissue and the ventricular system, and at the contact surface of brain tissue and subarachnoid space during an episode of migraine, we randomly sampled 10^5 sets of parameters, following a uniform distribution over a 18-dimensional parameter space and compared the average absolute sodium flux (q_v) between brain tissue and ventricular CSF,

with the average absolute sodium flux (q_s) between the brain tissue and subarachnoid CSF. The average absolute fluxes q_v and q_s are defined by

$$q_v = \frac{\int_0^{t_{max}} \left| P_{vb}\lambda(C_v - \frac{C_{br}(t,r_i)}{V_{br}}) \right| dt}{t_{max}} \tag{13}$$

$$q_s = \frac{\int_0^{t_{max}} \left| P_{sb}\lambda(C_s - \frac{C_{br}(t,r_o)}{V_{br}}) \right| dt}{t_{max}} \quad , \tag{14}$$

where $t_{max} = 2$ h. Figure 8 shows the ratio of q_v to q_s for the 10^5 randomly sampled parameters. Our results indicate that the ratio of q_v to q_s is greater than 1 for the majority of the samples, which indicates that the absolute sodium flux at the interface of the ventricular system and the brain tissue is greater than the absolute sodium flux at the contact surface of the subarachnoid space and the brain tissue. Similar results were obtained for other total experiment times including $t_{max} = 10$ min, 30 min, 1 h (data not shown).

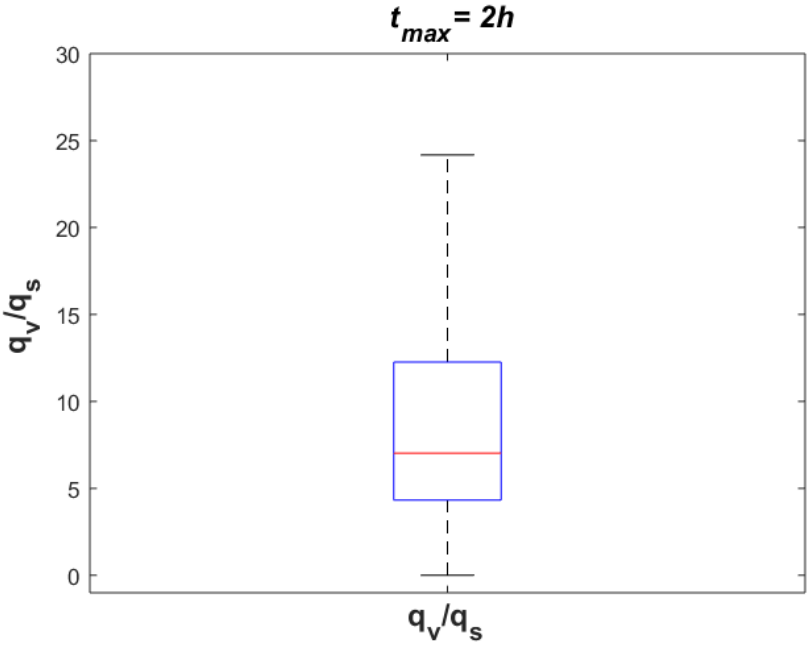

Figure 8. The ratio of absolute sodium flux at the interface of the ventricular system and the brain tissue (q_v) to absolute sodium flux at the interface of the subarachnoid space and the brain

tissue (q_s). 10^5 points were sampled randomly following a uniform distribution to generate this Figure.

4.4. Discussion

Previous studies [2-5] have indicated that migraine sufferers have higher levels of CSF and brain tissue sodium than the control group. However, blood levels of sodium remain unchanged during migraine [2]. Under the hypothesis that these elevated sodium levels are due to variations in the influx and/or efflux permeability of the BCSFB and/or the BBB to sodium, we investigated the significance of variations in the influx and efflux permeabilities of the BCSFB and the BBB to sodium in influencing CSF and brain tissue sodium levels. In this regard, first we developed a computational model for sodium exchange between different brain compartments, i.e. blood, brain tissue, ventricular and subarachnoid CSF. The model presented in this paper is similar in some respects to that of Smith and Rapoport [11]. However, there are two major differences between our model and theirs. First, our model includes the ventricular system and subarachnoid space as separate compartments. Thus, our model can distinguish between the ventricular and subarachnoid CSF, as well as provide insight into the dynamics of sodium exchange between the CSF and brain tissue at the interface of brain tissue and the ventricular system, and at the contact surface of brain tissue and the subarachnoid space. Second, we have proposed a more realistic model of brain tissue compared to previous studies [11, 38, 39]. Unlike previous studies that modeled brain tissue as a rectangular sheet bathed on two opposite sides by CSF, we modeled brain tissue as the area between two concentric spheres. Concentric spheres are more similar to the real shape of a rat brain, which resembles an ellipsoid. As a result, the contact surface

area of the brain tissue and the subarachnoid space is larger than that of the brain tissue and the ventricular system in our model. Thus, sodium exchange between the CSF and brain tissue at the two contact surfaces, as well as sodium diffusion in the brain tissue have been modeled more accurately in this work than in previous studies.

We performed a global sensitivity analysis to compare the significance of the BCSFB and the BBB in controlling CSF and brain sodium levels. Our results indicate that pathophysiological variations of the BCSFB influx permeability coefficient to sodium (P_{BCSFB}) are more important than variations of the BCSFB efflux permeability coefficient (P'_{BCSFB}), the BBB influx permeability coefficient (P_{BBB}) and the BBB efflux permeability coefficient (P'_{BBB}) to sodium in controlling ventricular CSF sodium concentrations. Brain tissue and subarachnoid CSF sodium levels are more sensitive to pathophysiological variations of P_{BBB} and P'_{BBB} than to variations of P_{BCSFB} when total experiment time is 1, 5, 10 and 30 minutes, while P_{BCSFB} becomes more important that P_{BBB} and P'_{BBB} in influencing brain tissue and subarachnoid CSF sodium levels when total experiment time is 1, 2 and 3 h. Overall, our results show that P_{BCSFB} plays an important role in the regulation of brain sodium homeostasis. P_{BCSFB} represents the net movement of sodium from blood to CSF, which is regulated by a variety of BCSFB sodium transporters such as Na^+, K^+-ATPase [40-43], ENaC [40, 44] and NKCC1 [45]. Thus, variations in P_{BCSFB} can be attributed to hyperactivity and/or hypoactivity of one or more of these sodium transporters. Our theoretical mechanism implies that the disturbed sodium homeostasis in the brain during a migraine is most likely due to overactivity of Na^+, K^+-ATPases at the BCSFB and the BBB [36]. Na^+, K^+-ATPase is a highly-conserved membrane protein which is expressed in all cells. One Na^+, K^+-ATPase mediates active transport of three sodium ions out of the

cell for every two potassium ions entering the cell against the concentration gradients. We believe that disturbed homeostasis of Na^+, K^+-ATPase plays a key role in the pathophysiology of migraine [37], as many regulators of Na^+, K^+-ATPase such as estrogen, adrenaline, insulin [46, 47], dopamine [48, 49], glutamate [50], etc are involved in the pathophysiology of migraine (See [36] for a comprehensive review). Furthermore, there are several lines of evidence supporting that CSF secretion as well as sodium transport from the BCSFB cells, a.k.a choroid plexus epithelial cells, to CSF is mostly mediated by Na^+, K^+-ATPases, which are expressed on the CSF-facing (apical) membrane of the BCSFB cells [42, 51, 52]. It has been shown that intracerebroventricular infusion of ouabain, an Na^+, K^+-ATPase inhibitor, at 10 $\mu g/day$ decreases CSF sodium concentration by almost 8 mM in Wister rats on a high-salt diet [41]. Ouabain can also reduce sodium transport from blood to CSF by 34% and 60% in frogs and rabbits, respectively [42, 43]. Thus, not only can the altered homeostasis of BCSFB Na^+, K^+-ATPases be a potential cause of the elevated CSF sodium concentration in a migraine, but also BCSFB Na^+, K^+-ATPase could be a candidate drug target to correct the elevated levels of sodium in CSF of migraine sufferers, potentially treating migraine. This hypothesis needs to be tested experimentally for different migraine triggers. ENaC is another sodium transporter which can play a key role in the regulation of CSF sodium levels. ENaC mediates passive sodium transport along a concentration gradient across the BCSFB. In Wister rats, ENaC is expressed at both membranes of BCSFB cells with a higher density at the CSF-facing (apical) membrane compared to the blood-facing (basolateral) membrane [53, 54]. This suggests that ENaC may play a major role in sodium uptake from CSF into BCSFB cells [55]. It should be noted that sodium movement through ENaC is likely to be unidirectional; thus, variations in the activity levels of ENaC at the

apical membrane of BCSFB cells can potentially change P'_{BCSFB}, while variations in ENaC activity levels at the basolateral membrane of BCSFB cells can possibly change P_{BCSFB}. It is not known how the expression levels of ENaC on the different membranes of BCSFB cells are affected by migraine triggers. The other main BCSFB sodium transporter is NKCC1, which can regulate CSF production [56] and sodium movement from blood to CSF [45]. Overall, sodium transport from blood to CSF across the BCSFB is regulated by a variety of transporters, channels and proteins, whose interactions with each other are not well understood. Further experimental studies are needed to elucidate the potential effects of various migraine triggers on the activity and expression levels of BCSFB Na^+, K^+-ATPase, ENaC and NKCC1.

Our results suggest that the BBB can play a more important role than the BCSFB in the regulation of brain tissue and subarachnoid CSF sodium concentrations within 30 minutes of pathophysiological perturbations of P_{BCSFB}, P_{BBB}, P'_{BBB} and P'_{BCSFB}. P_{BBB} and P'_{BBB} were used in the current model to simulate the net movement of sodium from blood to brain tissue, and from brain tissue to blood, respectively. Variations in P_{BBB} and P'_{BBB} can be attributed to altered homeostasis of the transporters, which mediate sodium movement across the BBB. The principal routes for sodium entry across the luminal membrane of the BBB endothelial cells are likely to be NKCC1 [57, 58] and NHE1,2 [59], while sodium is mainly pumped out of the BBB endothelial cells into brain ISF by Na^+, K^+-ATPase [8, 60, 61]. It has been suggested that sodium transport from the brain ISF into the BBB endothelial cells is mainly mediated by sodium-linked transporters of organic solutes, including those for amino acids [8]. NHE 1,2 can also potentially contribute to sodium entry across the ISF-facing (abluminal) membrane of endothelial cells. However, the impacts of migraine

triggers on the activity and expression levels of these sodium transporters are yet to be understood. Our results suggest that alterations of BBB sodium transporters homeostasis have more significant effects than variations of BCSFB sodium transporters homeostasis on brain tissue sodium levels within 30 minutes of the perturbation onset. It should be noted that our results were obtained using GSA, which gives us some insight into the importance of influx and efflux permeability of the BCSFB and the BBB to sodium in controlling CSF and brain tissue sodium by covering the entire parameter space, where all model parameters can vary within the specified ranges. Thus, in a rat model, the intrinsic variations between a population of rats of the same type were considered in this work.

This study has some limitations. First, for simplicity, we modeled the rat brain with three spheres. However, the real geometry of a rat brain is more complicated. A more realistic model of the brain and ventricles can provide a better understanding of the phenomenon under study. Second, we modeled the CSF with two well-mixed compartments, i.e. the ventricular system and the subarachnoid space. However, CSF flows through the lateral ventricles, the third ventricle, the cerebral aqueduct, the fourth ventricle, the cisterns and the subarachnoid space. Sodium concentration can vary slightly to significantly from one ventricle to another one and to the subarachnoid space. Thus, the current model can be improved to include all of the ventricles and subarachnoid space as separate compartments. CSF flow can be modeled using various numerical methods [62-65]. However, further information regarding the dynamics of sodium transport between different ventricles and adjacent brain tissues is needed. Furthermore, we assumed that there is no rate-limiting diffusion between the CSF and brain tissue at the two contact surfaces of the CSF and brain tissue. This results in instantaneous equilibrium between CSF

sodium concentration and brain ISF sodium concentration at the contact surface of brain tissue and CSF [11]. This assumption may not be true for some ependymal regions such as those in the third ventricle as it has been shown that benzamil, an ENaC blocker can prevent sodium movement from the third ventricle CSF into brain tissue across the ependyma [55]. Third, for simplicity we assumed that the value of the sodium distribution factor (f_d) remains constant after perturbations of the BCSFB and the BBB permeability coefficients to sodium. Thus, we estimated the ISF sodium concentration by $\frac{C_{br}}{f_d}$ (Eq. 4). This assumption implies that the ratio of extracellular sodium concentration to intracellular sodium concentration remains unchanged at any time after perturbations of the permeability coefficients. In other words, sodium is always distributed between the ISF and the brain cells in the ratio of their physiological sodium contents. Previous studies made a somewhat similar assumption to estimate the ISF sodium concentration from brain tissue sodium levels, using the cerebral distribution volume of sodium [11]. The physiological value of f_d was found to be 0.34 ml/g using the average physiological ISF sodium concentration of 145 mM [16] and the average brain tissue sodium concentration of 50 mM (=50×10^{-6} mol/g) [66]. The obtained value of 0.34 ml/g for f_d in this work is the same as the value of the cerebral distribution volume of sodium [11]. The dynamics of sodium exchange between the brain cells and the ISF can be better understood by adding the brain cells as a new compartment to the current model. Our model can be expanded to include brain cells once more information becomes available regarding the permeability coefficients of different types of brain cell to sodium. One approach to modeling of dynamic sodium exchange between the brain cells and the ISF is to use neuron models which are based on Hodgkin-Huxley type dynamics and extended to include time-dependent intracellular and

extracellular sodium concentration [67-69]. These dynamic models include differential equations for concentration of sodium, potassium and chloride. However, coupling these models with the current model may require modeling of further mechanisms that regulate potassium and chloride in the CSF and ISF. Fourth, we perturbed P_{BCSFB}, P_{BBB}, P'_{BCSFB}, and P'_{BBB} at t=0 and kept them unchanged during the experiment time. However, in reality the BCSFB and the BBB permeability coefficients likely change over time. Thus, the model presented in this study can be used to study the contribution of the BCSFB and the BBB to variations in the brain tissue and CSF sodium concentrations once there is more information about time-dependent variations of the BBB and BCSFB permeabilities to sodium during an episode of migraine with a particular trigger. Fifth, we assumed that diffusion is the major mechanism of sodium movement in the brain tissue. Although there are several lines of evidence supporting the existence of a convective transport mechanism called the glymphatic system in the brain [9, 10], several aspects of glymphatic circulation, including whether interstitial transport is propagated by convective flow or diffusion [70, 71], the identity of the ISF bulk flow driving forces [72, 73], and the role of astrocyte water permeability/aquaporin4 [71] are still controversial. Furthermore, it is not well understood how the proposed transport mechanisms are affected during migraine and how these mechanisms interact with the BBB to regulate ionic homeostasis in the brain. In this work, we ignored sodium transport between the CSF and brain ISF via convection, as it has been shown that diffusion (without convection) in the brain tissue is enough to account for many experimental transport studies in the brain parenchyma [71]. Intuitively, we think that adding the convective CSF transport from the subarachnoid space to the brain ISF, based on the proposed glymphatic circulation, will increase the effects of subarachnoid CSF (in

general CSF) on the brain tissue sodium levels, as the convective transport mechanism allows more sodium to be transported in a shorter amount of time compared to diffusive transport. Thus, the BCSFB would become more important in controlling brain tissue sodium levels. However, the exact extent of the contribution of the glymphatic system to the regulation of brain sodium homeostasis depends on not only the dynamical properties of the glymphatic system such as the rate of glymphatic flow, the glymphatic efflux pathways and the ISF bulk flow driving force, but also the dynamic interactions between the glymphatic flow, the BBB and brain diffusive transport mechanisms. The current model can be expanded to include the convective CSF flow from the subarachnoid space to brain ISF once more information regarding the contribution of the glymphatic flow to the regulation of brain sodium homeostasis becomes available. Finally, we ignored water fluxes between the model compartments. Thus, the volumes of the model compartments remain unchanged during the experiment time. This is because variations of the permeability coefficients within the specified ranges in this study result in gradual changes in the brain ISF sodium concentration, which suggests that the ISF osmolality changes gradually. The gradual variations in the ISF osmolality give the brain cells enough time to adjust to the changes in the extracellular space; so that they can minimize the variations in their volume through regulating the influx and efflux of osmotically active solutes between the intracellular and extracellular fluids. Previous in vitro studies showed that the cultured cerebellar neurons and C6 rat glioma cells can exhibit isovolumetric regulation when the extracellular osmolality changes at a rate less than or equal to 1.8 and 3 mOsmol/kg/min, respectively [74, 75]. The maximum possible rate of change of ISF sodium concentration in this work is 1.5 mM/min, equivalent to 1.5 mOsmol/kg/min. Thus, we believe that the

brain cells, which make up 80% of total volume of the brain can significantly maintain their volume under the assumptions/conditions in our numerical simulation. This argument is in agreement with another experimental observation which suggests that a 50% decrease in the activity levels of Na^+, K^+-ATPase on the brain microvessels does not change total water content in the brain significantly [76]. Assuming that the brain tissue volume remains almost unchanged in this work, one can conclude that the CSF volume remains almost constant, due to the rigid confines of the skull. We have also assumed that the CSF secretion rate remains unchanged after pathophysiological variations of the influx and/or efflux permeability coefficients of the BCSFB to sodium. Although it has been suggested that there is a positive correlation between the CSF secretion and sodium transport rates across the BCSFB [8], it is not known how and to what extent water movement is linked to sodium transport in the BCSFB during migraine. Migraine is accompanied with a complex chain of biochemical changes in the CSF and brain which may contribute, together with sodium, to regulation of water movement across the BCSFB. For instance, it has been shown that CSF (and plasma) content of organic osmolytes such as taurine and glutamate, which can significantly regulate brain cell volume homeostasis [77, 78], changes during migraine [79-82]. However, it is yet to be determined how the variations in organic osmolyte levels can influence the osmotically driven water transport across the BCSFB. Thus, future experimental studies are needed to explore whether/how/to what extent the water movement rate depends on the sodium transport rate during migraine. The results presented in this work may vary depending on how the CSF flow rate changes during migraine. The current model can be extended to include dynamic water movement across the BCSFB once further

information regarding the extent to which water movement is linked to sodium transport during migraine becomes available,

The fact that the CSF and brain tissue sodium levels are higher in migraine and in an analogue of migraine in a rat model than the control groups [2, 3] has relevance to the pain of migraine, since increasing extracellular sodium concentration immediately increases the firing rate of primary cultures of neurons [7]. We propose that the increasing sodium concentration mainly arises from the BCSFB in the cerebral ventricles due to overactivity of Na^+, K^+-ATPases. When the higher CSF sodium concentration emerges from the fourth ventricle via the foramina of Luschka and Magendie, it meets the unmyelinated trigeminal nerves and the trigeminal ganglions. Unlike the cranial nerves such as the facial nerve that are protected by their myelin, we predict that firing of the trigeminal nerve would increase in the presence of the elevated sodium concentration, with trigeminal pain as a consequence. Moreover, we also predict that this CSF efflux from the fourth ventricle may well be lateralized through one of the small foramina of Luschka, and hence would give rise to unilateral trigeminal stimulation. An alternative interpretation to the primary effect of CSF sodium in the initiation of migraine is that the sodium is a consequence of migraine. We consider this to be less likely, since we have recently demonstrated that specific inhibition of the BCSFB Na^+, K^+-ATPase protected the animal migraine model from nitroglycerin-triggered sensitization [37].

It is important to note that the altered Na^+, K^+-ATPase activity simultaneously shifts sodium and potassium. However, we have not modeled potassium since we originally found that sodium concentration changed in CSF, while potassium concentration did not change during migraines [2]. Furthermore, the potassium concentration in the ISF and CSF is

maintained lower than in the remainder of the body by active astrocyte reuptake and, if potassium is not kept down, neurons will undergo apoptosis [83]. The mechanisms that regulate extracellular potassium concentration are substantially independent from Na^+, K^+-ATPase-driven changes in sodium. The current model can be improved to include more mechanisms once more experimental data for multiple ion and water fluxes and their regulation in conjunction with sodium becomes available.

4.5. Conclusions

Our proposed mechanism for migraine suggests that a disturbance in brain sodium homeostasis causes migraine [36]. This sodium dysregulation is most likely due to variations in the influx and/or efflux permeability of the BCSFB and/or the BBB to sodium. The influx and efflux permeability of the BCSFB and the BBB to sodium represent the net effect of all transporters, channels and enzymes which contribute to movement of sodium across the interfaces. Thus, variations of the permeability coefficients can be caused by altered homeostasis of one or some of the sodium transport mechanisms at the interfaces. Unfortunately, understanding migraine pathophysiology is difficult, not only because the effects of various triggers on permeability of the BCSFB and the BBB to sodium are not known, but also because migraines have different triggers in different people. To approach this problem, we used mechanistic modeling together with global sensitivity analysis (GSA) to assess the relative importance of the BCSFB and the BBB in controlling CSF and brain tissue sodium levels. GSA provides insight into the significance of the BCSFB and the BBB in the regulation of brain sodium concentration when the exact extents of variations in the influx and efflux permeability coefficients of the BCSFB and the BBB to sodium are unknown. Our results show that the ventricular CSF sodium concentration is highly

influenced by pathophysiological variations in the influx permeability coefficient of the BCSFB to sodium. Brain tissue and subarachnoid CSF sodium levels are more sensitive to pathophysiological variations in the BBB permeability coefficients than the BCSFB permeability coefficients to sodium at shorter total experiment times (such as 1,5, 10 and 30 minutes), while the BCSFB becomes more important that the BBB in influencing total brain tissue and subarachnoid CSF sodium levels at longer experiment times (such as 1, 2 and 3 h). These results suggest that the efficacy of different migraine treatment strategies may depend on the time elapsed from migraine onset. This prediction needs to be tested experimentally for different models of migraines. This study prompts the hypothesis that increased influx permeability of the BCSFB to sodium caused by altered homeostasis of the enzymes which transport sodium from blood to CSF is the potential cause of elevated brain sodium levels in migraines. This hypothesis needs to be tested experimentally. The current model can be used to simulate sodium transport across the BBB, the BCSFB and the ependymal surfaces for a particular migraine trigger, given that the effects of the migraine trigger on the BBB and the BCSFB permeabilities are known. Further studies on the activity levels of different BCSFB and BBB sodium transporters during migraine episodes with different triggers can help better understand migraine pathophysiology.

4.6. Supplementary Information

4.6.1. Global Sensitivity Analysis

In this work, we used a MATLAB toolbox called SAFE [23] to perform a global sensitivity analysis (GSA). SAFE implements several GSA methods such as the Elementary Effects Test, Regional Sensitivity Analysis, and Sobol's technique. Sobol’s method is a variance-based global sensitivity analysis technique which evaluates the sensitivity of the

solutions with respect to the model parameters as well as the interactions between different parameters. Using the principles of variance decomposition, Sobol's method ranks the parameters in terms of their importance. Given an integrable function f over a p-dimensional parameter space Ω^p,

$$y = f(x_1, x_2, \dots, x_p) \tag{S1}$$

Each parameter can vary within a finite range. Sobol's method considers expansion of the response into a set of functions of increasing dimensionality,

$$f(x) = f_0 + \sum_{i=1}^{p} f_i + \sum_{i=1}^{p} \sum_{j>i}^{p} f_{ij} + \cdots + f_{123\dots p}\,, \tag{S2}$$

where each individual term is a function of the parameters in its index. The total variance of the function output is defined by

$$D(y) = \int_{\Omega^p} f^2(x)\, dx - \left(\int_{\Omega^p} f(x)\, dx \right)^2 . \tag{S3}$$

Sobol's technique is based on decomposition of the total variance D into partial variances indicating the contributions from effects of individual parameters and combined effects of pairs of parameters. This decomposition is accomplished using the expansion of f into terms of increasing dimensions (Eq. S2),

$$D(y) = \sum_{i=1}^{p} D_i(y) + \sum_{i=1}^{p} \sum_{j>i}^{p} D_{ij}(y) + \cdots + D_{123\dots p}(y)\,. \tag{S4}$$

According to Sobol's method, the first-order sensitivity index for each parameter is given by

$$S_i = \frac{D_i(y)}{D(y)}\,, \tag{S5}$$

The first-order sensitivity index accounts for the main individual contribution of each model parameter to the variance of the model output. The Sobol's total-effect index, on the other

hand, represents total contribution of the input to the response variation. The total-effect index for parameter x_i is calculated by the sum of all sensitivity indices which have i in their index

$$S_{Ti} = S_i + \sum_{i \neq j} S_{ij} + \sum_{i \neq j, i \neq l, j < l} S_{ijl} + \cdots \quad \text{(S6)}$$

Based on Sobol's approach, the necessary and sufficient condition for parameter x_i to be a noninfluential factor is $S_{Ti} = 0$. However, previous studies have indicated that a parameter can be considered noninfluential if its total-effect sensitivity index is smaller than 0.01, and significantly smaller than total-effect sensitivity indices of the rest of the parameters [33, 34, 84-85].

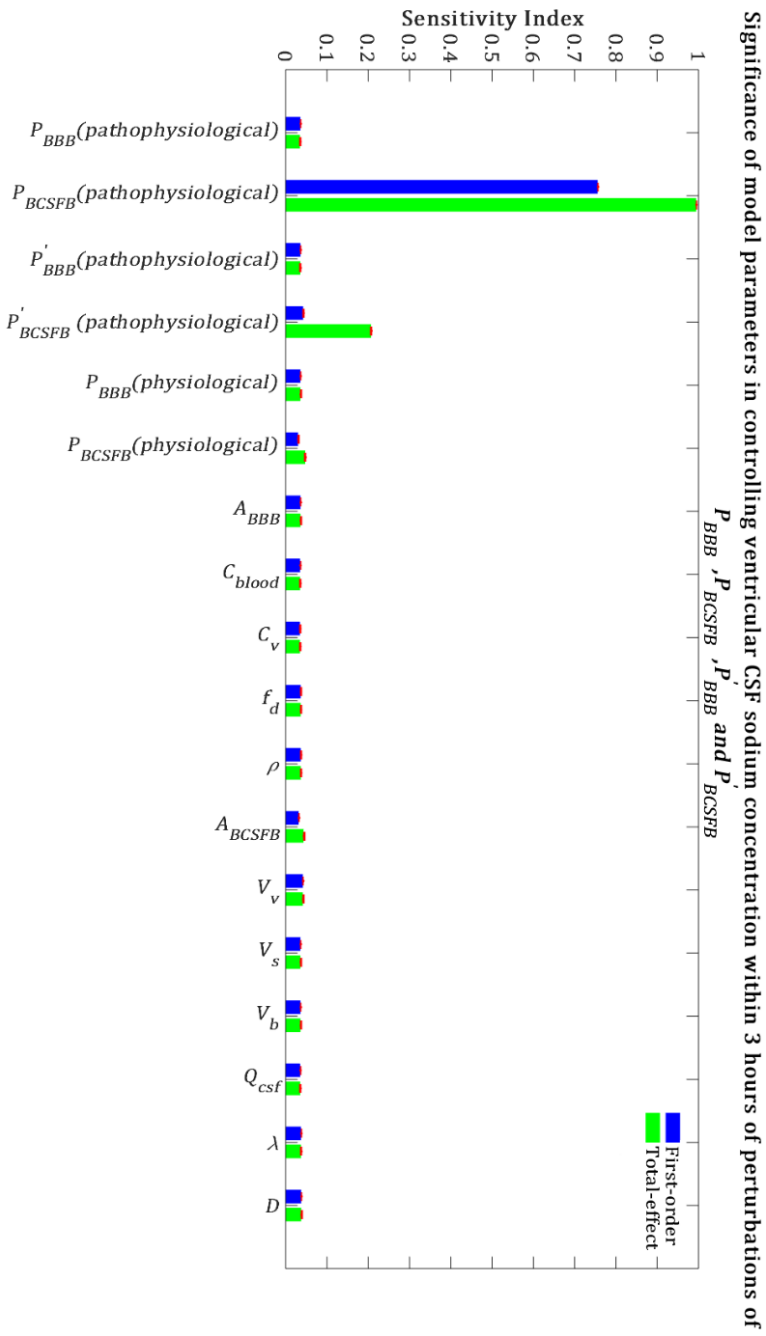

Figure S1. Relative significance of the model parameters in controlling ventricular CSF sodium concentration (C_v) within 3 hours of the perturbation onset ($t_{max} = 3$ h). The blue bars represent first-order sensitivity indices, while the green bars show the total-effect sensitivity indices. The error bars, shown in red, indicate the bootstrap confidence intervals (95% confidence intervals) of the mean values.

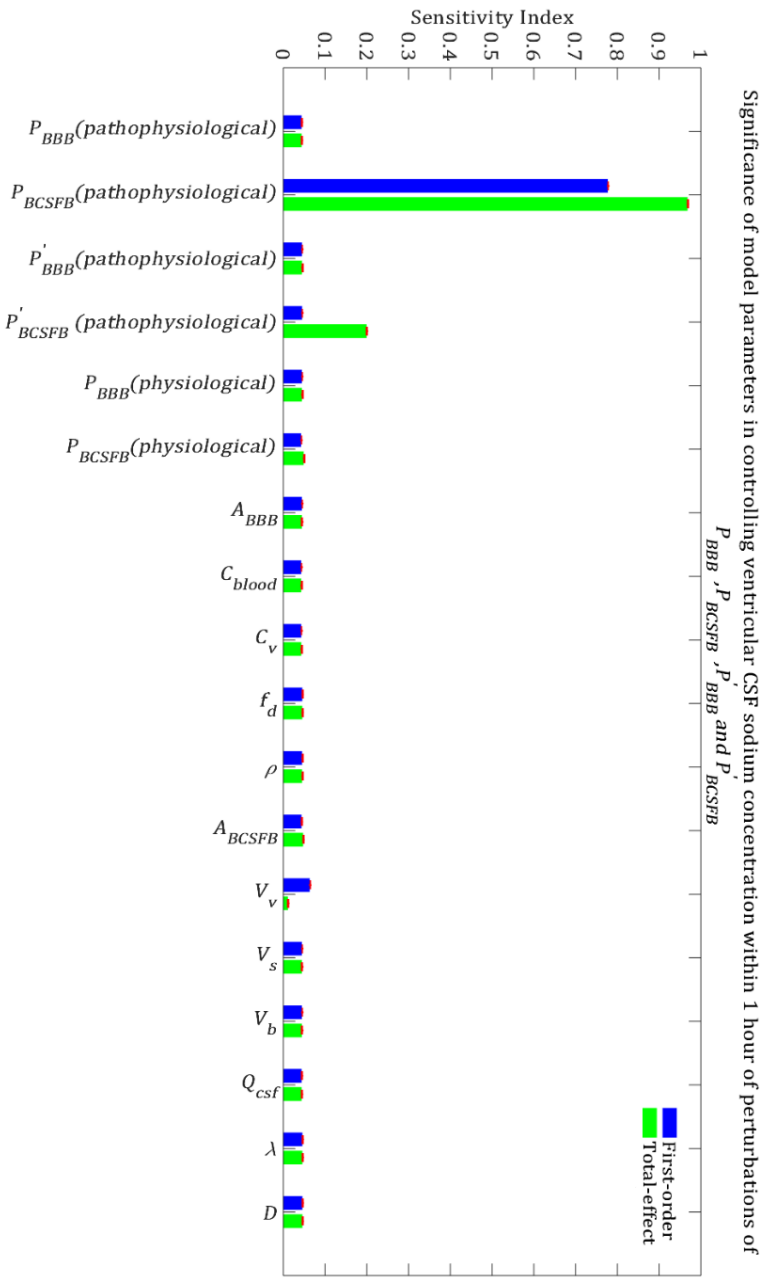

Figure S2. Relative significance of the model parameters in controlling ventricular CSF sodium concentration (C_v) within 1 hour of the perturbation onset ($t_{max} = 1$ h). The blue bars represent first-order sensitivity indices, while the green bars show the total-effect sensitivity indices. The error bars, shown in red, indicate the bootstrap confidence intervals (95% confidence intervals) of the mean values.

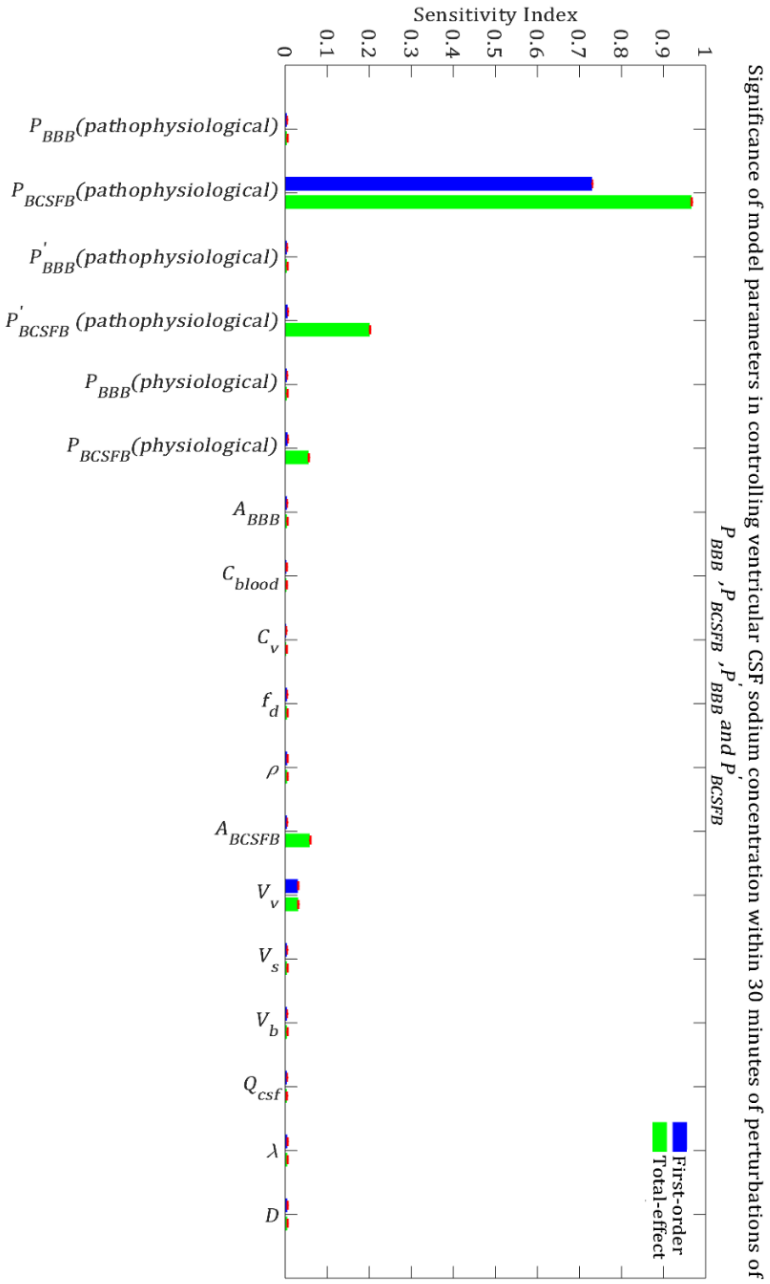

Figure S3. Relative significance of the model parameters in controlling ventricular CSF sodium concentration (C_v) within 30 minutes of the perturbation onset ($t_{max} = 30$ m). The blue bars represent first-order sensitivity indices, while the green bars show the total-effect sensitivity indices. The error bars, shown in red, indicate the bootstrap confidence intervals (95% confidence intervals) of the mean values.

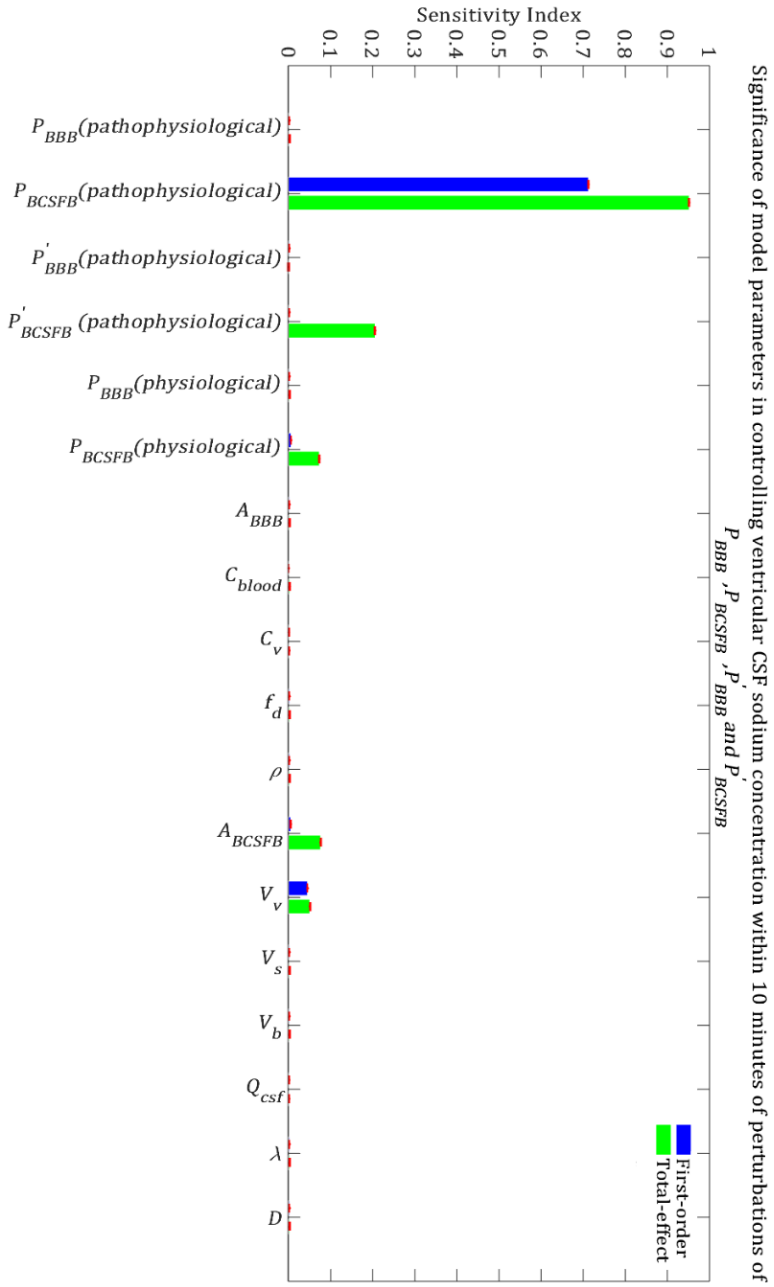

Figure S4. Relative significance of the model parameters in controlling ventricular CSF sodium concentration (C_v) within 10 minutes of the perturbation onset ($t_{max} = 10$ min). The blue bars represent first-order sensitivity indices, while the green bars show the total-effect sensitivity indices. The error bars, shown in red, indicate the bootstrap confidence intervals (95% confidence intervals) of the mean values.

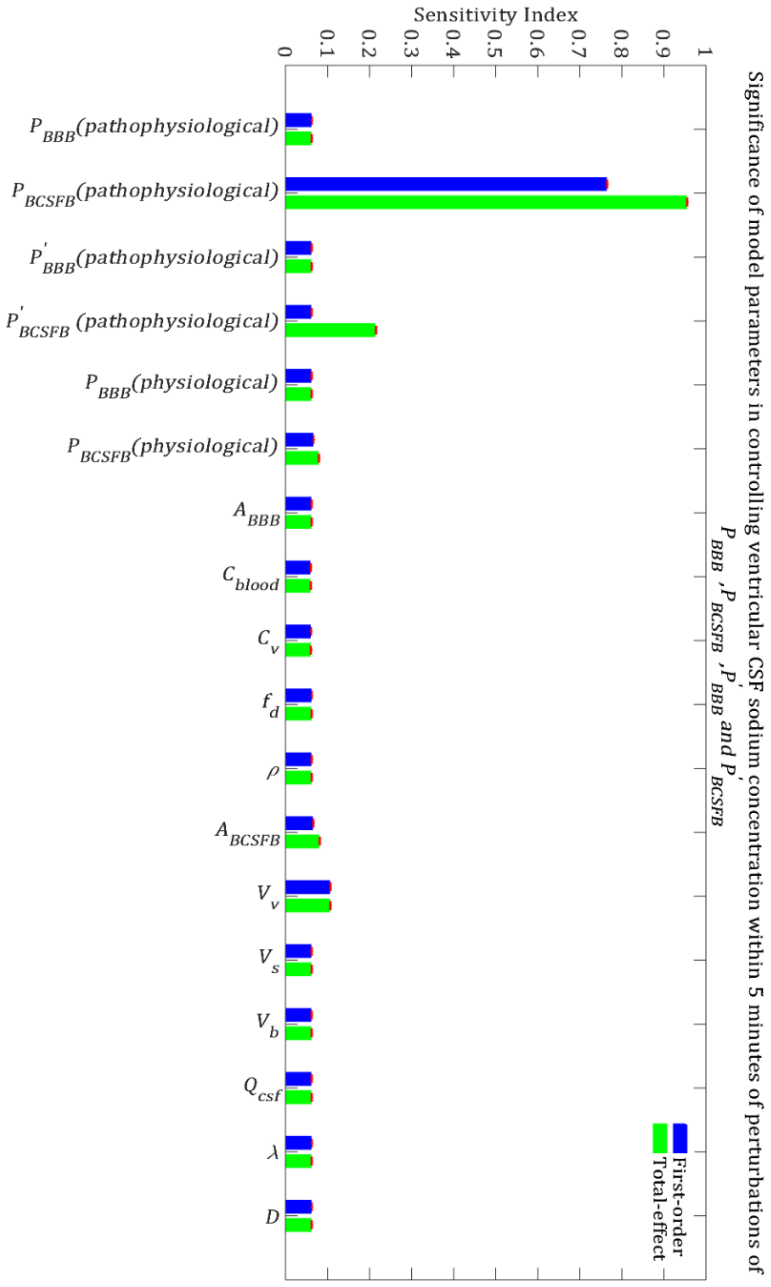

Figure S5. Relative significance of the model parameters in controlling ventricular CSF sodium concentration (C_v) within 5 minutes of the perturbation onset ($t_{max} = 5$ min). The blue bars represent first-order sensitivity indices, while the green bars show the total-effect sensitivity indices. The error bars, shown in red, indicate the bootstrap confidence intervals (95% confidence intervals) of the mean values.

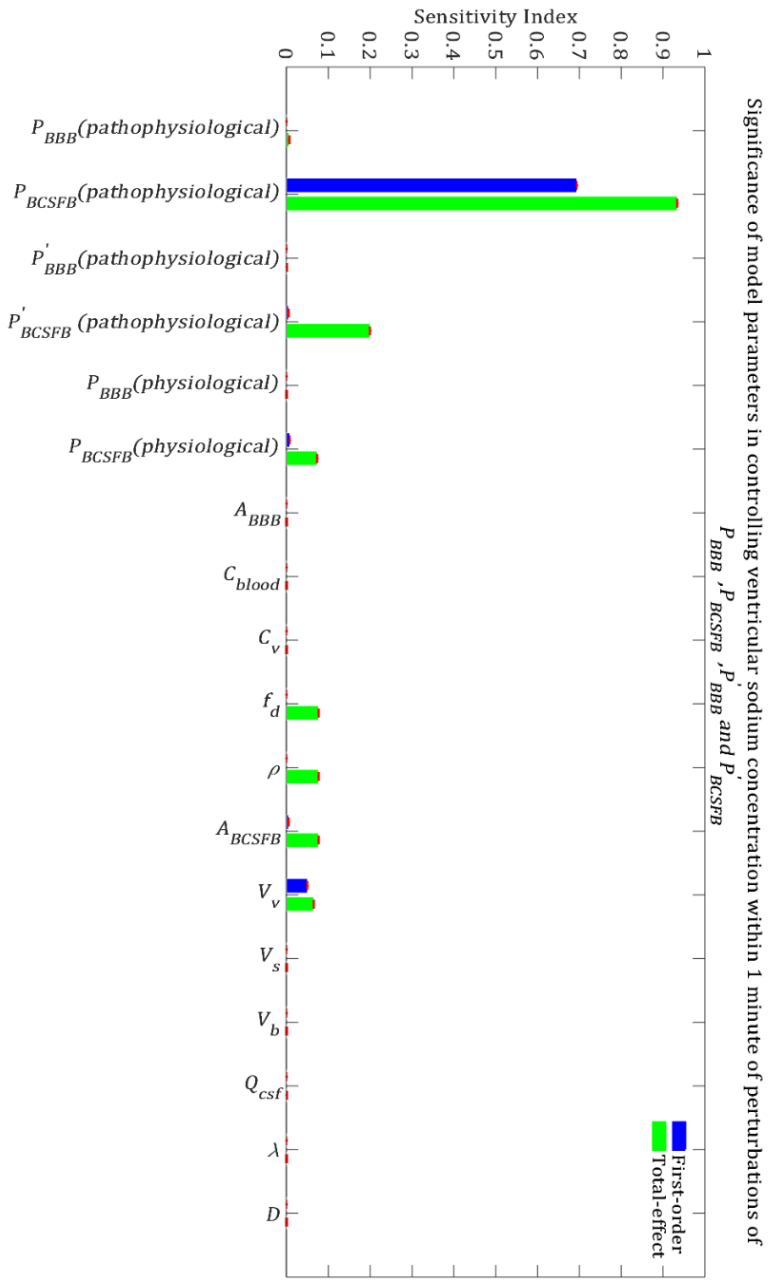

Figure S6. Relative significance of the model parameters in controlling ventricular CSF sodium concentration (C_v) within 1 minute of the perturbation onset ($t_{max} = 1$ min). The blue bars represent first-order sensitivity indices, while the green bars show the total-effect sensitivity indices. The error bars, shown in red, indicate the bootstrap confidence intervals (95% confidence intervals) of the mean values.

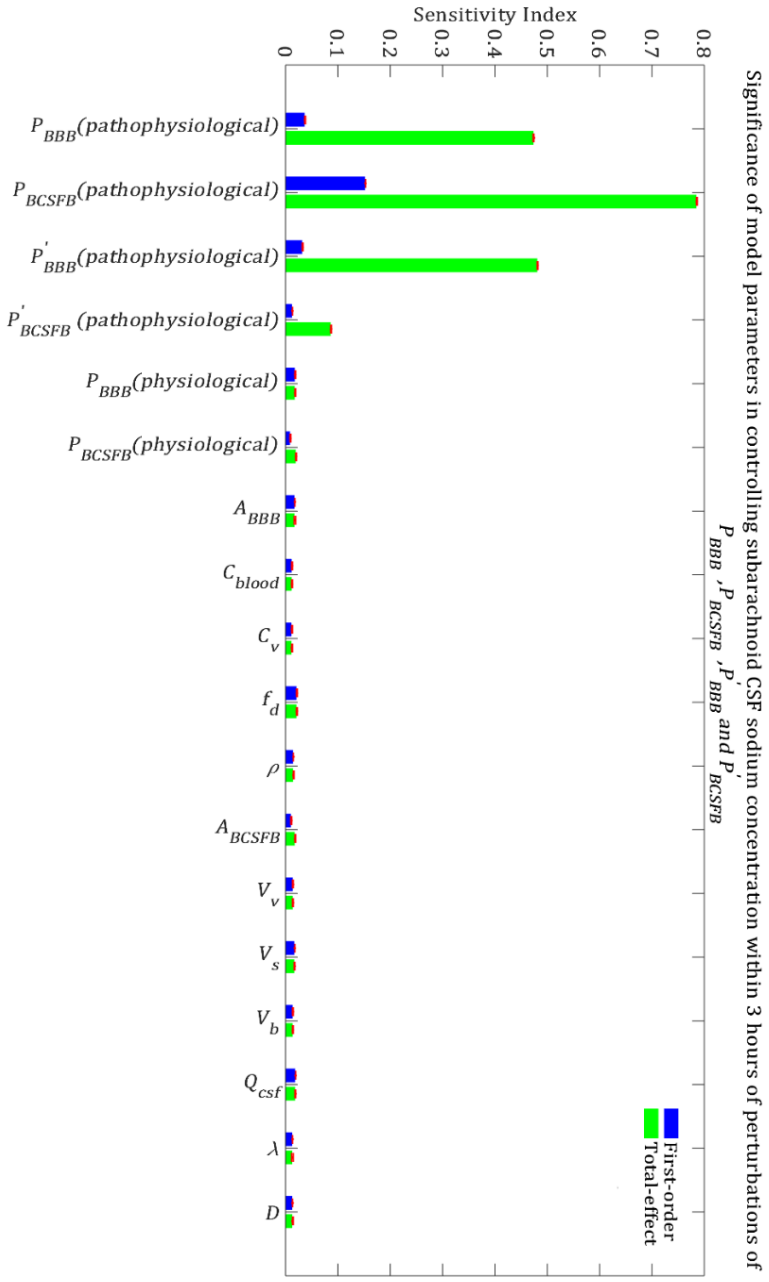

Figure S7. Relative significance of the model parameters in controlling subarachnoid CSF sodium concentration (C_s) within 3 hours of the perturbation onset ($t_{max} = 3$ h). The blue bars represent first-order sensitivity indices, while the green bars show the total-effect sensitivity indices. The error bars, shown in red, indicate the bootstrap confidence intervals (95% confidence intervals) of the mean values.

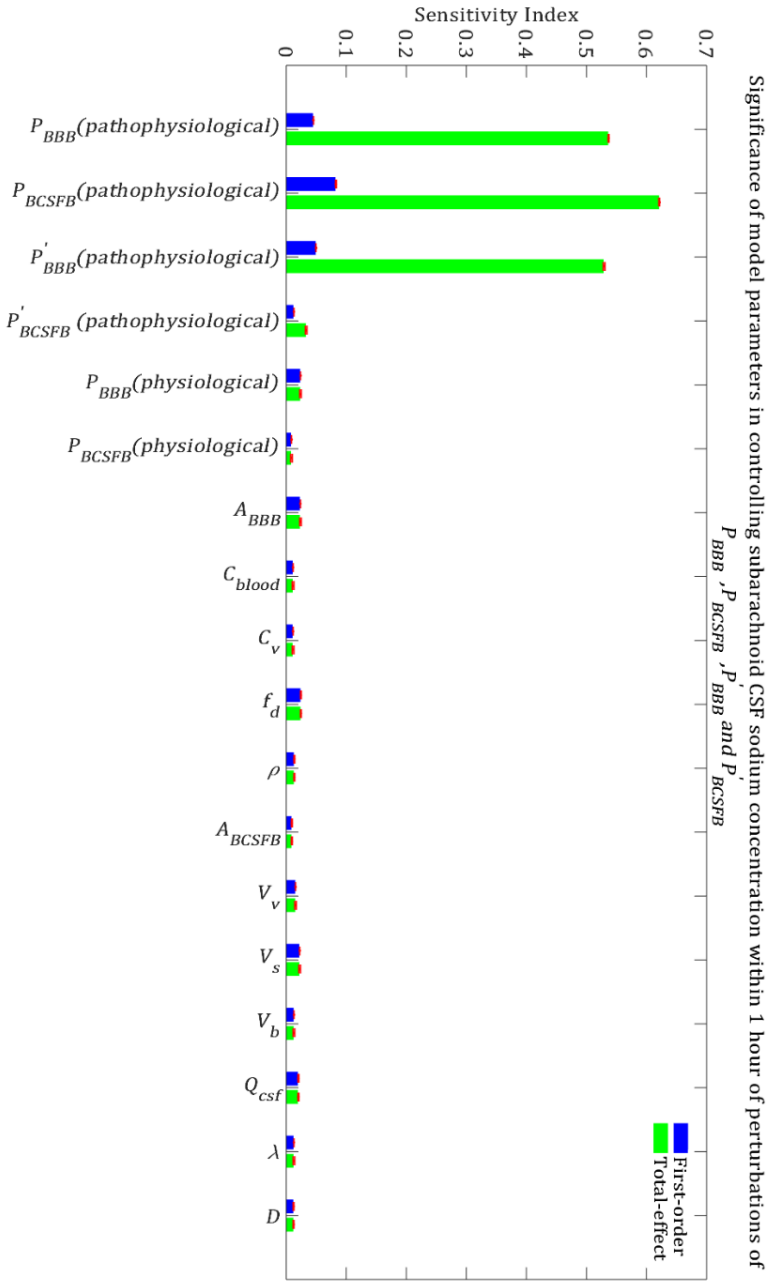

Figure S8. Relative significance of the model parameters in controlling subarachnoid CSF sodium concentration (C_s) within 1 hour of the perturbation onset ($t_{max} = 1$ h). The blue bars represent first-order sensitivity indices, while the green bars show the total-effect sensitivity indices. The error bars, shown in red, indicate the bootstrap confidence intervals (95% confidence intervals) of the mean values.

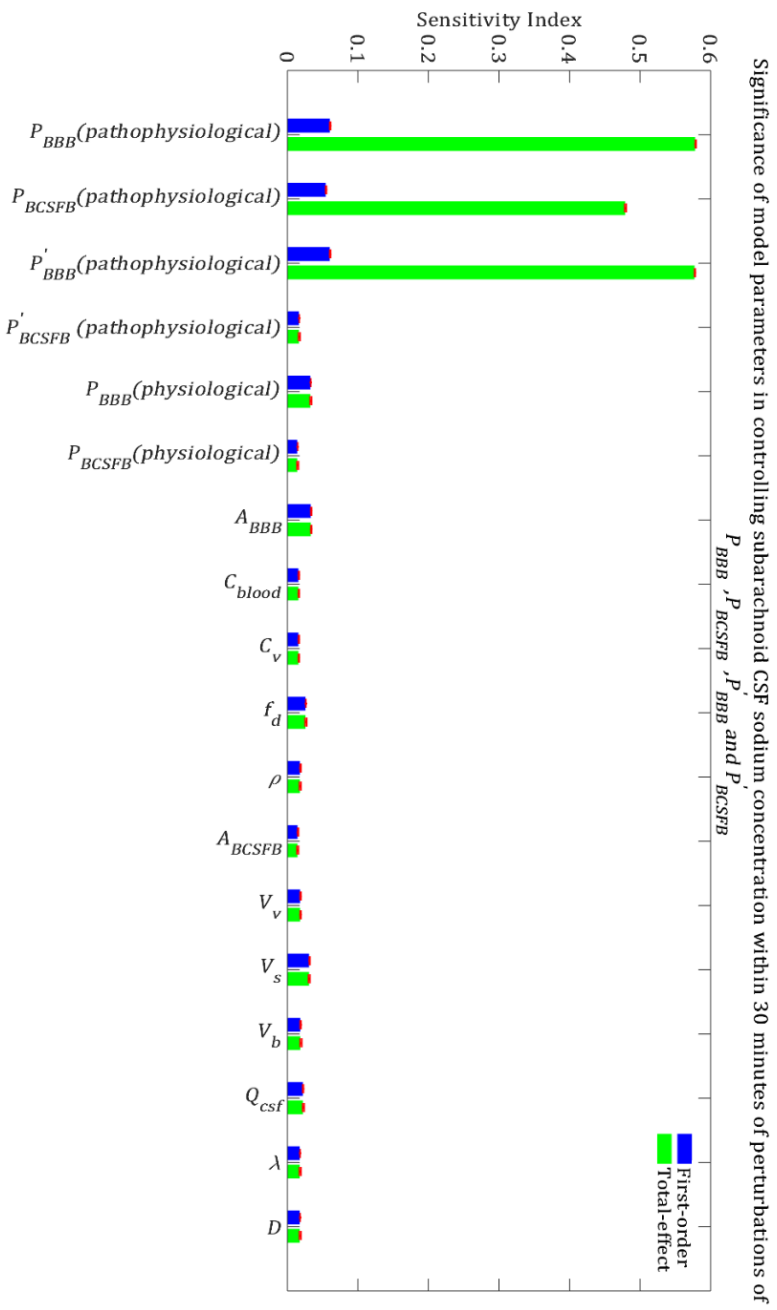

Figure S9. Relative significance of the model parameters in controlling subarachnoid CSF sodium concentration (C_s) within 30 minutes of the perturbation onset ($t_{max} = 30$ min). The blue bars represent first-order sensitivity indices, while the green bars show the total-effect sensitivity indices. The error bars, shown in red, indicate the bootstrap confidence intervals (95% confidence intervals) of the mean values.

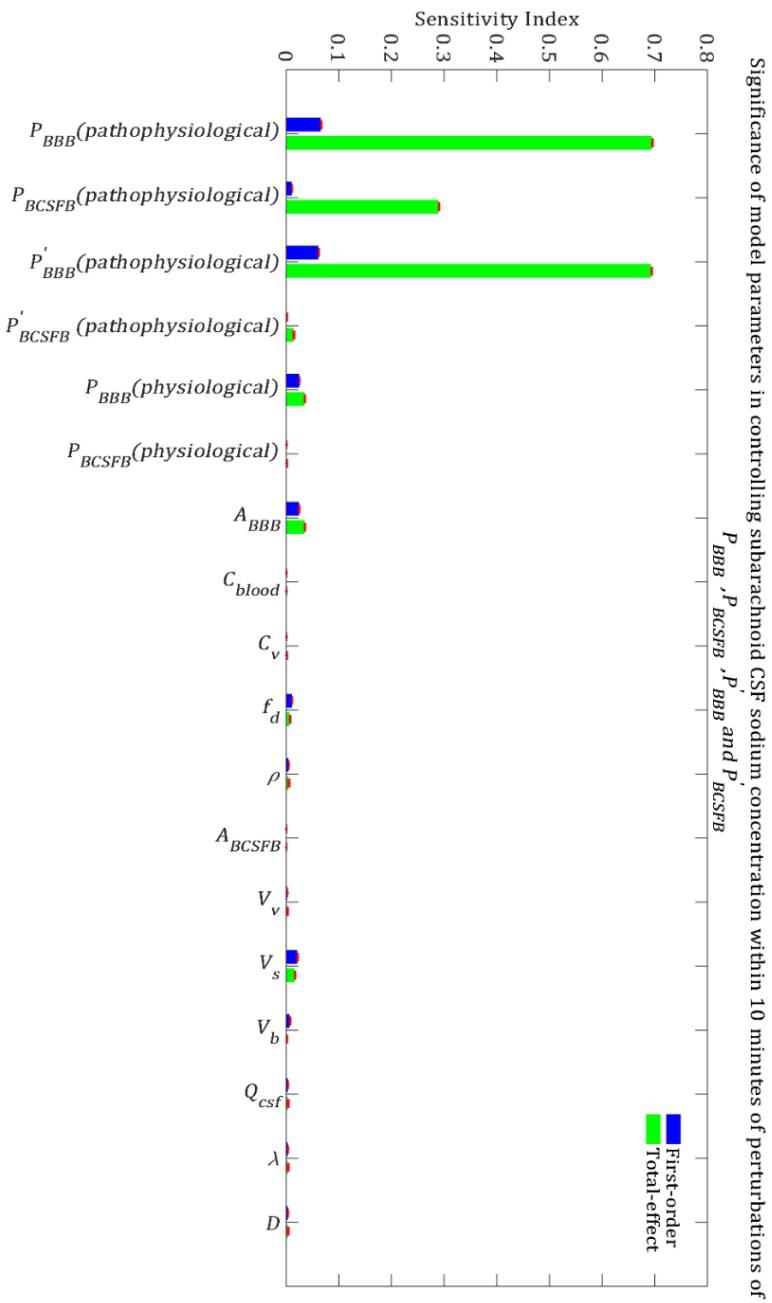

Figure S10. Relative significance of the model parameters in controlling subarachnoid CSF sodium concentration (C_s) within 10 minutes of the perturbation onset ($t_{max} = 10$ min). The blue bars represent first-order sensitivity indices, while the green bars show the total-effect sensitivity indices. The error bars, shown in red, indicate the bootstrap confidence intervals (95% confidence intervals) of the mean values.

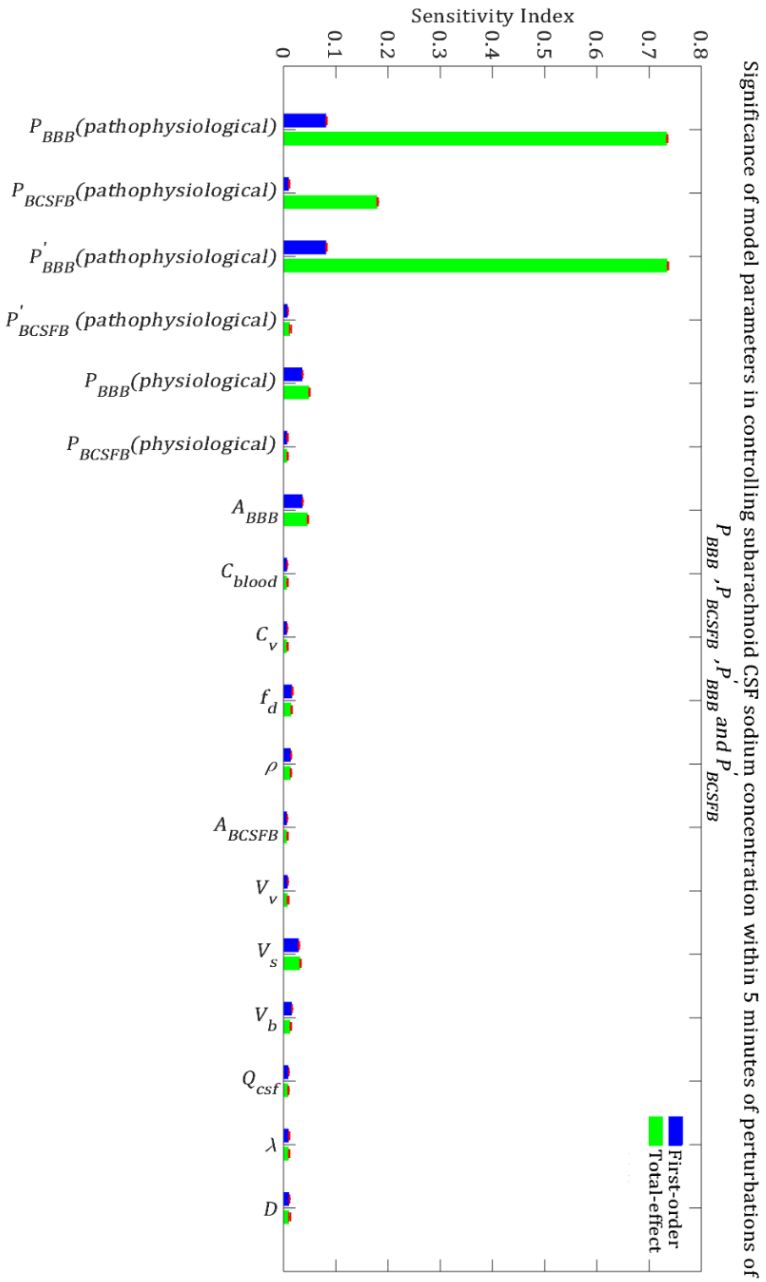

Figure S11. Relative significance of the model parameters in controlling subarachnoid CSF sodium concentration (C_s) within 5 minutes of the perturbation onset ($t_{max} = 5$ min). The blue bars represent first-order sensitivity indices, while the green bars show the total-effect sensitivity indices. The error bars, shown in red, indicate the bootstrap confidence intervals (95% confidence intervals) of the mean values.

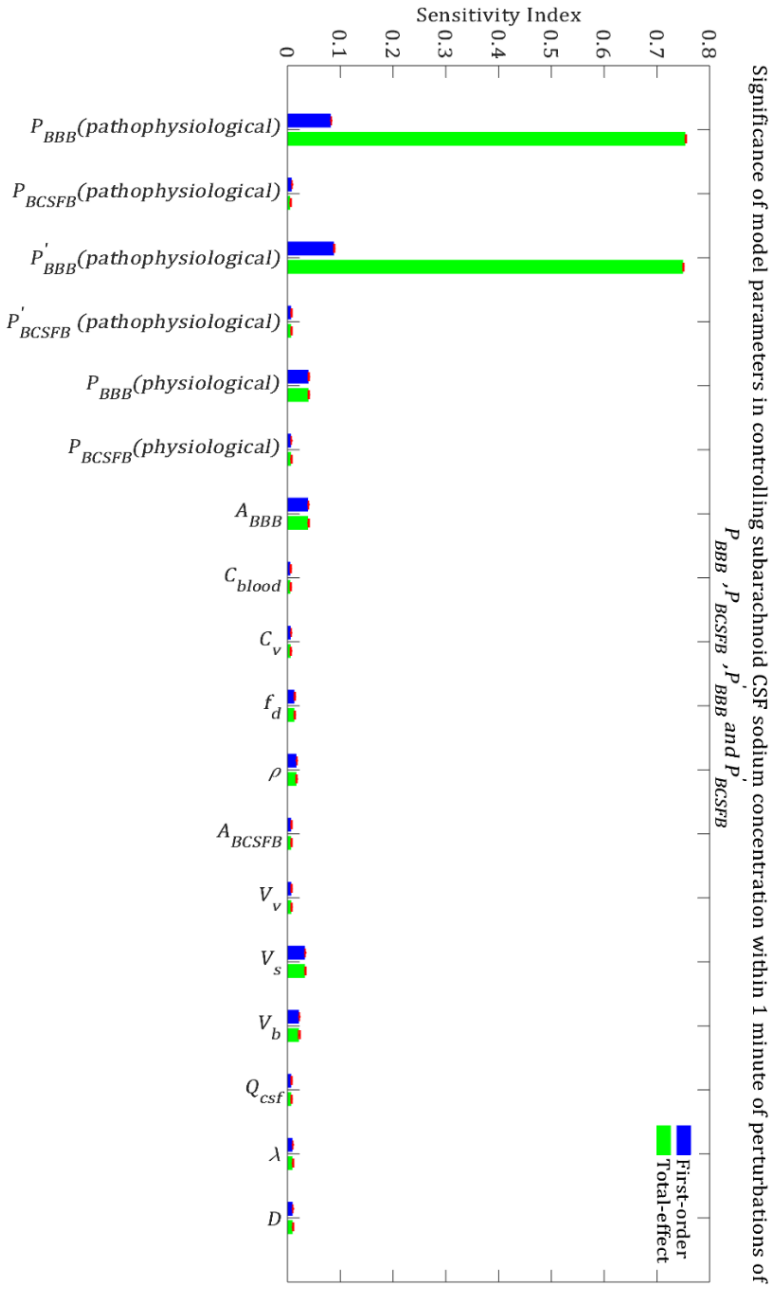

Figure S12. Relative significance of the model parameters in controlling subarachnoid CSF sodium concentration (C_s) within 1 minute of the perturbation onset ($t_{max} = 1$ min). The blue bars represent first-order sensitivity indices, while the green bars show the total-effect sensitivity indices. The error bars, shown in red, indicate the bootstrap confidence intervals (95% confidence intervals) of the mean values.

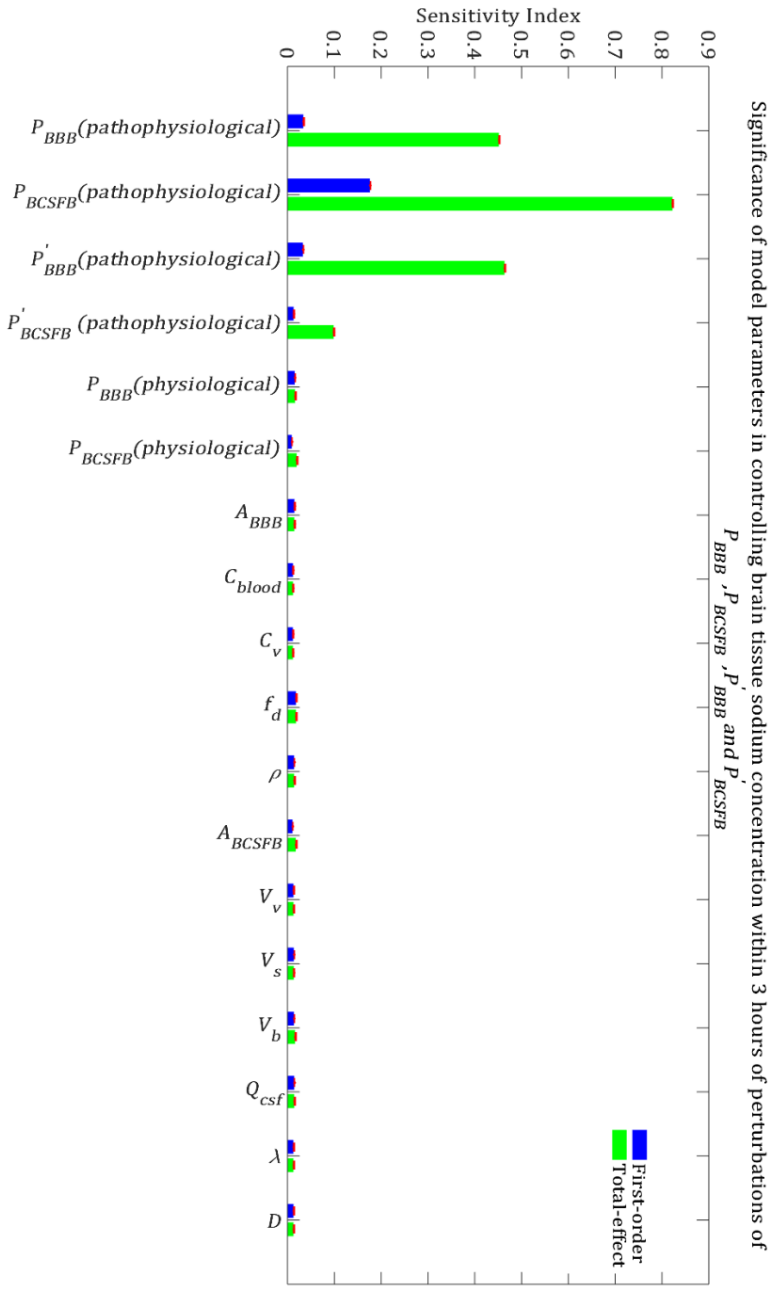

Figure S13. Relative importance of the model parameters in controlling brain tissue sodium levels within 3 hours of the perturbation onset ($t_{max} = 3$ h). The blue bars represent first-order sensitivity indices, while the green bars show the total-effect sensitivity indices. The error bars,

shown in red, indicate the bootstrap confidence intervals (95% confidence intervals) of the mean values.

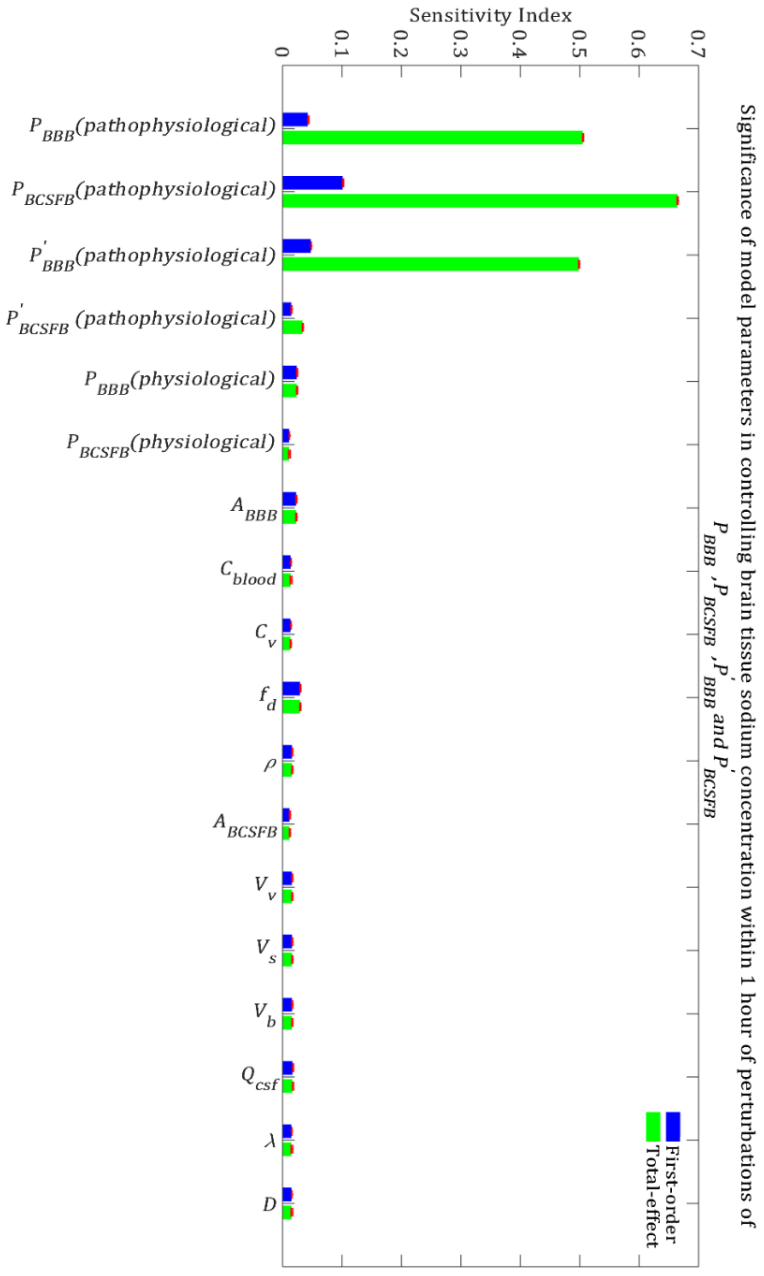

Figure S14. Relative importance of the model parameters in controlling brain tissue sodium levels within 1 hour of the perturbation onset ($t_{max} = 1$ h). The blue bars represent first-order sensitivity

indices, while the green bars show the total-effect sensitivity indices. The error bars, shown in red, indicate the bootstrap confidence intervals (95% confidence intervals) of the mean values.

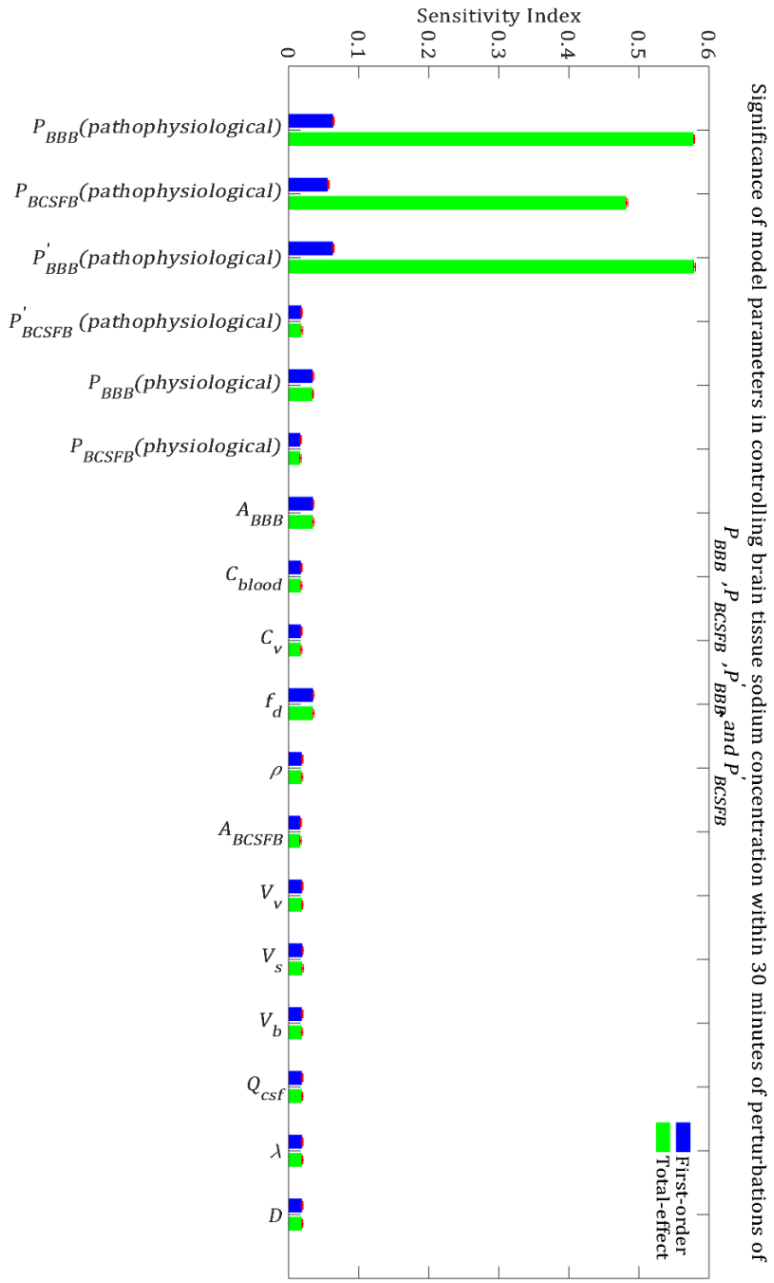

Figure S15. Relative importance of the model parameters in controlling brain tissue sodium levels within 30 minutes of the perturbation onset ($t_{max} = 30$ min). The blue bars represent first-order sensitivity indices, while the green bars show the total-effect sensitivity indices. The error bars,

shown in red, indicate the bootstrap confidence intervals (95% confidence intervals) of the mean values.

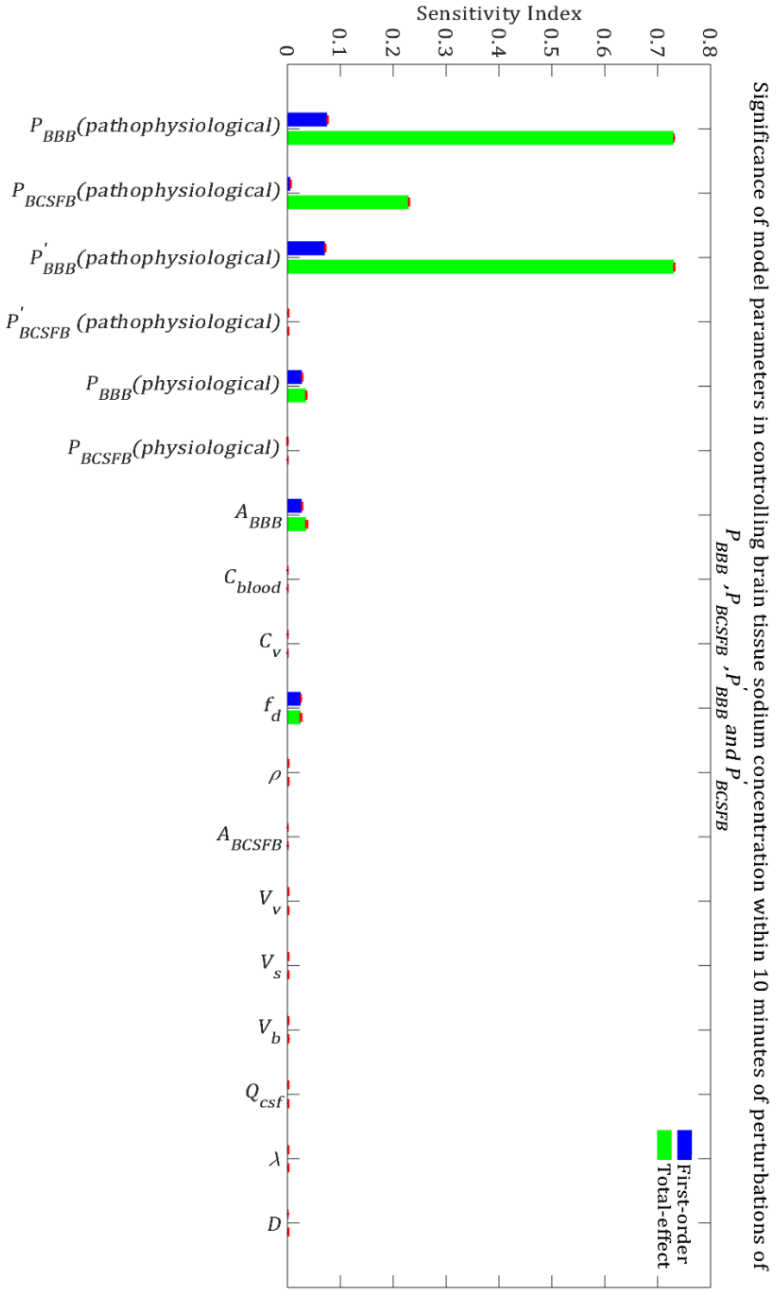

Figure S16. Relative importance of the model parameters in controlling brain tissue sodium levels within 10 minutes of the perturbation onset ($t_{max} = 10$ min). The blue bars represent first-order sensitivity indices, while the green bars show the total-effect sensitivity indices. The error bars,

shown in red, indicate the bootstrap confidence intervals (95% confidence intervals) of the mean values.

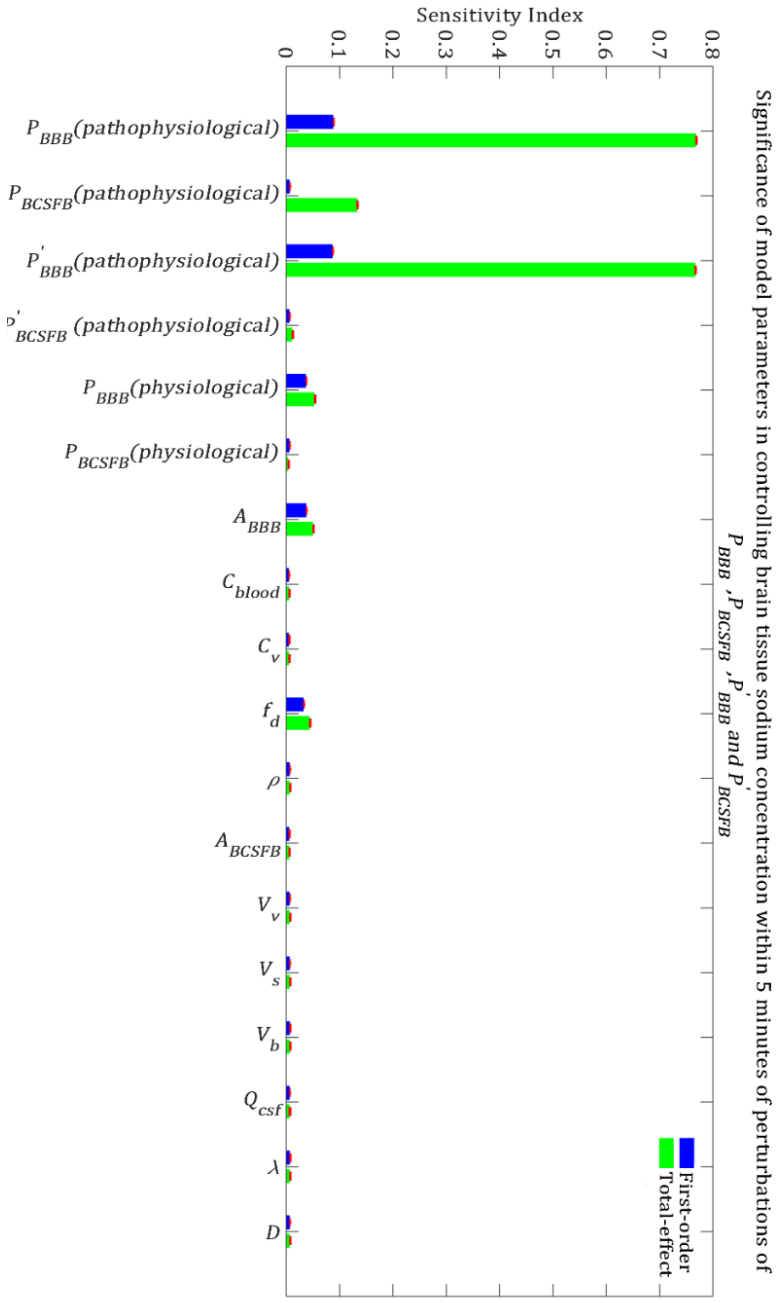

Figure S17. Relative importance of the model parameters in controlling brain tissue sodium levels within 5 minutes of the perturbation onset ($t_{max} = 5$ min). The blue bars represent first-order sensitivity indices, while the green bars show the total-effect sensitivity indices. The error bars,

shown in red, indicate the bootstrap confidence intervals (95% confidence intervals) of the mean values.

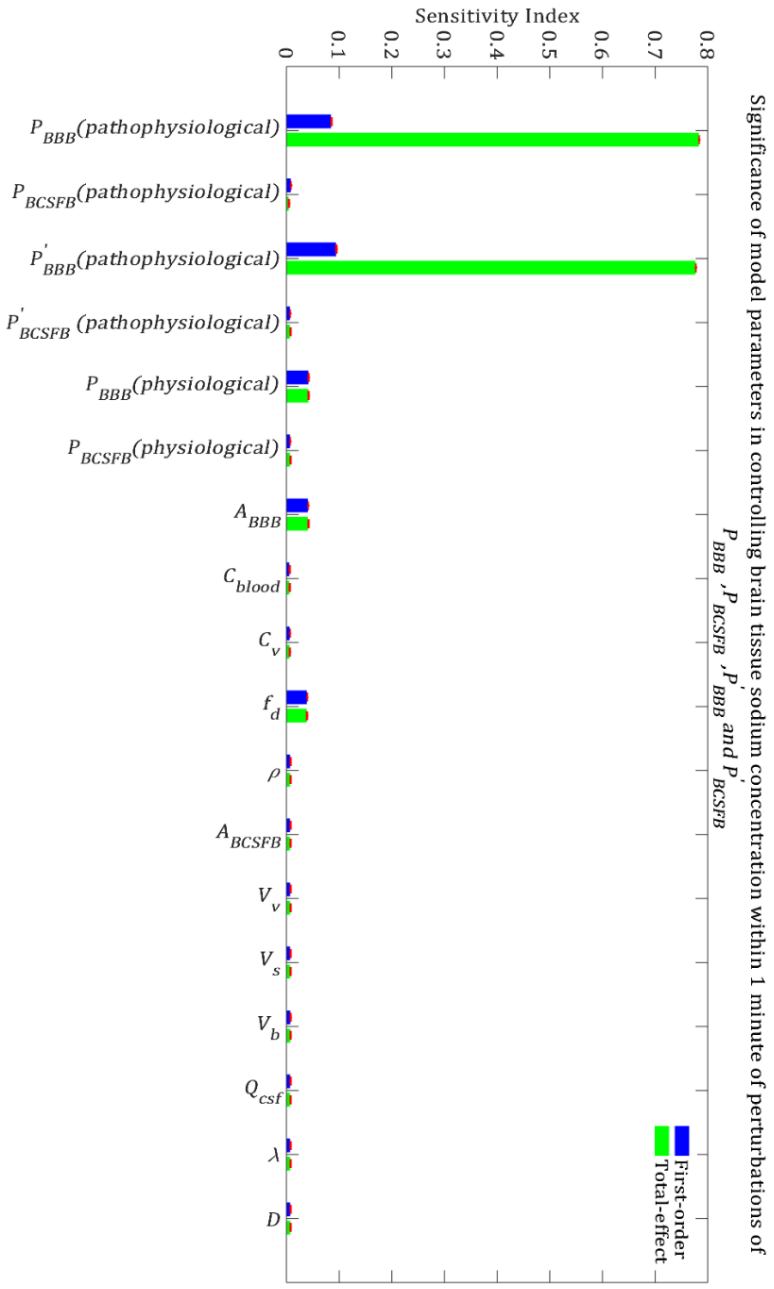

Figure S18. Relative importance of the model parameters in controlling brain tissue sodium levels within 1 minute of the perturbation onset ($t_{max} = 1$ min). The blue bars represent first-order sensitivity indices, while the green bars show the total-effect sensitivity indices. The error bars,

shown in red, indicate the bootstrap confidence intervals (95% confidence intervals) of the mean values.

4.7. References

1. Steiner TJ, Stovner LJ, Vos T, Jensen R, Katsarava Z: Migraine is first cause of disability in under 50s: will health politicians now take notice? In.; 2018.
2. Harrington MG, Fonteh AN, Cowan RP, Perrine K, Pogoda JM, Biringer RG, Hühmer AF: Cerebrospinal fluid sodium increases in migraine. *Headache: The Journal of Head and Face Pain* 2006, 46(7):1128-1135.
3. Abad N, Rosenberg JT, Hike DC, Harrington MG, Grant SC: Dynamic sodium imaging at ultra-high field reveals progression in a preclinical migraine model. *Pain* 2018, 159(10):2058-2065.
4. Harrington MG, Chekmenev EY, Schepkin V, Fonteh AN, Arakaki X: Sodium MRI in a rat migraine model and a NEURON simulation study support a role for sodium in migraine. *Cephalalgia* 2011, 31(12):1254-1265.
5. Meyer MM, Schmidt A, Benrath J, Konstandin S, Pilz LR, Harrington MG, Budjan J, Meyer M, Schad LR, Schoenberg SO: Cerebral sodium (23 Na) magnetic resonance imaging in patients with migraine—a case-control study. *European radiology* 2019:1-8.
6. Hodgkin AL, Katz B: The effect of sodium ions on the electrical activity of the giant axon of the squid. *The Journal of physiology* 1949, 108(1):37-77.
7. Arakaki X, Foster H, Su L, Do H, Wain AJ, Fonteh AN, Zhou F, Harrington MG: Extracellular sodium modulates the excitability of cultured hippocampal pyramidal cells. *Brain research* 2011, 1401:85-94.
8. Hladky SB, Barrand MA: Fluid and ion transfer across the blood–brain and blood–cerebrospinal fluid barriers; a comparative account of mechanisms and roles. *Fluids and Barriers of the CNS* 2016, 13(1):19.
9. Iliff JJ, Wang M, Liao Y, Plogg BA, Peng W, Gundersen GA, Benveniste H, Vates GE, Deane R, Goldman SA: A paravascular pathway facilitates CSF flow through the brain parenchyma and the clearance of interstitial solutes, including amyloid β. *Science translational medicine* 2012, 4(147):147ra111-147ra111.
10. Nedergaard M: Garbage truck of the brain. *Science* 2013, 340(6140):1529-1530.
11. Smith QR, Rapoport SI: Cerebrovascular permeability coefficients to sodium, potassium, and chloride. *Journal of neurochemistry* 1986, 46(6):1732-1742.
12. Brøchner CB, Holst CB, Møllgård K: Outer brain barriers in rat and human development. *Frontiers in neuroscience* 2015, 9:75.
13. Sahin B, Aslan H, Unal B, Canan S, Bilgic S, Kaplan S, Tumkaya L: Brain volumes of the lamb, rat and bird do not show hemispheric asymmetry: a stereological study. *Image Analysis & Stereology* 2011, 20(1):9-13.
14. Goodman JA, Kroenke CD, Bretthorst GL, Ackerman JJ, Neil JJ: Sodium ion apparent diffusion coefficient in living rat brain. *Magnetic Resonance in Medicine: An Official Journal of the International Society for Magnetic Resonance in Medicine* 2005, 53(5):1040-1045.
15. Lei Y, Han H, Yuan F, Javeed A, Zhao Y: The brain interstitial system: Anatomy, modeling, in vivo measurement, and applications. *Progress in neurobiology* 2017, 157:230-246.
16. Kawano Y, Yoshida K, Kawamura M, Yoshimi H, Ashida T, Abe H, Imanishi M, Kimura G, Kojima S, Kuramochi M: Sodium and noradrenaline in cerebrospinal fluid and blood in salt-sensitive and non-salt-sensitive essential hypertension. *Clinical and experimental pharmacology and physiology* 1992, 19(4):235-241.

17. Gomes PM, Sá RWM, Aguiar GL, Paes MHS, Alzamora AC, Lima WG, de Oliveira LB, Stocker SD, Antunes VR, Cardoso LM: Chronic high-sodium diet intake after weaning lead to neurogenic hypertension in adult Wistar rats. *Scientific reports* 2017, 7(1):5655.
18. Levinger I: The cerebral ventricles of the rat. *Journal of anatomy* 1971, 108(Pt 3):447.
19. Dicke U, Roth G: Neuronal factors determining high intelligence. *Philosophical Transactions of the Royal Society B: Biological Sciences* 2016, 371(1685):20150180.
20. Bito L, Davson H: Local variations in cerebrospinal fluid composition and its relationship to the composition of the extracellular fluid of the cortex. *Experimental neurology* 1966, 14(3):264-280.
21. Olsen NS, Rudolph GG: Transfer of sodium and bromide ions between blood, cerebrospinal fluid and brain tissue. *American Journal of Physiology-Legacy Content* 1955, 183(3):427-432.
22. Cserr H, Cooper D, Suri P, Patlak C: Efflux of radiolabeled polyethylene glycols and albumin from rat brain. *American Journal of Physiology-Renal Physiology* 1981, 240(4):F319-F328.
23. Pianosi F, Sarrazin F, Wagener T: A Matlab toolbox for global sensitivity analysis. *Environmental Modelling & Software* 2015, 70:80-85.
24. Kim KA, Spencer SL, Albeck JG, Burke JM, Sorger PK, Gaudet S: Systematic calibration of a cell signaling network model. *BMC bioinformatics* 2010, 11(1):202.
25. Zhang XY, Birtwistle M, Gallo J: A General Network Pharmacodynamic Model–Based Design Pipeline for Customized Cancer Therapy Applied to the VEGFR Pathway. *CPT: pharmacometrics & systems pharmacology* 2014, 3(1):1-9.
26. Ghaffari H, Petzold LR: Identification of influential proteins in the classical retinoic acid signaling pathway. *Theoretical Biology and Medical Modelling* 2018, 15(1):16.
27. Sumner T, Shephard E, Bogle I: A methodology for global-sensitivity analysis of time-dependent outputs in systems biology modelling. *Journal of The Royal Society Interface* 2012, 9(74):2156-2166.
28. Arabghahestani M, Karimian S: Molecular dynamics simulation of rotating carbon nanotube in uniform liquid argon flow. *Journal of Molecular Liquids* 2017, 225:357-364.
29. Zhang XY, Trame M, Lesko L, Schmidt S: Sobol sensitivity analysis: a tool to guide the development and evaluation of systems pharmacology models. *CPT: pharmacometrics & systems pharmacology* 2015, 4(2):69-79.
30. Ghaffari H, Grant SC, Petzold LR, Harrington MG: Regulation of cerebrospinal fluid and brain tissue sodium levels by choroid plexus and brain capillary endothelial cell Na+, K+-ATPases during migraine. *bioRxiv* 2019:572727.

31. Biliouris K, Nestorov I, Naik H, Dai D, Xiao G, Wang Q, Pellerin A, Rabah D, Lesko LJ, Trame MN: A pre-clinical quantitative model predicts the pharmacokinetics/pharmacodynamics of an anti-BDCA2 monoclonal antibody in humans. *Journal of pharmacokinetics and pharmacodynamics* 2018, 45(6):817-827.
32. Ghaffari H, Saidi MS, Firoozabadi B: Biomechanical analysis of actin cytoskeleton function based on a spring network cell model. *Proceedings of the Institution of Mechanical Engineers, Part C: Journal of Mechanical Engineering Science* 2017, 231(7):1308-1323.
33. Sin G, Gernaey KV, Neumann MB, van Loosdrecht MC, Gujer W: Global sensitivity analysis in wastewater treatment plant model applications: prioritizing sources of uncertainty. *Water research* 2011, 45(2):639-651.
34. Tang T, Reed P, Wagener T, Van Werkhoven K: Comparing sensitivity analysis methods to advance lumped watershed model identification and evaluation. *Hydrology and Earth System Sciences Discussions* 2006, 3(6):3333-3395.

35. Murphy VA, Johanson CE: Acidosis, Acetazolamide, and Amiloride: Effects on 22Na Transfer Across the Blood-Brain and Blood-CSF Barriers. *Journal of neurochemistry* 1989, 52(4):1058-1063.
36. Harrington MG, Fonteh AN, Arakaki X, Cowan RP, Ecke LE, Foster H, Hühmer AF, Biringer RG: Capillary endothelial Na+, K+, ATPase transporter homeostasis and a new theory for migraine pathophysiology. *Headache: The Journal of Head and Face Pain* 2010, 50(3):459-478.
37. Gross NB, Abad N, Lichtstein D, Taron S, Aparicio L, Fonteh AN, Arakaki X, Cowan RP, Grant SC, Harrington MG: Endogenous Na+, K+-ATPase inhibitors and CSF [Na+] contribute to migraine formation. *PloS one* 2019, 14(6):e0218041.
38. Collins JM, Dedrick RL: Distributed model for drug delivery to CSF and brain tissue. *American Journal of Physiology-Regulatory, Integrative and Comparative Physiology* 1983, 245(3):R303-R310.
39. Davson H, Welch K: The permeation of several materials into the fluids of the rabbit's brain. *The Journal of physiology* 1971, 218(2):337-351.
40. Leenen FH, Hou X, Wang HW, Ahmad M: Enhanced expression of epithelial sodium channels causes salt-induced hypertension in mice through inhibition of the α2-isoform of Na+, K+-ATPase. *Physiological reports* 2015, 3(5).
41. Huang BS, Van Vliet BN, Leenen FH: Increases in CSF [Na+] precede the increases in blood pressure in Dahl S rats and SHR on a high-salt diet. *American Journal of Physiology-Heart and Circulatory Physiology* 2004, 287(3):H1160-H1166.
42. Wright EM: Mechanisms of ion transport across the choroid plexus. *The Journal of physiology* 1972, 226(2):545-571.
43. Davson H, Segal M: Secretion and drainage of the cerebrospinal fluid. *Acta neurologica latinoamericana* 1971, 1:Suppl 1: 99-118.
44. Van Huysse JW, Amin MS, Yang B, Leenen FH: Salt-induced hypertension in a mouse model of Liddle syndrome is mediated by epithelial sodium channels in the brain. *Hypertension* 2012, 60(3):691-696.
45. Steffensen AB, Oernbo EK, Stoica A, Gerkau NJ, Barbuskaite D, Tritsaris K, Rose CR, MacAulay N: Cotransporter-mediated water transport underlying cerebrospinal fluid formation. *Nature communications* 2018, 9(1):2167.
46. Matsuda T, Murata Y, Kawamura N, Hayashi M, Tamada K, Takuma K, Maeda S, Baba A: Selective induction of α1 isoform of (Na++ K+)-ATPase by insulin/insulin-like growth factor-I in cultured rat astrocytes. *Archives of biochemistry and biophysics* 1993, 307(1):175-182.
47. Therien AG, Blostein R: Mechanisms of sodium pump regulation. *American Journal of Physiology-Cell Physiology* 2000, 279(3):C541-C566.
48. Nishi A, Fisone G, Snyder GL, Dulubova I, Aperia A, Nairn AC, Greengard P: Regulation of Na+, K+-ATPase isoforms in rat neostriatum by dopamine and protein kinase C. *Journal of neurochemistry* 1999, 73(4):1492-1501.
49. Hazelwood LA, Free RB, Cabrera DM, Skinbjerg M, Sibley DR: Reciprocal modulation of function between the D1 and D2 dopamine receptors and the Na+, K+-ATPase. *Journal of Biological Chemistry* 2008, 283(52):36441-36453.
50. Nathanson J, Scavone C, Scanlon C, McKee M: The cellular Na+ pump as a site of action for carbon monoxide and glutamate: a mechanism for long-term modulation of cellular activity. *Neuron* 1995, 14(4):781-794.
51. Davson H, Segal M: The effects of some inhibitors and accelerators of sodium transport on the turnover of 22Na in the cerebrospinal fluid and the brain. *The Journal of physiology* 1970, 209(1):131-153.
52. Pollay M, Hisey B, Reynolds E, Tomkins P, Stevens FA, Smith R: Choroid plexus Na+/K+-activated adenosine triphosphatase and cerebrospinal fluid formation. *Neurosurgery* 1985, 17(5):768-772.

53. Amin MS, Reza E, Wang H, Leenen FH: Sodium transport in the choroid plexus and salt-sensitive hypertension. *Hypertension* 2009, 54(4):860-867.
54. Leenen FH: The central role of the brain aldosterone–"ouabain" pathway in salt-sensitive hypertension. *Biochimica et Biophysica Acta (BBA)-Molecular Basis of Disease* 2010, 1802(12):1132-1139.
55. Wang H-W, Amin MS, El-Shahat E, Huang BS, Tuana BS, Leenen FH: Effects of central sodium on epithelial sodium channels in rat brain. *American Journal of Physiology-Regulatory, Integrative and Comparative Physiology* 2010, 299(1):R222-R233.
56. Javaheri S, Wagner KR: Bumetanide decreases canine cerebrospinal fluid production. In vivo evidence for NaCl cotransport in the central nervous system. *The Journal of clinical investigation* 1993, 92(5):2257-2261.
57. O'donnell ME, Tran L, Lam TI, Liu XB, Anderson SE: Bumetanide inhibition of the blood-brain barrier Na-K-Cl cotransporter reduces edema formation in the rat middle cerebral artery occlusion model of stroke. *Journal of Cerebral Blood Flow & Metabolism* 2004, 24(9):1046-1056.
58. Sun D, Lytle C, O'Donnell ME: Astroglial cell-induced expression of Na-K-Cl cotransporter in brain microvascular endothelial cells. *American Journal of Physiology-Cell Physiology* 1995, 269(6):C1506-C1512.
59. Ennis SR, Ren Xd, Betz AL: Mechanisms of Sodium Transport at the Blood-Brain Barrier Studied with In Situ Perfusion of Rat Brain. *Journal of neurochemistry* 1996, 66(2):756-763.
60. Del Pino MMS, Hawkins RA, Peterson DR: Biochemical discrimination between luminal and abluminal enzyme and transport activities of the blood-brain barrier. *Journal of Biological Chemistry* 1995, 270(25):14907-14912.
61. Betz AL, Firth JA, Goldstein GW: Polarity of the blood-brain barrier: distribution of enzymes between the luminal and antiluminal membranes of brain capillary endothelial cells. *Brain research* 1980, 192(1):17-28.
62. Kurtcuoglu V, Jain K, Martin BA: Modelling of Cerebrospinal Fluid Flow by Computational Fluid Dynamics. In: *Biomechanics of the Brain*. edn.: Springer; 2019: 215-241.
63. Linninger AA, Xenos M, Sweetman B, Ponkshe S, Guo X, Penn R: A mathematical model of blood, cerebrospinal fluid and brain dynamics. *Journal of mathematical biology* 2009, 59(6):729-759.
64. Arabghahestani M, Poozesh S, Akafuah NK: Advances in Computational Fluid Mechanics in Cellular Flow Manipulation: A Review. *Applied Sciences* 2019, 9(19):4041.
65. Howden L, Giddings D, Power H, Aroussi A, Vloeberghs M, Garnett M, Walker D: Three-dimensional cerebrospinal fluid flow within the human ventricular system. *Computer methods in biomechanics and biomedical engineering* 2008, 11(2):123-133.
66. Christensen JD, Barrère BJ, Boada FE, Vevea JM, Thulborn KR: Quantitative tissue sodium concentration mapping of normal rat brain. *Magnetic resonance in medicine* 1996, 36(1):83-89.
67. Hübel N, Schöll E, Dahlem MA: Bistable dynamics underlying excitability of ion homeostasis in neuron models. *PLoS computational biology* 2014, 10(5):e1003551.
68. Dahlem MA, Schumacher J, Hübel N: Linking a genetic defect in migraine to spreading depression in a computational model. *PeerJ* 2014, 2:e379.
69. Hübel N, Dahlem MA: Dynamics from seconds to hours in Hodgkin-Huxley model with time-dependent ion concentrations and buffer reservoirs. *PLoS computational biology* 2014, 10(12):e1003941.
70. Holter KE, Kehlet B, Devor A, Sejnowski TJ, Dale AM, Omholt SW, Ottersen OP, Nagelhus EA, Mardal K-A, Pettersen KH: Interstitial solute transport in 3D reconstructed neuropil

occurs by diffusion rather than bulk flow. *Proceedings of the National Academy of Sciences* 2017, 114(37):9894-9899.
71. Jin B-J, Smith AJ, Verkman AS: Spatial model of convective solute transport in brain extracellular space does not support a "glymphatic" mechanism. *The Journal of general physiology* 2016, 148(6):489-501.
72. Asgari M, De Zélicourt D, Kurtcuoglu V: Glymphatic solute transport does not require bulk flow. *Scientific reports* 2016, 6:38635.
73. Faghih MM, Sharp MK: Is bulk flow plausible in perivascular, paravascular and paravenous channels? *Fluids and Barriers of the CNS* 2018, 15(1):17.
74. Tuz K, Ordaz B, Vaca L, Quesada O, Pasantes-Morales H: Isovolumetric regulation mechanisms in cultured cerebellar granule neurons. *Journal of neurochemistry* 2001, 79(1):143-151.
75. Mountian I, Van Driessche W: Isovolumetric regulation of C6 rat glioma cells in hyperosmotic media. *American Journal of Physiology-Cell Physiology* 1997, 272(1):C318-C323.
76. Moufarrij NA, Harik SI: The effect of locus ceruleus lesion on water, sodium and potassium content of the rat cerebral cortex. *Neurological research* 1989, 11(2):97-100.
77. Schousboe A, Pasantes-Morales H: Role of taurine in neural cell volume regulation. *Canadian journal of physiology and pharmacology* 1992, 70(S1):S356-S361.
78. Fisher SK, Cheema TA, Foster DJ, Heacock AM: Volume-dependent osmolyte efflux from neural tissues: regulation by G-protein-coupled receptors. *Journal of neurochemistry* 2008, 106(5):1998-2014.
79. Abad N, Rosenberg JT, Roussel T, Grice DC, Harrington MG, Grant SC: Metabolic assessment of a migraine model using relaxation-enhanced 1 H spectroscopy at ultrahigh field. *Magnetic resonance in medicine* 2018, 79(3):1266-1275.
80. van Dongen RM, Zielman R, Noga M, Dekkers OM, Hankemeier T, van den Maagdenberg AM, Terwindt GM, Ferrari MD: Migraine biomarkers in cerebrospinal fluid: a systematic review and meta-analysis. *Cephalalgia* 2017, 37(1):49-63.
81. Cananzi A, D'andrea G, Perini F, Zamberlan F, Welch K: Platelet and plasma levels of glutamate and glutamine in migraine with and without aura. *Cephalalgia* 1995, 15(2):132-135.
82. Martinez F, Castillo J, Leira R, Prieto J, Lema M, Noya M: Taurine levels in plasma and cerebrospinal fluid in migraine patients. *Headache: The Journal of Head and Face Pain* 1993, 33(6):324-327.
83. Hertz L, Chen Y: Importance of astrocytes for potassium ion (K+) homeostasis in brain and glial effects of K+ and its transporters on learning. *Neuroscience & Biobehavioral Reviews* 2016, 71:484-505.
84. Cosenza A, Mannina G, Vanrolleghem PA, Neumann MB: Global sensitivity analysis in wastewater applications: A comprehensive comparison of different methods. *Environmental modelling & software* 2013, 49:40-52.

85. Ghaffari H, Grant SC, Petzold LR, Harrington MG. Regulation of CSF and brain tissue sodium levels by the blood-CSF and blood-brain barriers during migraine. *Frontiers in Computational Neuroscience* 2020 Feb 4;14:4.